EVOLUTION OF AN ACOUSTIC DISTURBANCE TO TRANSITION IN THE BOUNDARY LAYER ON AN AIRFOIL

by

Howard S. Kanner

Dissertation submitted to the Faculty of

Virginia Polytechnic and State University

In partial fulfillment of the requirements of the degree of

Doctor of Philosophy

In

Aerospace Engineering

Joseph Schetz, Chairman
Richard Barnwell
Meelan Choudhari
James Marchman
Wing Ng
Richard Wlezien

22 - February 1999

Blacksburg, Virginia

Keywords: Boundary Layer, Receptivity, Tollmien-Schlichting Wave

EVOLUTION OF AN ACOUSTIC DISTURBANCE TO TRANSITION IN THE BOUNDARY LAYER ON AN AIRFOIL

Howard S. Kanner

Abstract

An experiment has been conducted to examine the generation and subsequent evolution of boundary-layer disturbances on a two-dimensional airfoil up through transition to turbulent flow. The experiment was conducted at the NASA Langley Research Center "2 ft by 3 ft Low Speed Wind Tunnel Facility." The primary objective of the experiment was to generate a comprehensive database that includes the effect of the external disturbance environment on the transition process and can be used as a benchmark for future transition prediction tools. The airfoil used for this experiment was custom designed. The model was a 6% thick, 4-ft chord unswept symmetric wing. A description of the design procedure, along with the theoretical stability characteristics of the airfoil will be presented in this paper. The experiment consisted of establishing the mean flow conditions, forcing two-dimensional Tollmien-Schlichting (T-S) waves in the boundary layer using modulated acoustic bursts in the free-stream, and acquiring the mean boundary-layer data and fluctuating disturbance data using hot-wire probes. The acoustic receptivity due to surface roughness near Branch I has been examined. The surface roughness consisted of two-dimensional strips of tape applied at and symmetrically spaced about Branch I. Repeated roughness elements were spaced one wavelength apart based upon the wavelength of the primary forcing frequency as determined by linear-stability theory. The test conditions consisted of mean flow velocities of 15 and 20 m/s, which correspond to chord Reynolds numbers of 1.25 and 1.68 million, respectively. Boundary-layer disturbance profiles and constant boundary-layer height chordwise traverses were acquired and examined at individual frequencies and in total energy amplitude / broadband forms. The experimental results match well with linear stability theory and linear parabolized stability equations, indicating breakdown of disturbances between N-factors of 7 and 11 with surface roughness on the model. It was observed that when the flow physics change, differences between linear-stability theory and experiment are strongly apparent. An amplitude-based breakdown criterion was defined for the developing boundary-layer responses, which were burst-type packets like the acoustic forcing signal. A criterion was defined for the breakdown of both maxima of the T-S-

like disturbance profile. Overall, the effects of surface roughness and free-stream acoustic forcing on boundary-layer receptivity and stability were examined in a well-documented disturbance environment. These results will be used to validate and refine non-linear flow theories as well as help to provide an improved understanding and improved methods to control flow transition.

Acknowledgements

I would like to thank my advisor, Professor Joseph Schetz for all of his guidance, support and encouragement throughout this work. I would also like to thank Dr. Richard Wlezien, NASA Langley Research Center, for all of our technical discussions and his support and guidance.

I am grateful to all whom have made this project possible including Dr. Meelan Choudhari, High Technology Corporation, and Dr. Ronald Joslin, NASA Langley Research Center, and to Dave Chestnutt and Rita Aguillard of the Virginia Consortium for Engineering and Science Universities who helped make the virtual campus a smaller world.

I would like to express my appreciation to Innovative Aerodynamic Technologies for use of the LAMDA airfoil analysis package and Fei Li of High Technology Corporation for completing linear PSE solutions.

Finally, I would like to express my deep gratitude to my wife Amy and my daughters Quinn and Bryce who were always there for me.

This work was performed with the support of NASA Grant NAG-1-1682

Contents

Appendices:

Nomenclature

a, speed of sound
b, span
b, gaussian waveform coefficient
C_p, pressure coefficient
c, chord
c, convection wave speed
e, hot-wire voltage
$F = 2 \pi f \nu / U^2 \times 10^6$, dimensionless frequency
g, gaussian envelope function
h, roughness height
$M = U / a$, Mach number
N-factor $= \ln (u_{TS} / u_{ref})$, logarithmic disturbance amplitude ratio
$OHR = r_{hw} / r_{cold} - 1$, hot-wire over-heat ratio
$Re_x = \rho U x / \mu$, Reynolds number based upon length scale x
SF_{in}, boundary-layer stepping scale factor for traversing inside the boundary layer
SF_{out}, boundary-layer stepping scale factor for traversing above the boundary layer
$S = \omega \rho / U_\infty$, Strouhal number
T, temperature
t, airfoil thickness
U, mean streamwise velocity
u, fluctuating streamwise velocity component
x, chordwise or stream-wsie coordinate
y, chord-normal coordinate
α, angle of attack
α_o, hot-wire temperature coefficient of resistivity at reference temperature T_o
δ, boundary-layer thickness
δ^*, displacement thickness
f, frequency
λ, wavelength
μ, absolute viscosity
$\nu = \mu / \rho$, kinematic viscosity
θ, momentum thickness
ρ, density

Subscripts

cal, calibration
c, corrected
d, disturbance
DS, downstream source
fs, ∞, free-stream
LPSE, linear parabolized stability equations
LST, linear stability theory
min, minimum
p-p, peak-to-peak amplitude
rms, root-mean-square energy amplitude
s, acoustic source signal
th, theory
T-S, Tollmien-Schlichting disturbance
US, upstream source

Figures

Tables

1 Introduction

1.1 Background

Knowledge of the stability and transition to turbulence of boundary layers is a highly desired goal in the fields of fluid mechanics and aerodynamics[1]. Laminar flow is sometimes a desired flow condition because a laminar boundary layer exhibits significantly less drag than a turbulent boundary layer, except in the case of flow separation, where a more energetic turbulent boundary layer can delay or prevent flow separation. Once an understanding of the flow physics is made, then control of the flow can be effectively completed, and performance benefits can be achieved. The physics of flow transition consists of several processes, receptivity, linear growth, non-linear breakdown and finally turbulent flow. Flow transition can occur over an extended distance, as will be examined herein, as well as over an immeasurably small distance via a bypass mechanism.

A significant application of using the knowledge of transitional flow physics is Laminar Flow Control (LFC), the process of delaying boundary-layer transition[2]. The development of Laminar Flow Control technology for application to transport aircraft (Pfenninger et al.[3]) requires an understanding of boundary-layer transition physics and transition prediction capabilities. While this dissertation will not go into a detailed discussion of the current status of LFC research, the author will discuss the recent efforts in the more general field of boundary-layer stability from receptivity through transition.

1.2 History of Boundary-Layer Stability Studies

Flow stability and transition were first investigated by Reynolds in 1883 with his classic pipe flow experiment. Stability theory has been developing dramatically since the 1920's, when Tollmien[4, 5], Schlichting[6, 7], made their contributions. Tollmien and Schlichting examined solutions to the Orr-Sommerfeld equation, using the method of small oscillations on flat plates and rotating cylinders. The Orr-Sommerfeld equation is a simplification of the Navier-Stokes equations of motion, which assumes laminar, incompressible, two-dimensional, constant property, and parallel flow. However, the Orr-Sommerfeld equation is used as a good

approximation to solve near parallel flows, because the neglected terms have little effect on the solution[8]. The method used by Tollmien and Schlichting identified disturbance eigen-solutions too small to be measured with the state of technology current at that time. With the development of low turbulence wind tunnels, Schubauer and Skramstad[9] first experimentally identified the sinusoidal oscillations within the laminar boundary layer on a flat plate in the early 1940's. By the 1960's, flight tests were being performed with suction being used to stabilize the boundary layer on swept wings[10]. Morkovin[11] completed a detailed evaluation of flow transition research as of 1968, where he summarized low-speed and high-speed efforts with the intent to identify future research in hypersonic flow stability. Extensive bibliographies of LFC research have been completed by Bushnell and Tuttle[12], summarizing research efforts as of 1978, and Tuttle and Maddalon[13], summarizing efforts as of 1991.

In low disturbance environments, boundary-layer transition involves the internalization of external disturbances in the form of linear instability waves (receptivity), followed by the linear growth and non-linear breakdown of disturbances up to the onset of turbulent flow. Work by Murdock[14] identified the leading-edge region as one where a plane sound wave can interact with the boundary layer and subsequently generate a Tollmien-Schlichting (T-S) wave. Murdock also noted that the two waves are independent of each other elsewhere over the boundary layer. The physical mechanisms behind receptivity were first explained by Goldstein[15, 16], where he showed that while the asymptotic eigen-solutions of Lam and Rott[17] couple with free-stream disturbances and match onto T-S waves further downstream in the flow, they originate in the boundary layer at the receptivity site. This was later re-derived by Ackerberg and Phillips[18].

For this experiment, only Tollmien-Schlichting (T-S) boundary-layer disturbances are expected to be generated. T-S disturbances are viscous instabilities that can be characterized as eigenmodes of the Orr-Sommerfeld equation[19]. They are sinusoidal in time. Acoustic forcing was selected to generate such disturbances for this experiment. T-S disturbances are not the only boundary-layer disturbances that have been historically examined, but they are applicable disturbances for this experiment. Crossflow disturbances are inviscid flow instabilities typical on swept wings. Taylor-Goertler vortices are characteristic of flows past concave walls[20]. All of the above-described disturbances are known to amplify and decay within the boundary layer,

significantly affecting the stability of the boundary layer. The boundary layer also will contain an acoustic, or Stokes wave, since the acoustic field is a plane traveling wave.

The two most common types of free-stream disturbances in low speed flows that can couple with boundary-layer instabilities are acoustic and vortical. Most research in this field has centered upon forcing the boundary layer with known free-stream disturbances. To date, receptivity experiments with T-S disturbances have been limited to flat plate geometry. However, Radeztsky, et al., have recently examined the excitation of crossflow instabilities[21] on a swept wing.

While the physical mechanisms that lead to transition, such as receptivity, linear amplification, and breakdown to turbulence, have been extensively studied individually[1, 22, 23, 24, 25], there exist few experiments that track the transition process continuously from receptivity to non-linear breakdown, especially over surfaces of engineering interest. Hence, there is a need for careful transition experiments with clearly documented disturbance environments.

The study of acoustic boundary-layer receptivity on an airfoil geometry promises significant improvement in the current understanding of receptivity, as an airfoil, no matter how simple, is a more practical geometry than a flat plate to current flying configurations. Flat plates have been examined in previous experiments[26, 27, 28, 29, 30, 31, 32, 33, 34, 35, 36, 37], and they typically had elliptic leading edges and a zero or constant pressure gradient. There was a discontinuity in curvature at the juncture between the elliptical leading edge and the flat plate. This surface discontinuity resulted in large local pressure gradients and presented a strong source for receptivity, overwhelming the receptivity due to the non-parallel nature of the flow just aft of the stagnation point. In analyzing an airfoil, a leading-edge receptivity mechanism similar to that examined by Goldstein[15] can be studied. This mechanism is receptivity due to the non-parallel nature of the flow. Unlike flat plates with various leading edge geometries incorporated, airfoil shapes in practice do not have such large local pressure gradients at a leading-edge-body juncture because of continuous geometry, slope and curvature. Therefore, receptivity on aerodynamic surfaces is likely to be quite different from that on a flat plate.

Transition in a low-disturbance environment involves three stages: receptivity or the generation of boundary-layer instability waves, linear amplification of the waves, and non-linear interactions and breakdown to turbulence. A detailed discussion of boundary-layer transition and an overview of the theory are presented in Saric[38], including details on receptivity and experimental techniques.

1.2.1 Receptivity

The initial stage of transition in which external disturbances interact with the boundary layer to generate unstable eigen-modes of the boundary layer is called "Receptivity," a word originally suggested by Morkovin[11]. Typically, in order to excite a particular mode of instability, the forcing signal needs to be of the same order of magnitude in frequency and spatial scale. However, free-stream disturbances are generally governed by inviscid flow dynamics, and their wavelengths are much longer than the wavelengths of the instability within the boundary layer. Hence, the free-stream unsteadiness must be "tuned" to the instability length scale. This occurs when the flow is non-parallel in nature; i.e. the mean flow exhibits rapid variations in the streamwise direction[39]. Non-parallel flow can occur in the leading-edge region near the stagnation point, in the vicinity of an inhomogeneity on the surface, and near flow separation. In the leading-edge region, the non-parallel flow results from the rapidly changing thickness of the boundary layer. Surface inhomogeneities can disturb the parallel flow either locally or continuously over a region. Such inhomogeneities can consist of surface roughness or non-uniformities in surface distributions (suction/blowing velocity, porosity, and temperature). Flow separation due to a locally adverse pressure gradient also can trigger the receptivity of a boundary layer and lead to turbulent flow. Ruban[26] examines the interaction of sound waves with a single surface irregularity. Several receptivity mechanisms have been theoretically examined by Choudhari and Streett[27] and Crouch[40] comparing classical stability theory with numerical solutions of the parabolized stability equations, the full Navier-Stokes equations, and experiments. Acoustic receptivity associated with leading edges[41, 42, 43], porous surfaces with and without net suction[28, 29, 44], surface temperature variations[30, 31], two- and three-dimensional roughness[32, 33, 34, 35, 36, 45], and continuous wall waviness[35, 40, 37] have all been examined theoretically, and to some extent, experimentally.

1.2.1.1 Receptivity to Modulated Bursts

There has been only a little research into examining the effects of modulated bursts on boundary-layer stability. Gaster[22, 46], Shaikh and Gaster[47], and Medeiros and Gaster[48] examined the evolution and non-linear breakdown of acoustic point sources. It was observed that modulated waves displayed non-linear behavior at smaller amplitudes than regular wave trains. It should be noted that the above work involved a three-dimensional forcing field, while the experiment to be described herein involved a two-dimensional acoustic forcing field.

Saric, et al.[49] and Saric and White[50] examined the effects of modulated acoustic bursts on a flat plate with modified super ellipse leading-edge geometry for both leading-edge receptivity and two-dimensional roughness receptivity. The latter work also examined the white noise / broadband response of the boundary layer. The results demonstrated how the different wave speeds of the T-S response and the Stokes wave / acoustic forcing signal temporally result in separate signals in the time domain. Ensemble averaging multiple bursts reduced the error and minimized the effects of low frequency oscillations in the test environment. This is a much simpler method than methods previously used, as described by Wlezien[51] and Saric[38], which involve decomposing a boundary-layer signal of its T-S and Stokes components which occur simultaneously.

Dietz[52, 53, 54] performed experiments where he generated free-stream forcing from a vibrating ribbon located upstream of a flat plate with an elliptic leading edge. He examined the effects of single and multiple two-dimensional roughness elements with various single and broadband forcing signals. Dietz noted in the above articles that the boundary-layer responses due to broadband forcing could be modeled by the linear superposition of the responses due to discrete frequencies. Dietz also noted that three-dimensional wave packets, such as those due to turbulence, had significantly lower response amplitudes[53].

1.2.2 Transition Prediction

Traditional transition prediction methods account only for the linear amplification phase of the transition process. The linear analysis addresses unsteady linear disturbances as they propagate through the steady, laminar flow in the boundary layer. Typically, the boundary-layer flow is assumed to be quasi-parallel for the purpose of linear stability analysis. Linear stability theory is discussed in detail by Mack[55].

The Smith-Van Ingen e^N or amplification-ratio method[56, 57] postulates that transition occurs when the N-Factor defined as

$$N = ln\left(A/A_0\right) = \int_{x_0}^{x} -\alpha_i dx \qquad \textbf{Equation 1-1}$$

reaches a predefined value, typically about 9 or 10, which was based upon past experience[58]. Here, A_o is the amplitude of the disturbance at the lower branch of the neutral stability curve, A is the amplitude of the disturbance at a distance x downstream of the lower branch, and α_i is the imaginary component of the boundary-layer disturbance wave number in the streamwise direction. The e^N method has had considerable success in predicting transition in a variety of flows, which have been summarized in reviews by Bushnell and Malik[2] and Reed, Saric and Arnal[19].

Technical advances in recent years have opened the possibility of incorporating the receptivity stage and the non-linear stage into transition prediction. Amplitude methods incorporate the receptivity process and more detailed flow physics than linear analyses, and work with absolute amplitudes of the boundary-layer instabilities. By incorporating receptivity, amplitude methods enable transition prediction to be based upon absolute disturbance amplitudes, as compared to an amplitude ratio used in linear analysis methods. This is because the calculations follow the entire growth cycle of the disturbance and absolute amplitude data is available. Amplitude methods are significant because they offer a way to incorporate additional physics into the transition prediction and reduce empiricism. Amplitude methods will allow for the effects of free-stream disturbances and surface disturbances on transition, as well as account for non-linear, non-parallel and curvature effects with the boundary layer on transition.

The predictions of amplitude methods can be verified by introducing sources of controlled disturbances in different forms in experiments and observing the effect on the transition location, and possibly on the mode of non-linear interactions. The experiments have to be carefully designed and performed, in such a way as to minimize extraneous disturbances and to introduce only known disturbances into the free-stream and possibly at the surface.

1.2.3 Free-Stream Disturbances

The two most common types of free-stream disturbances for low speed flows are acoustic and vortical disturbances. Acoustic disturbances are those which propagate at the speed of sound and where the free-stream disturbance wavelength, λ_d, is 1 - 2 orders of magnitude larger than the boundary-layer disturbance wavelength at the same frequency. Vortical disturbances can be modeled as sinusoidal vorticity distributions and can be interpreted as a two-dimensional model of weak free-stream turbulence according to Saric, et al.[41]. Experimentally, free-stream vortical wave trains are created with vibrating ribbons or cylinder wakes and they convect at the local free-stream velocity.

For acoustic disturbances, the magnitude of receptivity and the disturbance response have a strong dependence on geometry. According to Saric, et al.[41] who used acoustic free-stream disturbances to excite T-S disturbances, the T-S disturbance amplitude at Branch I decreased as an elliptic nose on a flat plate was sharpened. Branch I is the location on the surface of the model where a boundary-layer disturbance of a particular frequency becomes unstable. It is also referred to as the lower branch (the upstream crossing) of the neutral stability curve, which is a Reynolds number-frequency plot of the equilibrium envelope of T-S eigenmodes. Also, when the surface curvature discontinuity was smoothed, the receptivity at that location was reduced by a factor of two. Lastly, the disturbance growth was noted to start at the location of maximum adverse pressure gradient. Kerschen[44] has shown that with vortical gusts, receptivity is produced mainly by the parallel component of the free-stream disturbance velocity.

In comparing receptivity due to acoustic and vortical free-stream disturbances, it was noted that stationary disturbances induce stronger receptivity for acoustic free-stream disturbances as

compared with the receptivity found when the free-stream disturbances correspond to convected vortical disturbances, according to Kerschen[59] and Choudhari and Streett[27]. This difference was identified to be primarily caused by the fact that a convected free-stream disturbance does not produce significant unsteady fluctuation in the region close to the surface where the mean flow perturbation produced by surface non-uniformities is the strongest and where a T-S-wave is excited most efficiently.

1.3 Experimental Disturbance Environment

The primary goal of this research effort is to develop an experimental database of boundary-layer data as the boundary-layer flow develops from laminar through transition for the verification of theoretical transition tools in a well documented disturbance environment over an airfoil shape. Such an experiment follows the intentions described by Haynes, et al.[60], and Reed, et al.[61], who discuss current theoretical methods, the state of code validation and suggestions for future work. Within these articles, the necessity of matching the basic flow state for the theoretical analyses to experiment is identified as being very important for theory to be effectively validated. There are many properties and variations in the basic state too small to be measured which add to the complexity of the situation. As a start, if one can show a comparison with linear stability theory, then the modeling of the experimental basic state is likely an adequate representation. The significance of the airfoil shape is to expand upon the types of receptivity experiments that have been performed previously, which have been typically zero-pressure-gradient boundary layers[62]. The airfoil shape also provides a continuous leading-edge geometry as well as a surface with varying curvature and slope.

One of the delicate tasks involved in accomplishing this project was to choose the right degree of complexity in the disturbance environment. The disturbance environment should be reasonably complex (so as to approximate the real environment, albeit in a crude sense), but at the same time not excessively complex for the prediction capabilities in the near term future as well as limitations determined by experimental constraints. The acoustic forcing used in this experiment consisted of modulated bursts, which vary in both time and space. This type of disturbance can be tracked with both temporal and spatial prediction codes. The bursts were of a single acoustic

forcing frequency of varying amplitude. The surface condition examined initially contained no surface roughness. Later, single and multiple roughness elements were added symmetrically about Branch I, and spaced a wavelength apart, based upon the frequency that theoretically reached transition first.

1.4 Overview of this document

Now that literature has been reviewed and the problem has been defined, details of the experimental set-up and facilities are described in **Chapter 2**. The airfoil model is detailed in **Chapter 3**, including design specifications and fabrication details and results. **Chapter 4** presents the discussion of the experimental techniques and data acquisition methods. The results are presented and discussed in **Chapter 5**, including mean data, surface-normal modeshape data and constant boundary-layer height chordwise traverses. Here, the results are also compared with linear stability theory. Finally, **Chapter 6** provides concluding remarks and suggested future work.

2 Facility and Instrumentation

2.1 Facility

The experiment was performed at the NASA Langley Research Center "2 ft by 3 ft Low Speed Wind Tunnel Facility" (**Figure 1**) {0.61 m x 0.91 m cross section}. Velocities up to 42.7 m/s {140 fps} are attainable. The transition Reynolds number has been previously measured to approach 3 million on a flat plate based upon a virtual origin. Turbulence intensity has been measured consistently between 0.05 and 0.07%. Previous receptivity experiments have been successfully performed in this facility, e.g. Smith[31].

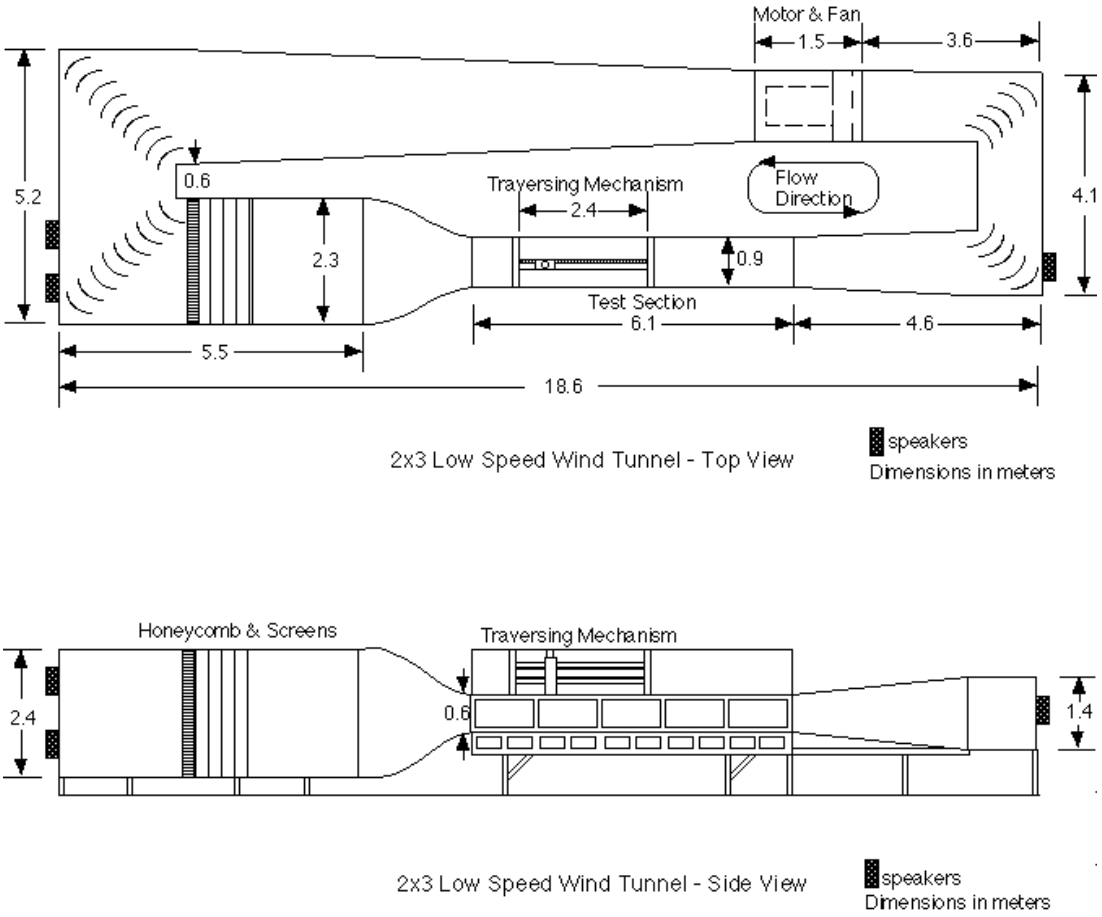

Figure 1: NASA Langley Research Center 2 ft x 3 ft Low Speed Wind Tunnel Facility

The low turbulence value of the facility is a result of the quality of the flow conditioning upstream of the test section. Upstream of the test section is a 9.87:1 contraction, followed by four stainless steel mesh screens, a honeycomb, and turning vanes. The two furthest upstream

stainless steel mesh screens have single horizontal seams located 1.75 m / 2.4 m {69 in / 95 in} from the floor. The two seamless downstream screens minimize the effect of these seams on the flow quality.

The facility includes a speaker array for the application of acoustic disturbances. There are four speakers upstream of the test section. There is one speaker downstream of the test section, expansion and turning vanes. All of the speakers are mounted such that the diaphragms are normal to the flow direction, and are sealed in boxes with 0.64 cm {$^1/_4$-inch} bleed holes to equilibrate the pressure around the speaker with the local tunnel conditions. The speakers are Rockford Fosgate RFP-1808 Punch Woofers. The acoustic waveform was generated by a Hewlett Packard 3245 Universal Source. The source has two channels, for dual speaker control. Waveforms had a resolution of 0.001 Hz with a 0.4% amplitude accuracy. The signal was driven by a Gemini Triton SA-501 Stereo Power Amplifier.

The facility also has a traverse mechanism. This hardware has a horizontal range of 2.4 m {8 ft} and a horizontal resolution of 50800 steps / mm {2000 steps / inch}. The traverse mechanism also has a vertical range of 15.24 cm {6 inches} and a vertical resolution of 1000 steps / mm. The traverse system had two stepper motors controlled by a Unidex 12 Motion Controller.

2.2 Instrumentation

All of the hardware used is itemized in **Appendix B** with a brief description of the purpose of the equipment.

Mean pressures along the airfoil surface and tunnel ceiling were acquired using a PSI 8400 Pressure Measurement System with a 16-bit Scanner Digitizer Unit, a 1.0 PSID Pressure Calibration Unit and three 32-port 10-inch Water Column (ESP) Pressure Modules. Mean local tunnel pressures were measured using a Mensor DPG-II 0-20 PSIA Silicon Pressure Transducer and a Mensor DPG-II 0-2 PSID Quartz Pressure Transducer, as well as Datametrics 10-Torr Pressure Transducers (Barocel) with #525 Thermal Bases and a Ruska DDR6000 100-mm Hg Differential Pressure Transducer. Temperature and relative humidity measurements were made using a General Eastern Model 800LC Relative Humidity and Temperature Indicator.

Fluctuating hot-wire velocities were acquired using a Dantec Streamline Anemometer with 55P01 hot-wire probes, Stanford Research Systems SR650 Dual Channel Filters, and an IOTech ADC488/8SA 16-bit A/D Converter with simultaneous sampling capabilities. Most of the mean measurements were acquired using a VXI/HPE1413B, allowing the voltage outputs from instruments to be acquired from computer. The VXI/HPE1413B was used as a high-speed averaging voltmeter and a 16-bit A/D converter.

2.2.1 Hot-Wire Probe Supports

The hot-wires were supported by four different probe support configurations (**Figure 2 (a,b,c) Hot Wire Probe Supports**), which included a single wire support, two variations of a 7.6 cm {3 inch} vertically spaced dual wire support, and a ±10.2 cm {±4 inches} off-centerline spanwise dual wire support.

The single wire support (**Figure 2 (a,b,c) Hot Wire Probe Supports**) was initially used. It consisted of a streamlined profile, 7.0-cm {$2^{3}/_{4}$-inch} chord length, and 0.64-cm {$^{1}/_{4}$-inch} thick steel bar with a wooden trailing edge. There is a 0.48-cm {$^{3}/_{16}$-inch} outer diameter brass tube at a 45° downward angle that holds the wire. The wire was about 8.9 cm {$3^{1}/_{2}$ inches} upstream and below the leading edge of the support.

The dual vertical wire support was a modification to the single wire support, where a steel extension was placed on the base of the single wire support. This made the base of the support 1.3-cm {$^{1}/_{2}$-inch} thick and, consequently, a new trailing edge was added, increasing the chord length to 8.3-cm {$3^{1}/_{4}$-inches} thick. The second wire was 7.6-cm {3-inches} below the first, also extending downward at a 45° angle. The first configuration consisted of the brass tube extending the same as in the single probe support, locating the wire 8.9-cm {$3^{1}/_{2}$-inches} upstream and below the leading edge of the support. The second configuration had the wire positioned 4.4-cm {$1^{3}/_{4}$-inches} upstream and below the leading edge of the support. It also included the adding of a streamlined wooden base, as indicated in **Figure 2 (a,b,c) Hot Wire Probe Supports**. The changes in the configuration were made to reduce the possible influences

of vortex shedding frequencies and unsteady separation along the base of the support upon the measurements. The vortex shedding frequencies associated with brass tube (a swept cylinder in the flow) were calculated to be on the order of the frequencies of concern.

The last hot-wire probe support configuration was the dual span wire support **Figure 2 (a,b,c) Hot Wire Probe Supports**. This support was made with a streamlined 0.64-cm {$^1/_4$-inch} thick, 3.8-cm {$1^1/_2$-inch} chord length vertical support. The angled supports were 0.32 cm {$^1/_8$-inch} thick with rounded leading and trailing edges and a 3.2-cm {$1^1/_4$-inch} chord length. The horizontal stiffener was a 0.16-cm {$^1/_{16}$-inch} thick by 2.5-cm {1 inch} steel bar. The wires were located at ±10.2-cm {±4 inches} off of the centerline, 6.4-cm {$2^1/_2$-inches} upstream and 8.9 cm {$3^1/_2$-inches} below the horizontal stiffener at a 45° downward angle. This configuration was used to make measurements off the centerline of the model to allow for examination of the symmetry of the flow across the model as well as to verify that the sidewall turbulent wedge does not encroach upon the measurement domain.

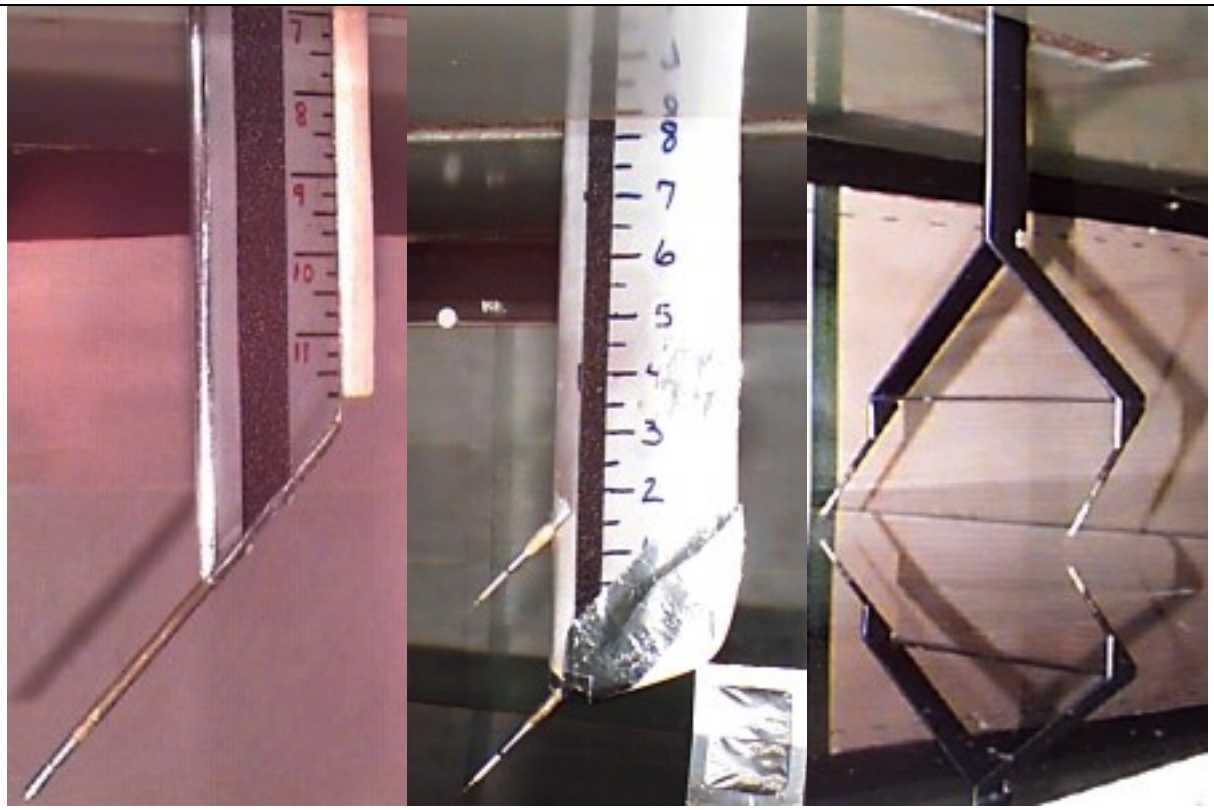

a) Single Hot-Wire Probe Support | b) Dual Hot-Wire Vertical Probe Support | c) Dual Hot-Wire Spanwise Probe Support

Figure 2 (a,b,c) Hot Wire Probe Supports

3 The Airfoil Model

The design of the airfoil involved starting with a baseline airfoil geometry. This baseline airfoil had some of the desired characteristics for the test case, such as the general location of pressure minimum and a reasonable functional range of angles of attack. The baseline test conditions are listed in **Table 1**.

Table 1: HSK-R01 Design/Baseline Conditions

Free-stream Velocity, U_{fs} = 20 m/s {66 fps}
Chord Reynolds Number, $Re_c = 1.68x10^6$
Angle of Attack, $\alpha = 0°$
Surface Roughness: None
Acoustic Forcing: None / 300 Hz {F = 68}
Transition: 57 - 67% chord due to 300 Hz T-S disturbance; N-factor = 9 - 12

Ideally, the actual airfoil shape for such an experiment needs to be determined accounting for tunnel wall effects in order to maintain a desired pressure distribution on the airfoil surface. An alternative to this would be to work in a facility with either large enough space to effectively isolate the airfoil from the wall effects or to work in a facility with adjustable wall surfaces to contour free-stream flow streamlines. The airfoil surface needs to be smooth with respect to the disturbance wavelengths; thus surface roughness effects would be negligible, except when specifically applied on the surface. In addition to the sufficiently smooth model surface, it is desired that natural transition occur on the model over an extended surface length to provide a large domain for examining the evolution of the boundary-layer disturbances.

First, using an Euler code, MSES[63, 64, 65], the inviscid pressure distribution was calculated. A laminar boundary layer was then calculated with the BLSTA[66] code. From the boundary-layer analysis, the boundary-layer thickness and skin friction were examined to determine experimental measurability within the boundary layer with a hot-wire probe and to identify the possibility of marginal separation. Next, a preliminary stability analysis was performed using the SALLY Stability Analysis Code[67, 68]. Later during the airfoil design, the LAMDA[69] interface package was used, which included the NYU Potential Flow Solver[70, 71], the Kaups-Cebeci

Laminar Boundary-Layer Code[72], and the SALLY Code. The stability analysis provided frequencies for the disturbances most likely to grow within the boundary layer. These frequencies are to be generated acoustically for the experiment. The disturbance was desired to lead to transition near x/c = 0.7. This value provides margin to vary the transition location later in the experiment; such as by varying the angle of attack or adding surface roughness which would move the transition location upstream. The disturbance wavelengths also will have significance, identifying whether roughness elements can generate such wavelengths.

During the design process, several airfoils were examined based upon the initial analysis intentions, including NACA 4-digit, 4-digit modified and 6-series airfoils. The final airfoil was based upon the Selig and Donovan SD8020 symmetric airfoil[73] with customized leading-edge and trailing-edge geometries and a scaled thickness. The thickness was determined by considering possible structural concerns as well as the disturbance growth rate in the linear growth region. Marginal separation was found not to be a practical concern for this experiment, though it was initially considered in the original design criteria. For the limited size of the wind tunnel test section, the geometry would be the source of the flow separation, not the angle of attack, and such airfoils were not adequate for the baseline disturbance growth analysis case. **Table 2** lists the final model design characteristics. The design airfoil coordinates are tabulated in **Appendix A**.

Table 2: HSK-R01 Physical Characteristics

Chord, c = 1.2 m {48 inches}	Thickness, t/c = 0.06 at x/c = 0.275
Span, b = 0.91 m {36 inches}	$C_{p,\,min}\,|_{\alpha=0}$ at x/c = 0.08

Model fabrication issues were important in the design of the model. These included mounting into the test section and defining surface quality specifications[74], such as surface finish (short length-scale variations, or roughness), surface tolerance (deviation from the desired shape), and surface waviness (long length-scale variations). A description of the surface quality specifications as they were presented to the model shop for fabrication constraints is listed in **Table 3**.

Table 3: Surface Quality Specifications used for Design Fabrication Constraints

Surface Tolerance	Deviation from the design coordinates ≤ ±0.25 mm {±0.010 inches}
	Based upon a trade study of scaling the geometry y-coordinate and examining the effect on transition location
Surface Roughness	Short length-scale surface variations ≤ 0.0002 mm {8 rms μ-inches}
	Based upon Smith[31]
Surface Waviness	Long length-scale surface variations ≤ 0.0064 mm {0.00025 inches} amplitude per 2.5 cm {1 inch} streamwise distance
	Surface waviness is comparable to repeated roughness elements, which have been shown to be a strong source of receptivity if located near Branch I. This is a factor of 10 smaller than the applied roughness used by Smith[31] to induce receptivity. Wiegel[37] has shown that receptivity due to wall waviness versus single element roughness is O(10). The wavelengths of instabilities in the boundary layer that indicated strong amplification by transition (N>4.5) range from 1.2 - 4.4 cm {0.5 - 1.75 inches}. (calculated using LAMDA/SALLY)

The model was made with an 8-lb foam core with a 0.64 cm {0.25-inch} fiberglass skin. The final surface finish consisted of two layers of lacquer primer and two layers of gloss black lacquer. Between lacquer layers, spot putty was use to fill any surface voids, and successively finer sanding was performed, ending with an equivalent of a 6000 grit liquid abrasive. Embedded in the fiberglass skin were the pressure tube channels, which were 0.20 mm {0.008 inches} below the surface (**Figure 3**). Aluminum end-caps were also used to add to the structural rigidity. The model mount design allowed for testing at ±4° in 0.25° increments. The model was designed with one surface for surface pressure measurements ("Pressure Port" surface), and the other surface, mostly clean of ports ("Stability Measurement" surface), for the sensitive boundary-layer measurements. There were 51 pressure ports located along the centerline and at ±10.2 and ±20.3 cm {±4- and ±8-inches} off-centerline for verification that flow was two-dimensional and that the model was installed without a spanwise slope. The locations of the pressure ports on the model surface are tabulated in **Appendix A**. The surface pressure ports were created by drilling holes normal to the surface to the embedded pressure tubes or resin-

coated channels within the fiberglass. The stability measurement surface had a few pressure ports at off-centerline locations to capture the stagnation point for angle of attack verification while minimizing the impact on receptivity. The number of surface pressure ports was such that up to two pressure transducer modules could be located within the model (ESP 10-inch water column module for a PSI 8400 system). An overall trade study was performed to determine model fabrication material, balancing cost, surface quality and pressure port installation issues.

Figure 3: Model Pressure Port Layout

The final model geometry (**Figure 4**) worked well within the physical constraints of the facility and instrumentation including having a theoretical boundary layer that would be measurable using a hot-wire probe and exhibiting natural transition near 70% chord, as determined using linear-stability theory.

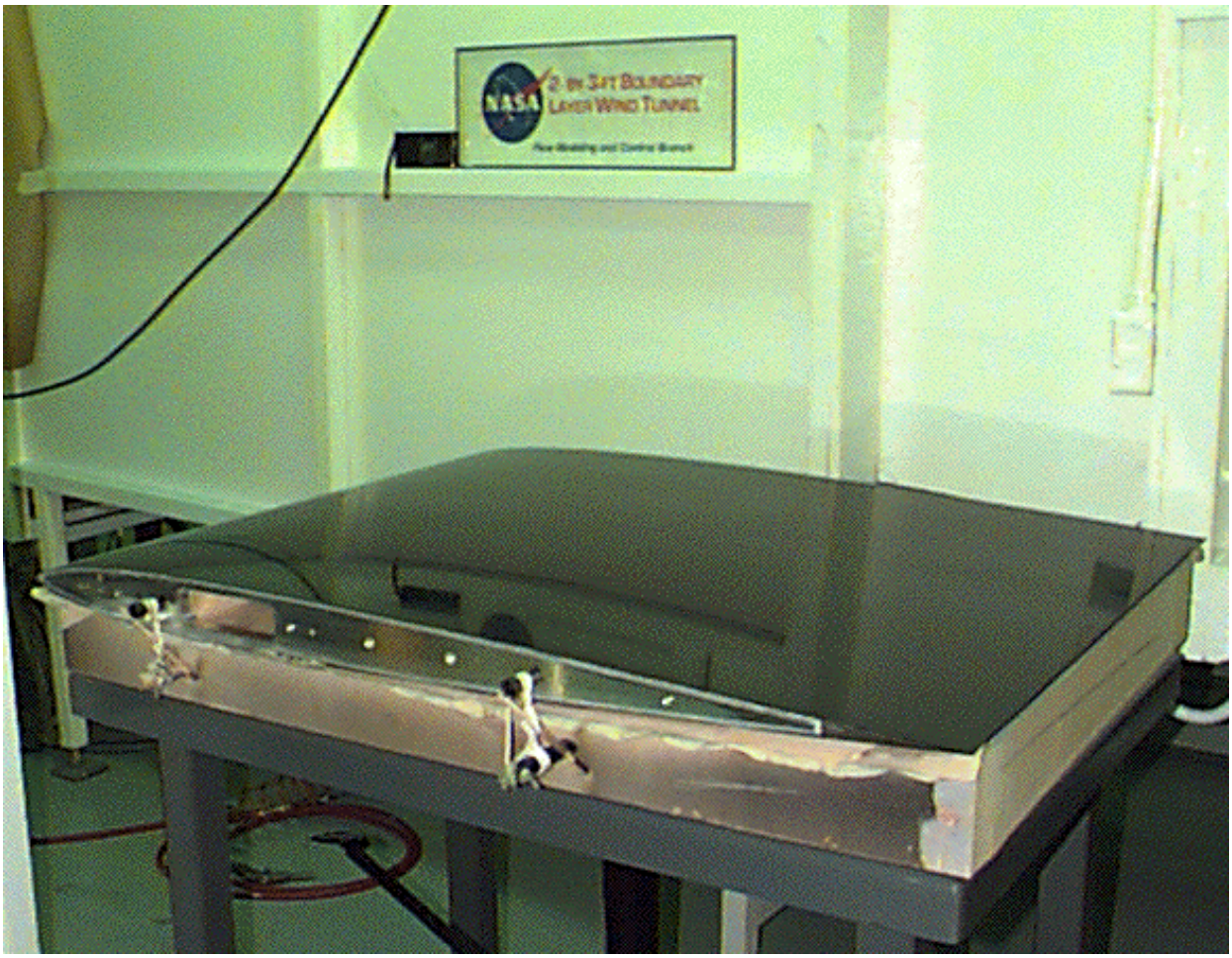

Figure 4: HSK-R01 Model

3.1 Model Installation and Alignment

The model was installed approximately two chordlengths downstream of the test section entrance and 0.25 chordlengths from the floor and from the ceiling (vertically centered in the test section). Initial tunnel entries, where no stability measurements were made, consisted of the model located one chordlength downstream of the test section entrance. The model was later moved downstream to provide the flow a longer streamwise distance to stabilize immediately downstream of the tunnel nozzle and test section entrance.

After the model was installed in the test section, its alignment angle was initially set using a digital inclinometer aligned to the chordline of the model. This initial alignment assumed that the flow in the test section was symmetric vertically in the test section. The model alignment

angle was corrected by using several mean boundary-layer profile measurements to locate the model surface at various chordwise locations. Once the actual surface was located, it was straightforward to determine the model effective alignment angle and correct it, however the sensitivity of the model orientation in the test section limited confidence in the angle measurement to 0.3°. The spanwise dihedral was set to 0° by using the digital inclinometer at the chordwise station determined by the back edge of the front mounting brackets (11.3% chord) and at the trailing edge of the model.

3.2 Test Section Set-Up

The test section was set up to take advantage of the flexible ceiling and floor. The ceiling and floor contours were set to match the predicted streamlines at the tunnel wall locations to reduce, if not eliminate, the wall effects on the model pressure distribution. This was completed by determining the inviscid streamline using MSES[63, 64, 65] and determining the boundary-layer growth on this effective surface using BL2D[75]. The target contour was determined by offsetting the inviscid streamline coordinates by the computed displacement thickness. ESP pressure taps were located at 15.2 cm {6-inch} intervals along the test section ceiling. Adjustment jacks were located at approximately 45.7 cm {18-inch} intervals along the ceiling and floor. Exact locations of the adjustment jacks, measured in chordlengths from the test section entrance, are presented in **Table 4**. The ceiling and floor were made of a G-10 fiberglass, and adjacent panels were joined using lap joints that provided smooth surface transitions between adjacent panels. The tunnel velocity was measured using the Ruska as well as a Barocel, connected to one of the ceiling ports upstream of the model where the model influence was small and the streamline pressure variation was also small. The flow velocity at this ceiling location was determined to match the velocity at the center of the test section when measured with a pitot probe.

Table 4: Tunnel Ceiling and Floor Adjustment Jack Locations

$(X/C)_{Ceiling}$	$(X/C)_{Floor}$
0.47	0.42
0.97	0.93
1.47	1.42
1.97	1.84
2.46	2.34
2.89	2.84
3.39	3.42
3.89	3.90
4.37	4.39
4.87	4.91

3.3 Roughness Configurations

For this experiment, two-dimensional roughness was used in addition to the smooth surface condition. The roughness consisted of strips of tape located at constant chordwise stations on the model, as indicated in **Table 5**. Repeated roughness was examined as well as several single element test cases with various thickness elements. The repeated roughness elements were spaced one wavelength apart, based upon the wavelength of the central forcing frequency.

Table 5: Surface Roughness Element Locations

Tape LE Location	Test Cases Used
11.348% chord	5 element
13.274% chord	3, 5 element
15.189% chord	1, 3, 5 element
17.126% chord	3, 5 element
19.041% chord	5 element

All of the tapes used are 3M Protective Tapes with low tack adhesives and designed for use with polished and glossy painted surfaces (**Table 6**). For reference, a typical sheet of paper is about 0.1 mm {4 mil} thick. All of the tape heights used for this experiment were under conditions such that the Reynolds number based on roughness height was below the critical roughness height, Re_h = 120 – 150. These height-based Reynolds numbers ranged from 56 – 87.5 for the 20 m/s test cases, and from 40 – 51 for the 15 m/s test cases. The non-dimensional roughness height, h/δ^*, ranged from 0.50 – 0.80% δ^* and 0.53 – 0.83% δ^* for the 20 m/s and 15 m/s flow cases, respectively.

Table 6: Roughness Tape Specifications

0.04 mm x 2.54 cm {1.6mil x 1 inch}	Polyester Tape with Rubber Adhesive (#335)
0.05 mm x 0.95 cm {2.0mil x $^3/_8$ inch}	Polyethylene Tape with Acrylic Adhesive (#2112)
0.06 mm x 0.95 cm {2.5mil x $^3/_8$ inch}	Co-Extruded Polyethylene Tape with Acrylic Adhesive (#25A12)

The roughness elements were applied to the model surface after it was polished and a thin film of mildly soapy distilled water was applied to the roughness application region. After the tape was applied, the water allowed for some adjustment of the tape position. The water was finally cleaned from under the tape by use of a squeegee. This method was selected because of the nature of the task of applying the tape across a 0.91 m {3 ft} length, where the flexibility of the thin tape became a significant issue. **Figure 5** shows how the tape looked on the surface for the Test 10, the five repeated roughness element case. It can be seen that the above method worked well for eliminating air bubbles under the tape surface, however the low tack adhesive was not as effective near the edges of the tape strips. The tape thickness was measured at NASA Langley Research Center Quality Assurance and Inspection Branch. It was found that the polyester / rubber adhesive tape (#335) was consistently 1.6 mil thick. However, the polyethylene / acrylic adhesive tapes (#2112 and #25A12) were up to 0.3 mil thinner than the specification, probably due to a loss of adhesive during the application of the tape on the model. Air bubble heights could not be measured because the measurement probe applied a pressure on the material that locally eliminated the air bubbles under the probe.

Figure 5: Test 10 Roughness Configuration - 5 Repeated Roughness Elements

3.4 Model Fabrication Results

A comparison of the design coordinates and the actual surface coordinates as measured by Quality Assurance and Inspection Branch at NASA Langley Research Center are in **Figures 6**, **7 and 8**, presenting a 1:1 scale comparison of the design and measured coordinates along the model centerline, the difference between the actual and measured coordinates along the centerline, and a full model comparison of the QA measured coordinates with respect to the design coordinates, respectively. The QA measurements along the model centerline are tabulated in **Appendix A** as well. For these comparisons, a certain vertical offset between the design and measured coordinates was assumed. Optimally setting this offset would indicate that the deviations are much closer to design tolerance on both surfaces over most of the model surface. It can be seen that the model is still close to the design tolerances, though one surface matches better than the other does. This difference had a very small effect on the flow and stability over the model, as determined by theoretical computations made with the QA model surface coordinates. Also, results from examining each surface separately correlated very well. It should be noted that the upper surface as presented in these results is the surface with the pressure ports and the lower surface is the "stability measurement" or "clean" surface over which the hot-wire measurements were completed. The three-dimensional surface measurements were acquired in both chordwise and spanwise directions. The chordwise data was measured at 0.63 and ±19.7 cm {0.25 and ±7.75 inches} for the full chord of the model. The span-wise data was acquired at 5-, 15- and 50- percent chord for ±30.5 cm {±12 inches} about the centerline of the model. Traverse locations were selected to be offset from existing pressure ports on the surface.

The leading-edge radius was measured to be 3.42 mm {0.135 inches}, whereas the design leading-edge radius was 2.81 mm {0.111 inches}. This indicated a Strouhal number of 0.322 instead of the design value of 0.265.

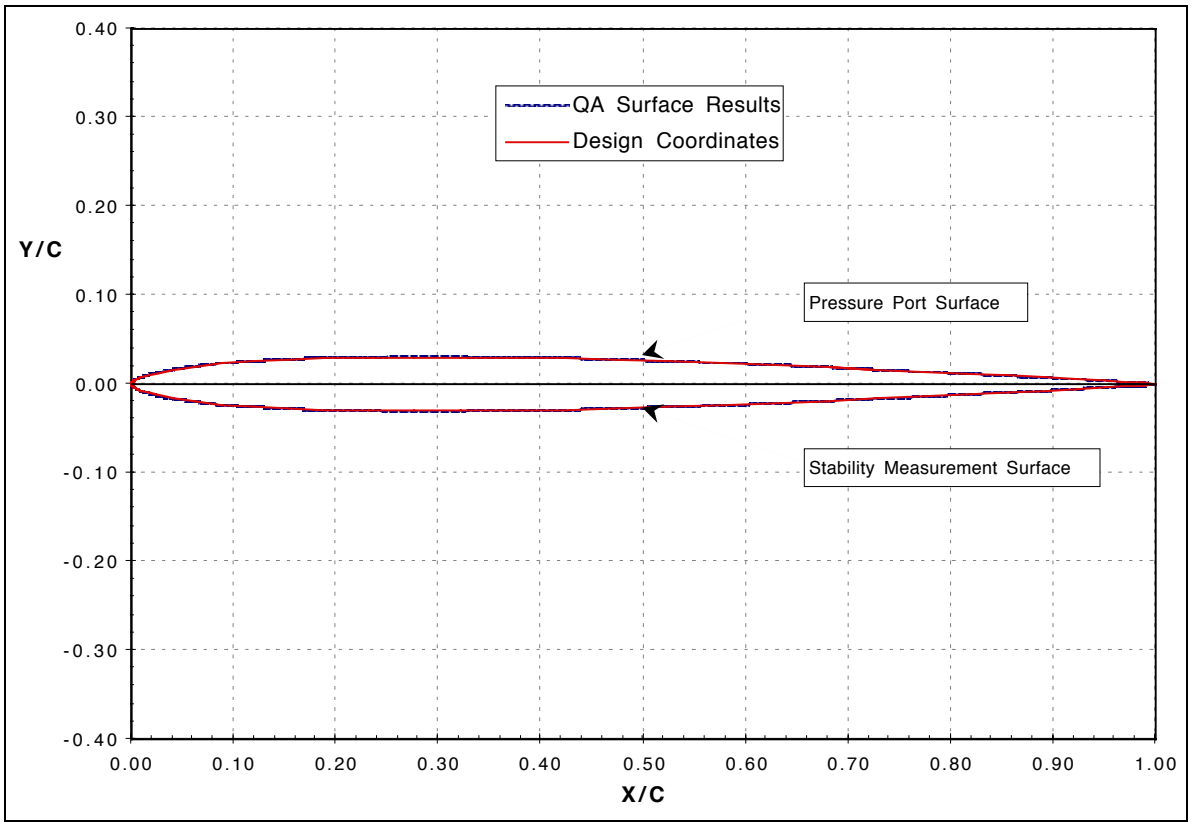

Figure 6: Design vs. Actual Surface Coordinates Along the Model CenterLine

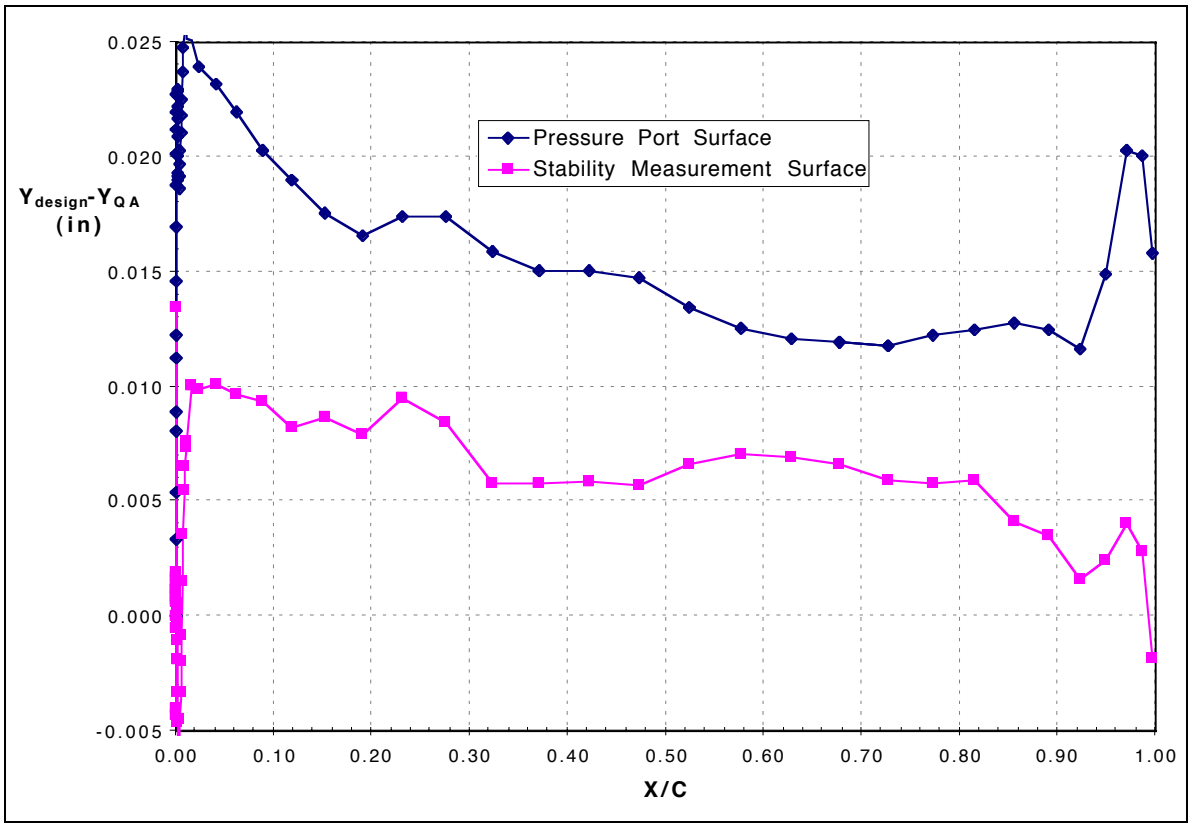

Figure 7: Difference between Design and Actual Airfoil Coordinates

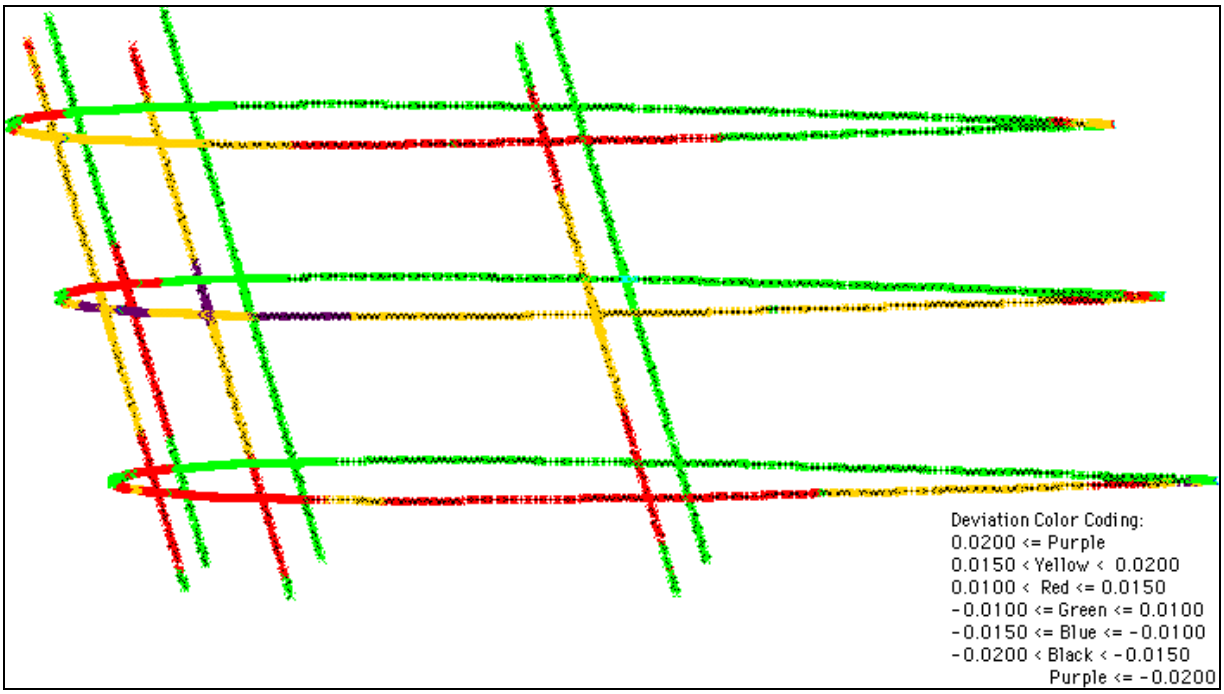

Figure 8: Design vs. Actual Surface Coordinates over Entire Model

4 Experimental Techniques and Data Acquisition

In this chapter, details of the methods and procedures used for setting up and running the experiment are presented. Outlines of the exact experimental procedures are presented in **Appendix C**.

4.1 Acoustic Forcing

The acoustic disturbance field is introduced in a controlled manner by way of acoustic sources located upstream and downstream of the test section to generate a traveling modulated acoustic burst. Modulating a constant frequency cosine wave created the bursts. A Gaussian waveform was used to modulate the signal for a predefined duration. The form of the Gaussian envelope is presented in **Equation 4-1**, where the constant b was 474.85 and Sa is the number of points in the waveform.

$$g(i) = \frac{\exp\left(-\frac{1}{2}\left[\left\{i - \mathrm{int}(Sa/2)\right\}/b\right]^2\right)}{b\sqrt{2\pi}} \qquad \textbf{Equation 4-1}$$

The downstream speaker was used for some test cases to cancel reflections from the downstream corner of the wind tunnel. For all of the final experimental data, 0.010-second bursts were used. For test cases at 20 m/s, the burst was processed one step further with a correction for the tunnel "transfer function", which included effects of the flow screens, honeycomb, turning vanes and the nozzle contraction. For the 15 m/s test cases, this was not necessary.

The determination of this transfer function is outlined in **Figure 9**. The transfer function is measured by generating a known input, $s_I(t)$, from the speakers, and measuring the corresponding output, $s_O(t)$, in the test section. The convolution of the input signal and the transfer function, $s_E(t)$, equals the output signal. The transfer function can be determined in Fourier-space. The desired output signal, $g_O(t)$, was the same as the above chosen known input signal $s_I(t)$. Using the transfer function, the desired input signal, $g_I(t)$ can be determined.

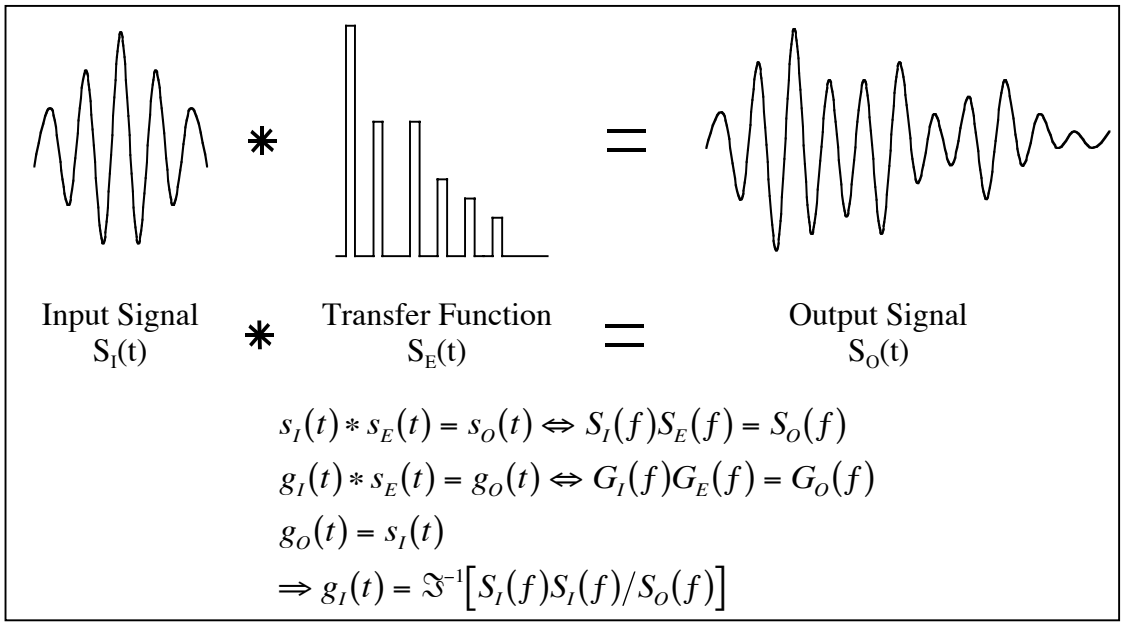

Figure 9: Determining the Tunnel Acoustic Transfer Function

A 300 Hz cosine wave was modulated for the 20 m/s test cases, while a 200 Hz cosine wave was modulated for the 15 m/s test cases. These primary frequencies were selected by examining the theoretical disturbance growth results using the SALLY stability analysis code, selecting the frequency that first reached an N-Factor of 9 at the test conditions. A comparison of the experimental free-stream forcing waveform and its corresponding power-spectral-density as compared with the ideal (desired) waveform can be seen in **Figures 10 and 11** for the 300 Hz / 10 ms and 200 Hz / 10 ms modulated bursts, respectively.

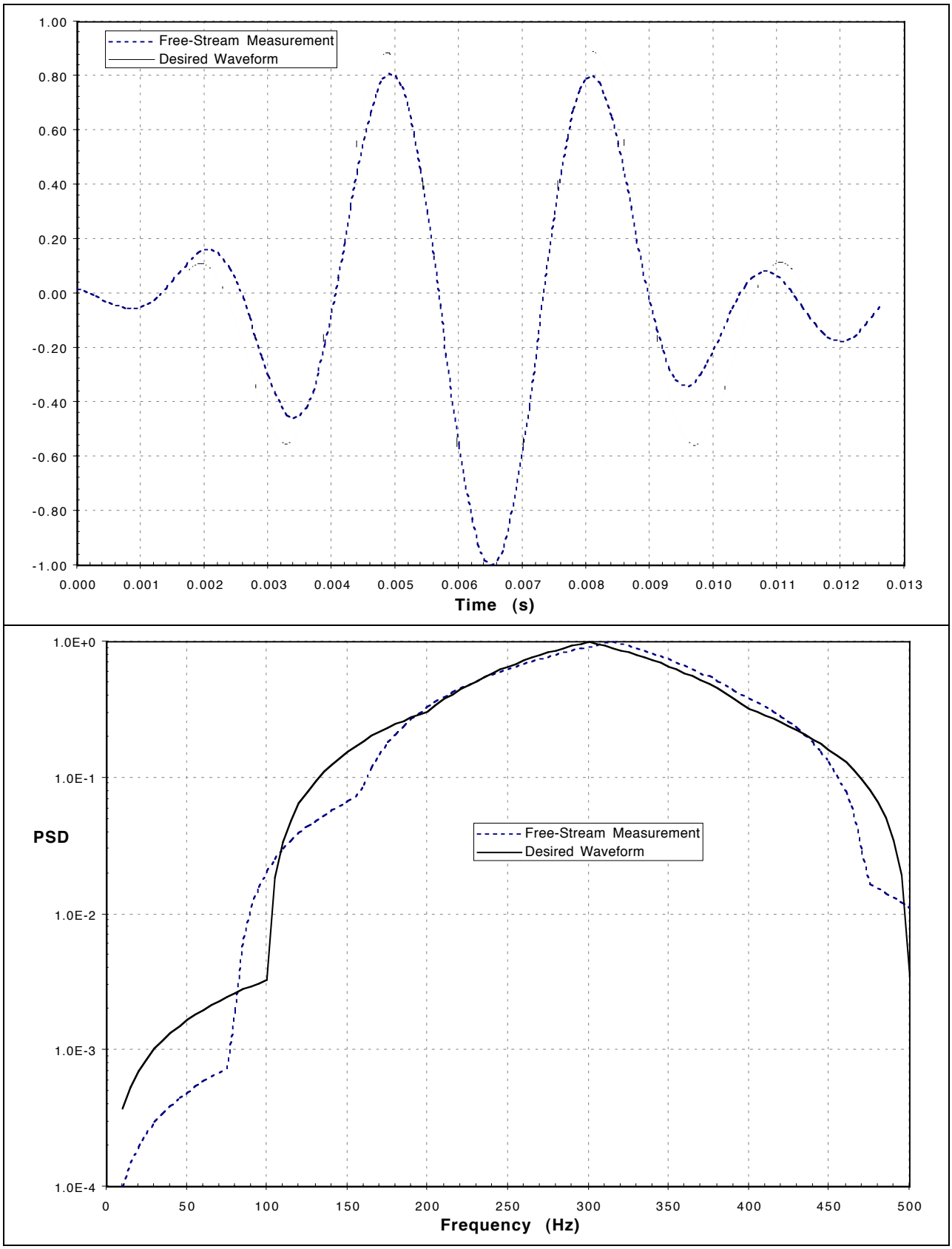

Figure 10: 300 Hz Acoustic Forcing Burst Time Trace and Power Spectral Density

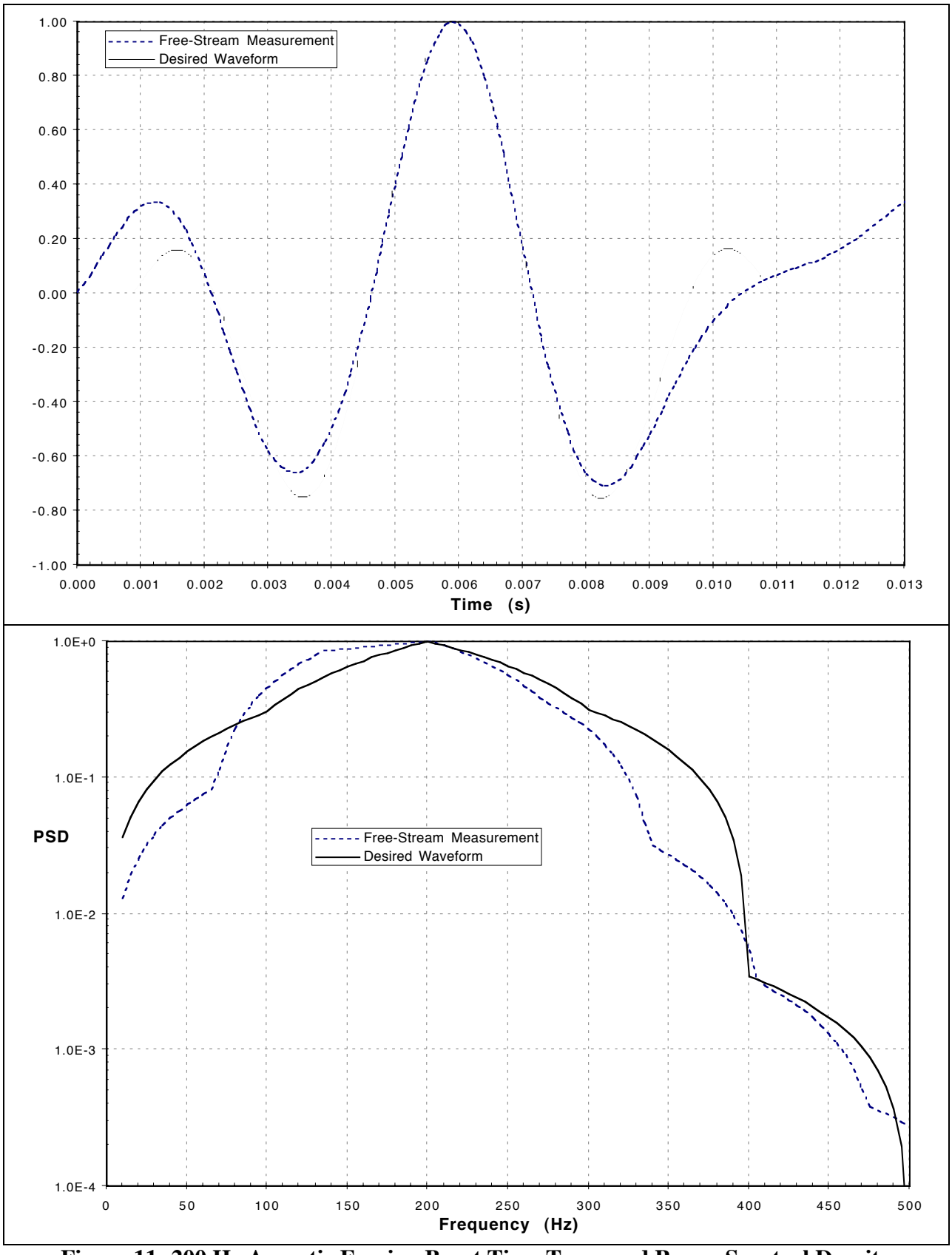

Figure 11: 200 Hz Acoustic Forcing Burst Time Trace and Power Spectral Density

4.2 Hot-Wire Probe Measurements

Hot wire probe measurements were used to acquire the acoustic and Tollmien-Schlichting (T-S) disturbance fields. The hot-wire probe was always calibrated in the same reference position against the free-stream velocity measured with a ceiling static port using 20 - 50 data points with a non-linearly spaced interval, weighted such that more points were taken at the lower speed conditions. The location was approximately 75% chord upstream of the model in the center of the test section. The ceiling static port measurements correlated to those of a Pitot tube located in the free-stream at the location where the hot-wire was positioned. The hot-wire measurements were corrected for temperature effects using a linear correction based upon the work of Abdel-Rahman et al.[76], also used by Smith[31] in the same facility. The linear correction formula can be reduced to **Equation 4-2**.

$$e_c = \frac{e}{\sqrt{1-\left(T-T_{cal}\right)\alpha_o/OHR}} \qquad \textbf{Equation 4-2}$$

The overheat ratio, OHR was 0.8, and the temperature coefficient of resistivity of the wire, α_o, was 0.0036/K {0.0020/R}. This correction formula has been shown to be accurate to ±2% for velocities above 1.5 m/s {5 fps}. A 4th-order polynomial was used to fit the calibration data every morning and occasionally more often if temperatures in the facility varied significantly. If the calibration was out of tolerance, the measurements were repeated. The wind tunnel was also run for 30 - 40 minutes prior to any data acquisition. This allowed for frictional heating of the closed-circuit wind tunnel to come to equilibrium with the facility heating / cooling system to minimize temperature drift during the duration of data set acquisition. The correction formula is applied during the hot-wire probe calibration as well as to all acquired data. Radetzsky, et al.[77] have verified the validity of a linear correction formula for a broad range of temperatures, and, like Smith, used a 4th-order polynomial to fit the calibration data.

4.2.1 Turbulence Intensity Measurements

Turbulence intensity measurements were made using the hot-wire probe located at the hot-wire calibration location. The hot-wire signal was filtered between 0.1 and 1000 Hz and sampled at a rate of 1 kHz for a duration of 25 seconds. The measurements were acquired over a range of test section velocities, 10 to 30 m/s.

4.2.2 Boundary-Layer Profile Measurements

Boundary-layer profiles were acquired using the hot wire. The software written moved the probe normal to the surface of the model at each chordwise station. The stepping algorithm consisted of stepping through two zones, above the boundary layer and inside the boundary layer. The algorithm used the predicted model surface location and theoretical boundary-layer thickness as inputs. The predicted model surface location was the model geometry as measured by the Quality Assurance and Inspection Branch at NASA Langley Research Center, accurate to 0.0086 mm {0.00034 inches}. The stepping algorithm also used two scale factors to refine the point distribution, SF_{out} and SF_{in} for outside and inside the boundary layer, respectively. These scale factors were varied during the experiment to yield 30 - 90 points within the boundary profiles.

The boundary-layer stepping algorithm was divided into several regions, including above the theoretical boundary layer, above the experimental boundary layer, above the theoretical model surface location, and below the theoretical model surface location. These different regions were necessary to limit the step size an ensure adequate resolution, as well as to minimize the chances of driving the hot-wire into the model surface. Typically, an initial boundary-layer profile was acquired to "find" the wall in order to zero the coordinates of the hot-wire probe motion controller. This initial profile was acquired using a large uncertainty in the surface location, which was at times larger than the actual boundary-layer thickness. The different step sizes can be seen in **Table 7**. The wall finding method used here is the same as used for post processing, but it was particularly used to predict the boundary-layer edge to verify that the traverse would start sufficiently outside the boundary layer.

When five consecutive data points decreased in velocity, the software changed the stepping algorithm for traversing inside the actual boundary layer. Here, the step size was based upon the local velocity ratio, where the reference velocity was the average of the first five acquired data points. If the velocity ratio happened to be above unity, then the step size used was based upon a fixed ratio because it would appear that the probe was falsely flagged to be within the boundary layer. Inside the boundary layer, a minimum step size was also implemented. The stepping algorithms can be seen in **Table 7**.

Table 7: Boundary-Layer Stepping Algorithms

Above the Boundary Layer	Inside the Boundary Layer
Above δ_{th}: $dS = \frac{dS_{start} - \delta_{th}}{SF_{out}}$	$\frac{U}{U_{ref}} > 1 : \left(dS = \frac{\delta_{th}}{SF_{in}} \frac{U}{U_{ref}} \right) : \left(dS = \frac{\delta_{th}}{SF_{in}} \frac{1}{2} \right)$
Below δ_{th}: $dS = \frac{2}{3} \frac{\delta_{th}}{SF_{out}}$	dS_{min} = 0.0041 mm {0.00016 inch}
Below Y_{wall}: $dS = \frac{1}{2} \frac{\delta_{th}}{SF_{out}}$	

The post processing of the boundary-layer data consisted of normalizing the measured velocities, extrapolating the data to the wall location and defining an edge velocity condition.

The velocities were first normalized by the mean free-stream value as measured by an upstream ceiling static pressure tap, the same port used during calibration of the hot-wire. The boundary-layer edge velocity was computed by stepping through the data and averaging all data points until the next data point was 0.5% lower than the average of all of the data points above it. It was found that using 1% made no noticeable difference in the results. The velocities were finally normalized by the edge velocity. It was determined that initially normalizing by the local free-stream velocity, as measured by the hot-wire above the boundary layer, also made no noticeable difference in the results.

The model wall location was determined by extrapolating the boundary-layer data for $U/U_e < 0.3$ using a linear least-squares technique. This method, while very simple, provided results that compared very well to a method that fit a spline to the data. A least-squares extrapolation method that accounted for the theoretical wall pressure gradient was also attempted, but this also compared well to the linear extrapolation method.

4.2.3 Boundary-Layer Chordwise Traverse Measurements

The hot-wire probe was also used to make chordwise boundary-layer traverses at constant boundary-layer height. The height above the surface was determined by using the measured

mean boundary-layer profiles to build a database of chordwise station, model surface location with respect to the model chordline and displacement thickness. Intermediate chordwise station values were determined by linear interpolation. The stepping algorithm consisted of vertically moving away from the model, traversing to the next chordwise station, then vertically moving down to the desired height in the boundary layer, minimizing the risk of scratching the model and damaging the hot-wire probe.

4.3 Boundary-Layer Responses to the Acoustic Excitation

Time traces of 50 acoustic bursts (phase averaged) were examined to provide the acoustic source signal and the Tollmien-Schlichting responses within the boundary layer. There were two predominant responses in the boundary layer. The signals were extracted from the time traces by manually locating the beginning and the end of the waveform. All data was acquired at a sampling rate of 10 kHz, unless otherwise specified. The hot-wire probe consistently could be tuned to over 40 kHz. The hot-wire signals were bandpass filtered between 190 and 500 Hz, unless otherwise specified.

Both of the predominant boundary-layer responses were due to receptivity near Branch I. The strongest of these responses was a result to the acoustic source signal generated at the speaker array upstream of the model. The other response was the result of an echo of the original acoustic source traveling upstream. This echo was generated at the downstream corner of the tunnel. The echo signal was measured at the chordwise station of the data point, not at the receptivity region. There could have been some interference in the free-stream with downstream traveling echoes that could have altered the waveform of the signal at Branch I. Also, for low source amplitudes, the echo signal was sometimes barely stronger than the facility noise floor, making the extraction of the echo signal difficult.

The strength of the acoustic forcing signals was determined by normalizing the peak-to-peak amplitude of the appropriate wave packet. This value, along with the gaussian envelope defined in **Equation 4-2**, is enough information to recreate the acoustic forcing signal.

Leading edge receptivity was desired to be examined, however this was not possible due to some unavoidable circumstances. The main reason this was not possible was because the response in the boundary layer due to leading-edge receptivity occurred in the time trace at the same location as the response to the upstream traveling echo. Based upon the facility geometry and T-S wave speeds for this experiment, the time required for the acoustic source to travel to the downstream corner and to return to Branch I in the free-stream (at acoustic wave speeds), was approximately the same time that a leading-edge receptivity boundary-layer response would travel within the boundary layer to Branch I (at T-S wave speeds, approximately 36 – 39% of the free-stream velocity). By the time any signal was measurable, the response had broadened to such a point that any differences were moot. Echo cancellation was considered, and attempted. Passive cancellation, using acoustic absorbing foam was determined to be impractical within the confines of the facility, because the frequencies of concern had long wavelengths in the free-stream. Active cancellation of the source signal using a signal from the downstream speaker was deemed impractical due to poor repeatability as well as intensive application requirements. Active cancellation was attempted by using a Stanford Research Systems SR535 digital delay generator to trigger a second signal from the downstream speaker. However, the delay was dependent upon the chordwise measurement station, and since it could not be determined with enough precision at a single location in the test section, using this procedure at multiple chordwise locations was not feasible.

Boundary-layer response convection wave speeds are computed from the extracted boundary-layer response signals. The extracted signals were padded with zeroes to maintain the time scale, which was based upon the same trigger event for all data points. The time step was determined from the difference of the peak value of the cross-correlation of two consecutive chord wise station results and the onset of the first signal. Local wave speed is determined from the time step and the known chordwise step size.

4.4 Data Acquisition Codes

Data acquisition software was written entirely with LabVIEW[78]. A master program controlled all features of running the experiment. These features included monitoring the tunnel

parameters, controlling the tunnel flow velocity, positioning the hot-wire probe, acquiring individual data points of mean, fluctuating, and burst data, acquiring data sets from mean boundary-layer traverses, fluctuating burst boundary-layer traverses and fluctuating burst chordwise traverses at a constant boundary-layer height for both dual-span and single-span hot-wire probe supports, and saving the data to file. Data monitoring was made with separate software, which allowed examining the mean boundary-layer profiles and the related parameters, as well as examining the fluctuating data time traces. Software drivers have been written to control the PSI 8400 Pressure Measurement System, the VXI / HPE1413B Data Acquisition Card, the 2 ft x 3 ft Tunnel Motor speed, the Unidex 11 Motion Controller, and the HP 3245 Universal Source. Software was also written to process the boundary-layer profiles and spectra using LabVIEW. Post processing was completed using LabVIEW programs, FORTRAN programs and Excel spreadsheets.

The hot-wire probe calibration software automatically controlled the tunnel speed and used a 4^{th} order polynomial to fit the results. Data acquisition software was written to automate hot-wire calibration, boundary-layer traverses and constant boundary-layer height chordwise traverses.

The tunnel ceiling pressures and model surface pressures were measured using the PSI 8400 Pressure Measurement System. Software was written that acquired the pressures as well as allowing on-line data plotting.

4.5 Computational Tools

To aid in the model design and for data comparison, several computer codes were used. For model design, LAMDA was primarily used. For setting the contoured ceiling and floor of the test section, MSES and BL2D were used. To compute theoretical results, LAMDA, MSES, BL2D and ECLIPSE were used.

LAMDA is an acronym for Laminar Airfoil Manager GUI for Design and Analysis. This software package is an interface linking several computer codes related to the design and analysis of airfoils. These codes include the NYU Inverse Swept Wing Code (FLO22)[70, 71], the Kaups-Cebeci Three-Dimensional Conical Laminar Boundary-Layer Code[72], and the SALLY

Stability Analysis Code[67, 68], as well as several other codes. The NYU code was used for analysis purposes only to provide a potential flow solution on the airfoil. The SALLY code was used to track temporally amplified disturbance modes, providing an N-factor, which was the ratio of the amplitude of the disturbance at any station to that of the disturbance at Branch I. LAMDA was used to perform the linear theory results during the model design to predict the disturbance amplifications and during post-processing for comparison with the experimental results.

Mark Drela's Multi-Element Streamtube Euler Solver (MSES) is an Euler solver with an integral boundary-layer solution option[63, 64, 65]. MSES was used during the design process to compute Euler flow solutions over the model, as well as compute inviscid and viscous angle of attack sweeps as it is a robust code that predicts separation fairly well. The code was also used to determine the inviscid free-stream streamline shape at the test section ceiling and floor locations. Solutions with the viscous mode active were made to generate surface pressure distributions that result from various transition locations, to examine the effect of transition location on the mean flow.

BL2D[75] is a fourth-order accurate, two-dimensional / axi-symmetric boundary-layer code with basic turbulence modeling. BL2D was used to compute theoretical results for mean flow comparisons as well as to generate the boundary layer along the inviscid boundary-layer streamline and compute δ^* to appropriately displace the surface. This was an iterative process used to have the effective streamline (the surface plus the boundary layer) match the theoretical inviscid streamline, resulting in an effectively isolated airfoil flow condition.

Eclipse is a linear parabolized stability equation (LPSE) code[79, 80] which was used for a few select test conditions. This code accounts for non-parallel flow effects and surface curvature effects.

4.6 Uncertainty Analysis

The uncertainty analysis was performed by accounting for all the known sources of error. The analysis was performed using methods based upon Coleman and Steele[81]. These included instrument accuracy based on percent full-scale and percent reading for all the instruments used to acquire a given value. Pressure measurements were made typically using a Barocel or Ruska

pressure transducers, which provided a voltage to the VXI/E1413 which provided another value to the computer where the voltage was converted to pressure. Temperature measurements were made in a similar fashion. The pressure measurements of the tunnel total pressure were made directly with a Mensor. The hot-wire probe was calibrated against a Barocel pressure measurement with a 4^{th} order polynomial. The Barocel pressure transducer was connected to a ceiling pressure port directly above the hot-wire probe. It was verified that the pressure measured with this ceiling port and a Pitot tube matched, and the process of using the Pitot tube involved opening the test section, where the process of using the ceiling port did not, which was preferred. If the mean-squared-error (MSE) of the hot-wire probe calibration exceeded the predetermined limit of 0.00048 $(m/s)^2$ {0.0050 fps^2}, then the hot-wire calibration would be repeated, although typical calibrations were an order of magnitude better. **Table 8** indicates the uncertainty of tunnel velocity as computed with a Barocel pressure transducer, hot-wire velocity and surface pressure coefficient measurements at various flow speeds.

Table 8: Velocity and Pressure Uncertainty

	1.8 m/s {6 fps}	**4.6 m/s {15 fps}**	**15 m/s {50 fps}**	**20 m/s {65 fps}**	**26 m/s {85 fps}**
Tunnel Velocity (Barocel)	6.78%	1.16%	0.20%	0.16%	0.14%
Hot-Wire Velocity	7.98%	1.63%	0.34%	0.27%	0.22%
Surface Pressure Coefficient (ESP, Ruska)	1.06%	1.02%	0.68%	0.55%	0.43%

5 Results and Discussion

5.1 Test Plan

A summary of all of the test conditions examined during this experiment is given in **Table 9**. All test cases were at a nominal angle of attack of 0° and sea level conditions. **Table 10** itemizes the specific test cases with the associated surface roughness conditions. The number of repeated elements, thickness and width of the tape define the surface roughness condition. Exact surface locations of the roughness elements are presented in **Table 5**. It should also be noted that the first four test cases were set-up, data acquisition code development, and preliminary data sets.

Table 9: Test Conditions

U_{fs}	M	Re_c	Acoustic Burst	Surface Roughness
20 m/s {66 fps}	0.0588	1.68 x 10^6	10 ms, 300 Hz F = 68.0	None; 1 x 1.6mil; 1 x 2.0mil; 1 x 2.5mil; 3 x 2.5mil; 5 x 2.5mil
15 m/s {50 fps}	0.0438	1.25 x 10^6	10 ms, 200 Hz F = 80.5	None; 1 x 1.6mil; 1 x 2.0mil; 1 x 2.5mil; 3 x 2.5mil; 5 x 2.5mil

Table 10: Roughness Test Cases

Surface Roughness	Test Case
None	Test 05, Test 11
1 x 0.04 mm x 2.54 cm {1.6mil x 1 inch}	Test 06
1 x 0.05 mm x 0.95 cm {2.0mil x $^3/_8$ inch}	Test 08
1 x 0.06 mm x 0.95 cm {2.5mil x $^3/_8$ inch}	Test 07
3 x 0.06 mm x 0.95 cm {2.5mil x $^3/_8$ inch}	Test 09
5 x 0.06 mm x 0.95 cm {2.5mil x $^3/_8$ inch}	Test 10

5.2 Experimental Results and Comparisons to Theory

Within this section, the experimental results will be presented and compared with some theoretical predictions. Mean flow results are compared with MSES and NYU code solutions. Stability results are compared with linear stability theory results from SALLY and limited linear parabolized stability equation (LPSE) results from ECLIPSE. The results from the theoretical computer codes differed somewhat from the experimental results for a variety of reasons. The theoretical codes assumed "ideal" test conditions such as "sea level" conditions, isolated airfoil analyses, precise flow speeds and exact angles of attack with a perfectly two-dimensional model.

Above this perfectly two-dimensional model, was assumed to be a uniform, two-dimensional flow field. It was determined that uncoupled boundary-layer solutions did not provide correlation with the experimental results as well as coupled boundary-layer solutions yielded.

5.2.1 Test Section Set-Up Results

Here, the ceiling / floor pressure distribution and contours are presented. Ceiling contours are presented in **Figures 12 and 13**, where the viscous solution are the inviscid results offset by the displacement thickness. Presented are the computed contours for both of the tunnel mount configurations used. The latter configuration consisted of the model mounted approximately two chordlengths downstream of the test section entrance and was used during all of the stability measurements.

Figure 14 presents the inviscid / design pressure distribution and the experimentally measured values. The experimental values were for the 20 m/s, zero angle of attack flow case.

All of the results presented in this section are first order attempts to address the test section contouring. The finite boundary-layer thickness at the test section entrance is because the input theoretical domain extended further upstream from the test section entrance location. The results could have been improved by starting the input domain, and thus the boundary-layer growth, at the test section entrance. Also, improvements could have been made by iterating the process between the inviscid and viscous solutions. However, it was determined that the limitations on the adjustment hardware had stronger influences on the results than the above crude estimates.

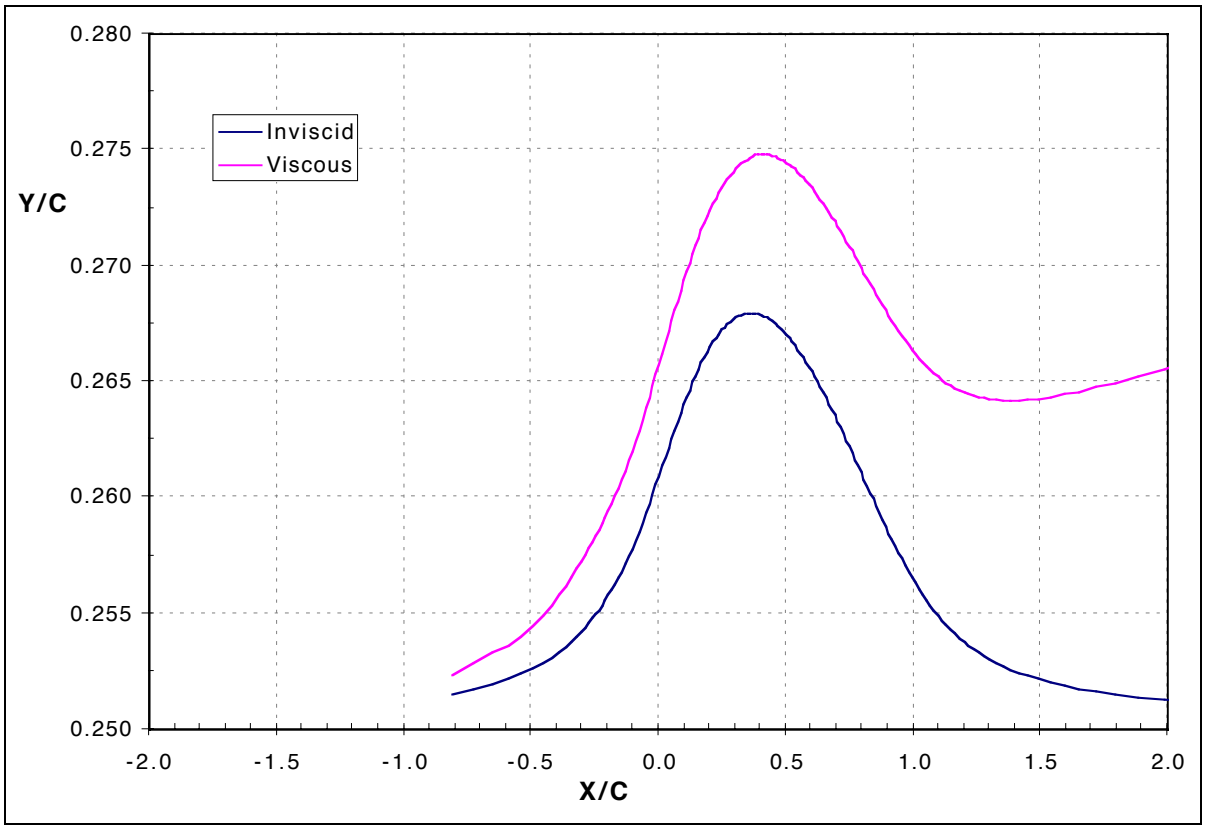

Figure 12: Test Section Ceiling Theoretical Surface Contour: Upstream Mount Location

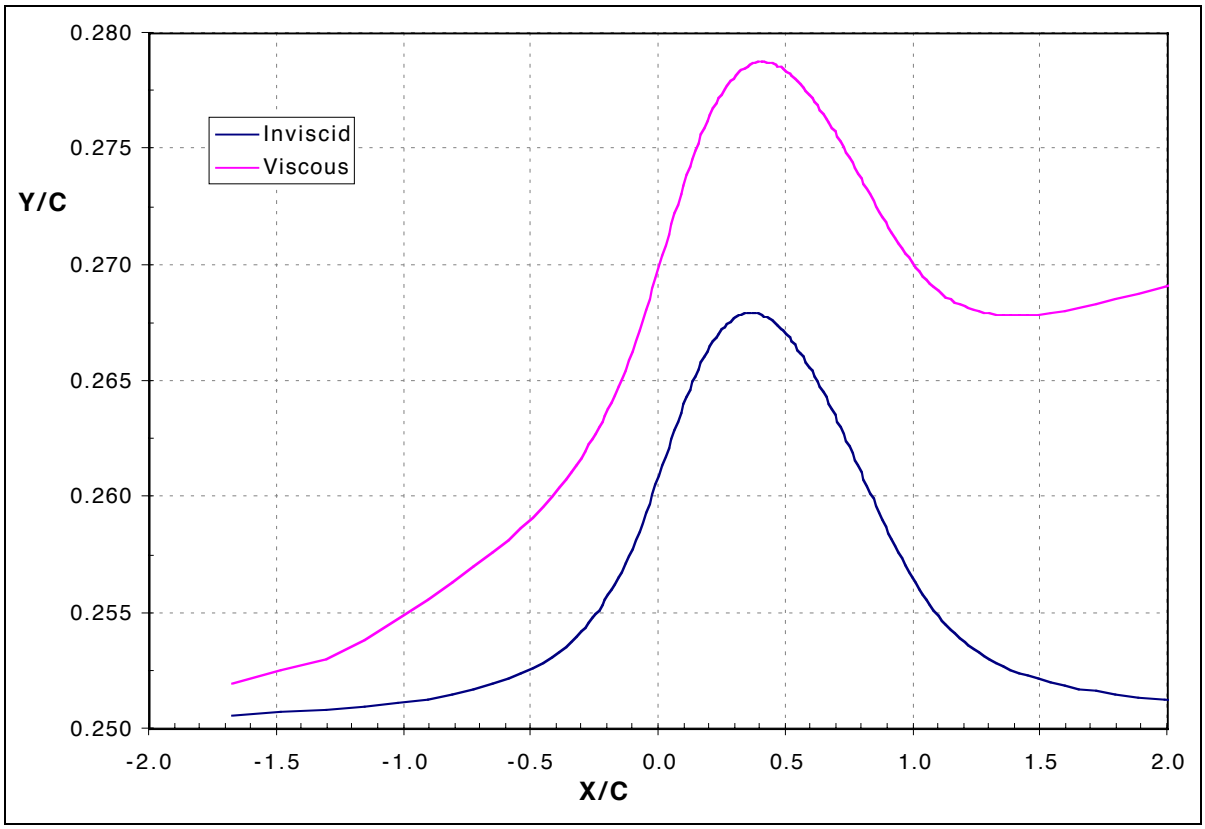

Figure 13: Test Section Ceiling Theoretical Surface Contour: Downstream Mount Location

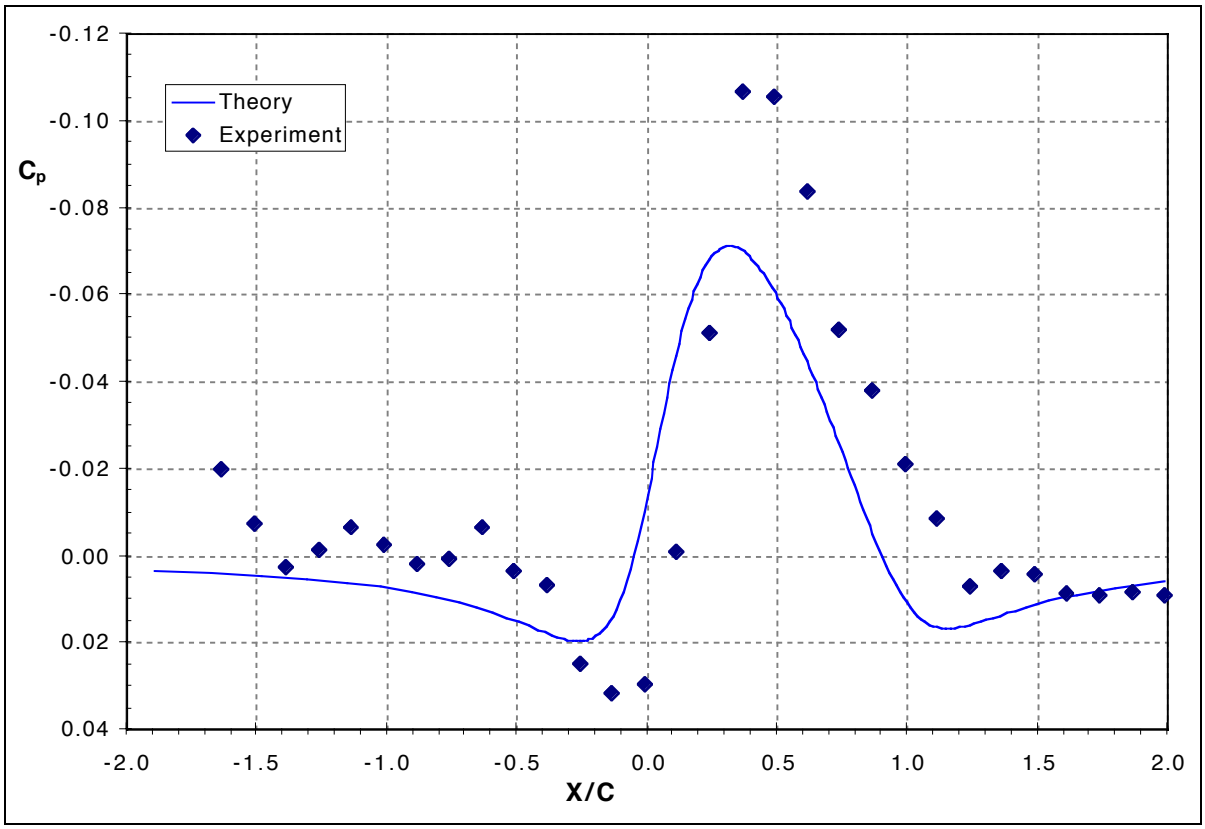

Figure 14: Test Section Ceiling Surface Pressure Distribution: Theory vs. Experiment

5.2.2 Mean Flow Results

Comparisons of the surface pressure distribution and boundary-layer parameters, and boundary-layer profiles for various surface roughness conditions are presented herein. Included are the model alignment angle measurements based upon the wall location at various chordwise stations and the location of the stagnation point on the model based upon a detailed analysis of the surface pressure distribution. All of the hot-wire probe velocity measurements were corrected based upon the simultaneously measured mean tunnel velocity. This correction accounts for variations in the free-stream conditions.

5.2.2.1 Model Alignment, Surface Pressure Distribution and Angle of Attack

The model alignment angle in the test section was computed by comparing the wall location measurements with the Quality Assurance and Measurement Branch (QA) surface coordinates measurements. The wall location was determined by extrapolating the mean velocity profiles to

a zero velocity condition, as explained in **Section 4.2.1** and the results from the various tunnel entries are presented in **Figure 15**. This method used provided a much more accurate determination of the alignment angle than could be achieved with the digital inclinometer used to align the model during installation. These measurements were as accurate as the wall finding algorithm, which broke down for a transitional boundary-layer profile where the boundary-layer velocity profile became strongly inflectional. This angle is geometric only, and does not account for flow angularity. It is the measure of the model alignment to the test section centerline.

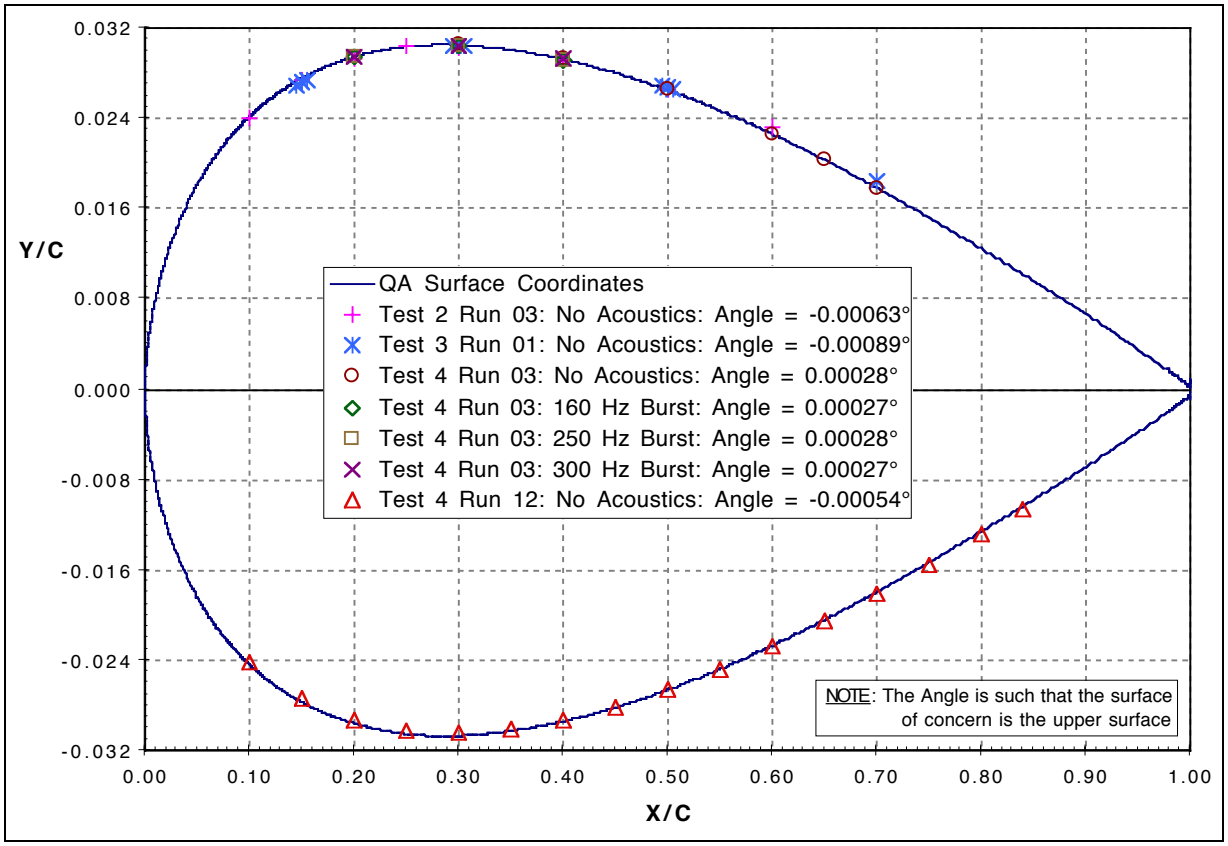

Figure 15: Model Alignment Angle as Computed by Y_{wall} Measurements

Test 2 and Test 3 are from the initial tunnel entry where the model was located one chordlength from the test section entrance and the surface with the detailed pressure port distribution was the upper surface. The Test 4 Run 03 cases were from the second tunnel entry where the model was located two chordlengths from the test section entrance. Again, the pressure port surface was the upper surface. The Test 4 Run 12 case was also the second tunnel entry where the model was located two chordlengths from the test section entrance, but the stability measurement surface was the upper surface.

The Test 4 Run 03 case was used to verify the model alignment angle and to verify the acquisition subroutines. For this test case the same model position as the surface pressure measurements was used, with the dense distribution of pressure ports on the upper surface. In comparing the model alignment angle measured with and without acoustic forcing, it can be seen that the forcing did not affect the mean flow results, as expected. Also, for these cases, it can be seen that the wall locating method presented consistent and repeatable results. The wall locating results were determined from profiles acquired at chordwise stations where the boundary-layer profile was not significantly inflectional close to the wall, thus data on the pressure port surface (upper surface in the plot) was limited to 70% chord. One can see that the geometric angle was a very small fraction of a degree indicating a high degree of repeatability.

The model surface pressure distribution is presented in **Figure 16**. It can be seen that for the surface measurements at the off-centerline span-wise stations, the results indicate a span-wise variation stronger at the upstream stations (5% and 30% chord). This correlates well with the results indicated from the QA surface measurements as presented in **Figure 8**, where the strongest spanwise variations existed in the leading-edge region (upstream of 15% chord) of the pressure port covered surface. Bad pressure ports can be seen at the 3% and 10% chord centerline locations. The variations in the theoretical results for the two model surfaces are due to asymmetric surface grids and differences in the true surface geometry. It should also be noted that the surface pressure measurements were made on the opposite surface from where the hot-wire measurements were made, where no surface pressure measurements were completed. The model, though designed to be symmetric, was not perfectly so, as indicated by the surface geometry comparison in **Figure 6** and the resultant theoretical pressure distribution. The effect of the slight variations was determined to be small after running a theoretical sensitivity study of the mean flow and flow stability over a model with slightly larger and smaller thickness as well as with slightly faster and slower mean flow velocities.

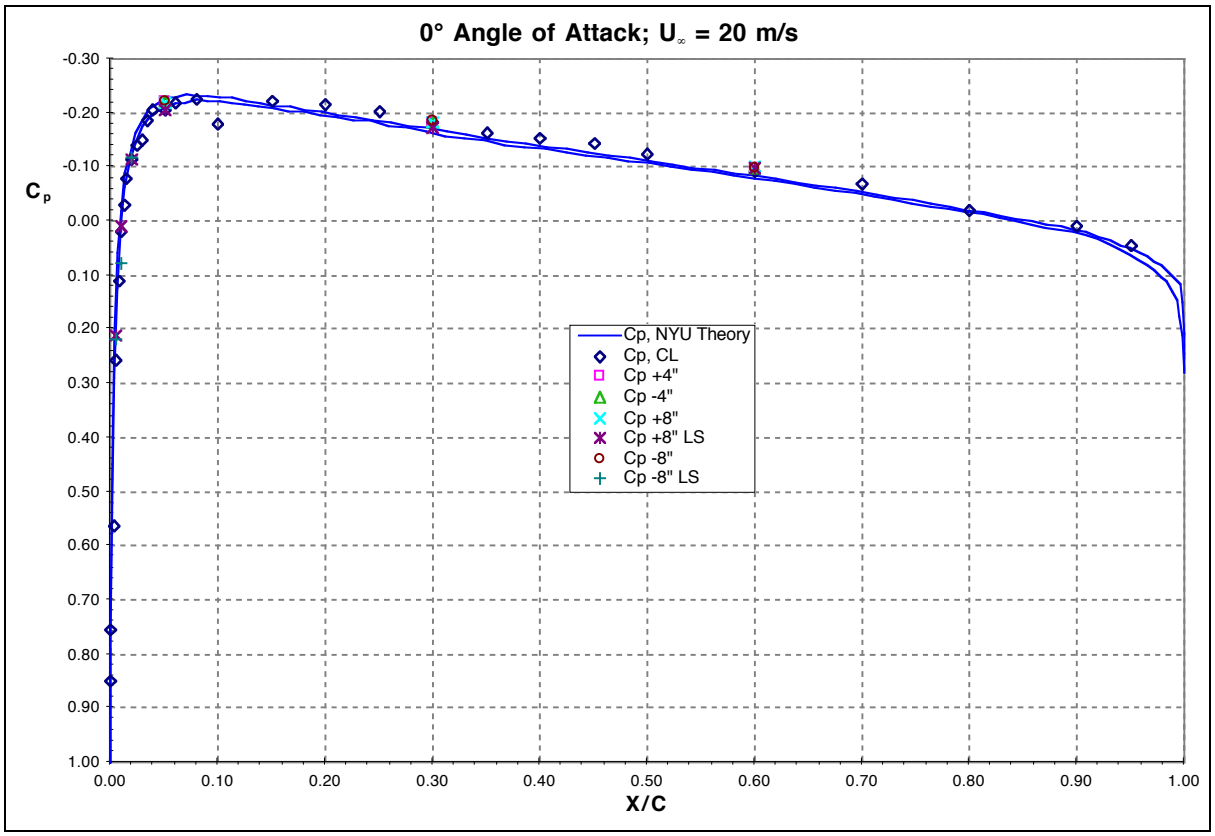

Figure 16: Model Surface Pressure Distribution

The location of the stagnation point can be used to determine the amount of flow angularity, or the angle of attack. The stagnation point location was determined by linearly interpolating the pressure data acquired in the expected region of the stagnation point. This interpolation scheme is performed in velocity-surface distance coordinates, because the velocity varies linearly in the vicinity of the stagnation point. By examining these results, it can be seen that the stagnation point can be bracketed between the leading-edge pressure tap and first pressure tap on the pressure port (upper surface), yielding a crude angle of attack range between 0 and -0.2°. By interpolating, the results show that the stagnation point is near 0.055% chord on the upper surface of the model, which roughly corresponds to a 0.067° nose down (negative) angle of attack. The interpolation results are presented in **Figure 17**. All surface pressure measurements were made on the pressure port surface when it was the upper surface of the model. Once the model was aligned and its orientation was marked, the model was flipped and the smooth surface was set to these markings. This method assumed a perfectly symmetric model, which is not the case, but the variations have been determined to be slight. An angle of attack trade study using

LAMDA indicated that if the model was at –0.15°, the predicted transition location (N = 9 for the 300 Hz disturbance) shifts approximately 5% chord downstream, with a different slope of the N-factor curve. However, such an angle of attack variation results in a very poor experimental to theoretical pressure distribution match. This would indicate that the stagnation point shift would likely be due to surface asymmetry, as the flow is very sensitive in the leading-edge region.

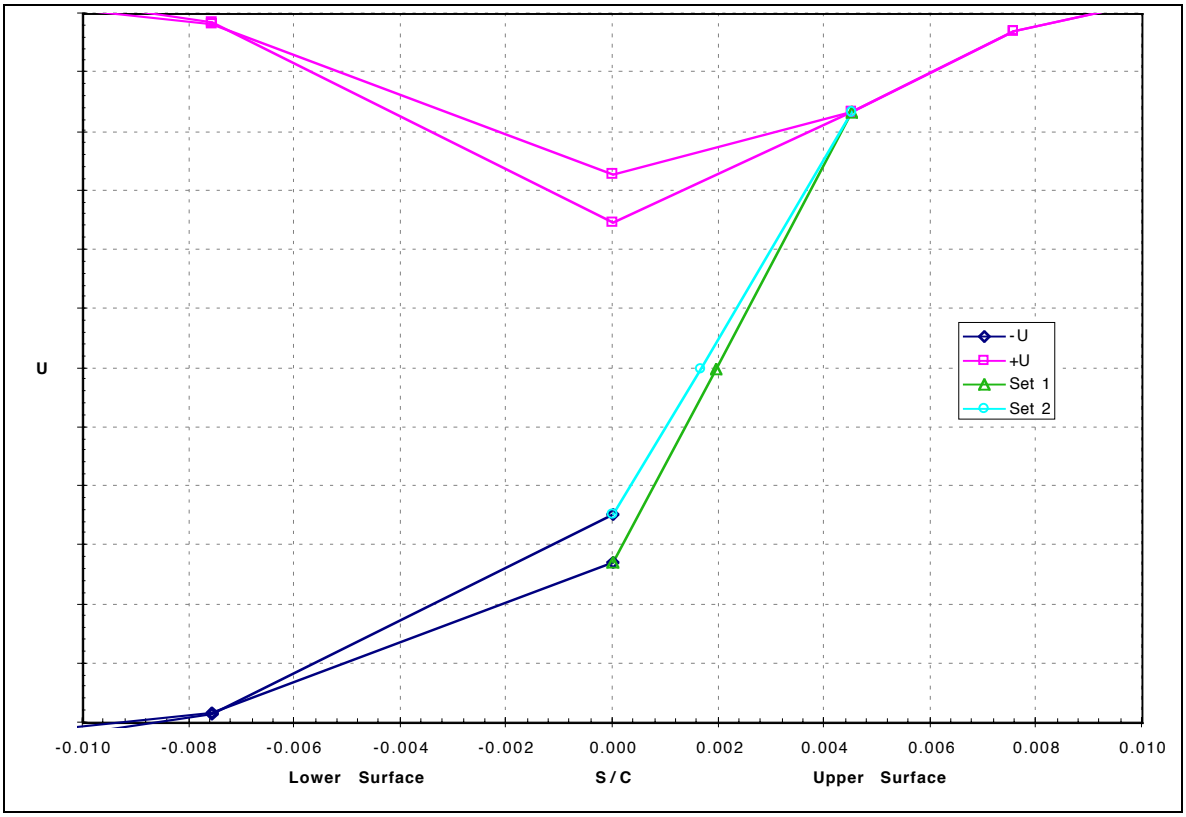

Figure 17: Locating the Stagnation Point

5.2.2.2 Theoretical Mean Flow Results

A comparison of several theoretical mean flow solutions are presented in **Figure 18**. The NYU/Cebeci results were determined by computing the potential flow field about the model (using the NYU Code) followed by applying a laminar boundary layer along the surface (using the Cebeci Code). The MSES/Cebeci results follow the use of an integral boundary-layer solution with forced transition on the model at 80% chord to determine the flow field about the model, using the MSES code. Then the laminar boundary layer solution is applied using that pressure field, using the Cebeci Code. The BL2D results use the potential flow field results from the NYU code, but include a higher order boundary-layer solution with a transition model. It can

be seen that the Cebeci and BL2D methods provide an excellent match in the laminar flow region of the model. This latter comparison was only made for the 20 m/s flow case. These plots indicate that if the boundary-layer influences are accounted for in the flow field solution, as with the MSES case, the effect of transition can be seen to influence the flow up to 20% chord upstream of the transition location.

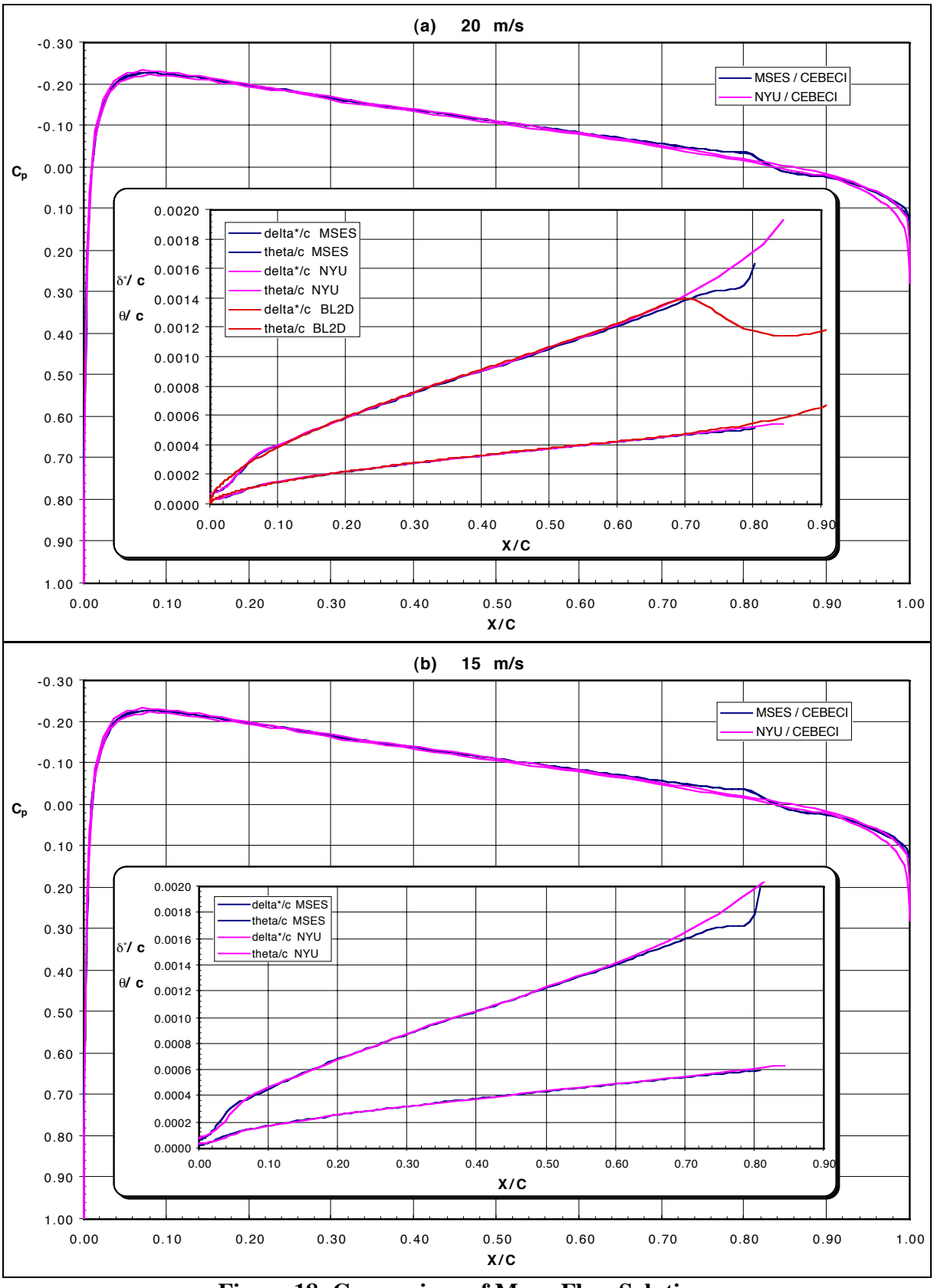

Figure 18: Comparison of Mean Flow Solutions

5.2.2.3 Experimental Mean Flow Results with Comparisons to Theory

The boundary-layer displacement thickness and momentum thickness are presented within this section. Mean data was acquired with and without acoustic forcing in the free-stream. Free-stream velocities of 15 m/s, 20 m/s, and 30 m/s were examined. An estimate of the surface pressure distribution is made using the determined edge velocity of each mean boundary-layer velocity profile. Displacement thickness and momentum thickness are also computed from the velocity profiles.

A summary of all of the test cases examined for a free-stream velocity of 20 m/s is presented in **Table 11**. It can be seen that data was acquired over both surfaces, which allows for comparison of the actual effects of the slight asymmetry of the model. Data was acquired with and without acoustic forcing in the free-stream. In the mean, this acoustic forcing should be zero and thus should not affect the mean boundary-layer results. The boundary-layer data was acquired using several different hot-wire probe supports and configurations of these supports. The effect of the different hot-wire probe supports is also examined.

Table 11: 20 m/s Mean Flow Test Cases

Test Case	Model Surface	Hot-wire Probe	Acoustic Forcing
Test 02 Run 03	Pressure	Single Extended	No
Test 03 Run 01	Pressure	Single Extended	No
Test 04 Run 11	Stability	Dual Vertical Extended	No
Test 04 Run 12	Stability	Dual Vertical Extended	No
Test 04 Run 15	Stability	Dual Vertical Short	Yes
Test 04 Run 17	Stability	Dual Vertical Short	Yes
Test 05 Run 01	Stability	Dual Vertical Short	No
Test 06 Run 01	Stability	Dual Vertical Short	Yes
Test 09 Run 02	Stability	Dual Vertical Short	Yes
Test 10 Run 04	Stability	Dual Vertical Short	Yes
Test 12 Run 03L	Stability	Dual Span	No
Test 12 Run 03R	Stability	Dual Span	No

The pressure distribution over the model was computed over the model using the determined boundary-layer edge velocities. The coefficient of pressure is found using **Equation 5-1**.

$$C_p = 1 - \left(\frac{U_e}{U_\infty} \right)^2 \qquad \textbf{Equation 5-1}$$

Data from all of the above test cases is presented in **Figure 19**, except Test 04 Run 11 where the data set did not extend far enough into the free-stream to yield an accurate representation of the boundary-layer edge velocity for most of the chordwise data sets. The scatter of the data is most significantly associated with the determination of the boundary-layer edge velocity. However, this plot indicates that the nominal pressure field over the model, with both the Pressure Port surface (solid symbols) and the clean (Stability) surface (hollow and line symbols), are consistent and repeatable, despite any slight asymmetry in the geometry.

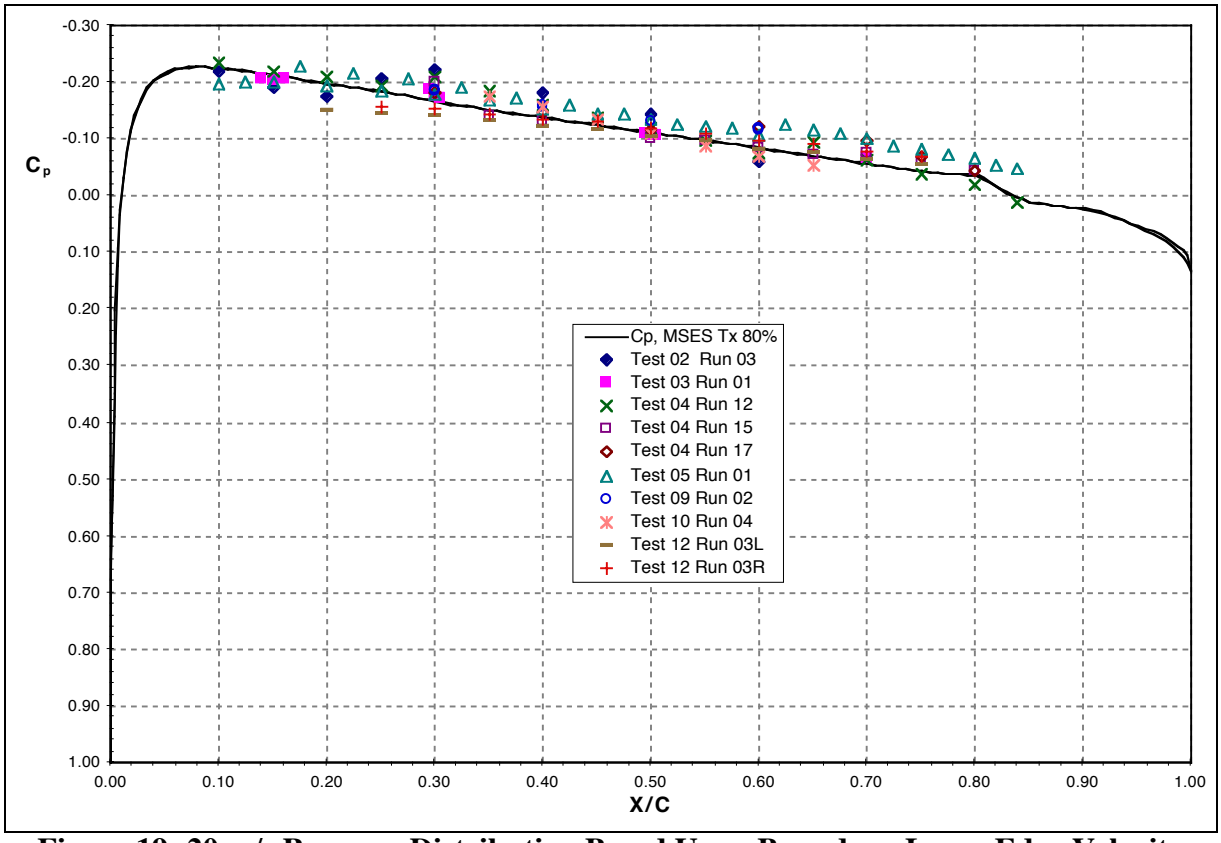

Figure 19: 20 m/s Pressure Distribution Based Upon Boundary-Layer Edge Velocity

The mean flow boundary-layer integral parameters, δ^* and θ, for the 20 m/s flow case are shown in **Figure 20**. The momentum thickness results, θ, correlate well with the MSES 80% chord forced transition theoretical test case, where the experimental results deviated from the theoretical results by 1 - 11%. The displacement thickness results, δ^*, do not match nearly as well. Here the experimental results deviated from the theoretical results by 4 - 20%. Because of the relative insensitivity of the displacement thickness and momentum thickness to the boundary-layer edge condition, even the profiles with an inadequate number of data points near

the edge yielded reasonable results. The experimental displacement thickness values were all consistently smaller than the theoretical value. This would indicate fuller profiles and possibly an accelerated flow field compared to that assumed in the theory, which could be associated with local flow blockage.

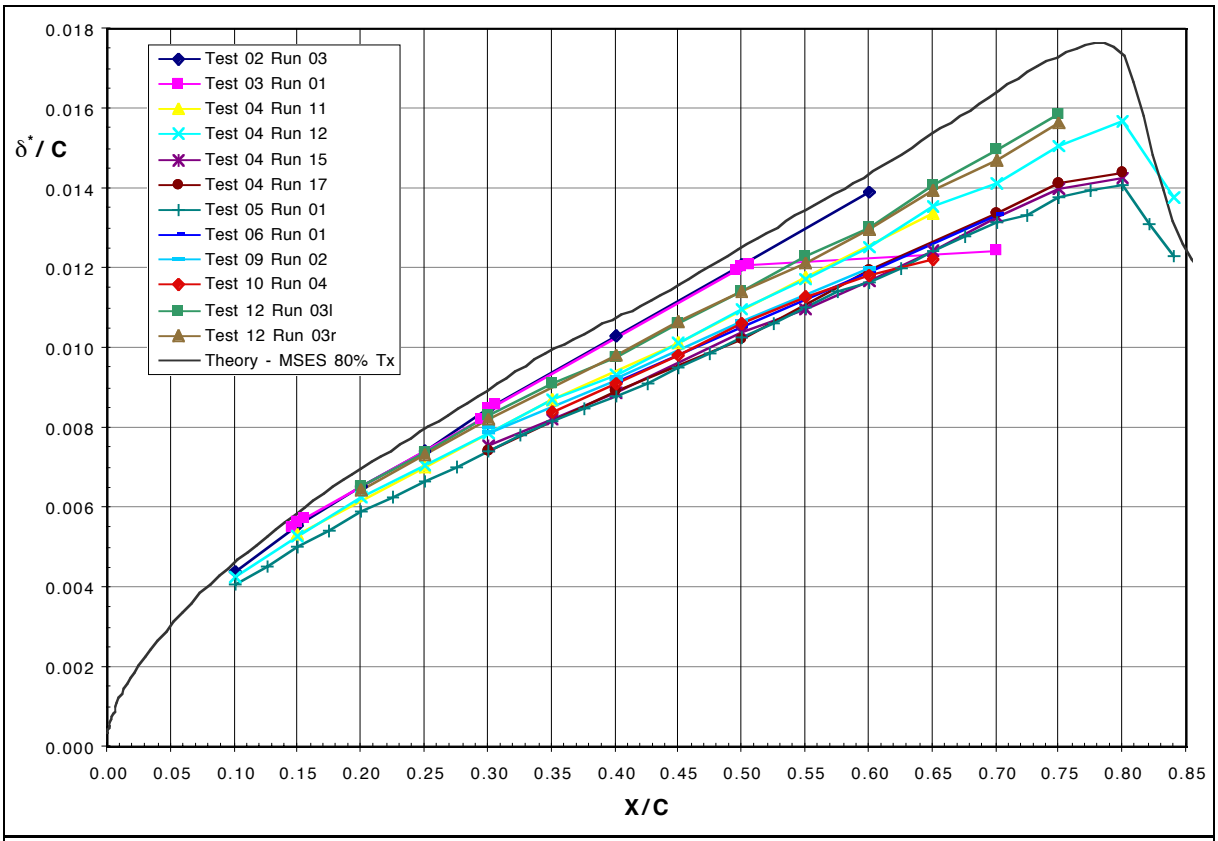

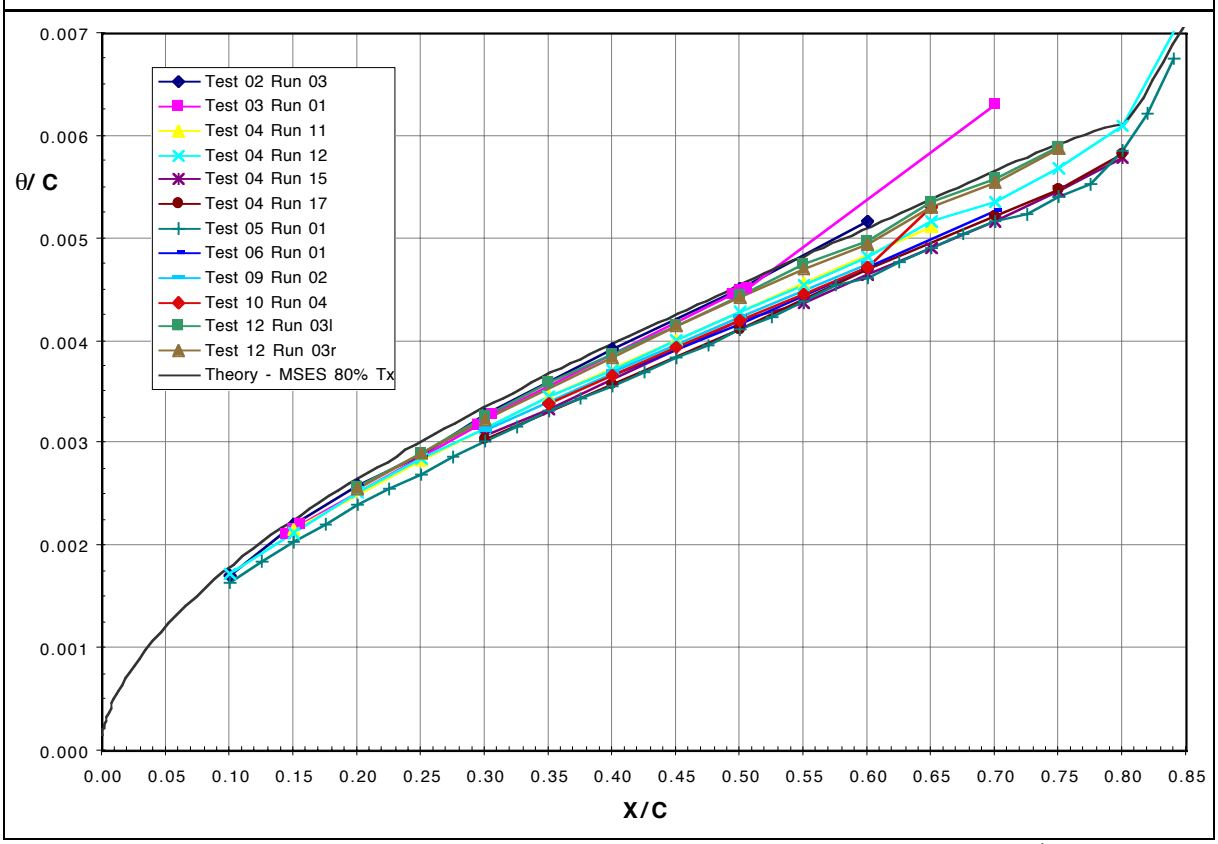

Figure 20: 20 m/s Mean Flow Boundary-Layer Integral Parameters, δ^* and θ

Similar results were also computed for the 15 m/s {50 fps} flow case. Overall, the results from this flow case followed the trends observed in the 20 m/s flow case. No hot-wire measurements were made over the Pressure Port surface. The following table presents the mean flow test cases examined at this flow speed.

Table 12: 15 m/s Mean Flow Test Cases

Test Case	Model Surface	Hot-wire Probe	Acoustic Forcing
Test 11 Run 02	Stability	Dual Vertical Short	Yes
Test 06 Run 04	Stability	Dual Vertical Short	No
Test 06 Run 05	Stability	Dual Vertical Short	Yes
Test 07 Run 01	Stability	Dual Vertical Short	Yes
Test 09 Run 04	Stability	Dual Vertical Short	Yes
Test 10 Run 02	Stability	Dual Vertical Short	Yes
Test 12 Run 01L	Stability	Dual Span	No
Test 12 Run 01R	Stability	Dual Span	No

In a similar manner as above for the 20 m/s flow condition, the surface pressure distribution for the 15 m/s flow condition was computed and is presented in **Figure 21**. It should also be noted that the surface pressure distribution was not measured for this flow condition using the surface pressure ports. The results indicate a reasonable correlation with theory.

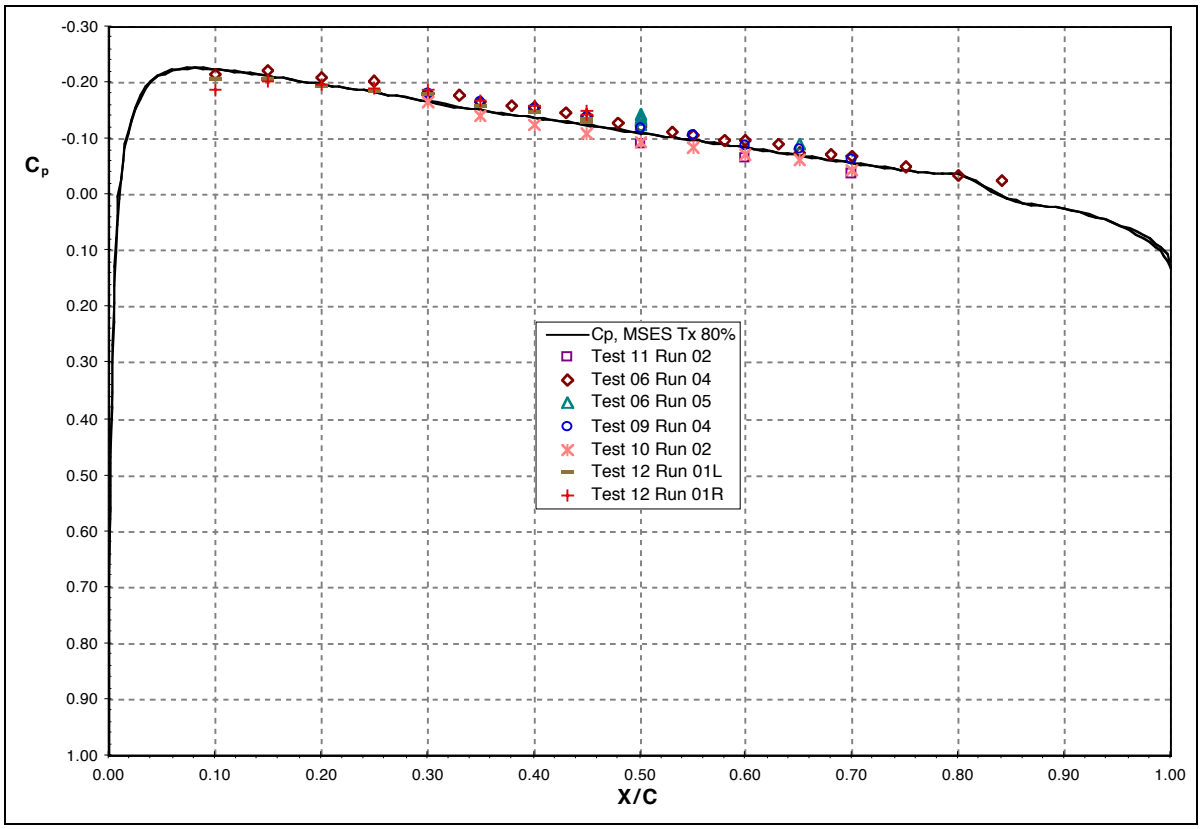

Figure 21: 15 m/s Pressure Distribution Based Upon Boundary-Layer Edge Velocity

On the same note, the mean boundary-layer parameters were also determined and compared to theory (MSES integral boundary-layer solution with forced transition at 80% chord). These results are presented in **Figure 22**. It is interesting to note that the deviation of the momentum and displacement thickness values between the experimental results and the MSES computations is about the same for the 15 m/s case as it was for the 20 m/s case (4 - 12% and 6 - 21%, respectively). Again, it appears that the experimental results indicate fuller profiles and possibly a more accelerated flow field, which could be associated with local flow blockage.

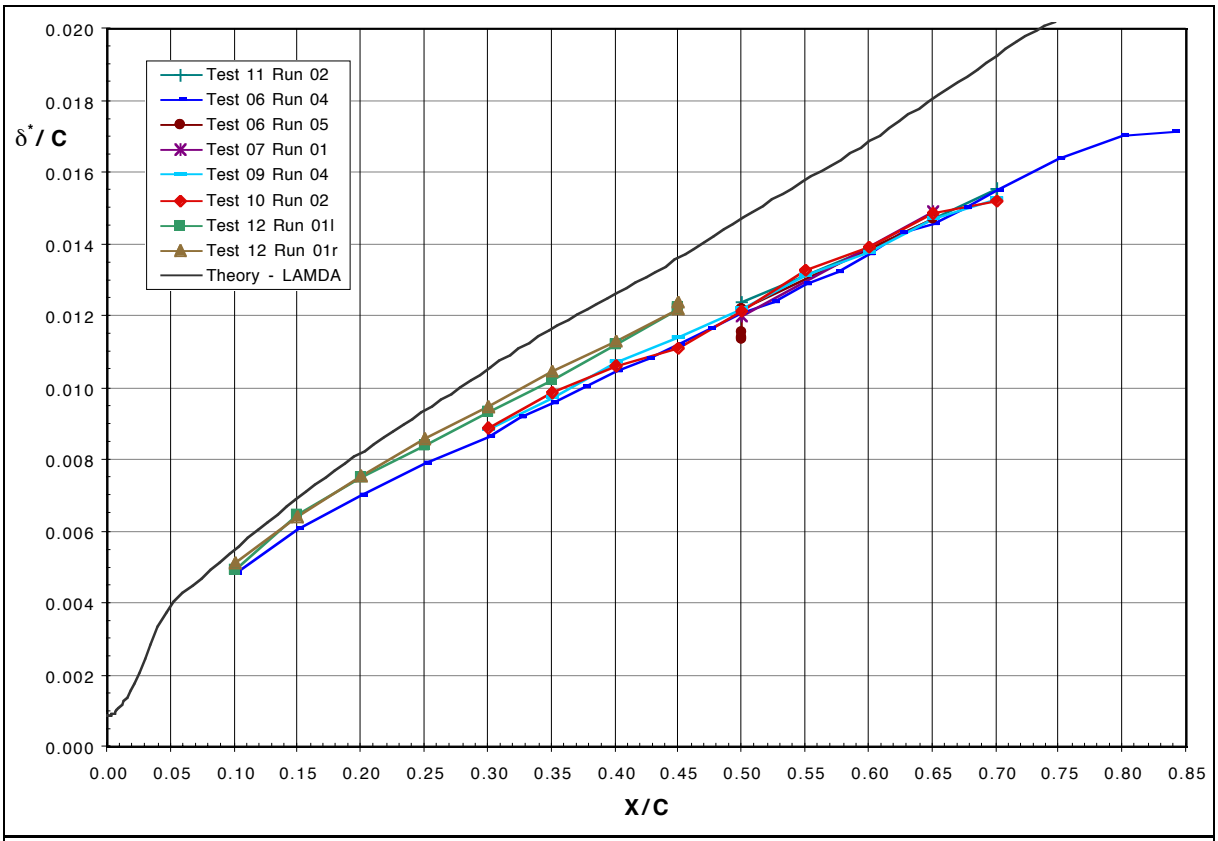

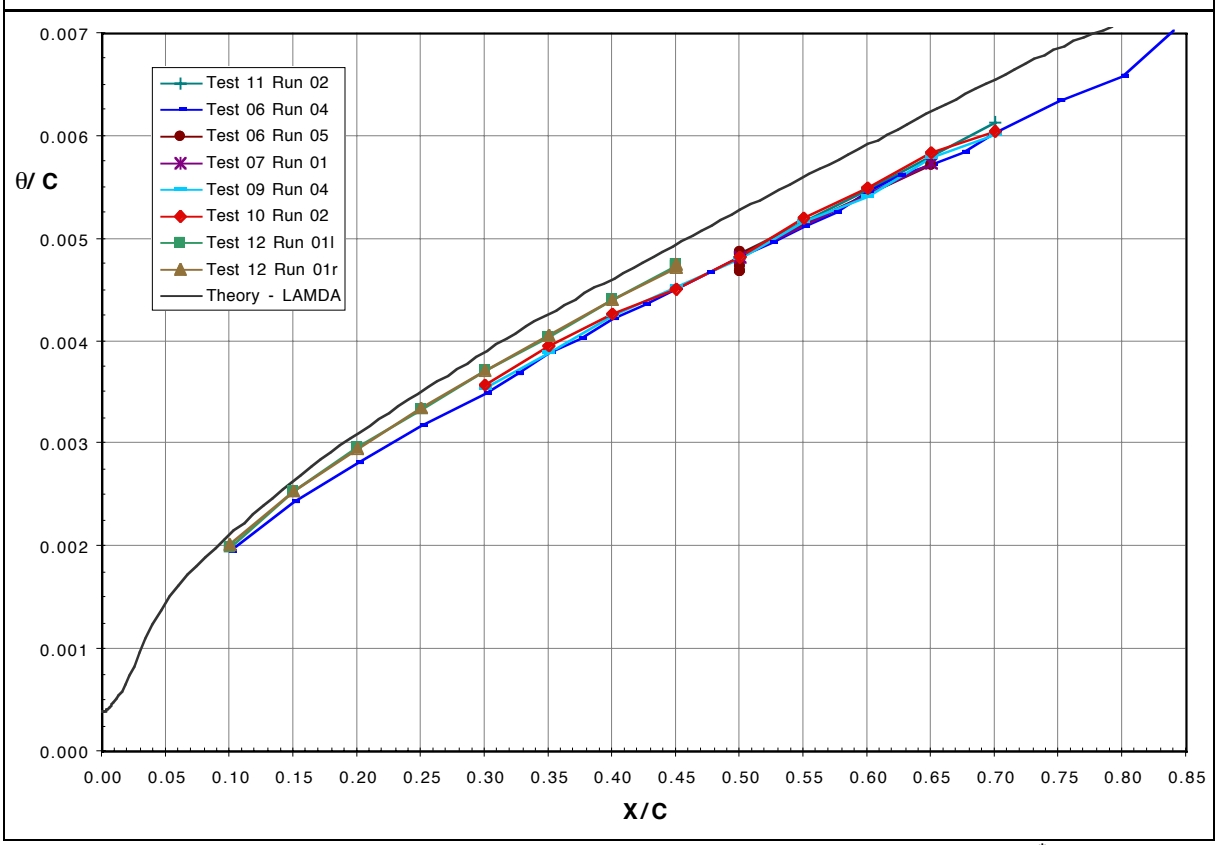

Figure 22: 15 m/s Mean Flow Boundary-Layer Integral Parameters, δ^* and θ

In a similar manner as above for the 15 and 20 m/s flow conditions, the surface pressure distribution for the 30 m/s flow condition was computed and is presented in **Figure 23**. It should also be noted that the surface pressure distribution was not measured for this flow condition using the surface pressure ports. These results were acquired over the stability measurement surface using the dual-vertically-spaced hot-wire probe support with extended in the short configuration (see **Section 2.2.1** for more details on the hot-wire probe support configurations). The results indicate a reasonable correlation with theory, a little more negative than either the 15 m/s and the 20 m/s corresponding results but well within the range of experimental scatter.

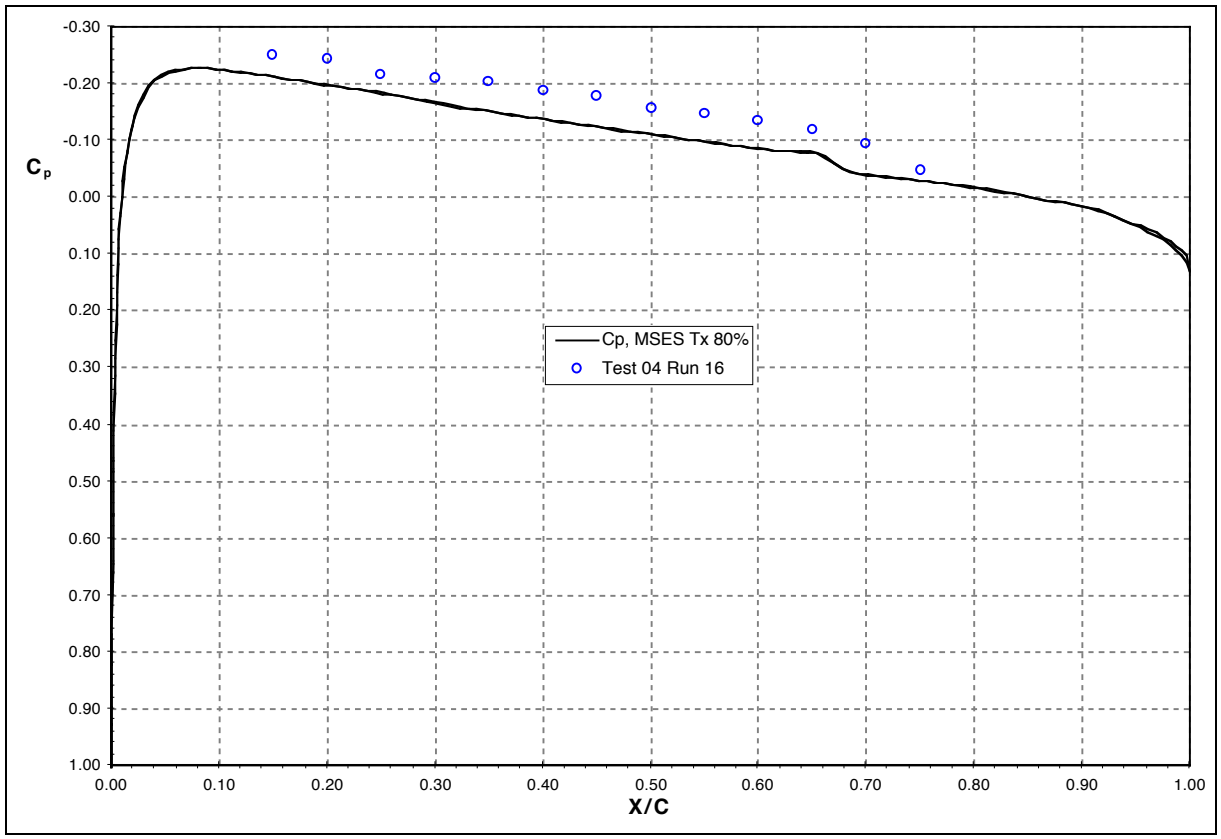

Figure 23: 30 m/s Pressure Distribution Based Upon Boundary-Layer Edge Velocity

In examining the mean flow results, it appears that the experimental data sets are grouped such that data acquired with like hot-wire probe configurations collapse. It would also appear that the larger, more bulky probe support yielded the lowest displacement thickness values, indicated possibly the greatest amount of flow blockage. At the same time, it was found that the presence of the free-stream acoustic disturbances had no noticeable effect on the mean flow results, as expected. Also, the presence of surface roughness located near the lower branch seemed to have

no significant effect on these results. The off-centerline data sets (Test 12) follow the theoretical results as well as the rest of the data. This would indicate that the spanwise variation of the model is not significant.

It should be noted that the deviation of the experimental and theoretical results, particularly in displacement thickness values has been an issue of concern. Various trade studies of theoretical codes were completed to examine the sensitivity of the results to slight variations in several parameters. These parameters consisted of model thickness (±10%), angle of attack (±0.5°), free-stream velocity (±10%), boundary-layer transition location (inviscid, 50 - 100% chord), number of points in the boundary-layer velocity profile (30 - 100), and wall locating algorithm (least-squares linear extrapolation, cubic spline extrapolation, and least-squares extrapolation accounting for the pressure gradient effects on the slope of the velocity profile at the wall). Also, the experimental pressure distribution was fit with a spline and used as an input to the theoretical codes. The latter analysis resulted in an oscillating pressure variation along the model centered about the theoretical values. It was determined that boundary-layer transition needed to be accounted for in the determination of the pressure distribution. The general results of the trade studies was that for the examined variation of variables, the Branch I location varied with 5% chord, the transition location varied within 10% chord, the disturbance frequency that first reached N = 9 varied within ±25Hz, and the slope of the theoretical N-factor curves varied as well.

Tunnel flow blockage is one explanation for the differences in the mean flow results from experiment to theory. While the ceiling and floor of the test section were contoured to simulate an isolated airfoil, the final results do indicate there was a difference in the mean flow field over the model, as indicated by the pressure distribution results. The hot-wire probe itself could be a plausible cause for the differences in experimental boundary-layer profiles with theoretical profiles. First, there is the possibility of probe support interference/blockage of the mean flow which hopefully would be limited to affecting the local mean flow and not the global stability, however according to Saric[1], the local pressure field around the probe support "can strongly influence T-S wave amplitude." Other concerns include probe/wire near wall effects (heat transfer, blockage effects), wire orientation (near the wall du/dy is strong and the wire would

"appear" to have a faster velocity at a lower location), and improper treatment of the raw experimental data, particularly the edge or wall conditions. All of the above could have a strong effect on the near-wall hot-wire measurements, but determining the specific effects would require more precise equipment than was available for this experiment.

5.2.2.4 Mean Boundary-Layer Velocity Profiles

The mean profiles are presented in **Figure 24** for the 20 m/s flow case. Test cases with no acoustic forcing and applied surface roughness are presented. Comparisons to theory are made for a selected number of chordwise stations. The theoretical code used for these comparisons was BL2D, which was run using the potential flow solution for the surface pressure distribution from the NYU code.

The mean velocity profiles indicate that the pressure ports on the Pressure Port surface influenced boundary-layer transition, shifting the location upstream by over 10% chord, as indicated by examining the profiles at 70% and 84% chord. This supports the necessity of the model design as symmetric, where the stability studies were conducted on the undisturbed side of the model.

Examining the results for all of the chordwise stations reveals a good level of consistency between the various data test cases.

It can be seen that the velocity profiles are fuller in the near-wall region than the theoretical profiles as far upstream as data was acquired at 10% chord. This would seem to indicate that this phenomena was not related to the effect of the growing the boundary layer on the flow field solution. The profile shape and the resulting mean flow parameters such as displacement thickness, momentum thickness and pressure coefficient seem to indicate that there is a local mean flow distortion when measurements were made close to the model surface. This statement is based upon the reasonable match of the edge condition with the theoretical and measured pressure coefficients which were not influenced by the hot-wire probe. Possible reasons for the discrepancies between measured and predicted mean-flow profiles have been discussed earlier.

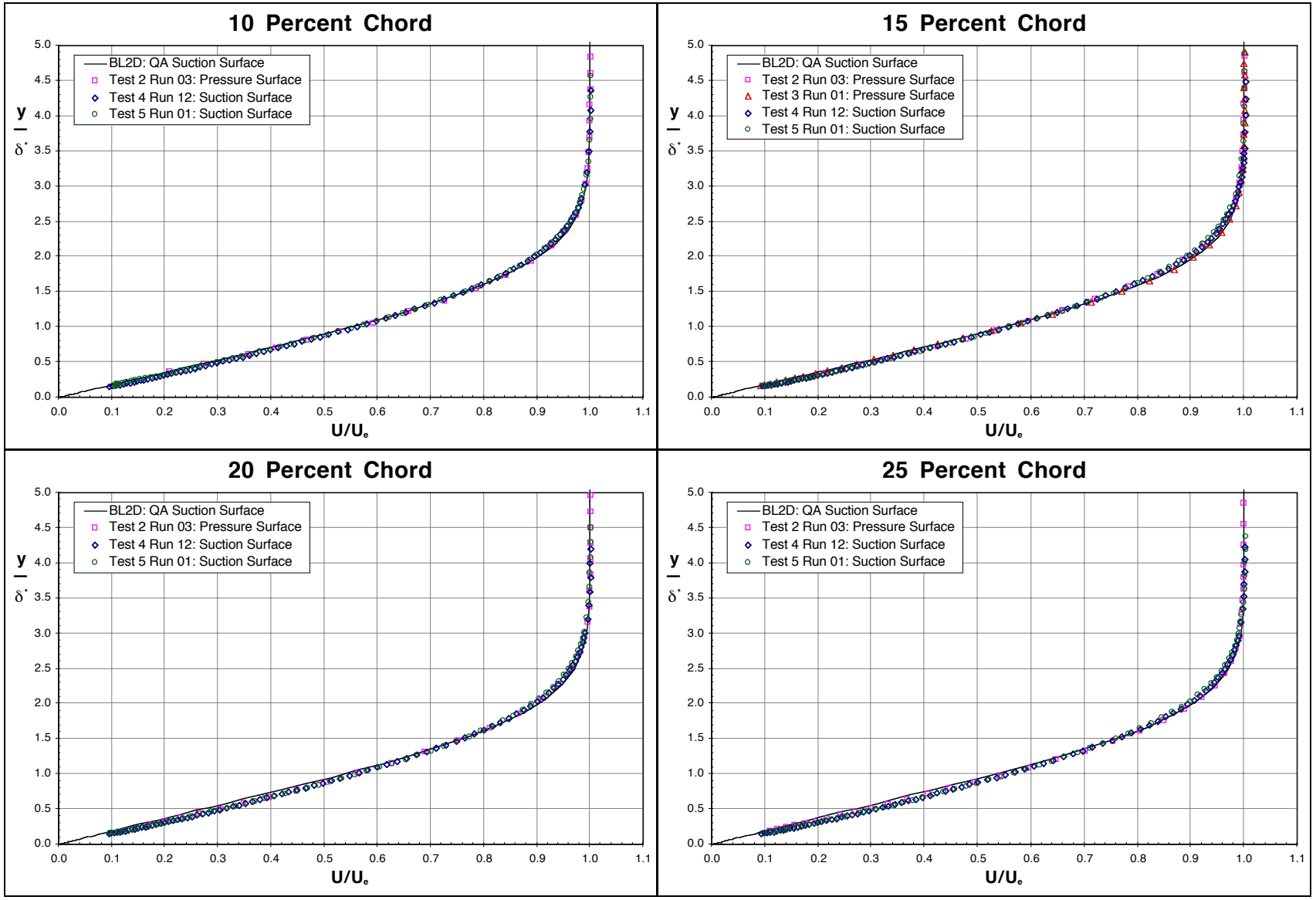

Figure 24: 20 m/s Mean Boundary-Layer Velocity Profiles

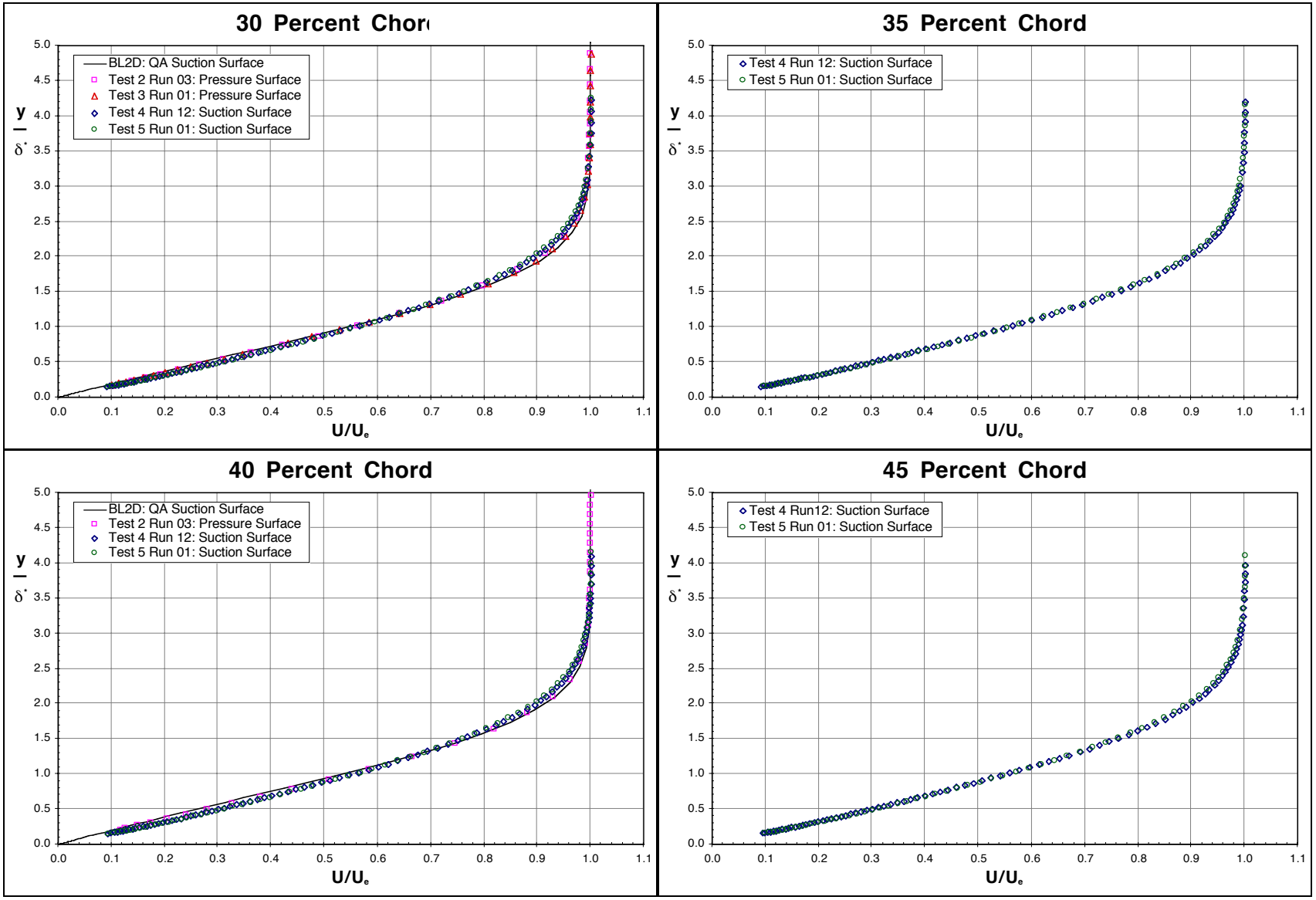

Figure 24: 20 m/s Mean Boundary-Layer Velocity Profiles

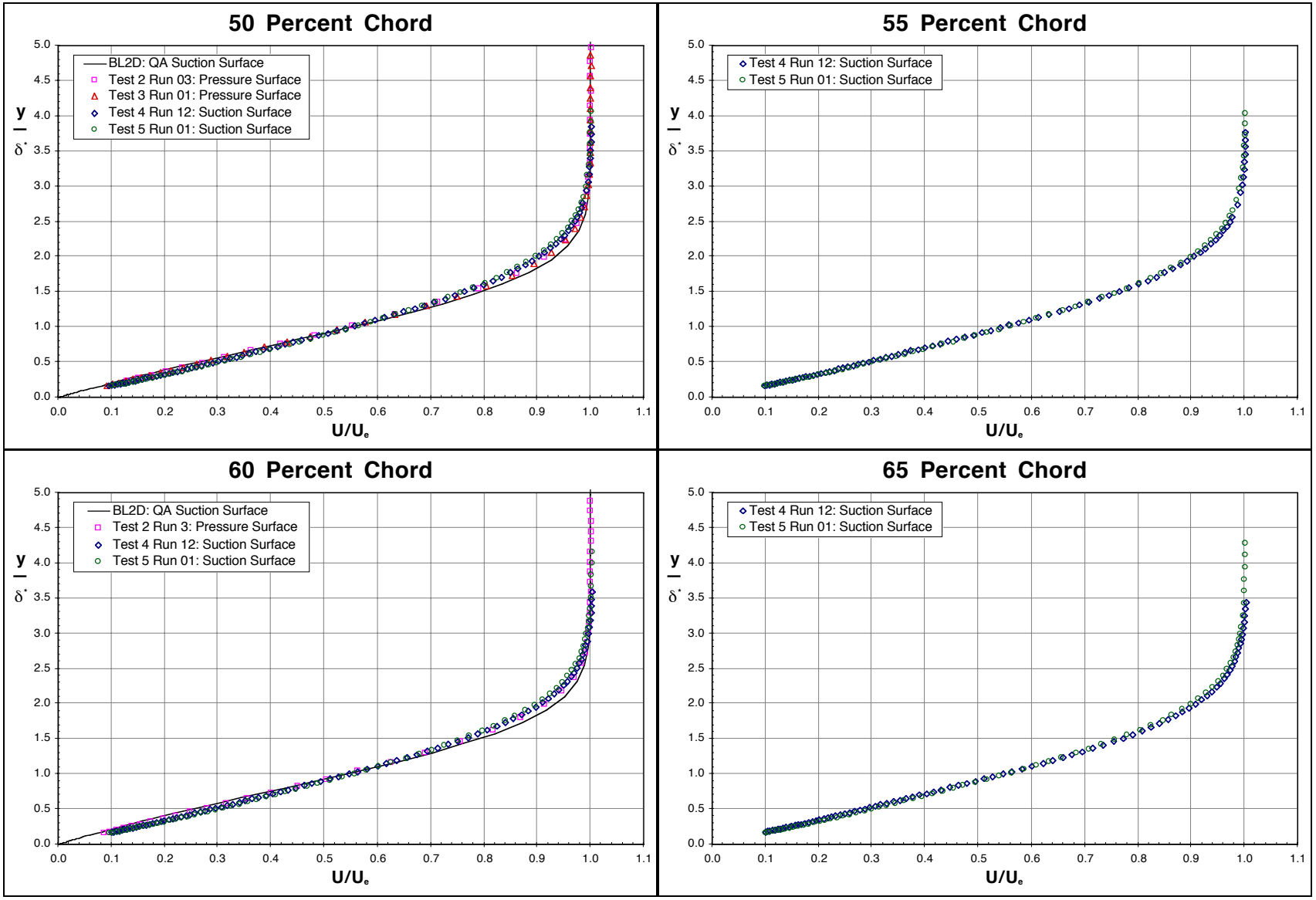

Figure 24: 20 m/s Mean Boundary-Layer Velocity Profiles

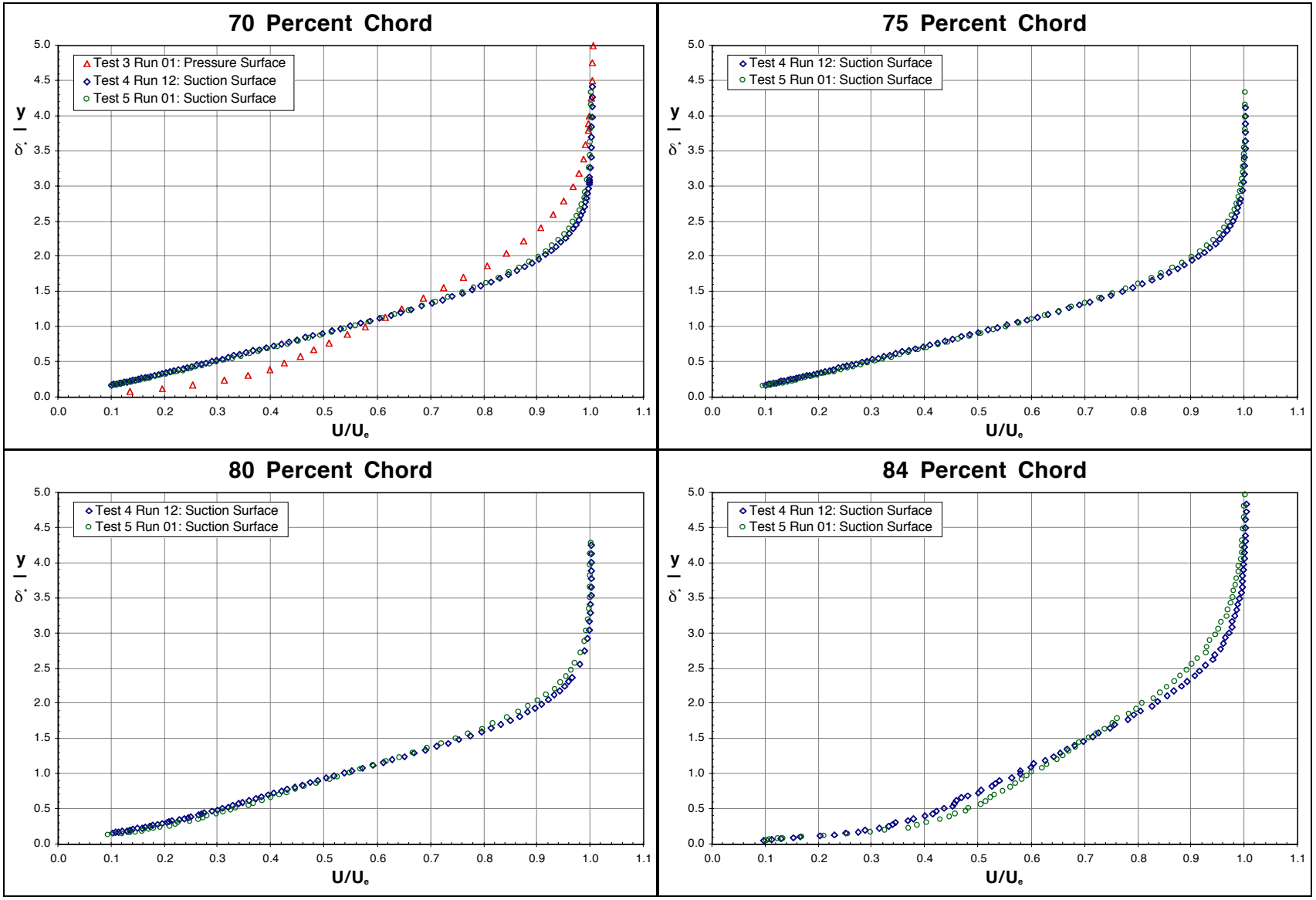

Figure 24: 20 m/s Mean Boundary-Layer Velocity Profiles

5.2.2.5 Flow Transition Analysis

The nature of the flow during the non-linear stages of the boundary-layer stability was examined and the results are displayed in **Figure 25**. Presented are the mean boundary-layer profiles and an extended time trace at a constant boundary-layer height, $(y/\delta^*) = 0.5$ (actually at constant distance from the surface). The flow velocity examined was 20 m/s. The data was processed with a 1 Hz – 1 kHz bandpass filter. The data was acquired at a sampling rate of 2000 points per second for a duration of 0.5 seconds. The variation of the RMS and peak-to-peak amplitude values of the time traces are presented in **Table 13**.

Table 13: Transition Study Time Trace Properties

Chordwise Station	RMS	Peak-to-Peak Values
70	0.945×10^{-3} m/s {0.0031 fps}	5.61×10^{-3} m/s {0.0184 fps}
72	1.16×10^{-3} m/s {0.0038 fps}	8.38×10^{-3} m/s {0.0275 fps}
74	2.19×10^{-3} m/s {0.0072 fps}	14.9×10^{-3} m/s {0.0488 fps}
76	5.03×10^{-3} m/s {0.0165 fps}	43.6×10^{-3} m/s {0.1432 fps}
78	10.4×10^{-3} m/s {0.0340 fps}	84.2×10^{-3} m/s {0.2762 fps}
80	18.6×10^{-3} m/s {0.0611 fps}	150.6×10^{-3} m/s {0.4940 fps}
82	32.0×10^{-3} m/s {0.1050 fps}	218.1×10^{-3} m/s {0.7157 fps}
84	39.6×10^{-3} m/s {0.1300 fps}	222.3×10^{-3} m/s {0.7293 fps}

Laminar boundary-layer theory, as solved using the Cebeci code, predicts laminar separation would occur just past 84% chord. The BL2D and MSES codes predict that the flow would be in the process of transition at this location. So, if the flow does not transition near 84% chord, it is predicted to separate. The case examined is under the conditions of weakest receptivity for the entire experiment – no surface roughness, including pressure ports, and no acoustic forcing. These experimental results indicate that the flow would naturally transition near this chordwise station. This supports MSES and BL2D results under the ideal conditions of low free-stream turbulence and a smooth surface. It is expected that actively forcing the boundary-layer with free-stream disturbances and applying surface roughness, particularly in the vicinity of the lower Branch corresponding to the acoustic forcing, would shift this transition location further upstream on the model surface. These results indicate that for the remainder of the experimental test conditions, the development of the boundary-layer disturbance could be tracked from when it first amplifies above the noise floor until the disturbance breaks down and turbulence begins.

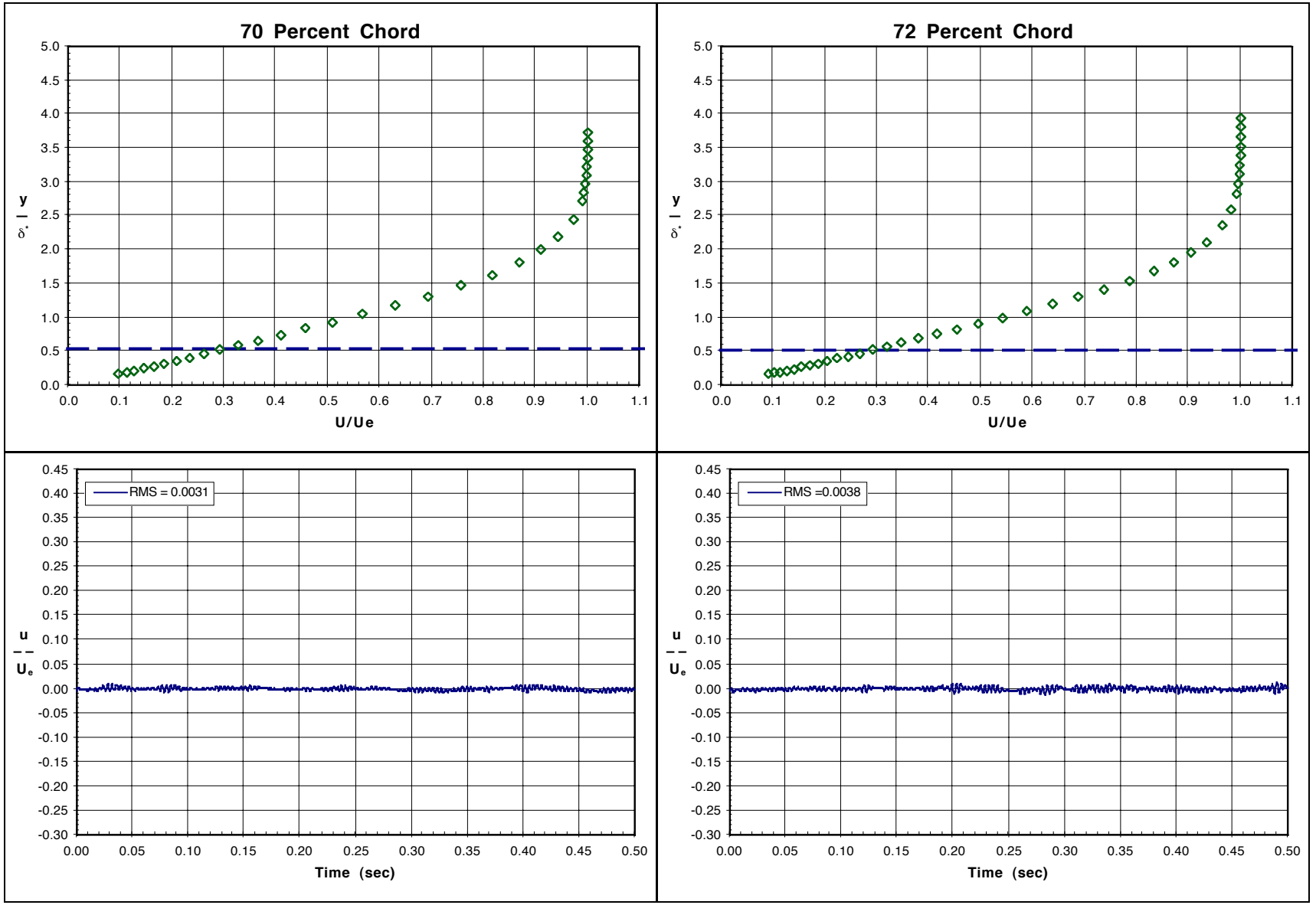

Figure 25: Flow Transition Study Results

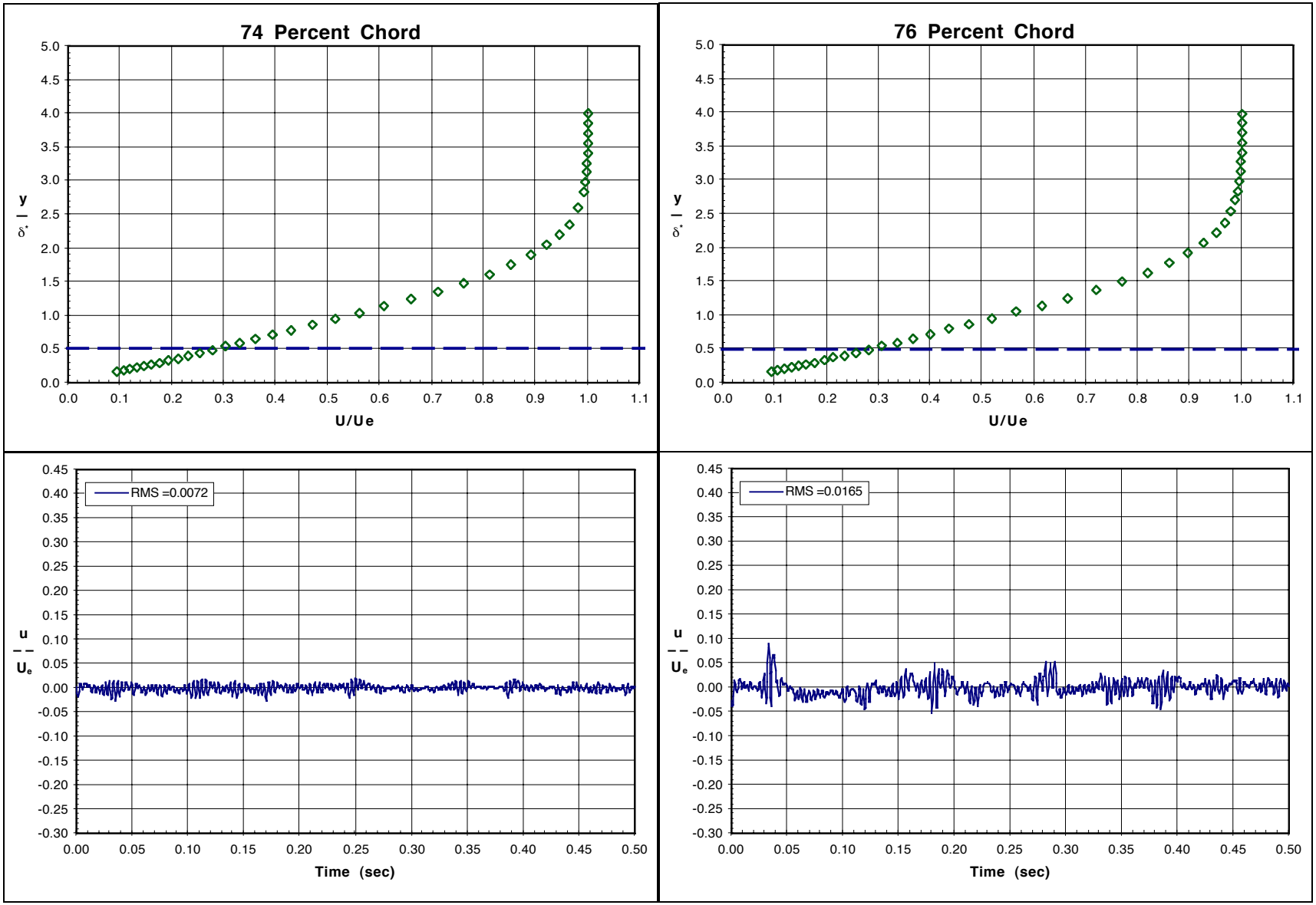

Figure 25: Flow Transition Study Results

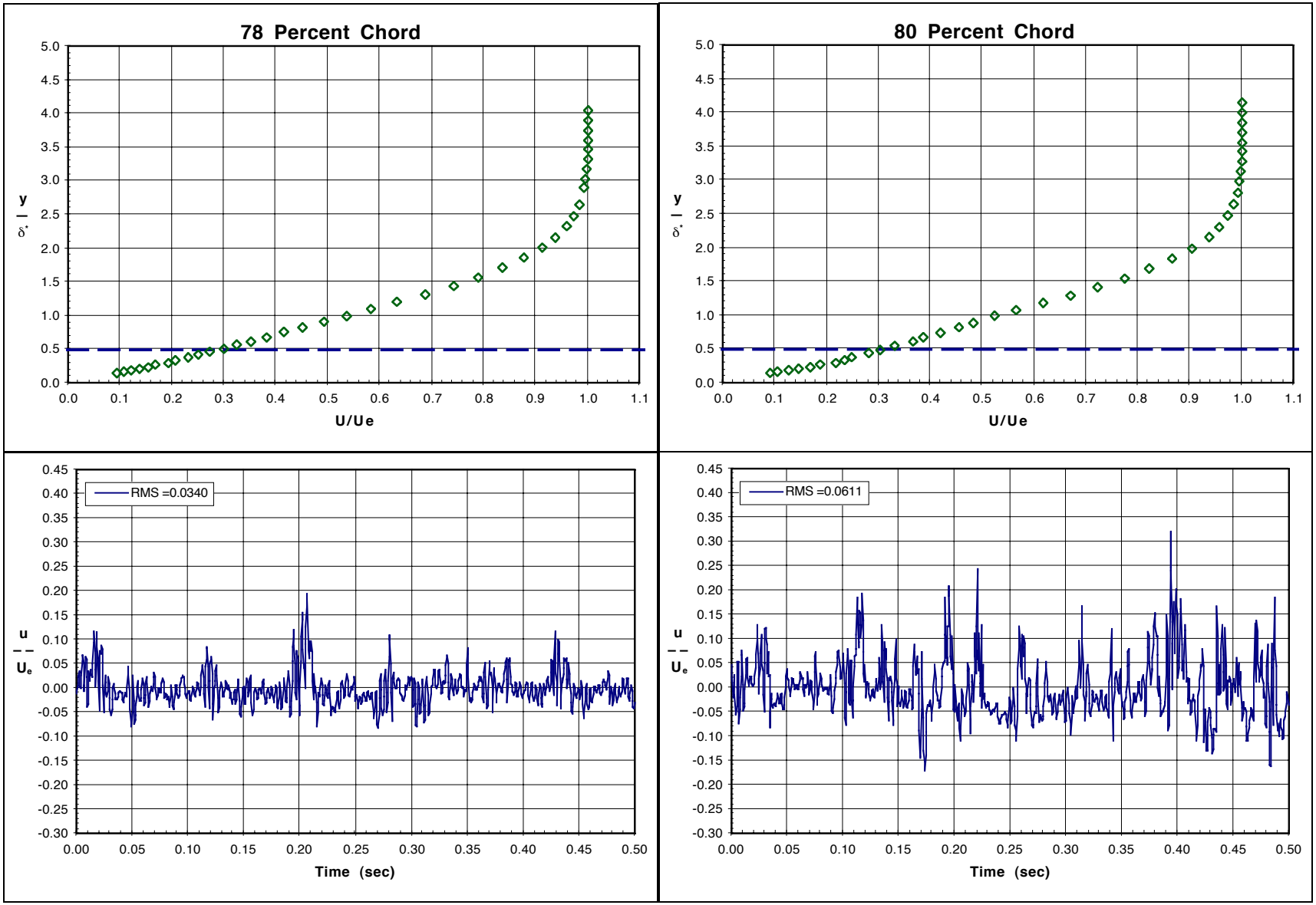

Figure 25: Flow Transition Study Results

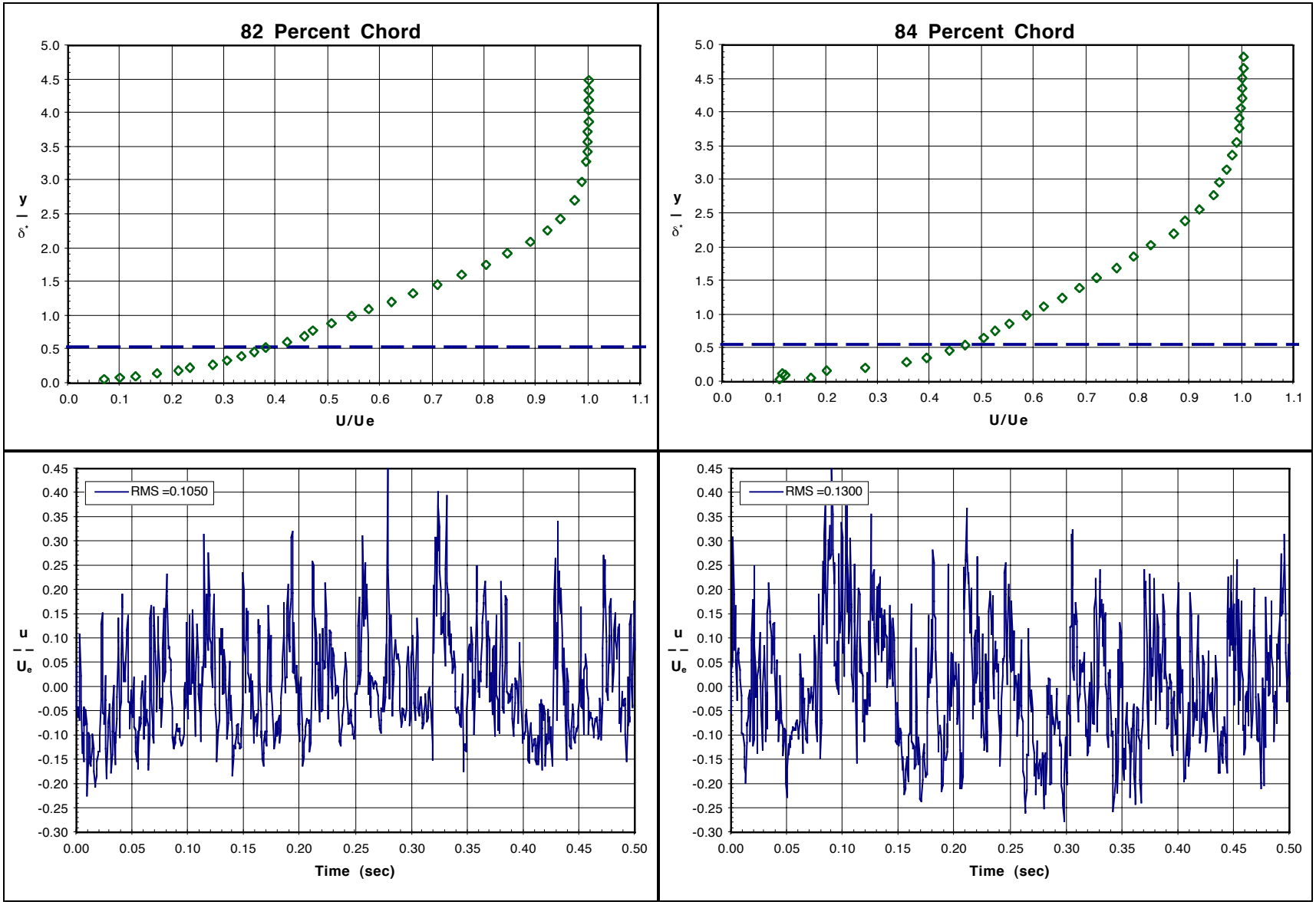

Figure 25: Flow Transition Study Results

5.2.3 Boundary-Layer Modeshape Results

Comparisons of the Tollmien-Schlichting modeshapes are presented here, including plots indicating how the modeshapes develop along the model surface for various surface roughness and acoustic forcing conditions. Results are presented for two different boundary-layer responses. These separate responses are for the free-stream acoustic forcing signal traveling downstream (referred to as BI or Downstream) and for the free-stream acoustic echo of the original signal traveling upstream (referred to as Echo or Upstream). The echo signal strength typically was 55.6 – 62.5% and 48.8 – 55.6% of the original source signal strength for the 20 m/s, 300 Hz and 15 m/s, 200 Hz cases, respectively. The responses to the above free-stream forcing signals experienced receptivity at Branch I or the surface roughness applied in the vicinity of Branch I.

5.2.3.1 Tollmien-Schlichting Modeshape Analysis

The non-dimensional modeshapes were determined by processing the time trace of the acoustic forcing signals and the time trace of the boundary-layer response signals. The processed time traces were the result of phase averaging 50 sample data blocks. Then, the wave packets of concern were extracted from the time trace, and the power spectral density was computed for a discrete range of frequencies within the range that the data was hardware filtered. This was completed with standard LabVIEW function libraries. This method yields a smooth signal in the time domain. Due to the short duration of the wave packets, the spectral results were fairly coarse in frequency resolution (typically greater than 50 Hz). The modeshape amplitude is defined as:

$$A = \left(\frac{u_{TS}}{u_s} \right)_f = \sqrt{\frac{PSD(u_{TS}, f)}{PSD(u_S, f)}} \qquad \textbf{Equation 5-2}$$

Where PSD(u,f) is the value of the power spectral density of the velocity packet time trace u at frequency f. The subscripts TS and S refer to Tollmien-Schlichting boundary-layer disturbance and the free-stream acoustic source signal, respectively. For the 20 m/s case, the 300 Hz component of the disturbance wave packet was tracked, while for the 15 m/s case, the 200 Hz component of the disturbance wave packet was tracked.

Each individual data point was corrected in a similar fashion as the individual hot-wire velocity measurements were corrected. The amplitudes were scaled by the ratio of the peak-to-peak velocity of the actual forcing signal (source strength) as measured in the free-stream with respect to the average of all the source strengths for a given chordwise data set. This correction factor was applied to compensate for slight variations in the forcing environment. Typically, this result ended up in a correction on the order of only a fraction of a percent.

Figures 26 and 27 present the modeshape results with different chordwise stations in the subplots at 20 m/s and 15 m/s, respectively. Each surface roughness condition is color-coded. The responses from the downstream traveling source and the upstream traveling source are distinguished by solid and hollow symbols, respectively. The actual forcing signal amplitude as compared with free-stream velocity is identified in the legend.

It can be seen how the different surface conditions affect the amplitude of the boundary-layer response. It is also apparent that the source strength has a significant effect on the amplitude as well, seen by examining the differences in the development of the upstream and downstream signal responses as well as within a few select cases where a broad range of free-stream acoustic forcing amplitudes was applied. From examining the 15 m/s results at 50, 60 and 65% chord, it can be seen that at comparable forcing levels, the application of a single element of roughness can increase the modeshape amplitude by 1 – 3 orders of magnitude. Repeating the number of roughness elements, as in Test Cases 9 and 10, indicated an additional increase in amplitude by another order of magnitude over the single element roughness case in Test 7, which had the same roughness height. It appears that incrementally increasing the number of repeated roughness elements has diminishing returns on the increase of disturbance amplitude. It can also be observed that the location of the minimum of the modeshape consistently was determined to be at about $2\delta^*$.

Figures 28 and 29 shows how the modeshape develops along the chord for a given surface condition at both the 20 m/s and 15 m/s flow speeds, respectively. Here, the effect on forcing signal amplitude and the nature of the breakdown of the disturbance can be seen. For all of the

chordwise stations examined for each of the surface conditions, the comparable acoustic forcing levels were applied. The solid lines and symbols correspond to the boundary-layer response from the downstream traveling source (BI), while the dashed lines and hollow symbols correspond to the upstream traveling source signal, the echo of the downstream source (EC).

From examining all of the plots, it can be seen that the deterioration of the modeshape initially begins in the lower lobe, located immediately above the model surface and where the shear stresses are greatest. Typically, the BI response is greater than the EC response. However, for the results between 50 and 60% chord for the 20 m/s flow case, the interference of the upstream traveling acoustic signal with the downstream traveling source signal response is strongly apparent. It is interesting to note the development of the 15 m/s Test 11 disturbance evolution (red symbols and lines, 50, 60 and 70% chord). Here, the modeshape appears to have an inflection point and / or a weak minimum near the wall, at $^1/_2\ \delta^*$. This phenomenon will be examined in more detail during the total energy amplitude results analysis.

It should be noted that these results only examine the development of a single frequency of the disturbance and do not account for what is occurring to modeshapes at other frequencies. It appears that the as the modeshape starts to breakdown near the latter chordwise stations, the energy level of the examined frequency approaches a saturation level as compared to the energy level of that frequency component of the acoustic forcing signal. The results are presented in logarithmic scale to be able to compare the modeshapes in all plots on the axis scale.

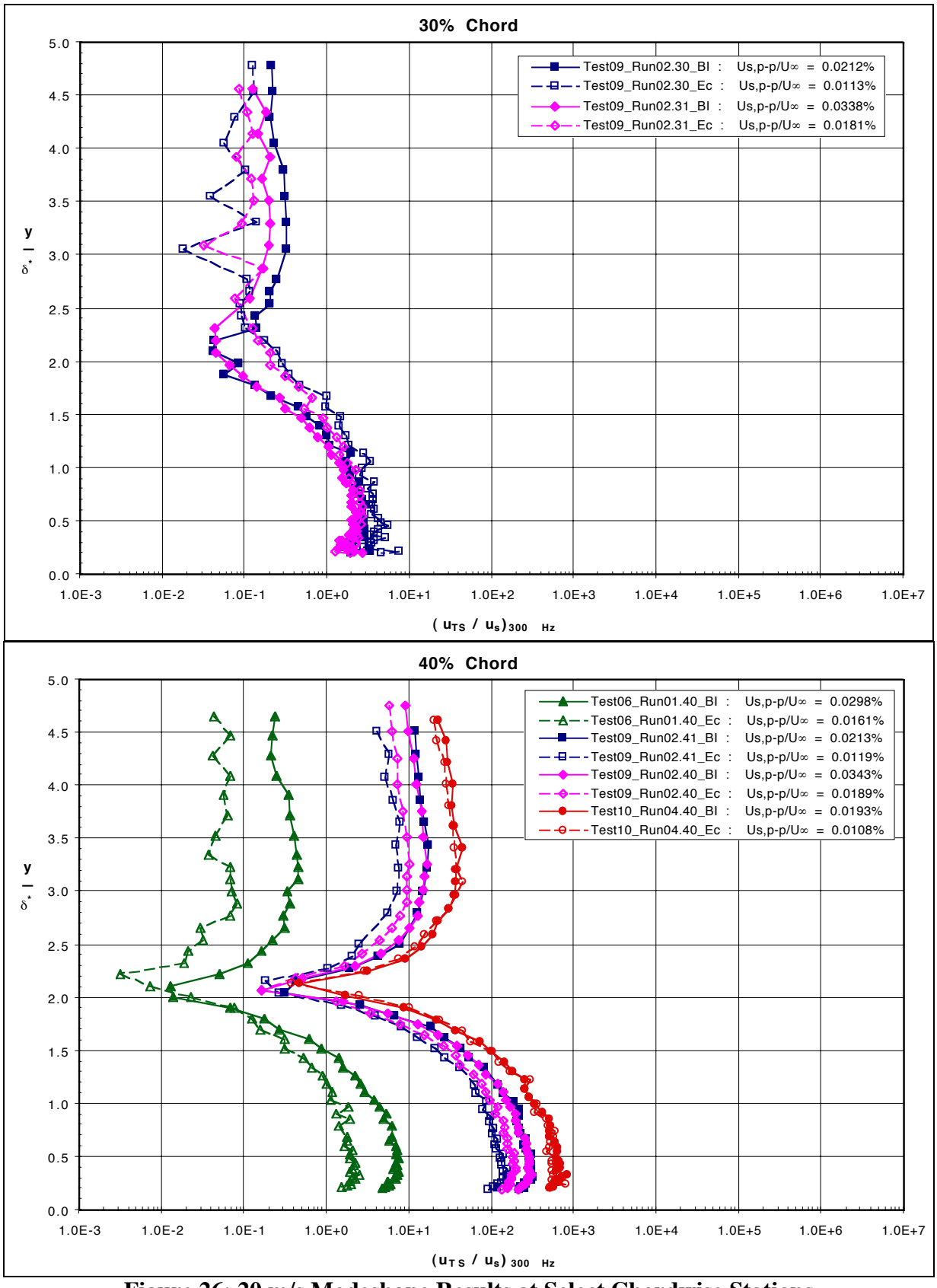

Figure 26: 20 m/s Modeshape Results at Select Chordwise Stations

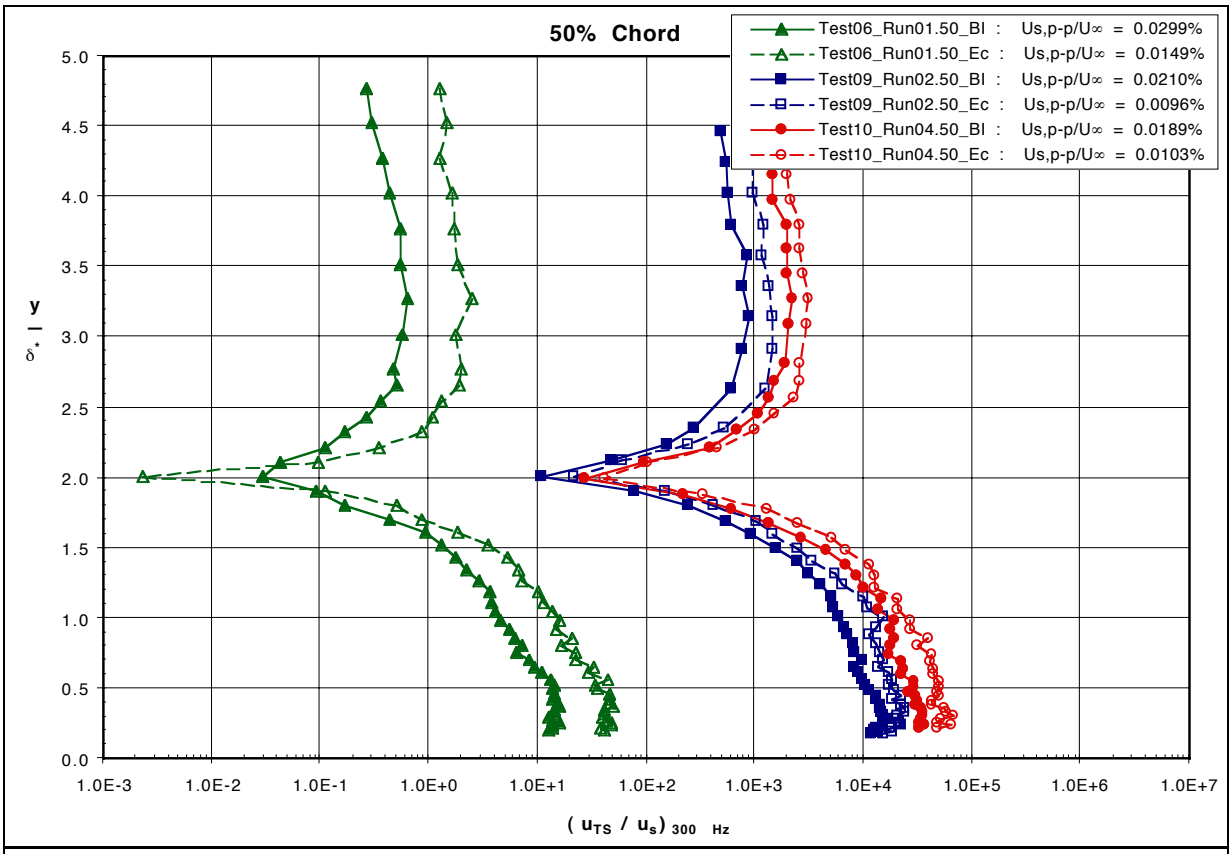

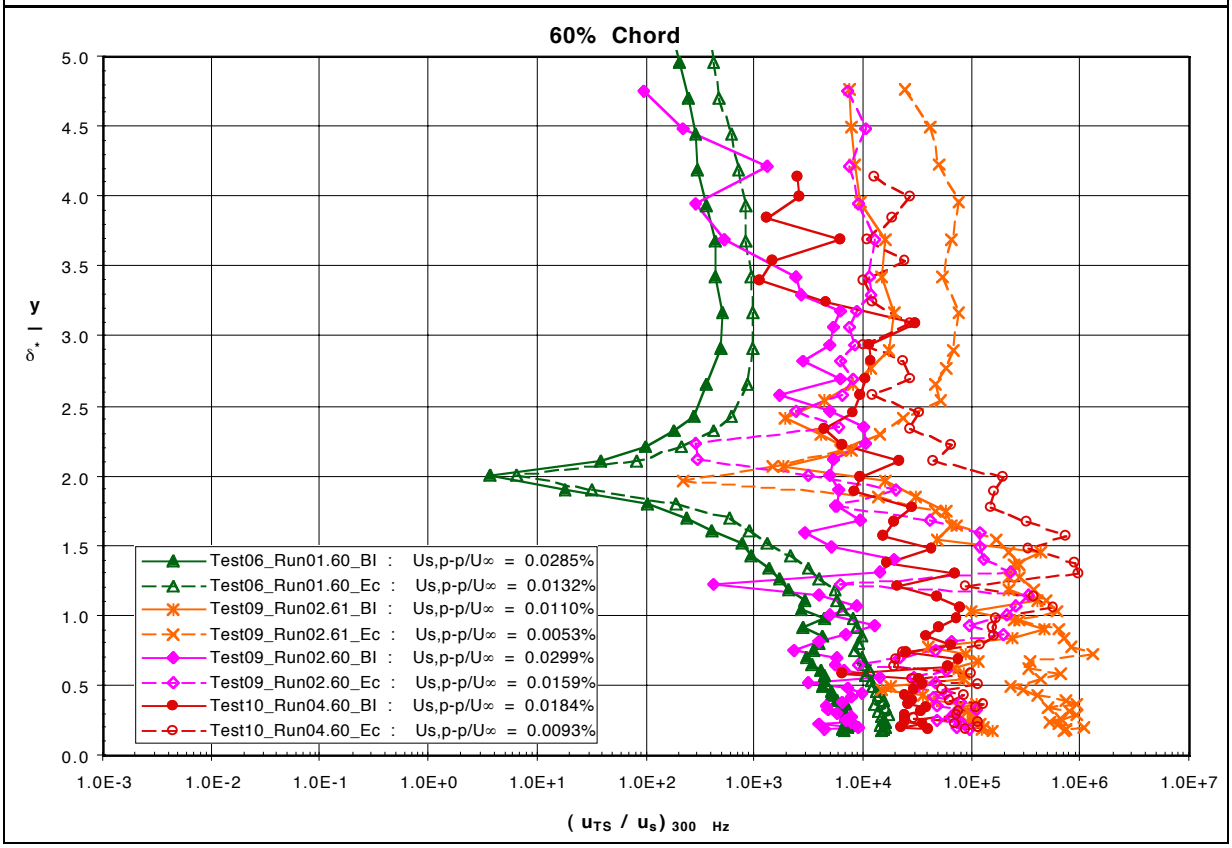

Figure 26: 20 m/s Modeshape Results at Select Chordwise Stations

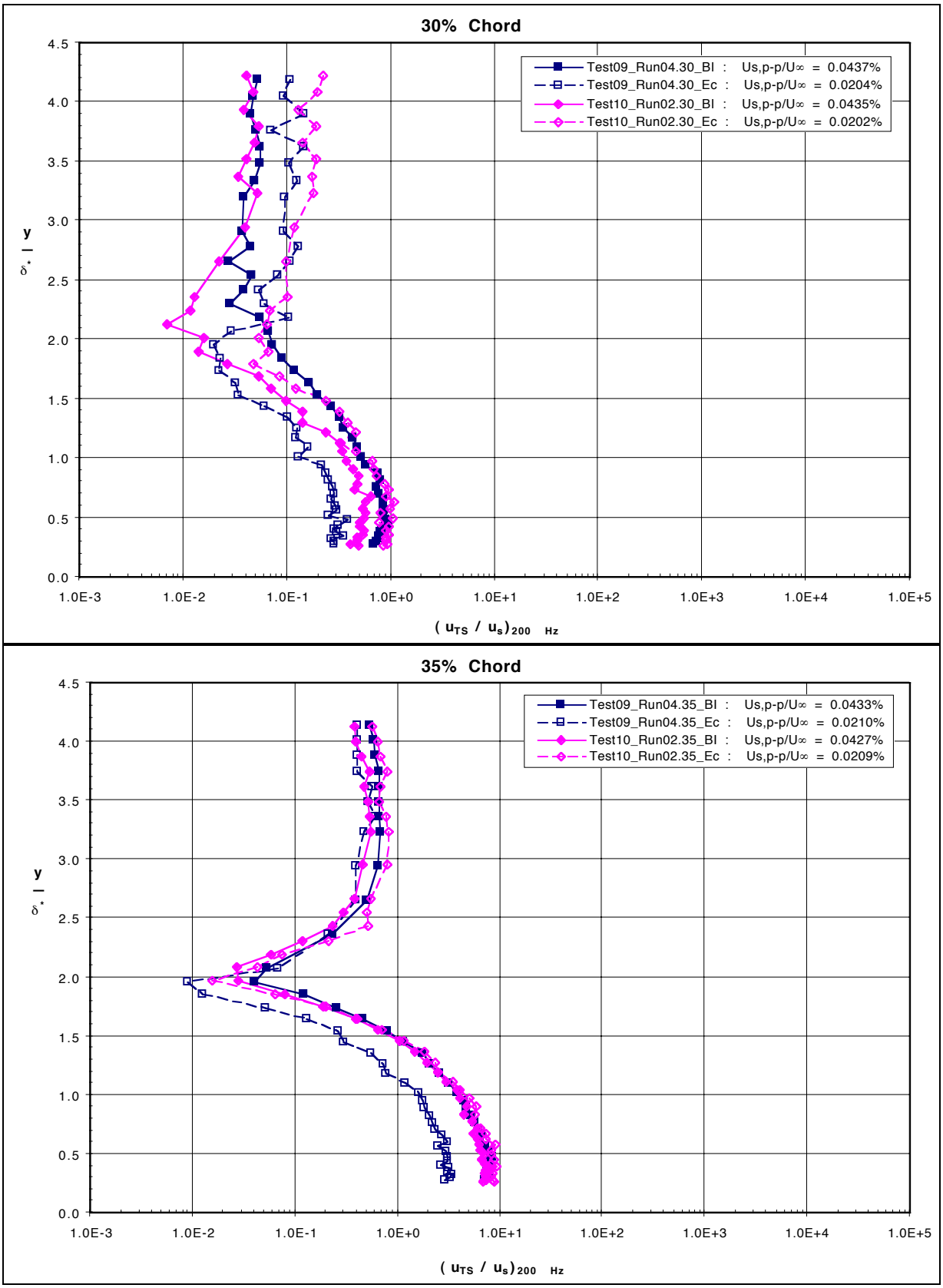

Figure 27: 15 m/s Modeshape Results at Select Chordwise Stations

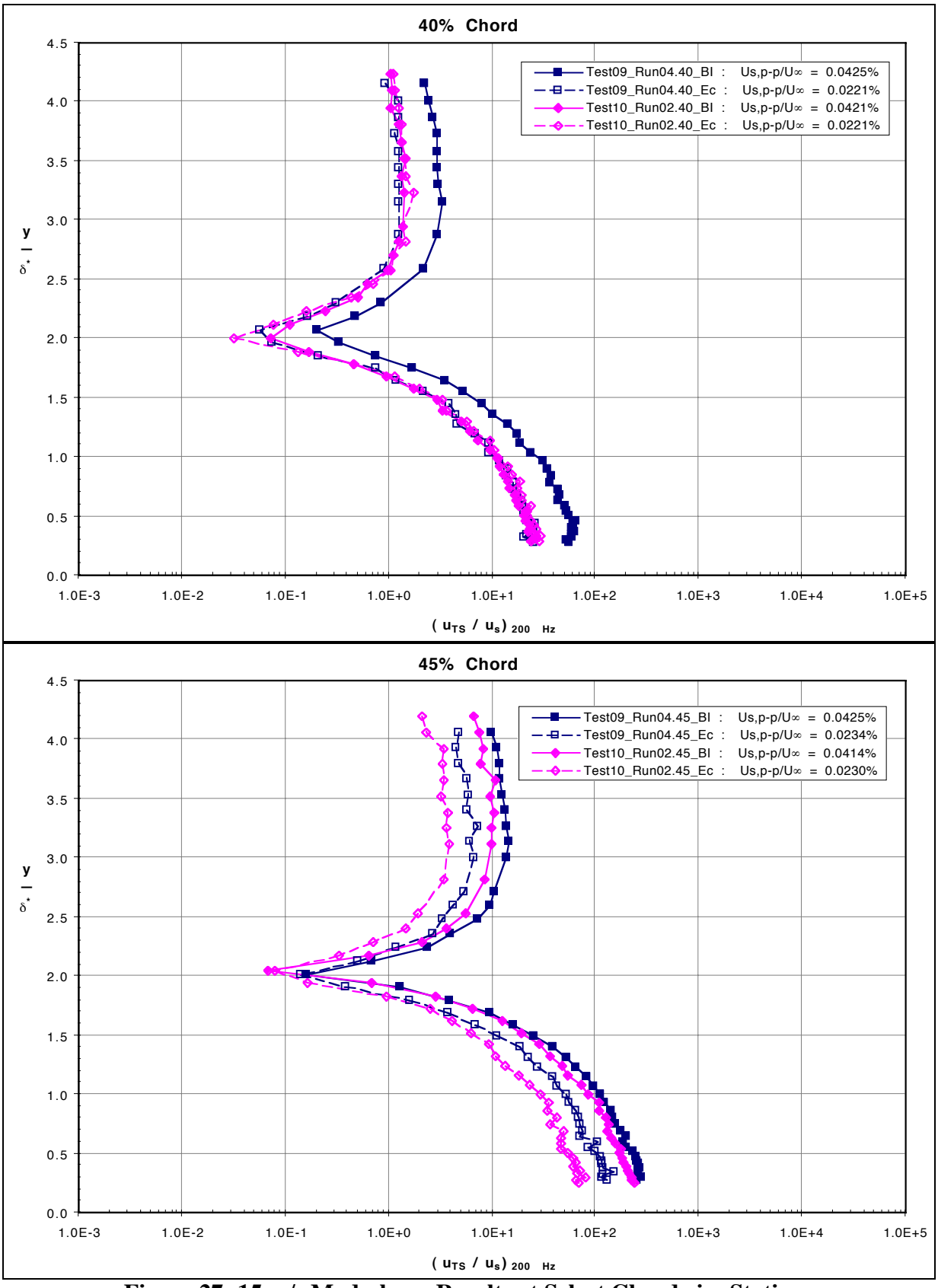

Figure 27: 15 m/s Modeshape Results at Select Chordwise Stations

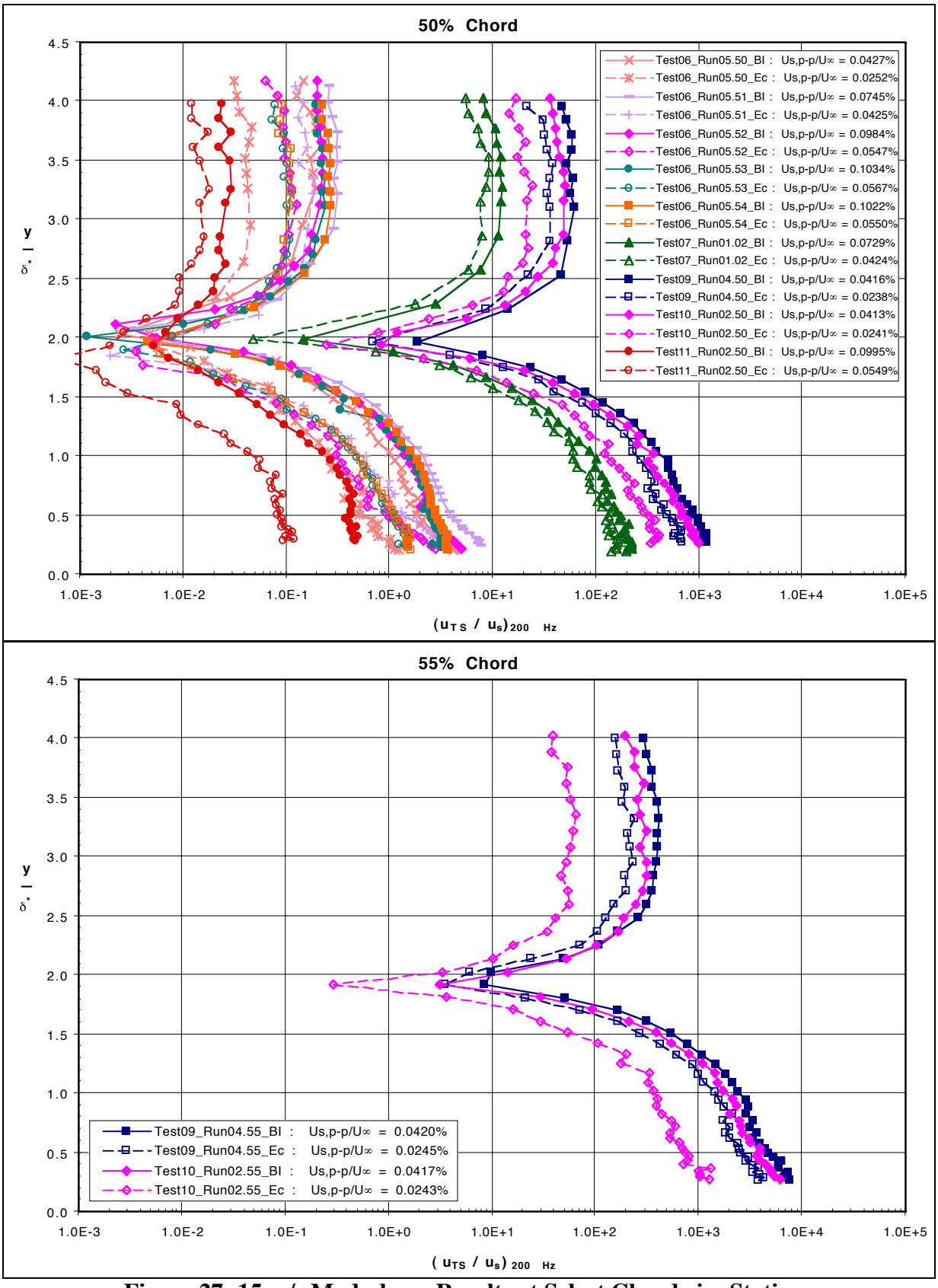

Figure 27: 15 m/s Modeshape Results at Select Chordwise Stations

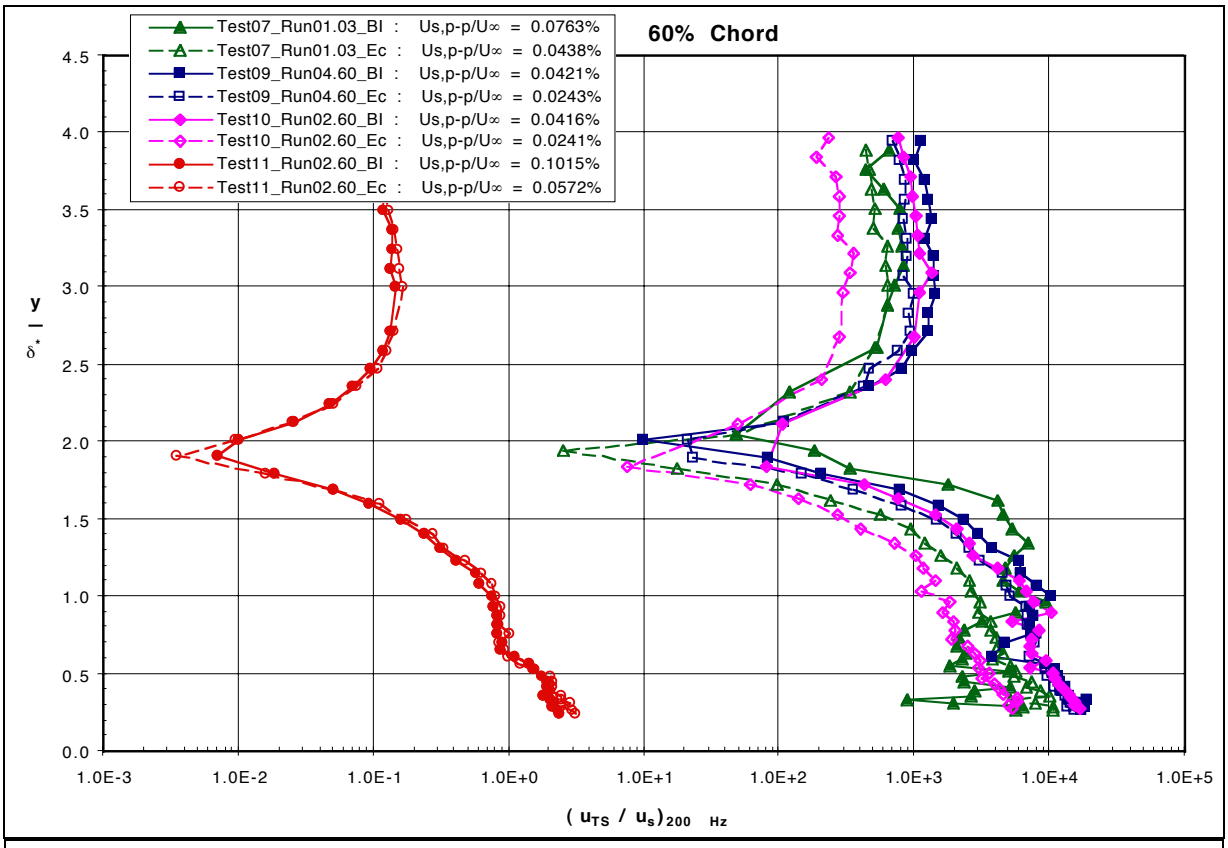

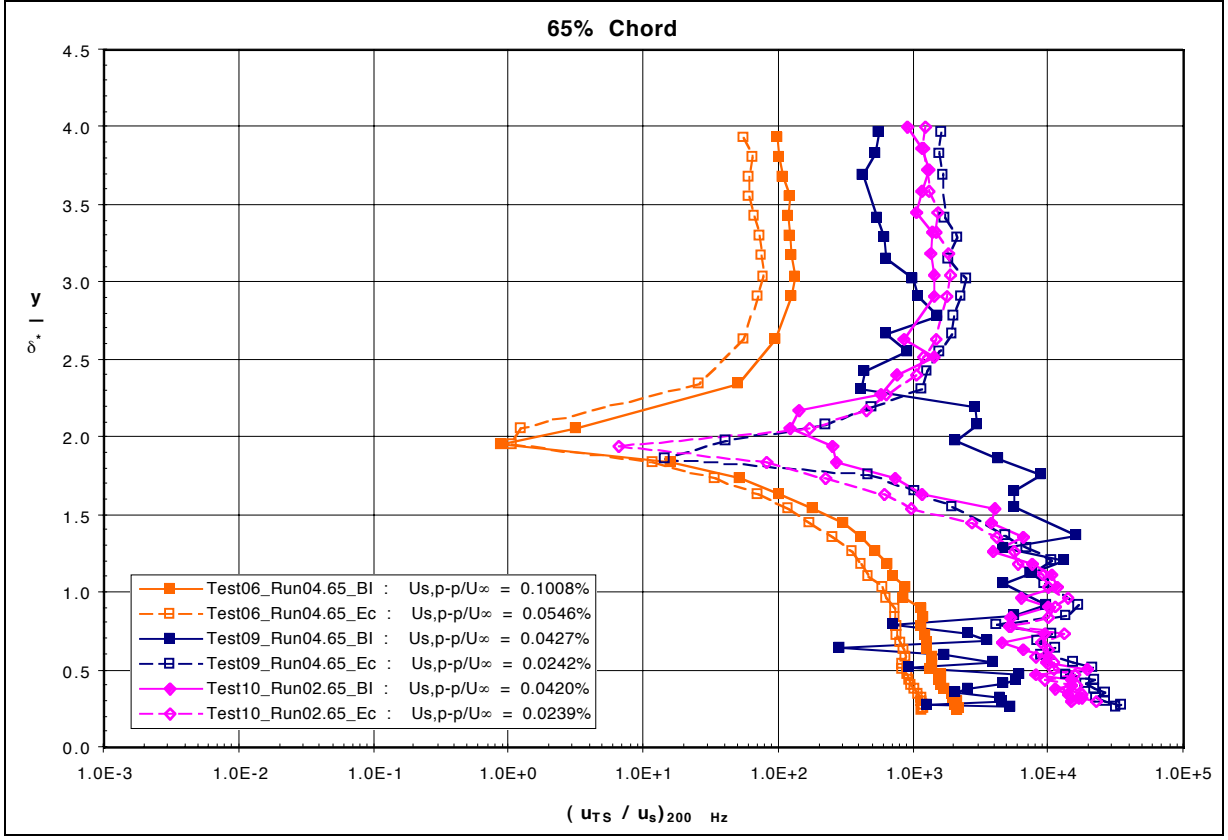

Figure 27: 15 m/s Modeshape Results at Select Chordwise Stations

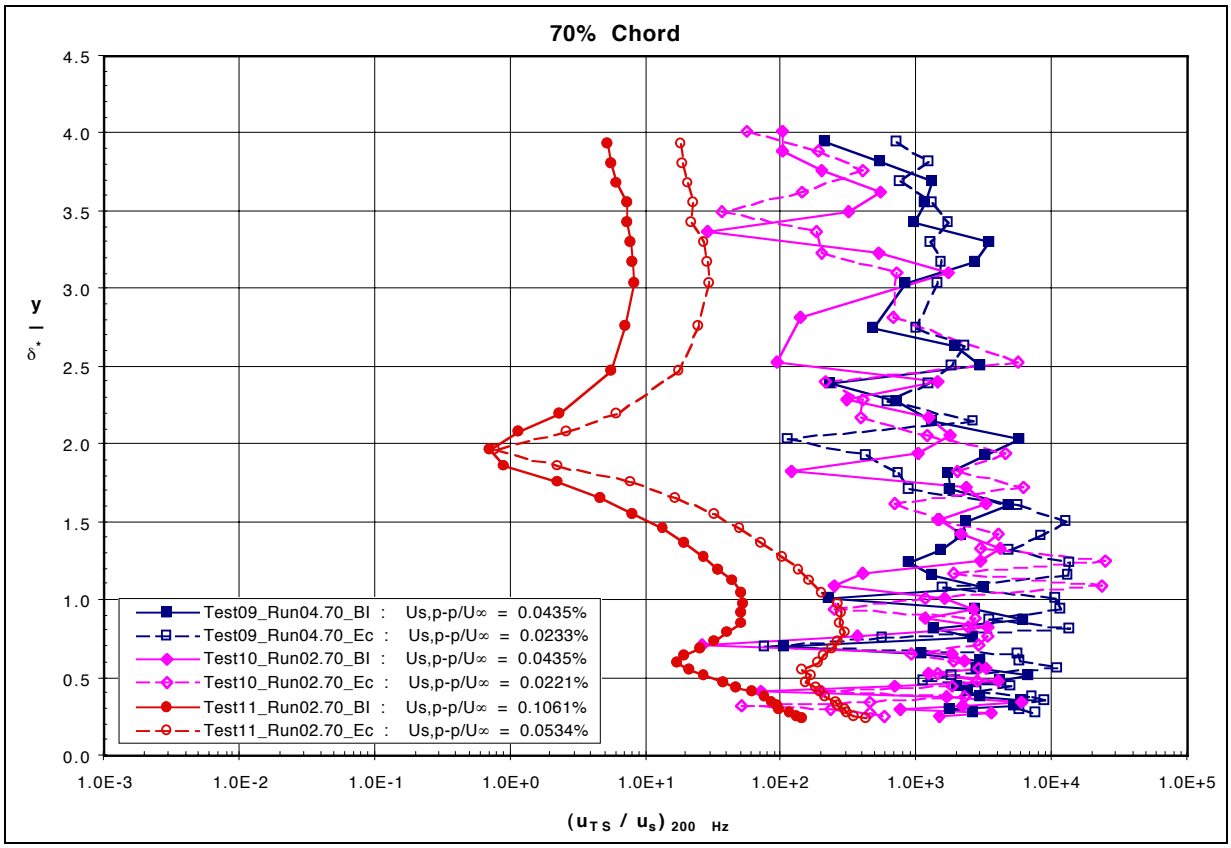

Figure 27: 15 m/s Modeshape Results at Select Chordwise Stations

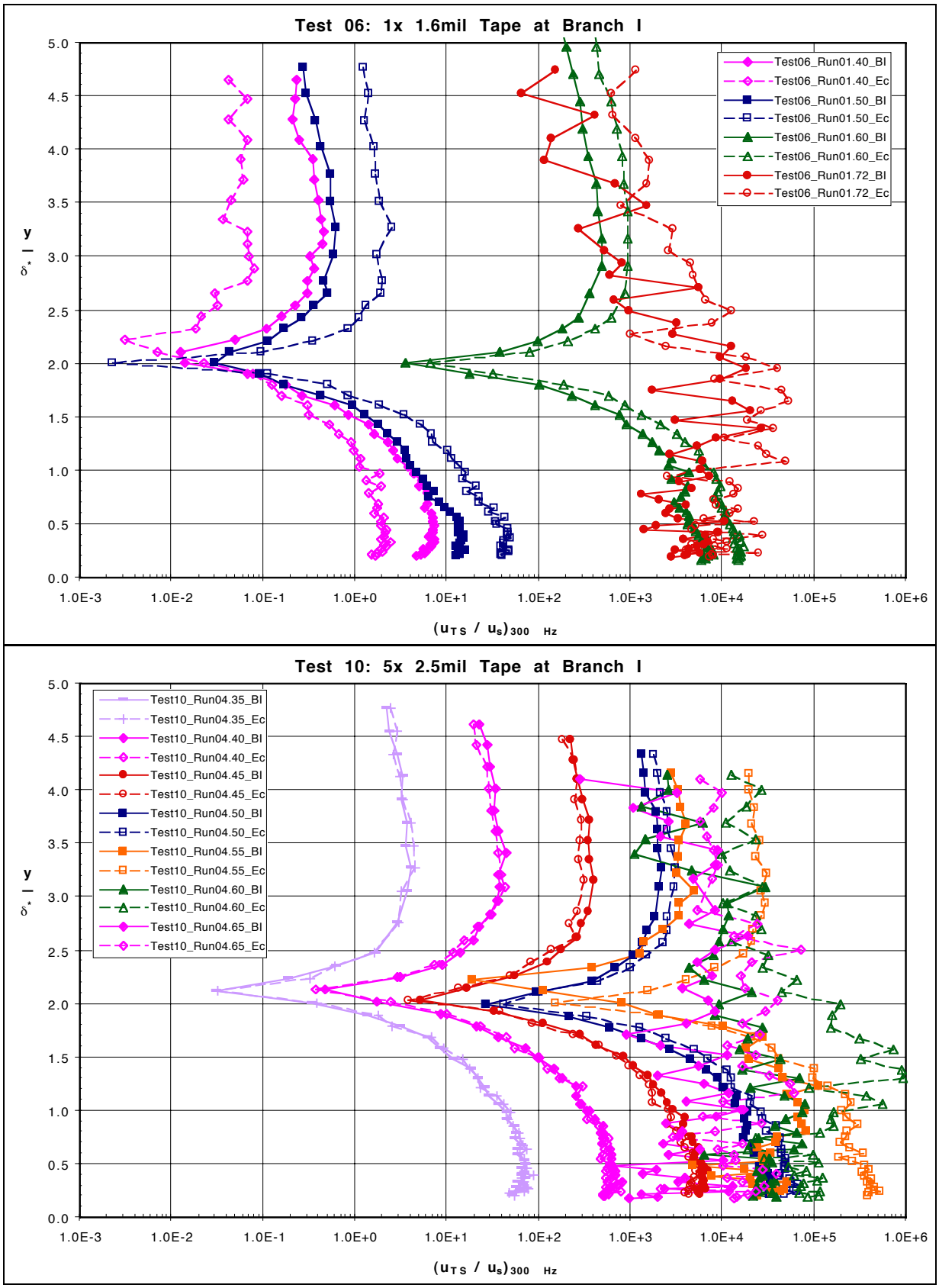

Figure 28: 20 m/s Modeshape Results for Select Surface Conditions

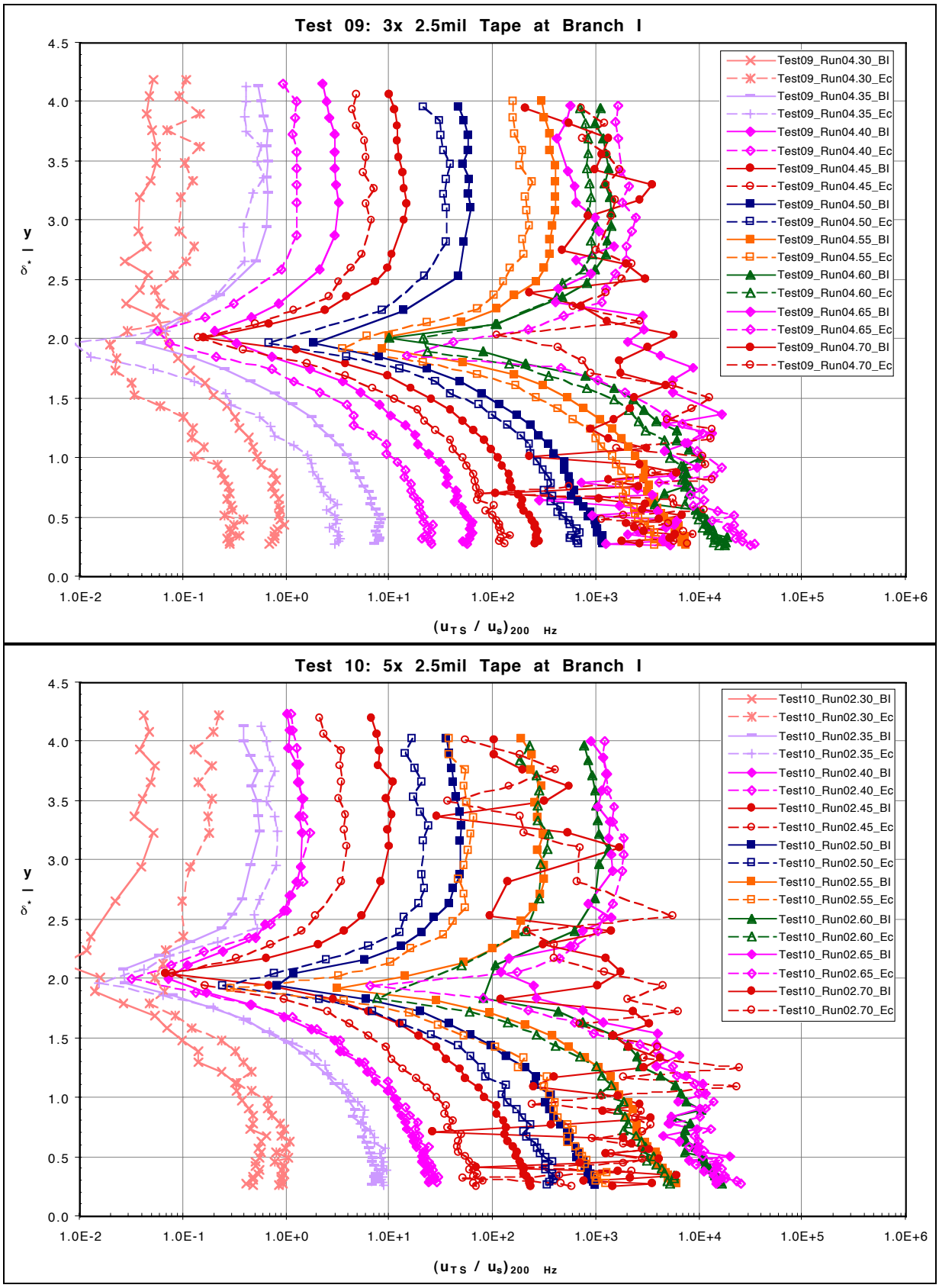

Figure 29: 15 m/s Modeshape Results for Select Surface Conditions

5.2.3.2 Frequency Spectra of Modeshape Results

The frequency spectra of the modeshape are examined next. The value of the amplitude used at each chordwise station is the result of integrating the lower lobe of the T-S modeshape, as indicated in the following equation:

$$A = \int_0^2 u_{TS}(f)/u_S(f)\, d\left(y/\delta^*\right) \qquad \textbf{Equation 5-3}$$

It should be noted that the range of the integral was from the wall to $(y/\delta^*) = 2$, which is the location of the minimum of the modeshape of the central forcing frequency and is not necessarily a significant value for modeshapes at other frequencies. The results presented extend beyond the range of the hardware filtered data. All results for frequencies below 200 Hz and above 500 Hz have undergone significant attenuation due to the filters used, which have a roll-off of 115 dB per octave. With this in mind, all results outside of the hardware filtered range can only be considered in terms of qualitative aspects, since the results are at a comparable amplitude of the signal noise floor, which was verified by examining the raw power-spectral density results. Only the Test 10 (five elements of repeated roughness) case is presented below, at both the 20 m/s (**Figure 30**) and 15 m/s (**Figure 31**) flow speeds. It can be seen from the spectra that as the disturbance propagates downstream, the energy near the first harmonic ($2f$) starts to amplify relative to the amplitude of the free-stream forcing signal. Actually, the peak starts closer to 500 Hz and gradually shifts towards the 1st integer harmonic near 450 Hz. The amplification of the harmonic corresponds to the onset of a K-type breakdown of the laminar flow[82]. The other peak appears to be due to receptivity based upon the tape width (0.95 cm, $^3/_8$ inch), whereas the primary mode examined was recepted based upon the tape spacing (2.34 cm, 0.925 inches). The equivalent frequency spectra of the surface roughness distributions for one, three and five elements of roughness are presented in **Figures 32 and 33**, where the length scale was converted to a time scale based upon a nominal T-S convection wave-speed. This result indicates that the receptivity strength based upon the surface condition is comparable. While the amplitudes relative to source strength are comparable for these peaks, the total energy amplitudes are not because of the disparity of the acoustic forcing levels.

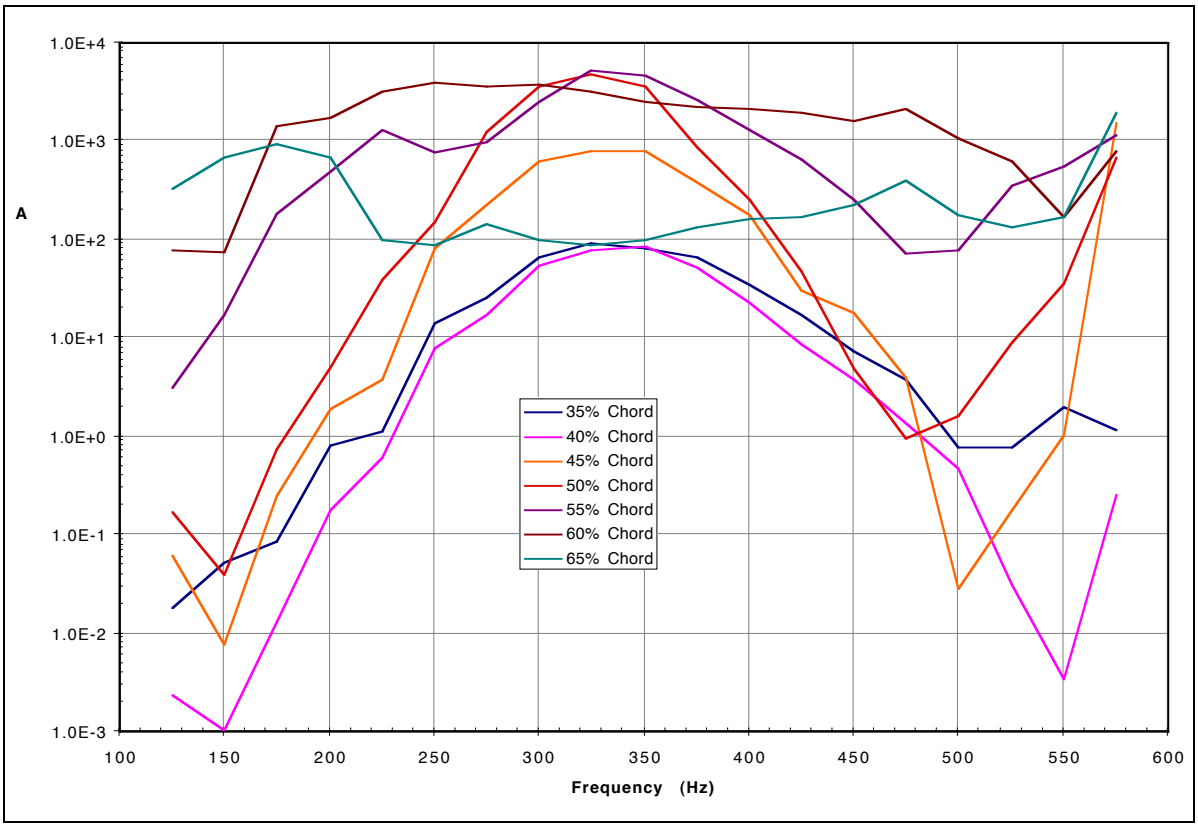

Figure 30: 20 m/s Frequency Spectra from Modeshape Results

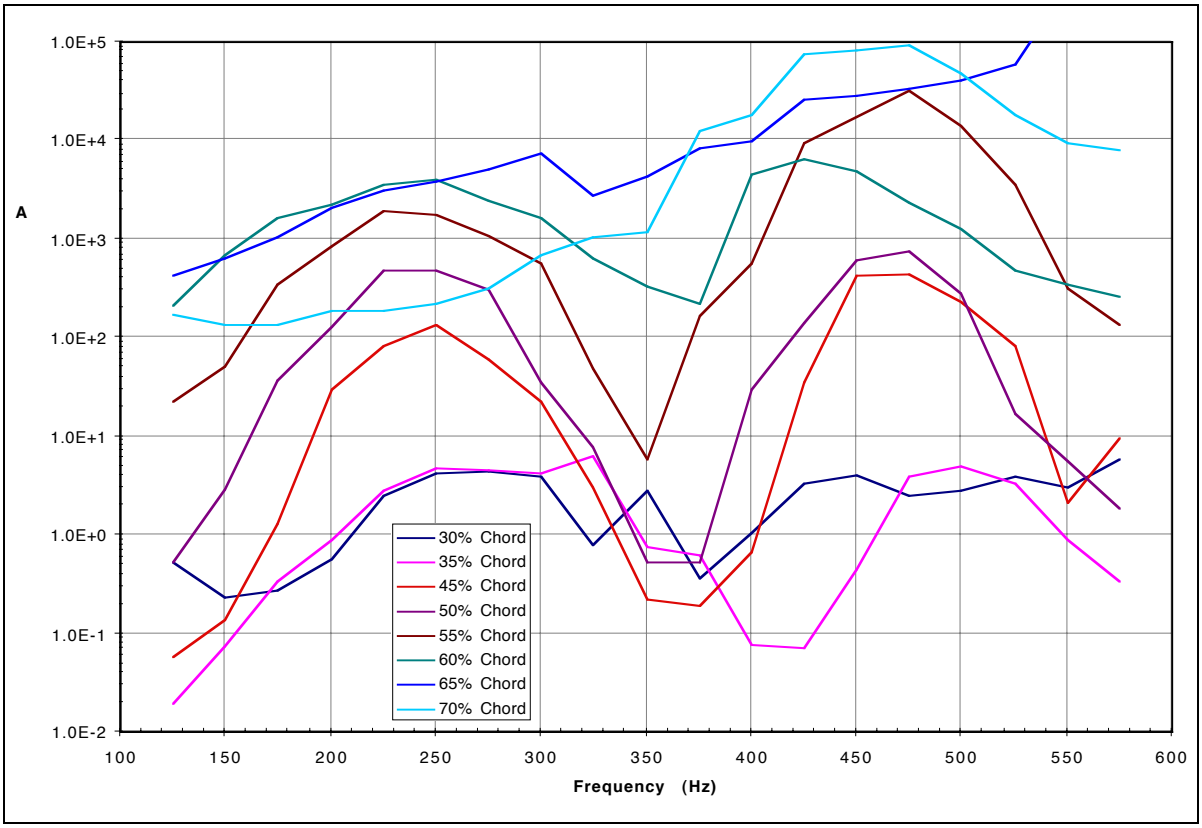

Figure 31: 15 m/s Frequency Spectra from Modeshape Results

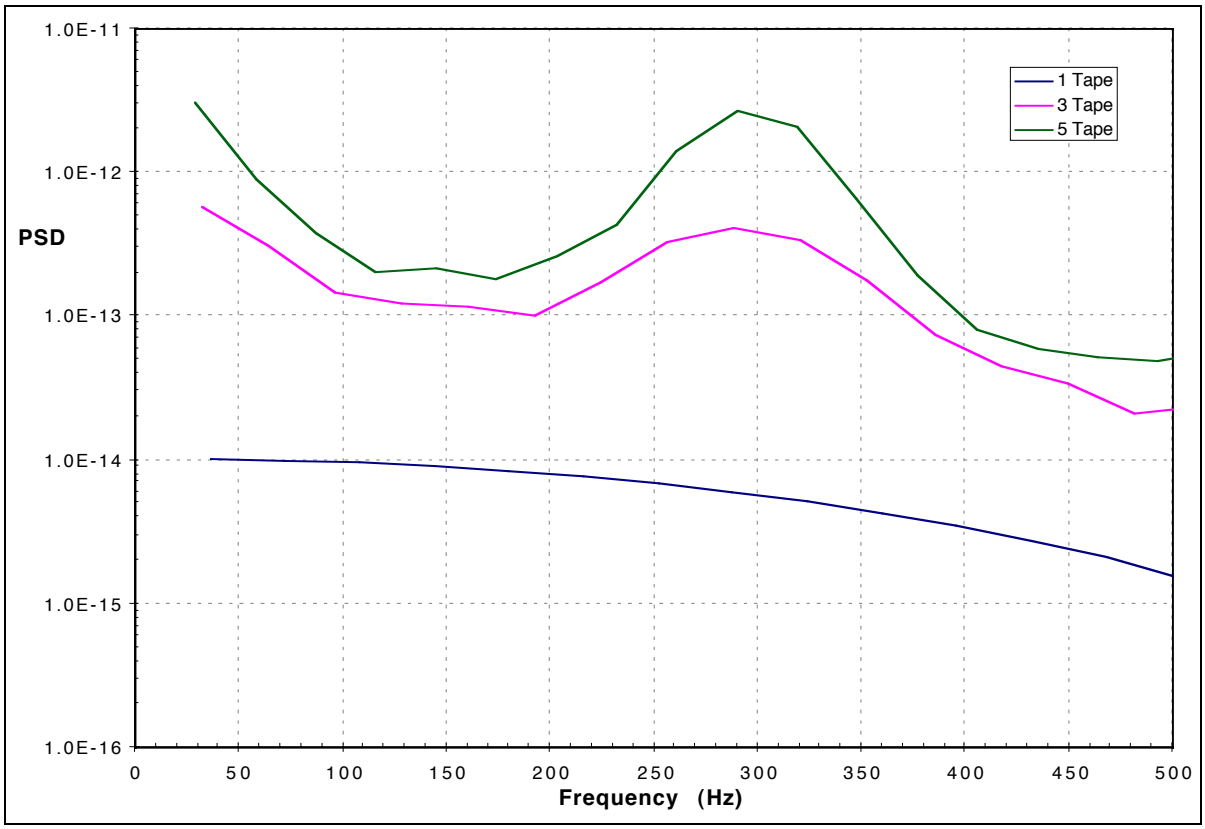

Figure 32: 20 m/s Surface Roughness Equivalent Frequency Spectra

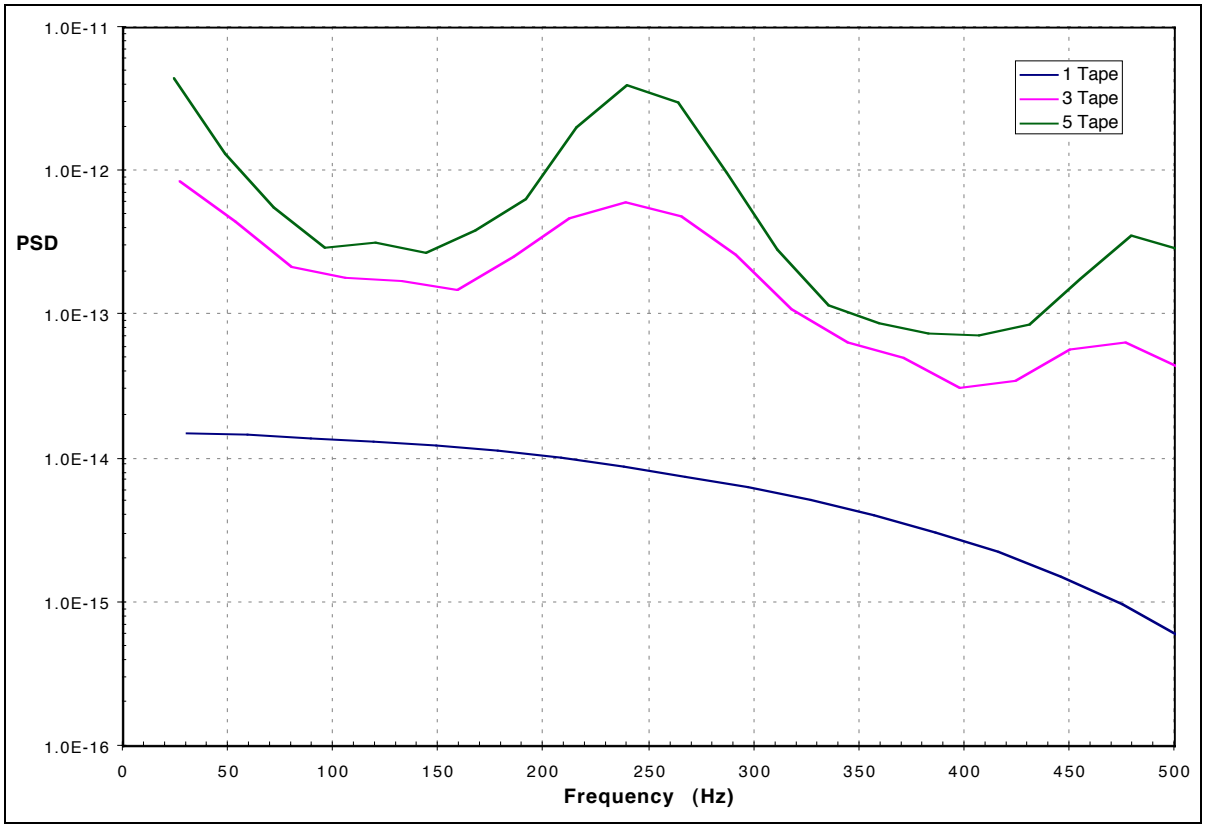

Figure 33: 15 m/s Surface Roughness Equivalent Frequency Spectra

5.2.3.3 Comparison of Experimental and LPSE Modeshapes

Comparisons of the 20 m/s, 300 Hz experimental data with LPSE results are presented for select data sets. While the entire shape function did not match, the location of the maxima and the minimum correlate well, and the shape of the "lobes" compare, particularly a characteristic of the lower lobe which indicates a bulge on the lobe between the maximum and the minimum. This shape is likely due to the existence of two modes (different wavenumbers, same frequency) growing along the model, possibly due to the pressure gradient on the model. Comparisons of the lower lobe at several chordwise stations are presented in **Figure 34**, while comparisons of the upper lobe at the same chordwise stations are presented in **Figure 35**. Linear stability theory modeshapes were not directly available from the programs used.

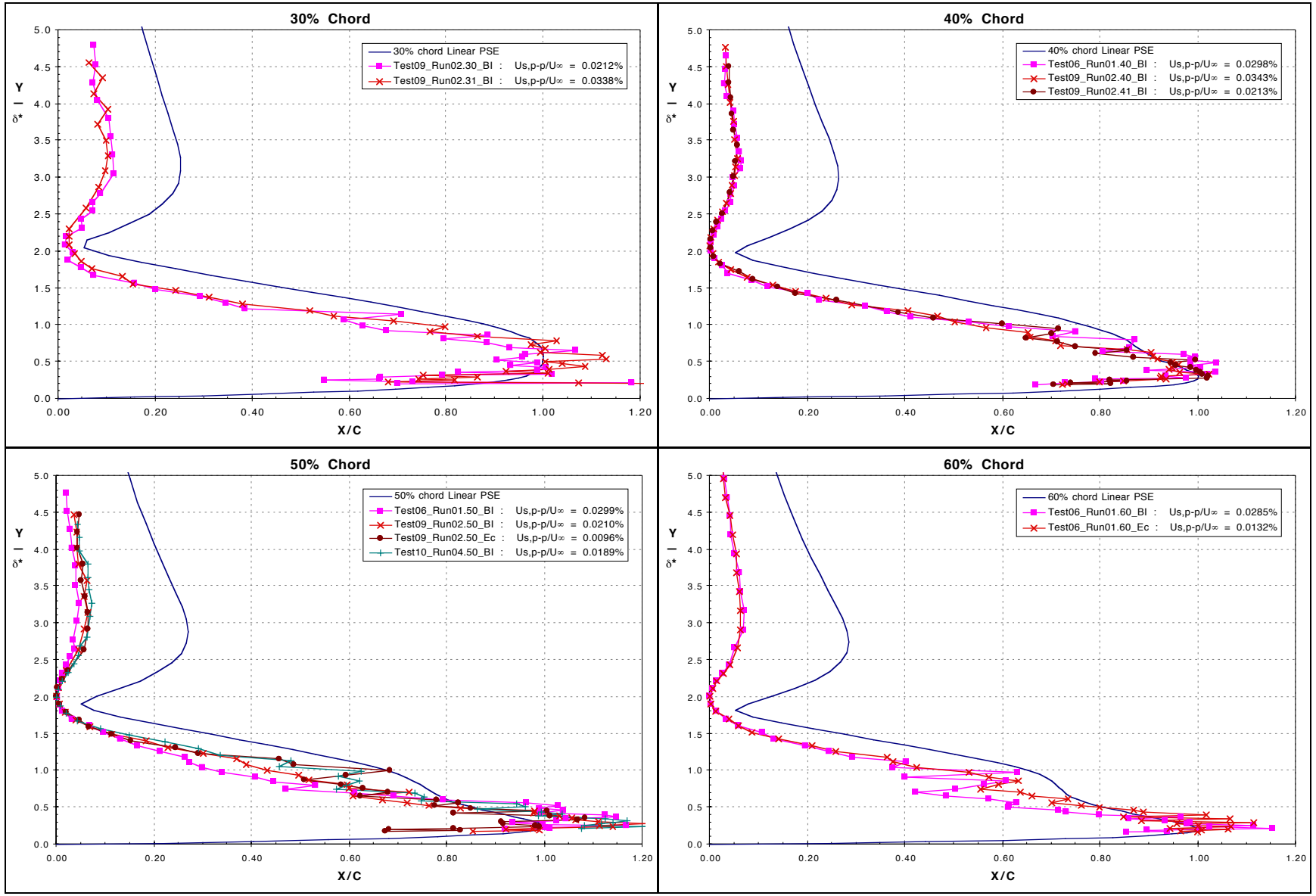

Figure 34: 20 m/s, 300 Hz LPSE Modeshape Comparison (Lower Lobe)

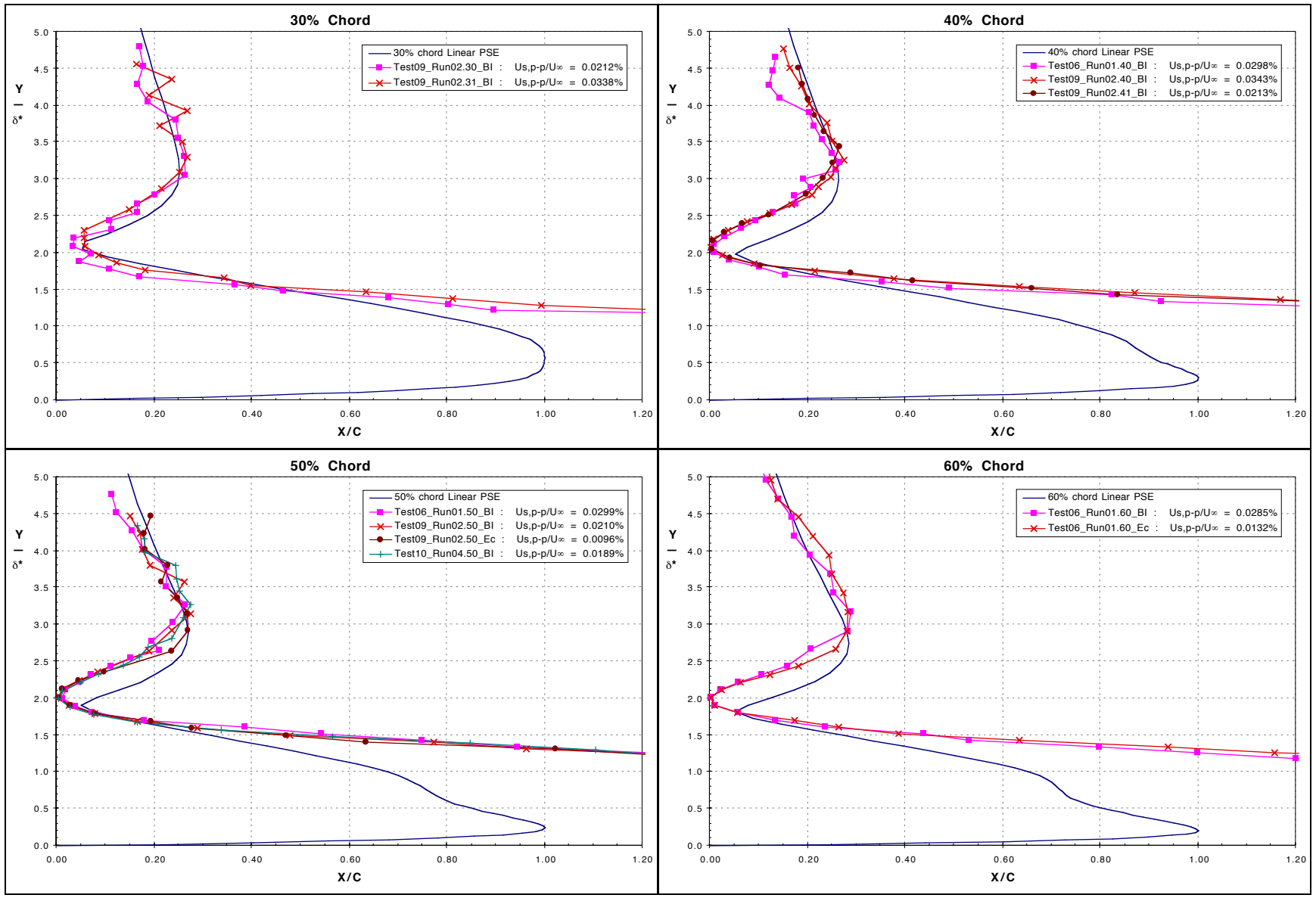

Figure 35: 20 m/s, 300 Hz LPSE Modeshape Comparison (Upper Lobe)

5.2.3.4 Chordwise Traverse of Modeshape Results

The amplitudes for chordwise traverses are computed by using the same integral of the modeshape as indicated in **Equation 5-3** and the same set of data. These results are presented in **Figures 36 and 37** for the Test 10 (five elements of repeated roughness) 20 m/s and 15 m/s cases, respectively. Data from outside of the hardware-filtered range is denoted by a dashed line. The central forcing frequency is denoted by a square symbol. For the 15 m/s test case, the $2f$ harmonic is denoted with a circle symbol. It can also be seen that as the disturbance develops, all of the frequencies end up with comparable amplitudes or energy. For the 20 m/s case, it can be seen that the higher frequency results initially have a much lower amplitude as compared to the central forcing frequency of 300 Hz. As the flow develops, the higher frequency modes amplify more strongly. It can be seen for the 15 m/s case that there is comparable growth near the central forcing frequency of 200 Hz and frequency of 500 Hz, which was accounted as being due to receptivity of the tape width. However, starting near 50% chord, the harmonic significantly increases in amplitude. By 60% chord, the data indicates transitional if not turbulent flow conditions for these surface conditions. The harmonic amplification also applies to the 20 m/s case and can be seen by examining the results from 275 and 550 Hz.

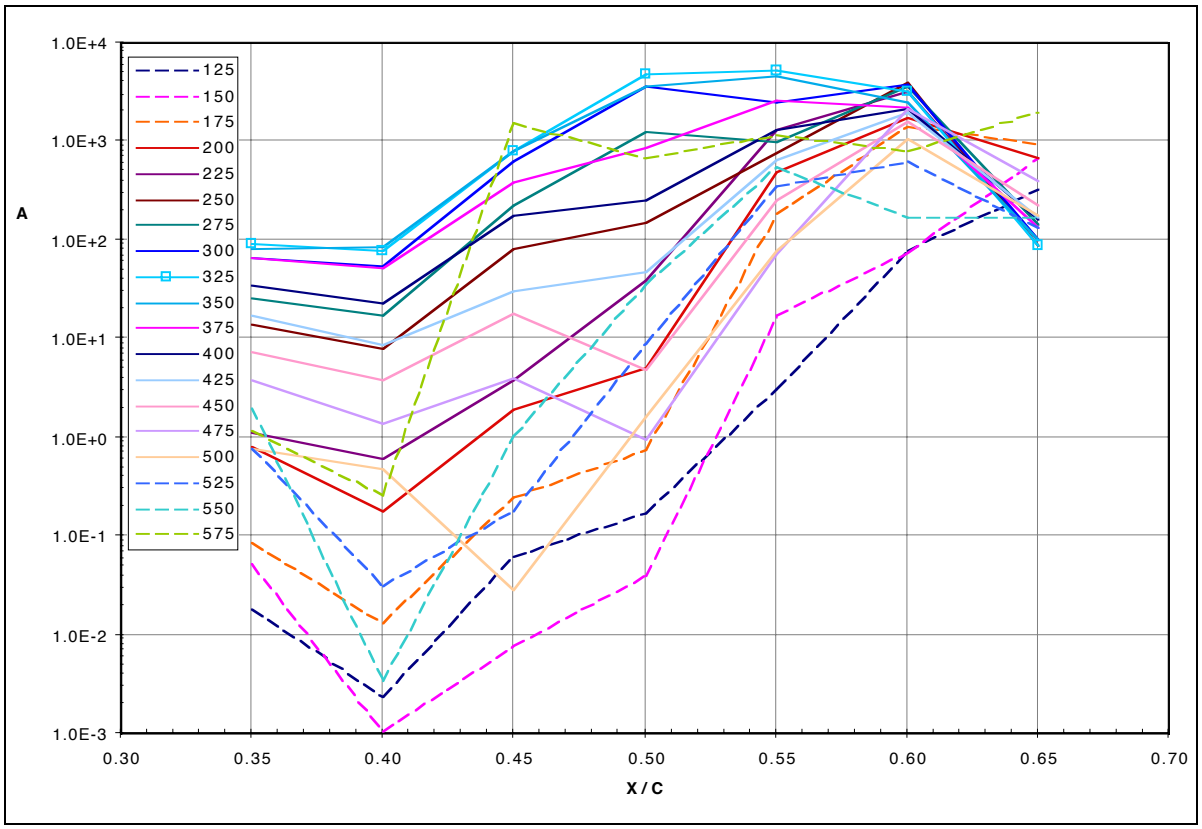

Figure 36: 20 m/s Chordwise Traverse from Modeshape Results

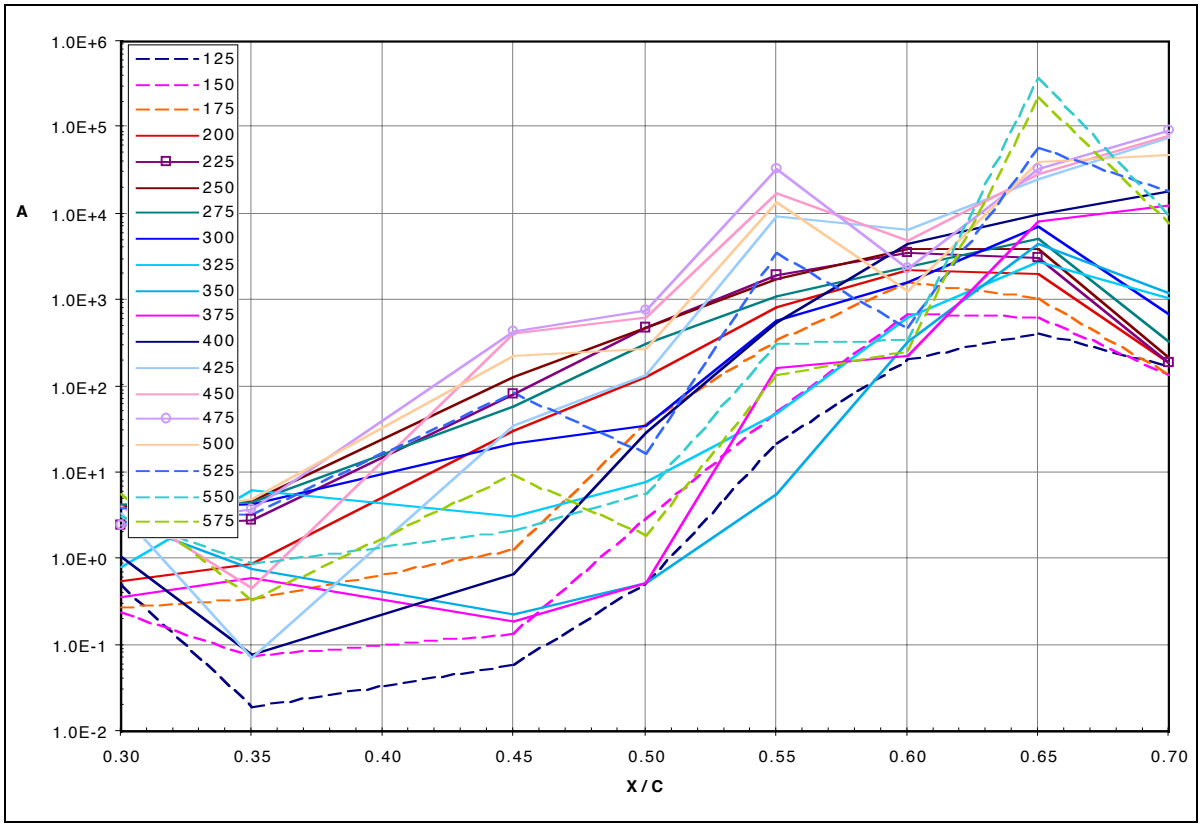

Figure 37: 15 m/s Chordwise Traverse from Modeshape Results

5.2.3.5 Total Energy Amplitude Disturbance Profiles

The disturbance profiles were also examined in total energy amplitude terms, where the disturbance profile is analogous to a modeshape which represents the amplitude due to all of the frequencies / energy instead of a single frequency. The total energy amplitude of the boundary-layer response packet is characterized in two ways, the peak-to-peak amplitude and the "energy/RMS" amplitude.

First, the results are presented in terms of the peak-to-peak amplitude of the boundary-layer response packet as it varies in the direction of the surface-normal coordinate. This amplitude is normalized by the tunnel free-stream velocity and given below. The results are presented for all surface conditions and acoustic-forcing conditions at given chordwise stations for both the 20 m/s and 15 m/s flow cases in **Figures 38 and 39**. Results are also presented for a given surface condition (with nominally constant acoustic forcing conditions) at a series of chordwise stations for both flow speed conditions in **Figures 40 and 41**. For these plots, solid lines and symbols are used to represent the results from the downstream traveling source signal (BI), while dashed lines and hollow symbols are used for the upstream traveling source response (EC).

It is interesting to note that the initial waveform of the disturbance profile strongly resembles that of the T-S modeshape at the central forcing frequency. This would indicate that the boundary-layer response packet is dominated by a narrow band of frequencies when the flow is laminar and that the boundary-layer stability can be modeled by linear stability theory. The observation of the narrow response band might be an artifact of the fairly narrow hardware bandpass filter. It can also be seen that the modeshape amplitude increases with increasing surface roughness or acoustic forcing level, as expected. Similar to the single-frequency modeshape results, there appears to be a point of diminishing returns when adding repeated roughness elements, as with going from Test 9 to Test 10 which consisted of comparable forcing signal amplitude but different number of repeated surface roughness elements (three and five, respectively). For the Test 7 15 m/s single roughness element case at 60% chord (green lines and symbols), the profile for the downstream signal response exhibits the same general form as with the Test 9 and 10 cases near the 65% chord location. This Test 7 case had twice the amplitude of the Test 9 and 10

cases. This observation supports the trade-off between forcing amplitude and surface roughness on the ultimate evolution and breakdown of the boundary-layer disturbances.

As with the modeshape results, a weak minimum near $(y/\delta^*) = {}^1/_2$ appears for the Test 11 (no surface roughness at 15 m/s) cases, which were acquired at 50, 60 and 70% chord (**Figure 42**). The cause of this phenomenon has not been determined. Probe-wall interference is one possible explanation, but would be inconsistent with the other results taken at these chordwise stations, which all had comparable values for δ^* and reasonable velocity measurements at chord-normal locations even closer to the model surface, as well as with the mean velocity profiles (**Figure 43**) which do not indicate a significant inflection. A similar near-wall effect was identified by Dagenhart[83]. Here, it was determined that the near-wall deficit / excess in the velocity variations was due to residue from the model cleaning process, which used supposedly lint-free clothes. While that research involved a disturbance field dominated by stationary crossflow, the fact that there were near-wall small-scale velocity effects and a similar model polishing routine was used for this experiment, this possibility cannot be discounted.

From examining the results from 50 - 60% chord, it can be seen that the interference effects of the upstream travelling source signal with the downstream forcing signal's response which altered the results for the single-frequency modeshapes do not appear in these total energy amplitude results. This is likely because the acoustic signal that interfered with the boundary-layer response was of a smaller amplitude and did not have a significant effect on the peak-peak amplitude of the response packet.

Again, the results are presented in logarithmic scaling to compare all chordwise stations and surface roughness conditions on the same plot and multiple plots with the same axis scale settings. Linear scale modeshape results are presented in **Figures 44 and 45.**

It is also interesting to note that as the disturbance profile decays from a smooth distribution within the boundary layer, the maxima of the profile closer to the wall saturates at what appears to be a near constant level for all forcing conditions at a given flow speed. This saturation level does not appear to vary strongly with chordwise location.

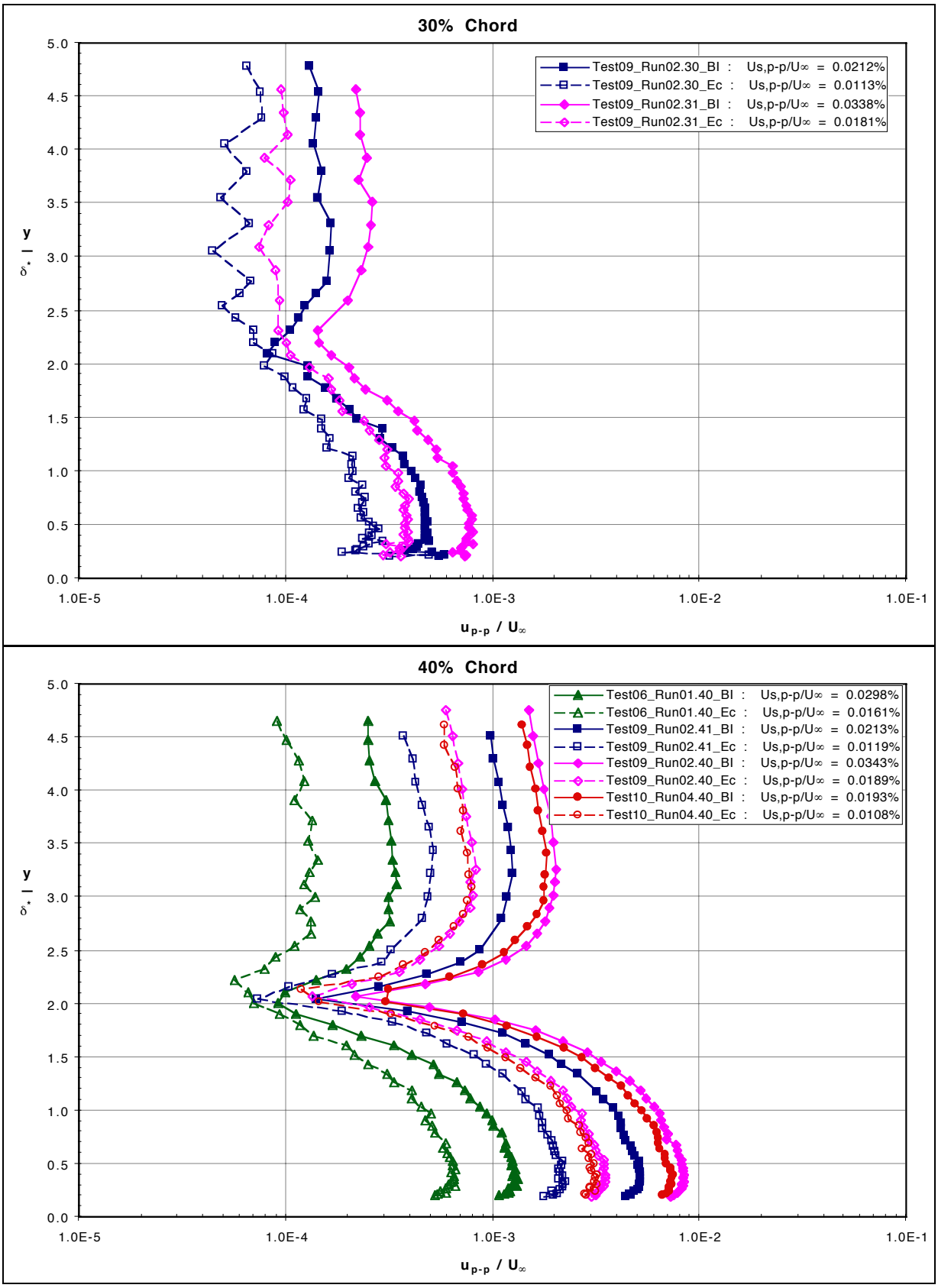

Figure 38: 20 m/s $U_{p\text{-}p}/U_{\infty}$ Disturbance Profiles at Select Chordwise Stations

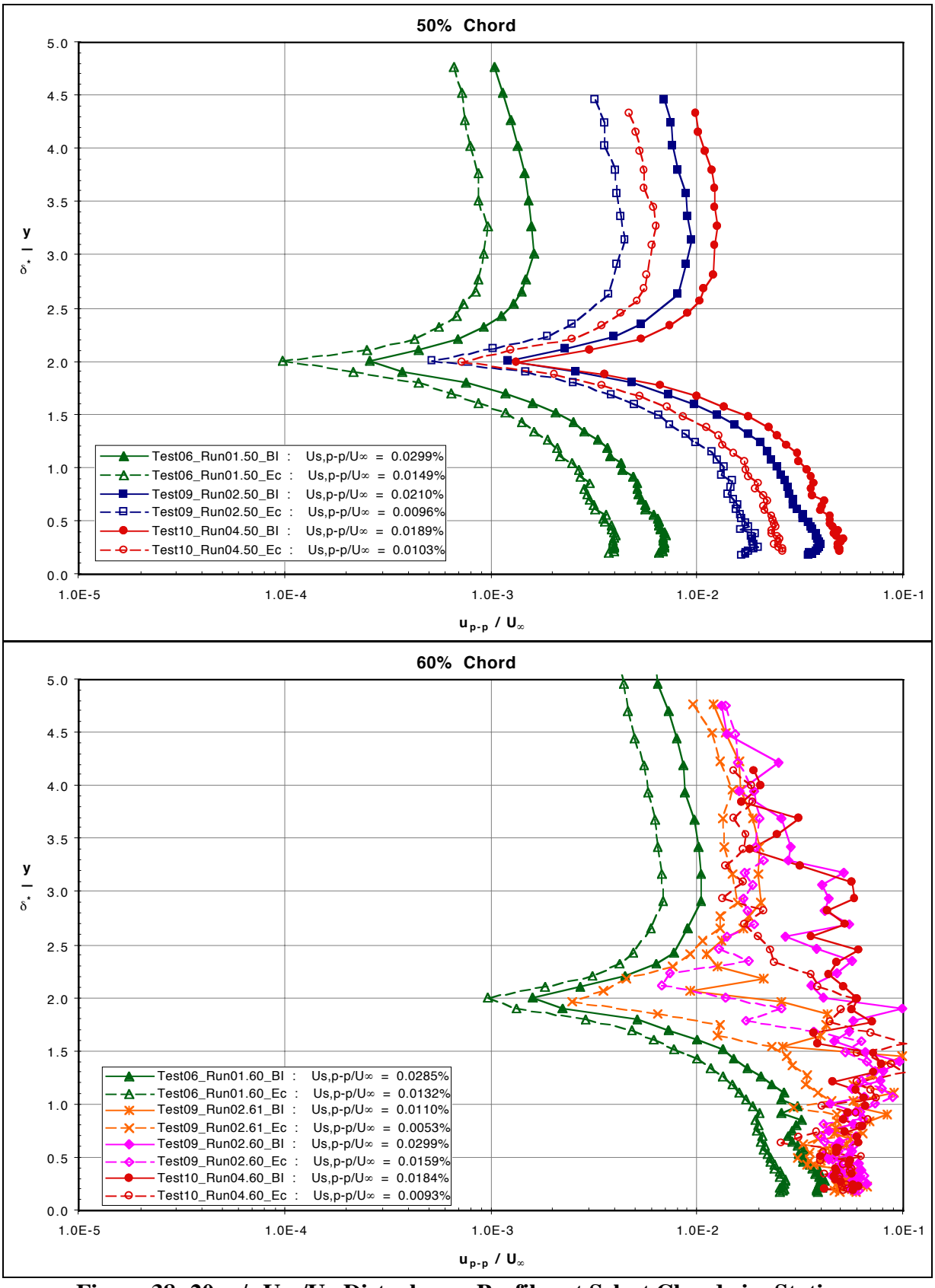

Figure 38: 20 m/s $U_{p\text{-}p}/U_\infty$ Disturbance Profiles at Select Chordwise Stations

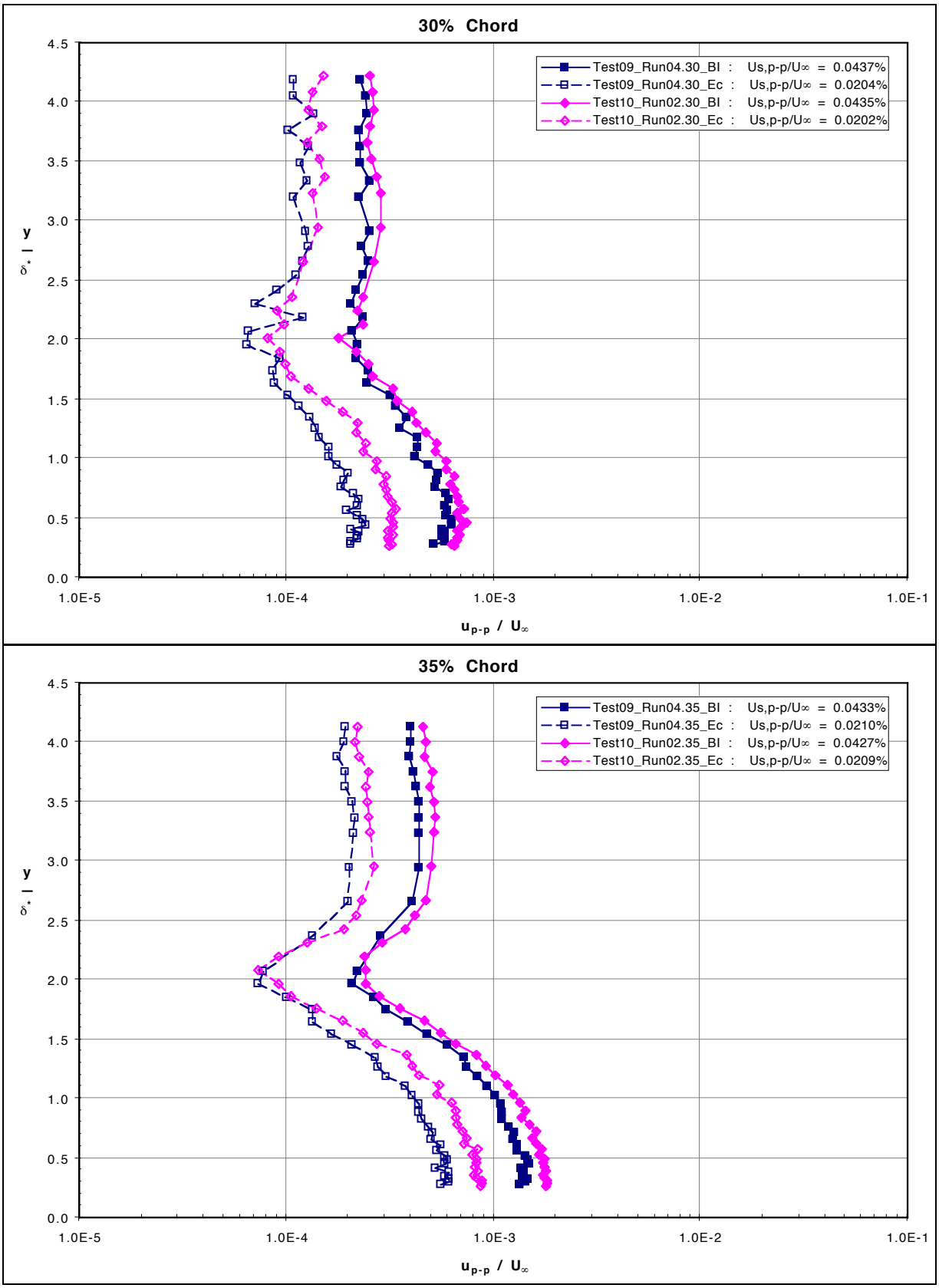

Figure 39: 15 m/s $U_{p\text{-}p}/U_\infty$ Disturbance Profiles at Select Chordwise Stations

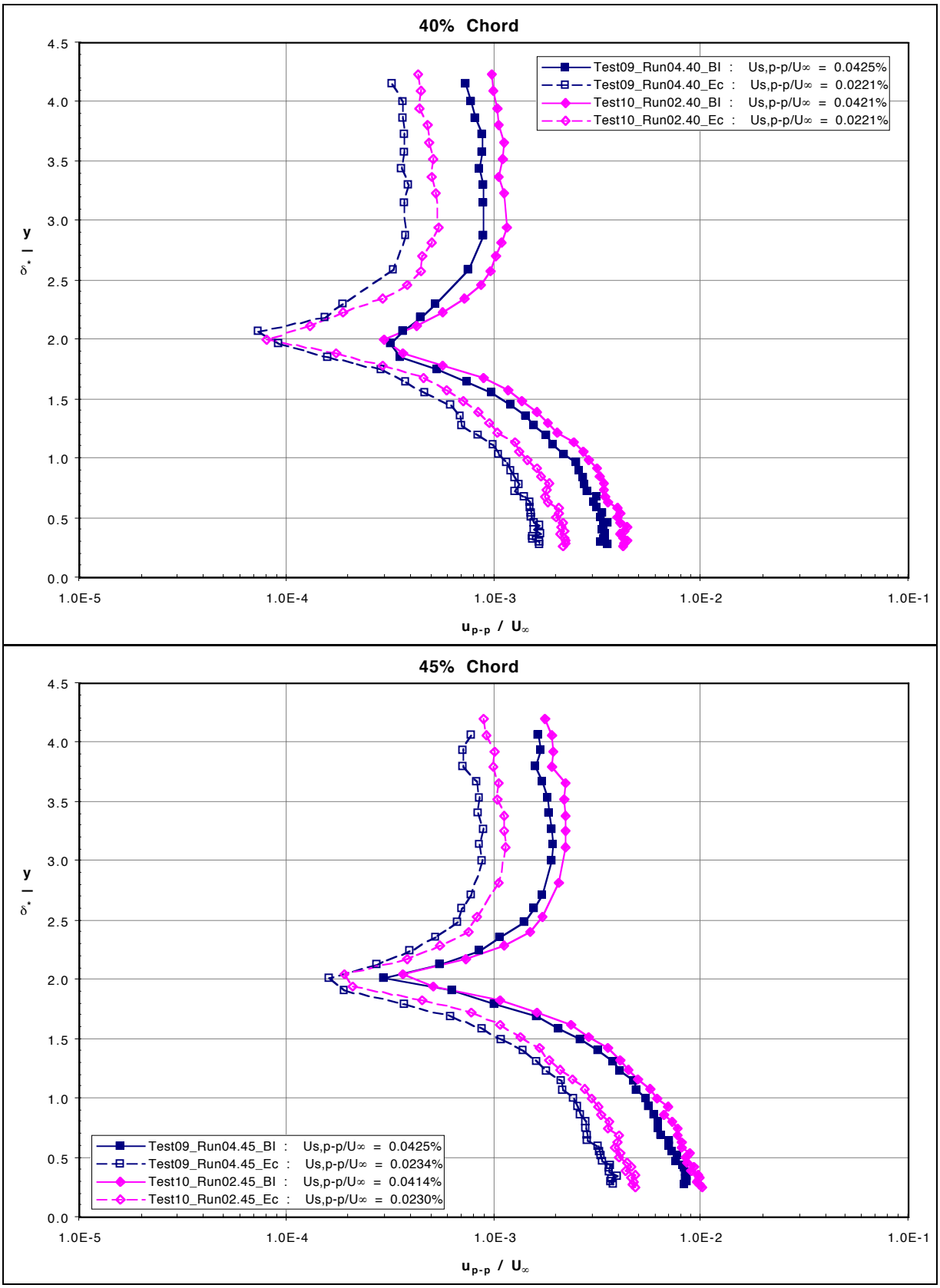

Figure 39: 15 m/s $U_{p\text{-}p}/U_{\infty}$ Disturbance Profiles at Select Chordwise Stations

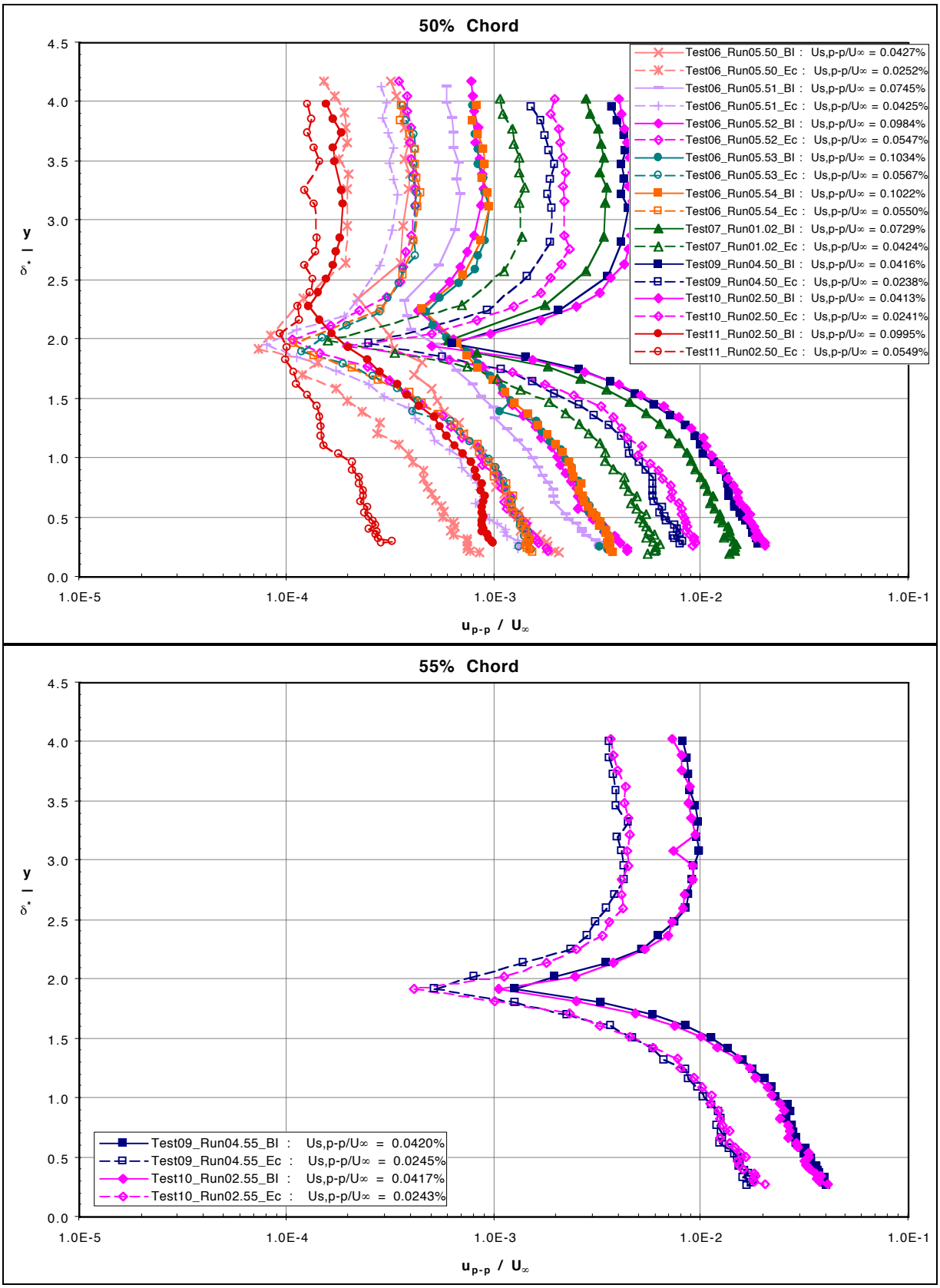

Figure 39: 15 m/s $U_{p\text{-}p}/U_{\infty}$ Disturbance Profiles at Select Chordwise Stations

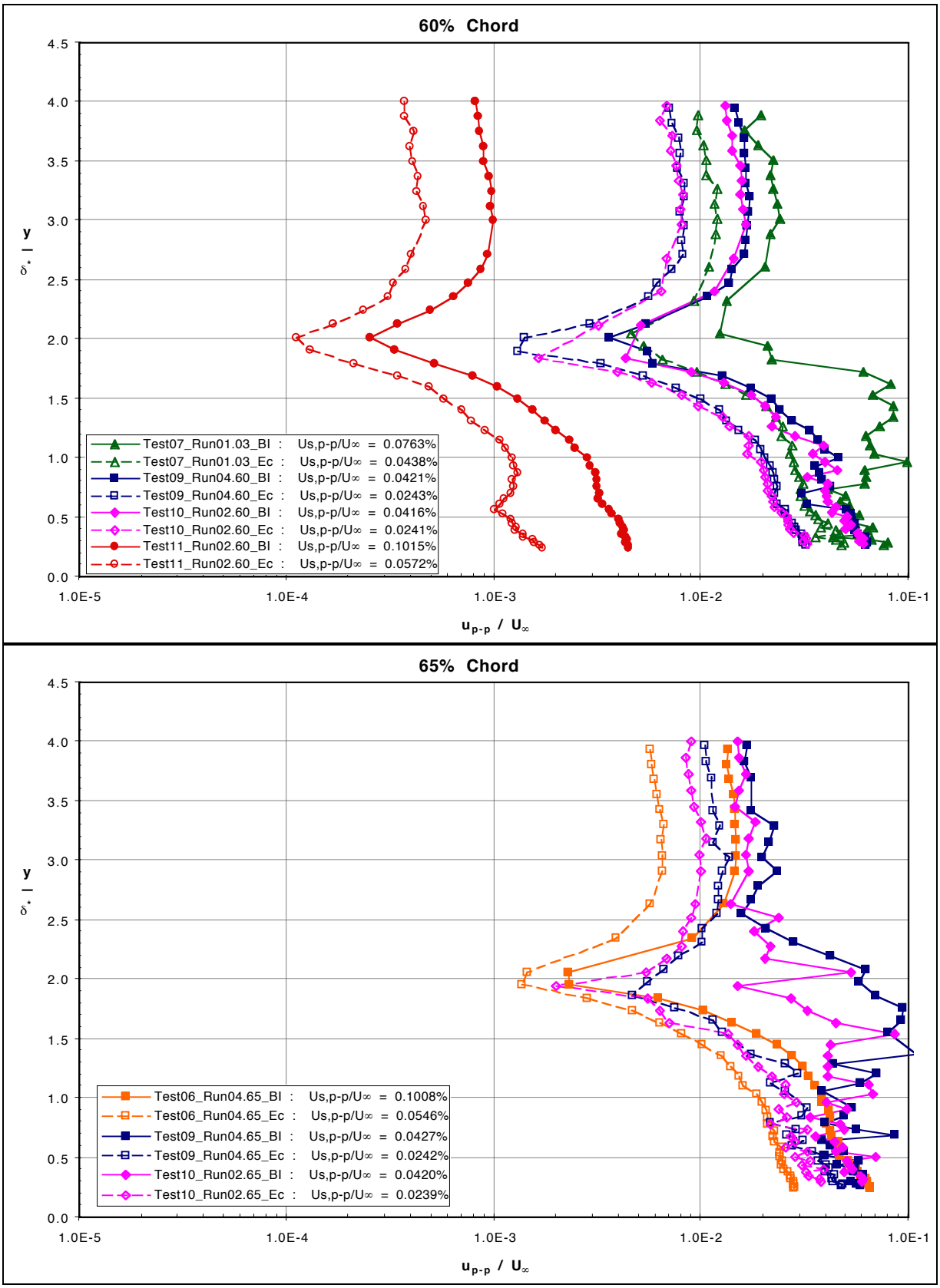

Figure 39: 15 m/s $U_{p\text{-}p}/U_\infty$ Disturbance Profiles at Select Chordwise Stations

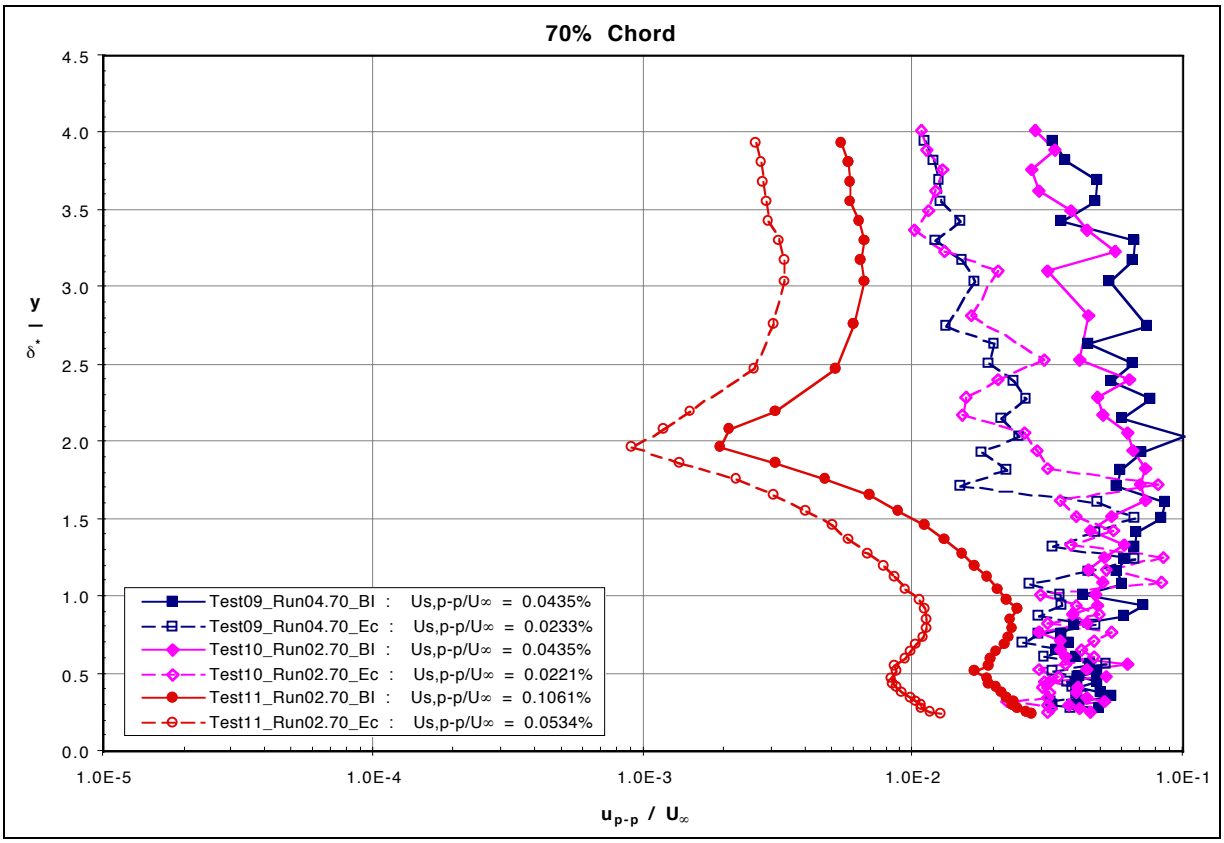

Figure 39: 15 m/s $U_{p\text{-}p}/U_\infty$ Disturbance Profiles at Select Chordwise Stations

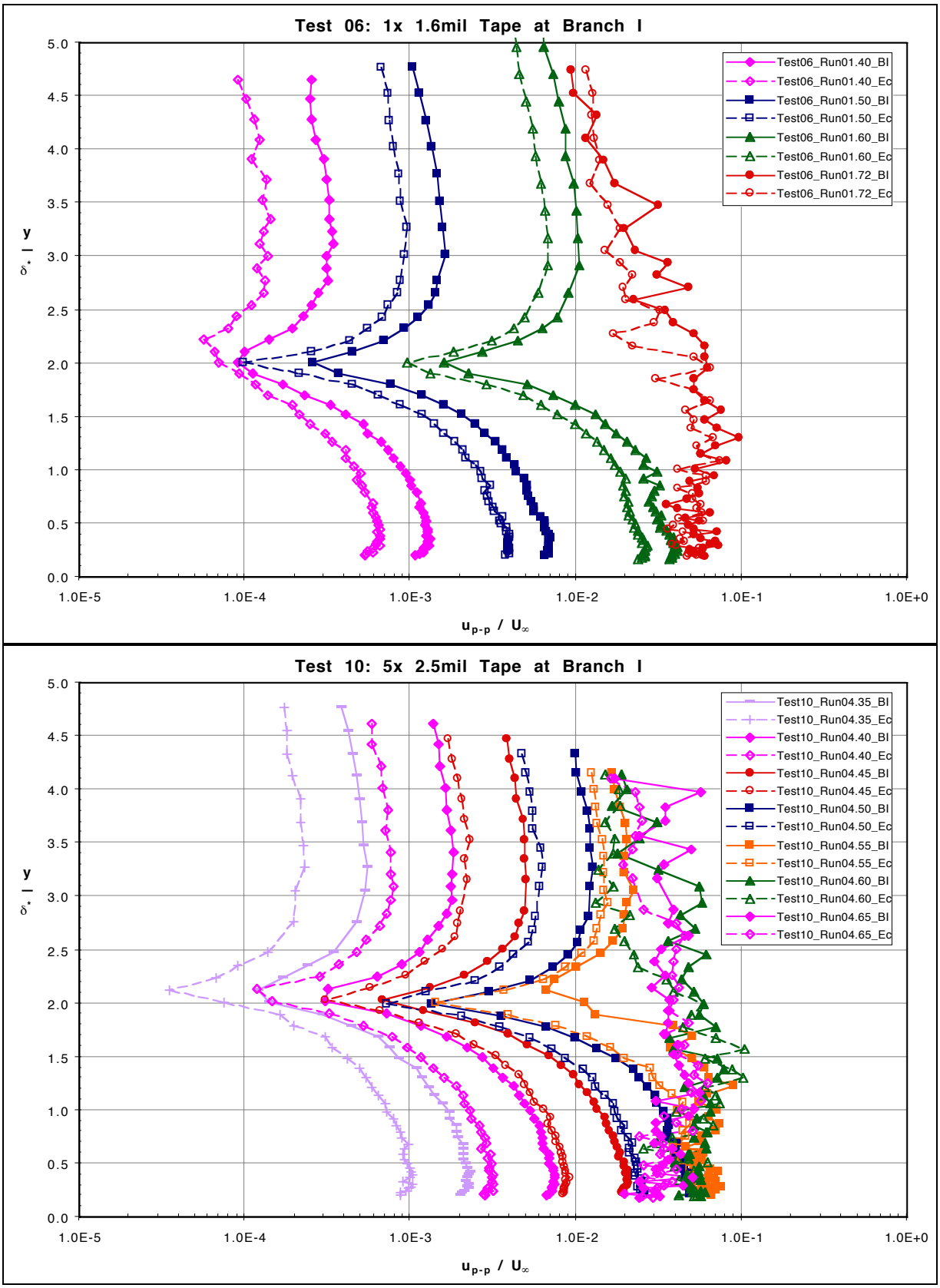

Figure 40: 20 m/s $U_{p\text{-}p}/U_\infty$ Disturbance Profiles for Select Surface Conditions

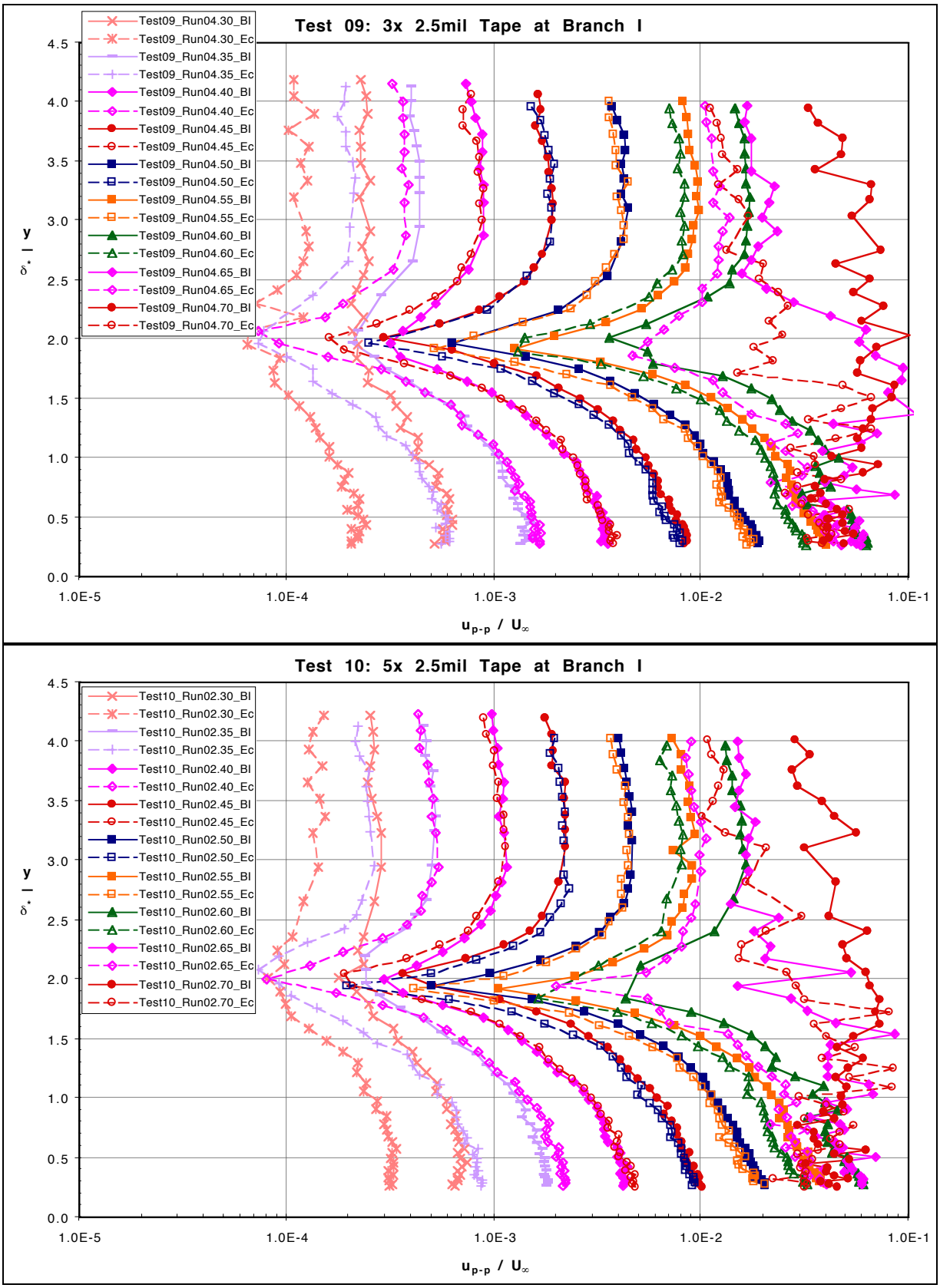

Figure 41: 15 m/s $U_{p\text{-}p}/U_{\infty}$ Disturbance Profiles for Select Surface Conditions

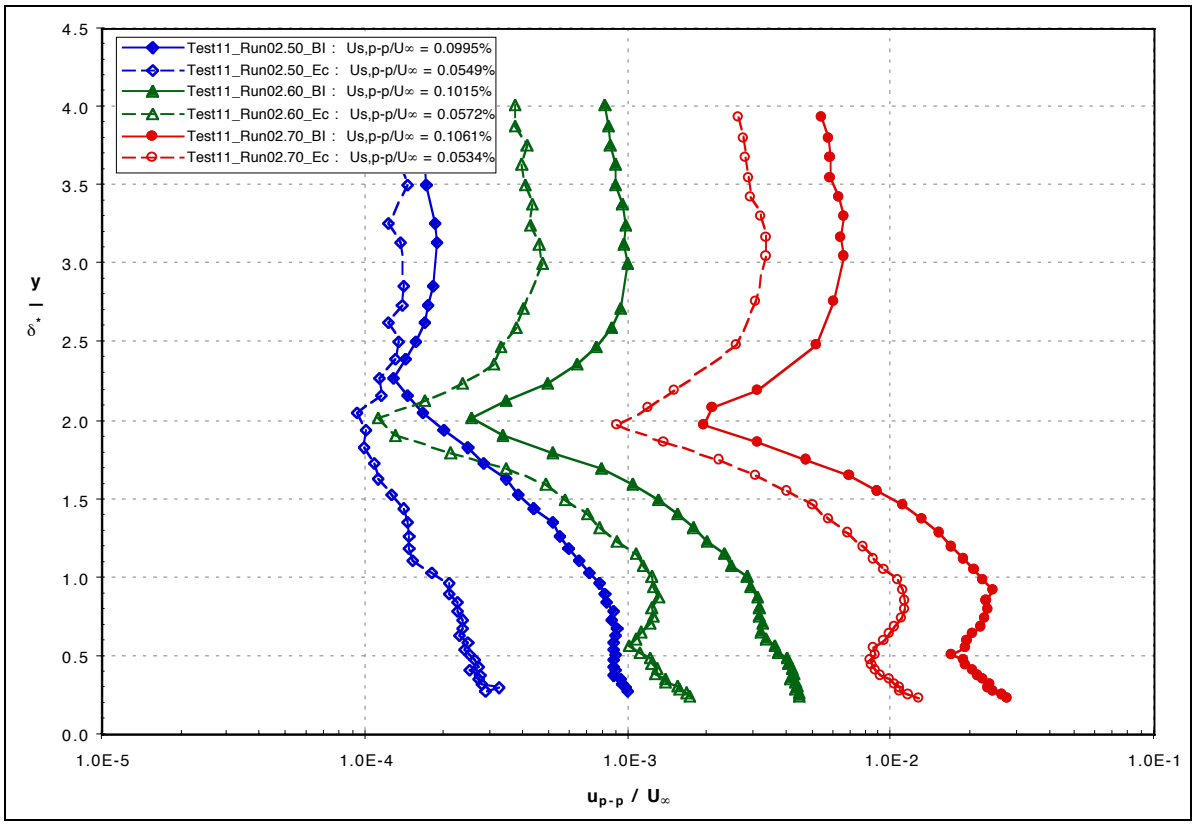

Figure 42: 15 m/s Test 11 Peak-to-Peak Disturbance Profiles

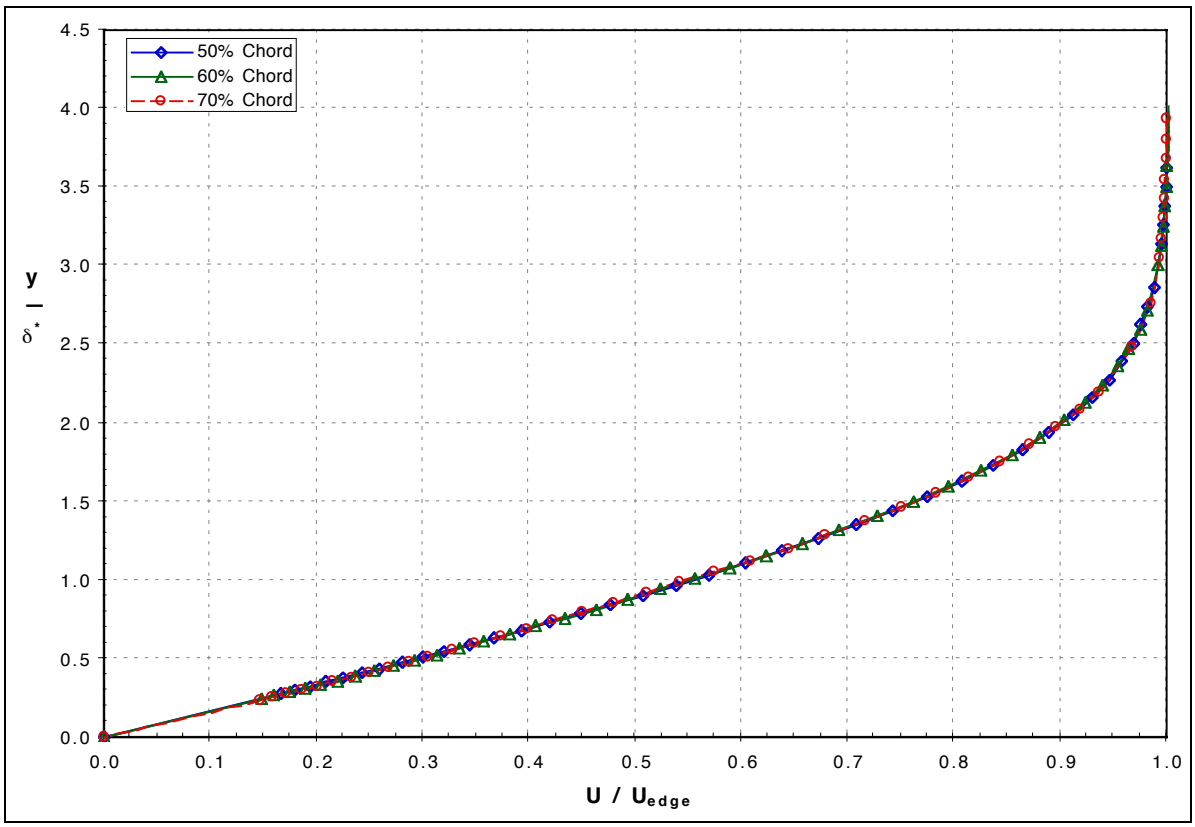

Figure 43: 15 m/s Test 11 Mean Velocity Profiles

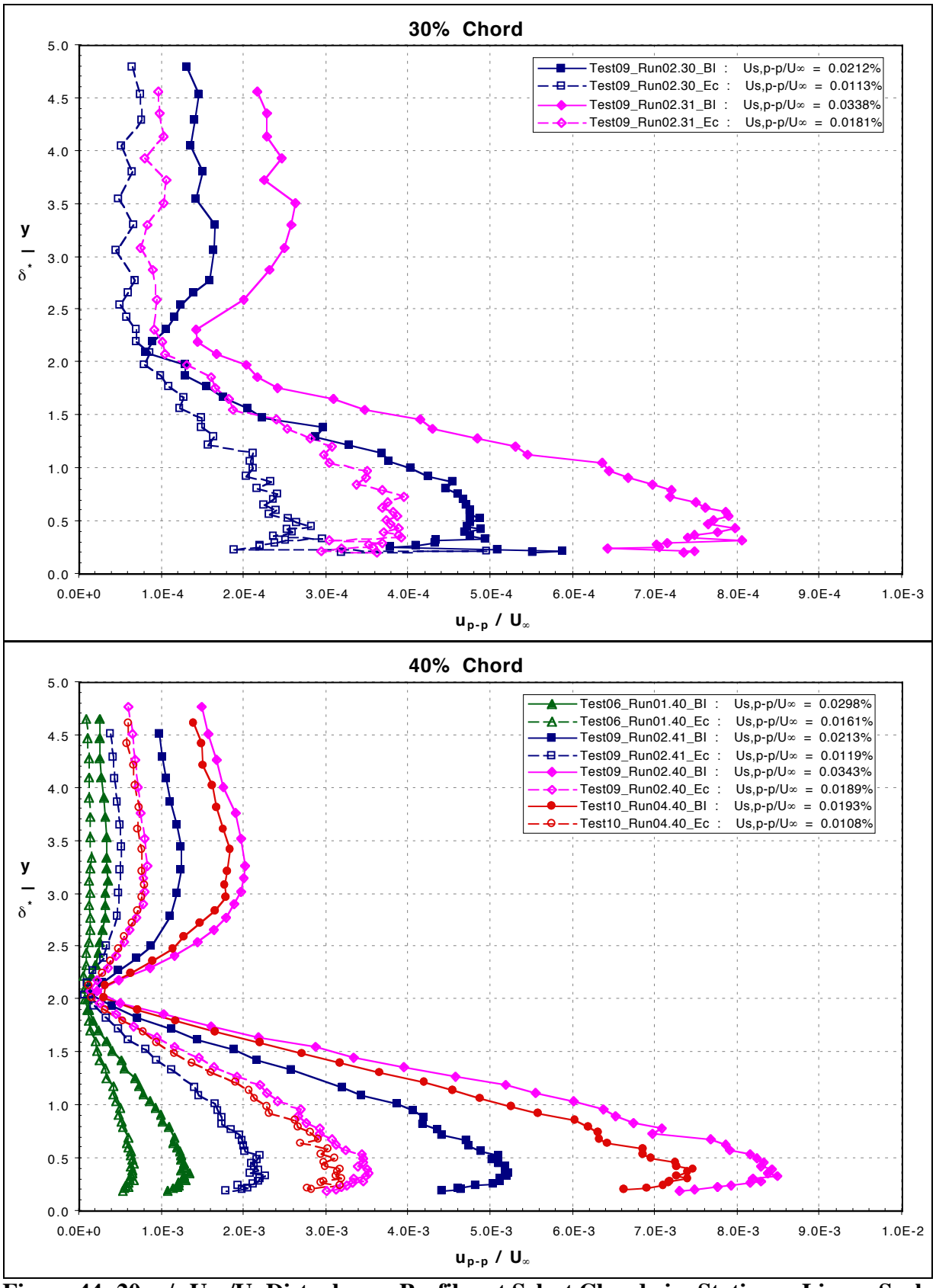

Figure 44: 20 m/s U_{p-p}/U_∞ Disturbance Profiles at Select Chordwise Stations - Linear Scale

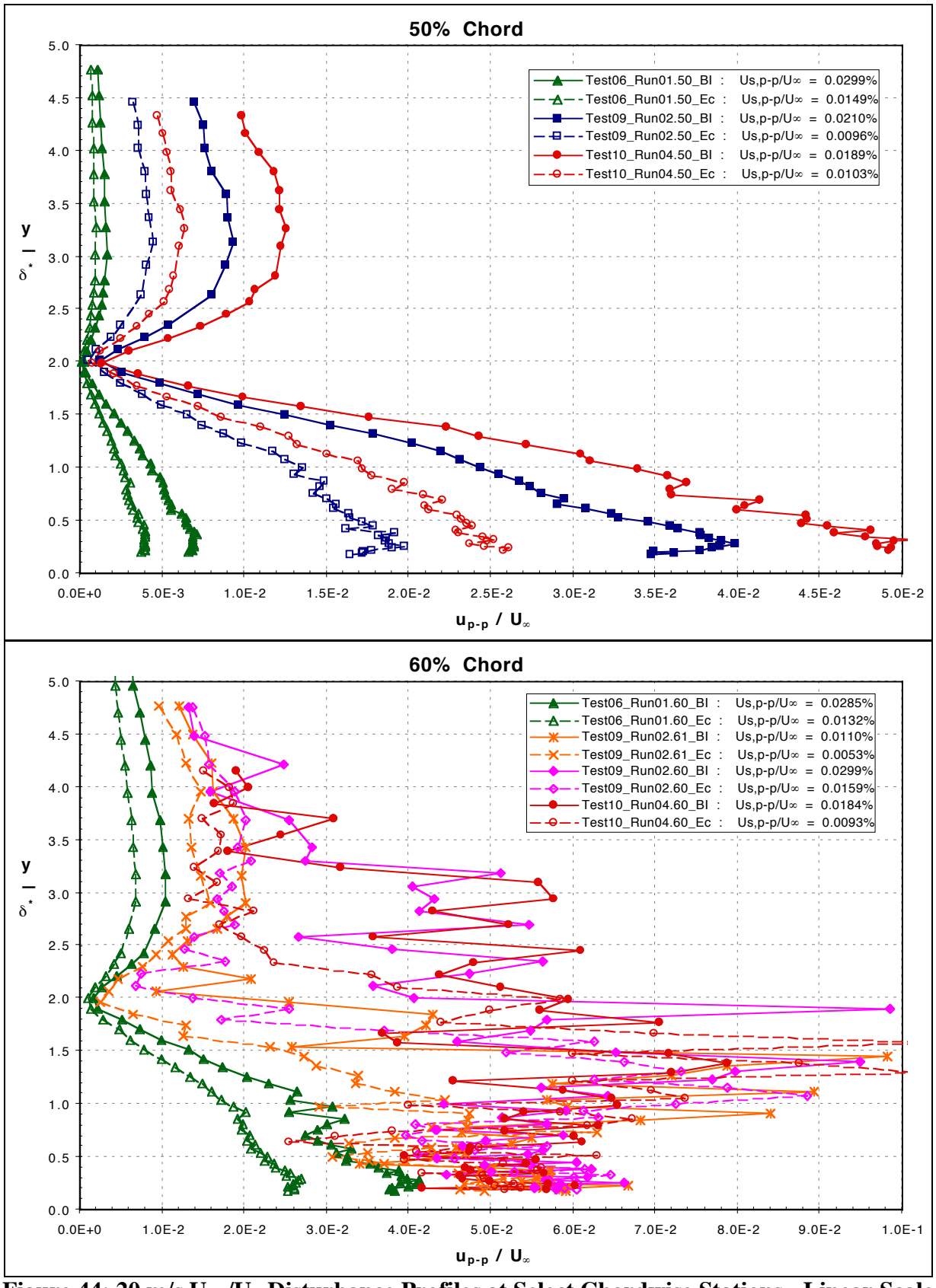

Figure 44: 20 m/s $U_{p\text{-}p}/U_\infty$ Disturbance Profiles at Select Chordwise Stations - Linear Scale

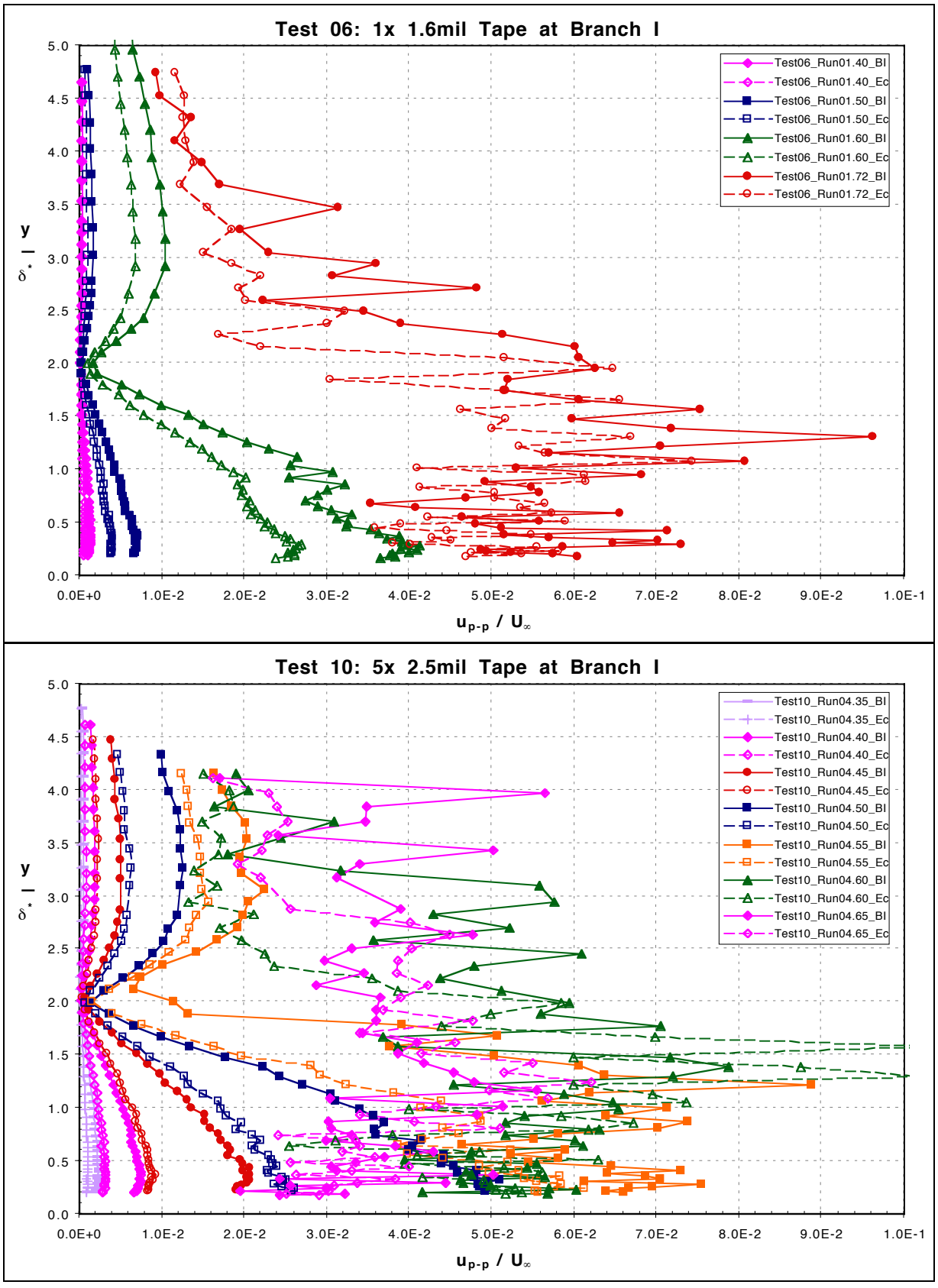

Figure 45: 20 m/s $U_{p\text{-}p}/U_\infty$ Disturbance Profiles at Select Surface Conditions - Linear Scale

The other form of total energy amplitude results is presented in an "energy/RMS" term defined as:

$$u_{rms} = \sqrt{\sum \left[u(t)\right]^2} \qquad \textbf{Equation 5-4}$$

The tunnel free-stream velocity is then used to normalize this component. This amplitude form encompasses the total energy or RMS within the disturbance packet, which grows spatially as well as temporally. Results in a similar format as the peak-to-peak results are presented in **Figures 46**, **47**, **48**, **and 49**. This amplitude characterization behaves comparably well to the peak-to-peak amplitude method with a similar dependence on surface condition, acoustic forcing level and with the existence of "some" saturation amplitude for a given flow speed. However, the energy amplitude method yielded "smoother" curves, which would be expected of an integral-type quantity.

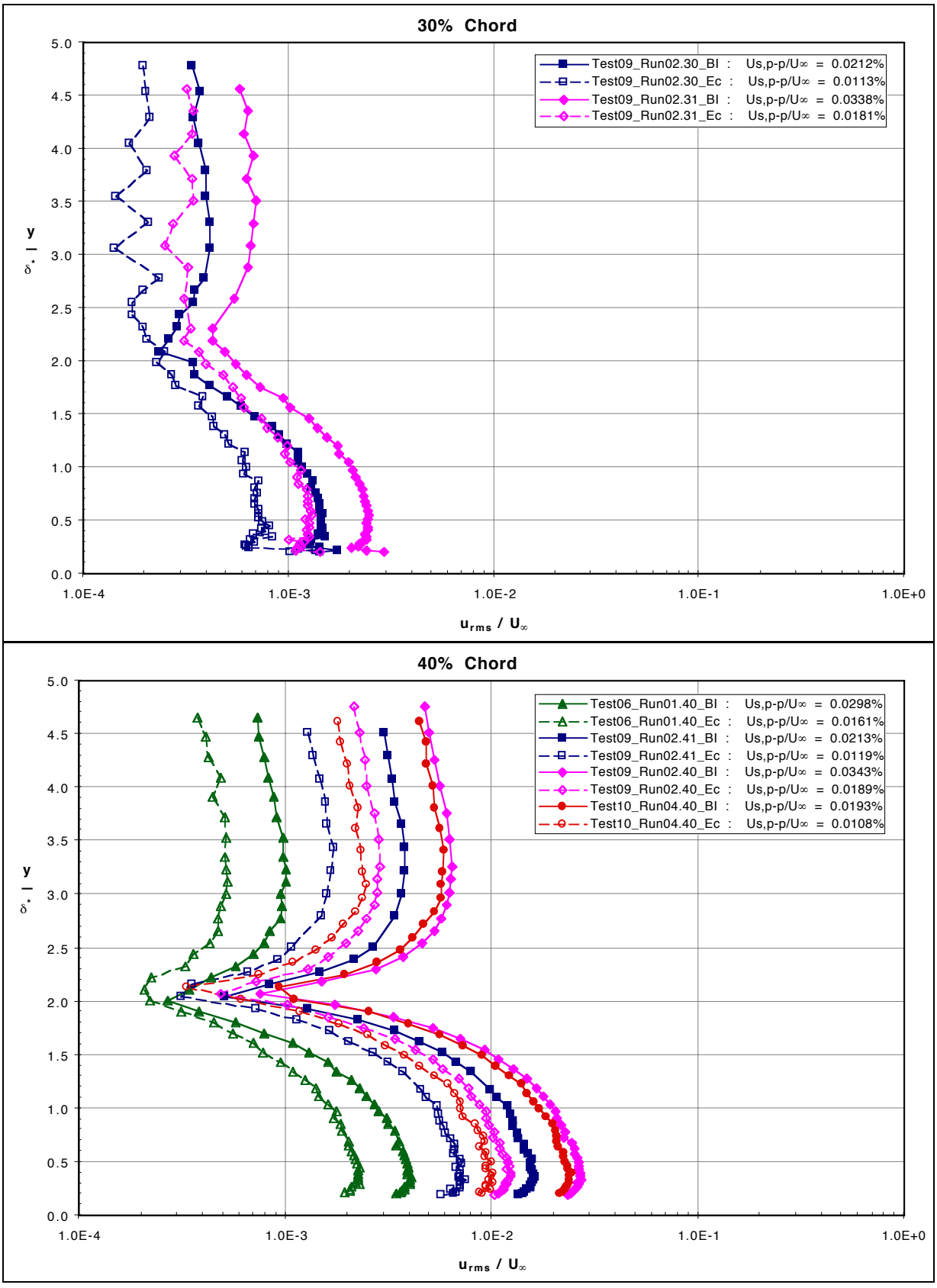

Figure 46: 20 m/s U_{rms}/U_{∞} Disturbance Profiles at Select Chordwise Stations

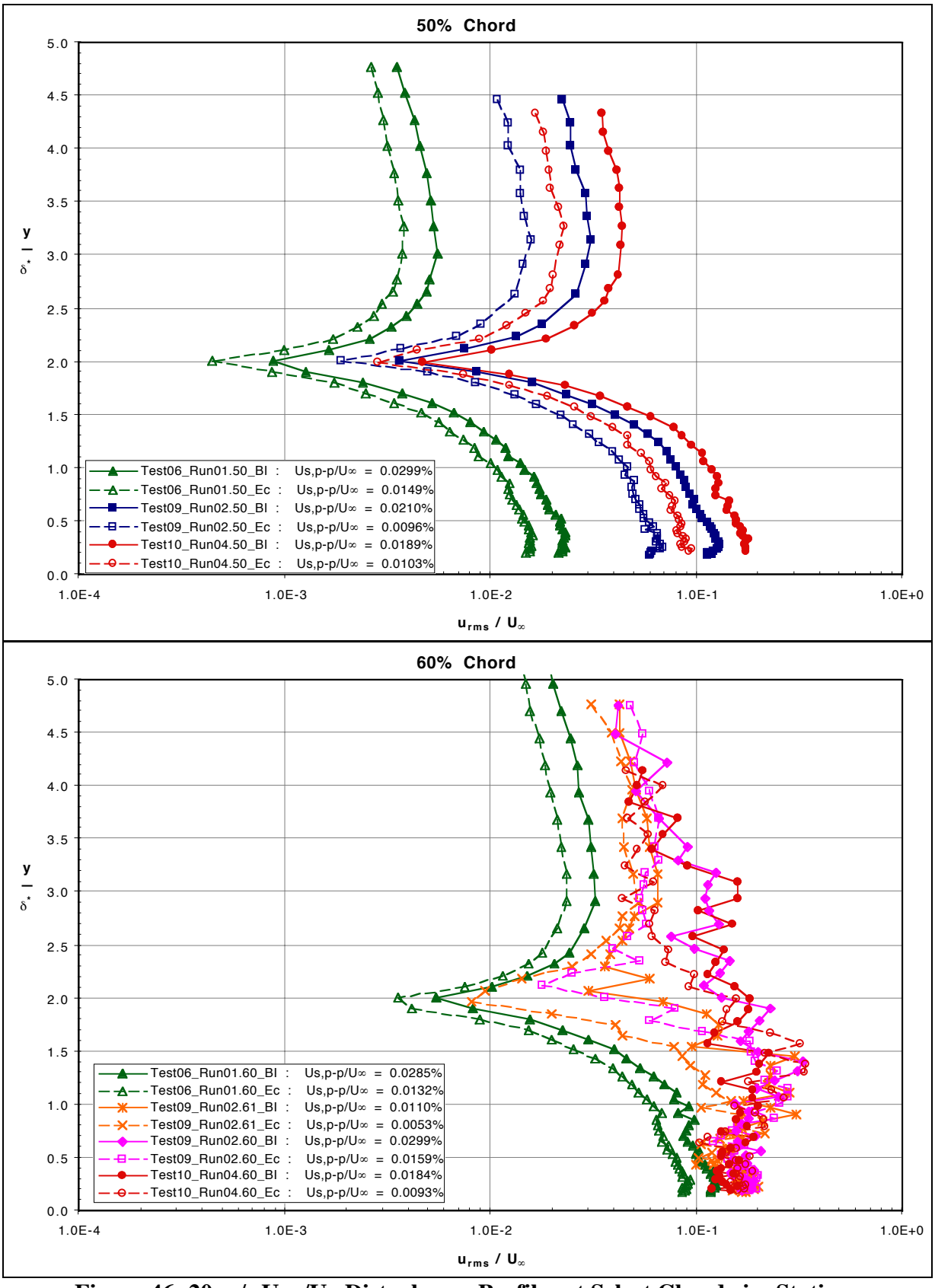

Figure 46: 20 m/s U_{rms}/U_{∞} Disturbance Profiles at Select Chordwise Stations

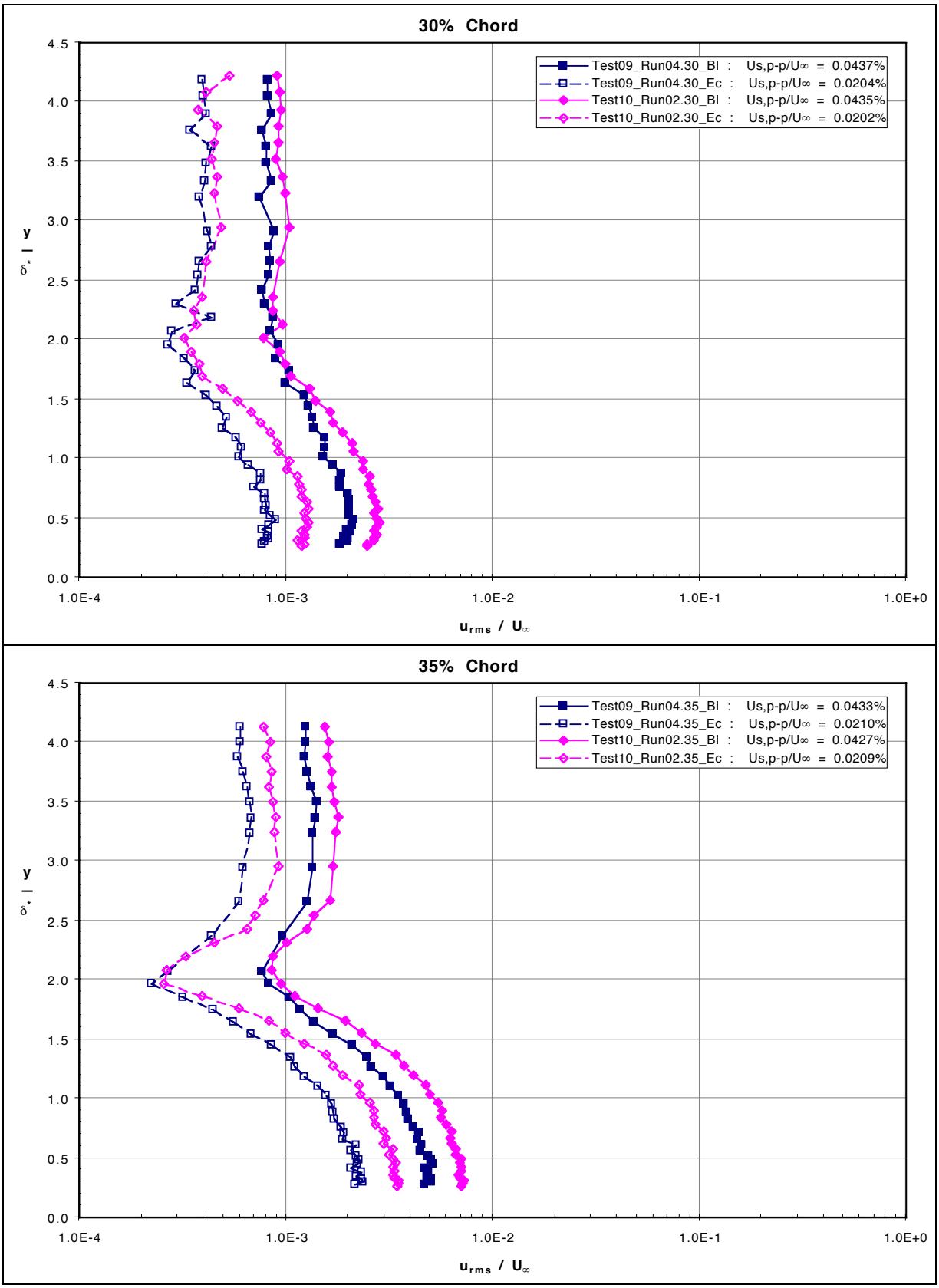

Figure 47: 15 m/s U_{rms}/U_{∞} Disturbance Profiles at Select Chordwise Stations

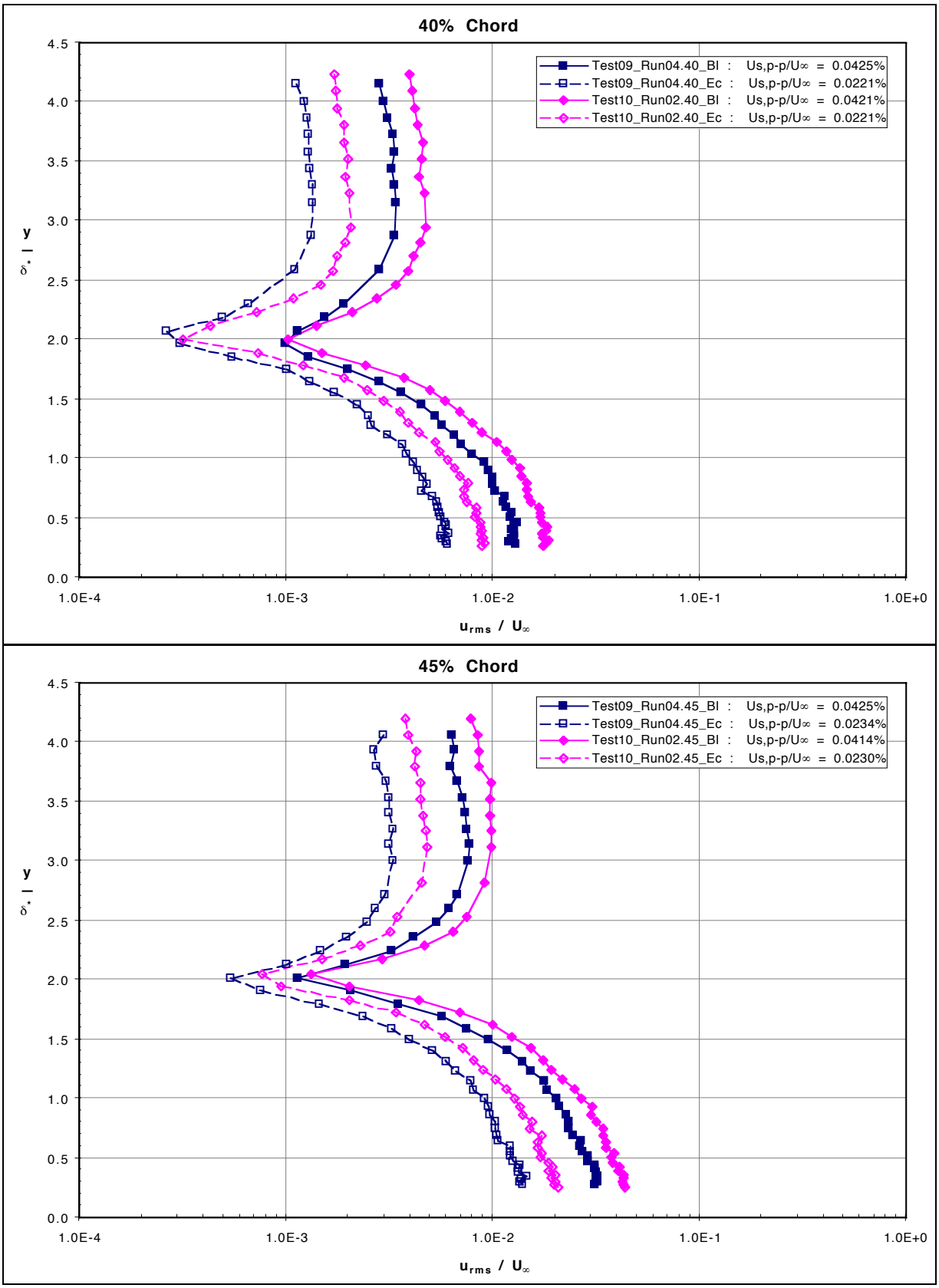

Figure 47: 15 m/s U_{rms}/U_{∞} Disturbance Profiles at Select Chordwise Stations

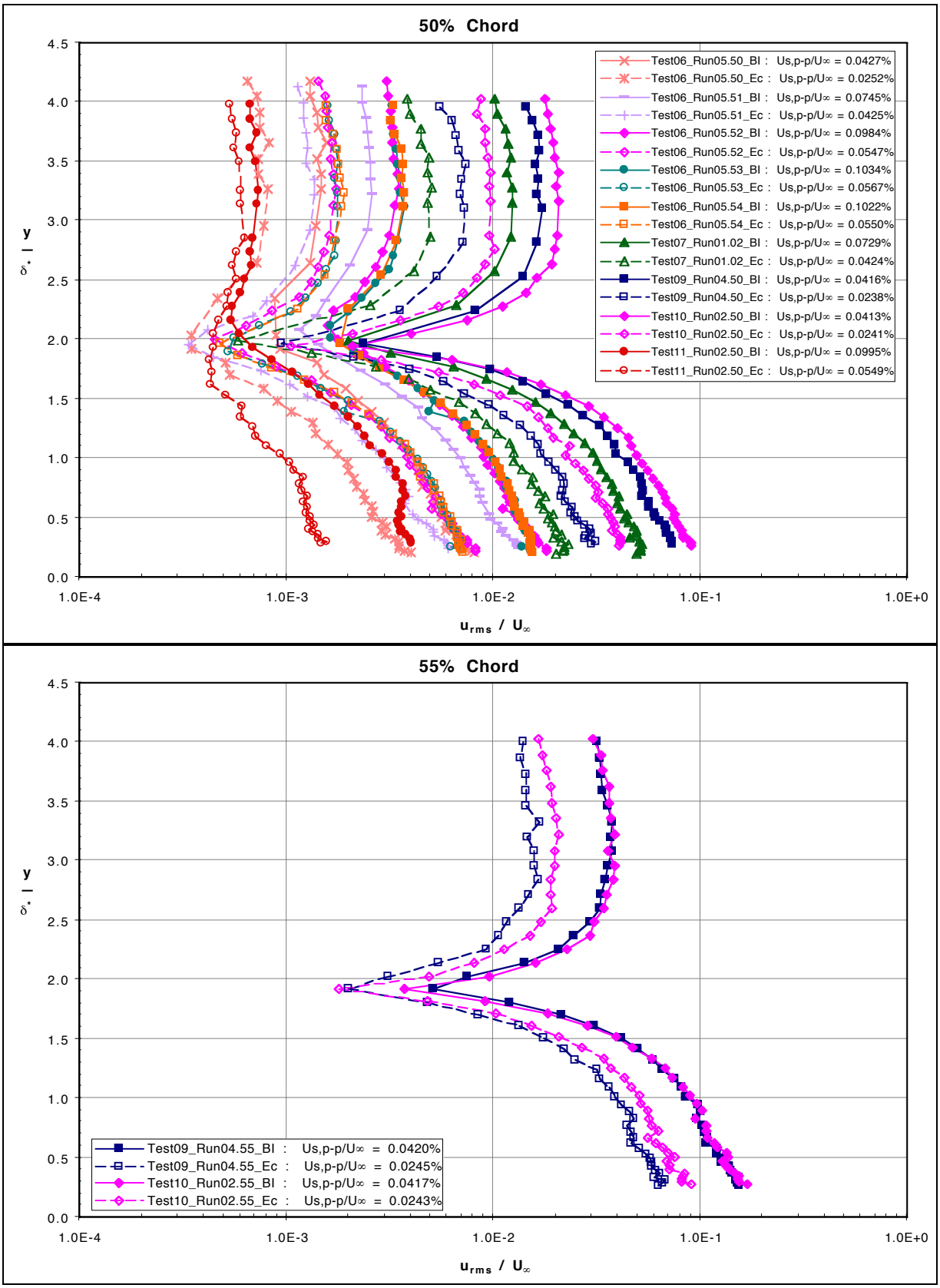

Figure 47: 15 m/s U_{rms}/U_{∞} Disturbance Profiles at Select Chordwise Stations

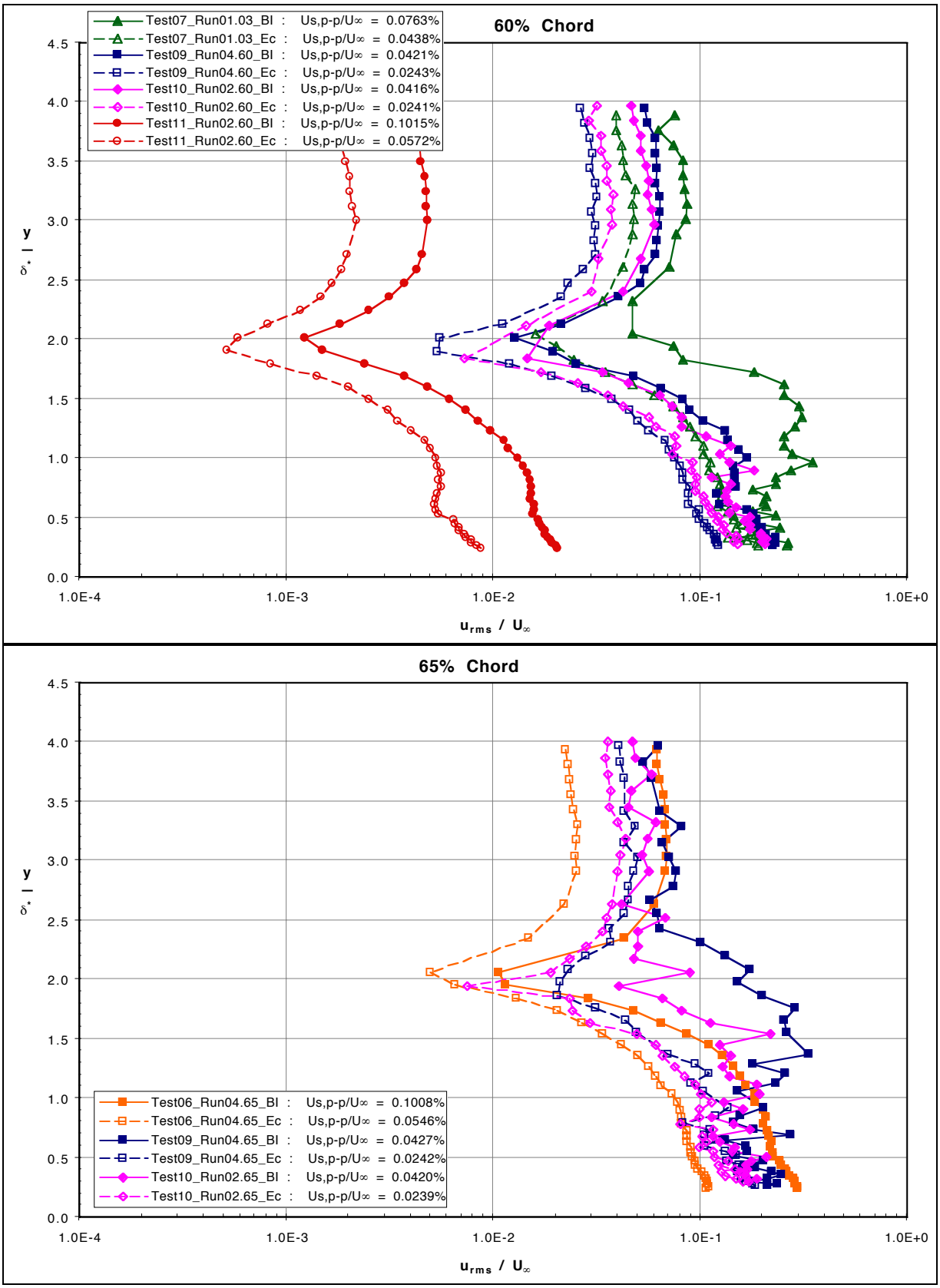

Figure 47: 15 m/s U_{rms}/U_{∞} Disturbance Profiles at Select Chordwise Stations

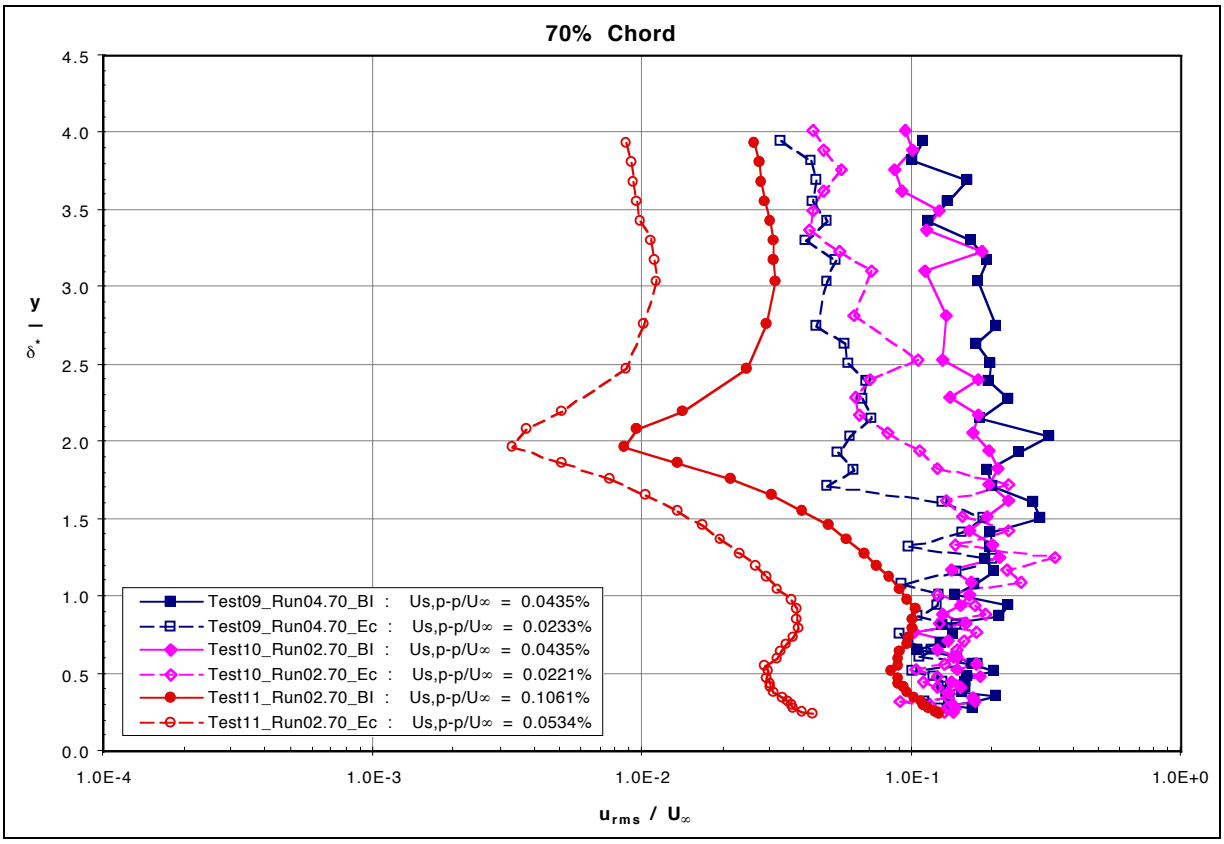

Figure 47: 15 m/s U_{rms}/U_{∞} Disturbance Profiles at Select Chordwise Stations

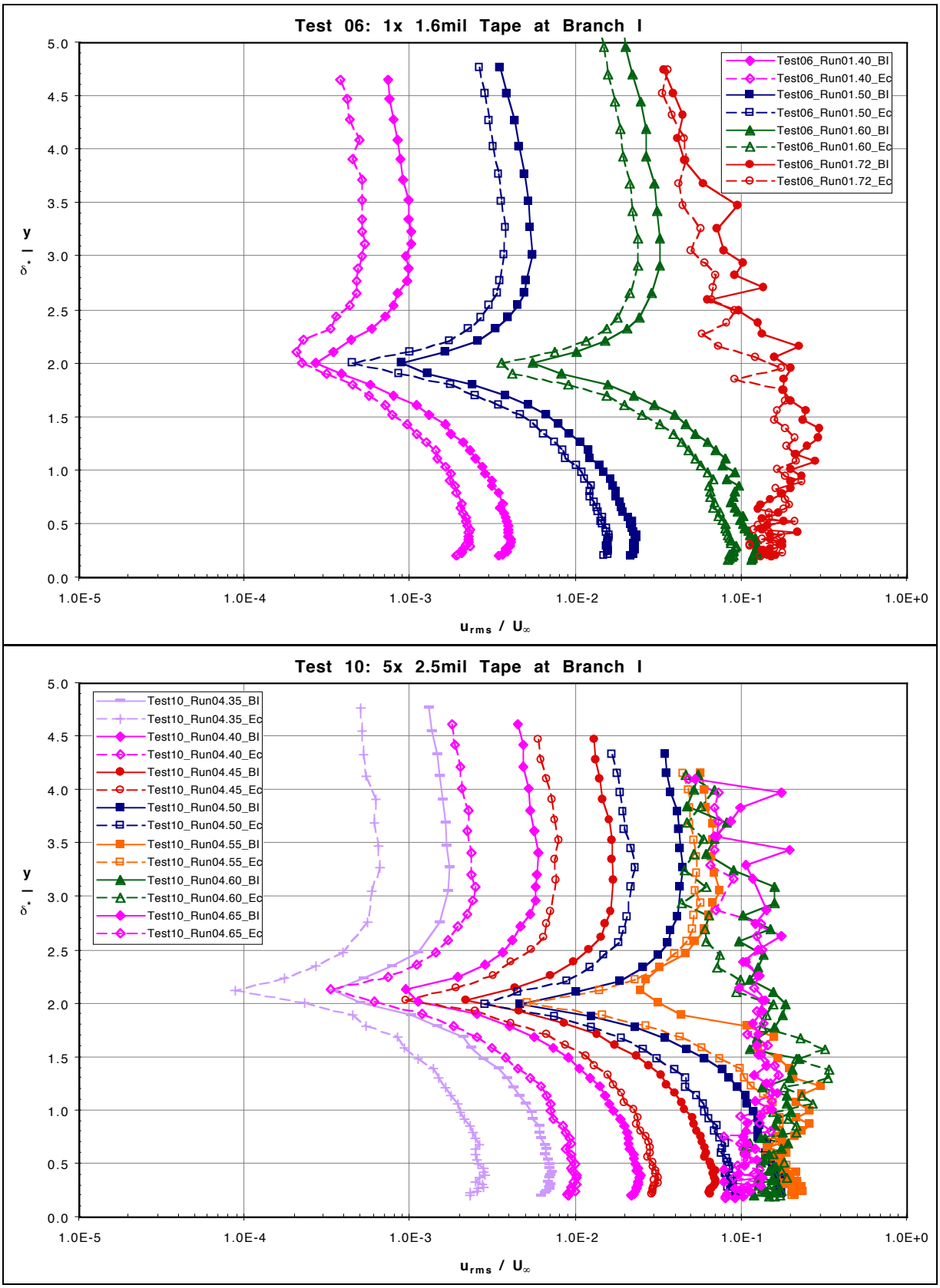

Figure 48: 20 m/s U_{rms}/U_{∞} Disturbance Profiles for Select Surface Conditions

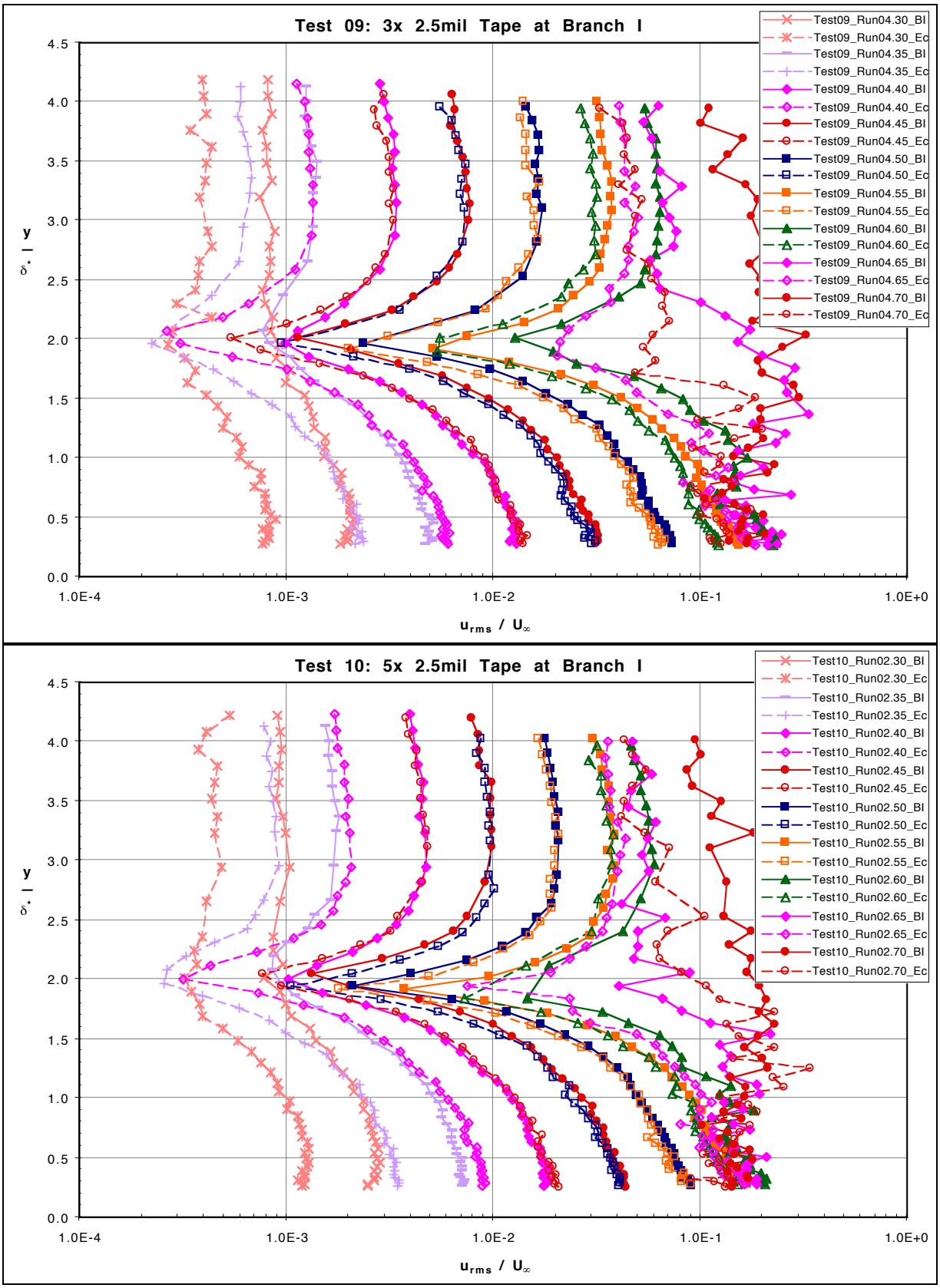

Figure 49: 15 m/s U_{rms}/U_{∞} Disturbance Profiles for Select Surface Conditions

5.2.3.6 Amplitude-Based Disturbance Breakdown Criterion from Disturbance Profile Results

From examining the total energy amplitude results from **Section 5.2.3.5**, a criterion was established to identify the onset of breakdown of the boundary-layer disturbances. This criterion is based upon the amplitude of the lower lobe of the disturbance waveform and is found to be consistent for both of the flow cases examined in this particular facility.

Table 14: Modeshape-Based Disturbance Breakdown Criterion

	Breakdown Amplitude	**Saturation Amplitude**
$U_{p\text{-}p}/U_\infty$	5%	7%
U_{rms}/U_∞	16%	20%

This disturbance criterion is strictly based upon amplitude of the disturbance. Another possible alternative to consider would be a criterion based upon the coherence between the forcing signal and the boundary-layer response. It should also be noted that this is a breakdown criterion for the traveling boundary-layer response to acoustic burst forcing. It has yet to be determined how this will compare with transition results from constant wave train forcing environments.

5.2.4 Boundary-Layer Chordwise Traverse Results

Comparisons of T-S boundary-layer responses from both of the Branch I receptivity cases for several surface roughness configurations and acoustic forcing conditions are presented in this section. All of the results have been acquired at a constant non-dimensional boundary-layer height, $(y/\delta^*) = 3$. This height was selected because it corresponded with the location of the maxima of the upper lobe of the Tollmien-Schlichting modeshape at the primary forcing frequency. The shape of the peak has been previously shown not to be sharp, thus measuring a representative value of the maximum could be consistently measured.

Amplitudes are presented in non-dimensional single-frequency form, as well as in two different total energy amplitude forms. The single-frequency form of the boundary-layer response amplitude is defined as the response amplitude relative to the forcing signal amplitude at a particular frequency, which is the same form as used for the modeshape results and defined in **Section 5.2.3.1**. The total energy amplitude forms are defined as a characteristic velocity of the

T-S wave packet relative to the free-stream velocity, again in the same form as used above with the disturbance profile analysis, defined in **Section 5.2.3.2**.

5.2.4.1 Time Traces and Wave Speed Results

Figure 50 shows an example of the time traces acquired during a chordwise traverse. The data shown is from a 20 m/s flow case with 2.54 cm {1 inch} wide 1.6 mil thick tape located with its leading edge at Branch I for a 300 Hz disturbance. The downstream source and downstream response signals are displayed in red and pink, respectively. The upstream source and upstream response signals are displayed in dark blue and blue, respectively. The traveling source amplitudes were about 0.0087% and 0.0049% free-stream velocity for the downstream and upstream traveling signals, respectively. The results are presented such that earlier chordwise station time traces are at a x100 scale, while further downstream data is at x10 and x1 scale, where the Y-coordinate is a measure of the velocity fluctuation amplitude staggered along the model chord. Actual velocity amplitude scale is not presented because the purpose of this figure is to present the general character of the time traces that was observed for all of the test conditions examined. The plots indicate the signals and responses for both the downstream and upstream sources, where the upstream traveling source is an echo of the downstream traveling source. All of the time traces begin at the triggering of the source signal upstream of the model.

From examining the figure, it can be seen that the source signals and responses are modulated and fairly symmetric, both in time and velocity. The source signals are measured in the free-stream above the boundary layer. The time traces of the free-stream acoustic signal and the boundary-layer Stokes wave are overlaid on the plot to indicate how well the Stokes response compares with the acoustic forcing signal at the upstream chord locations. It can also be seen that there exists a region where the upstream traveling forcing signal and the response to the downstream traveling forcing signal have the potential to locally interact if their amplitudes are comparable (near 50% chord). By nature of the different scaling used to display the time trace amplification, it can be seen that the source signals become dwarfed by the response signals at downstream chordwise stations. Overall, this figure presents the nature of the raw time traces acquired and identifies the various packets of concern used throughout the analysis of the data.

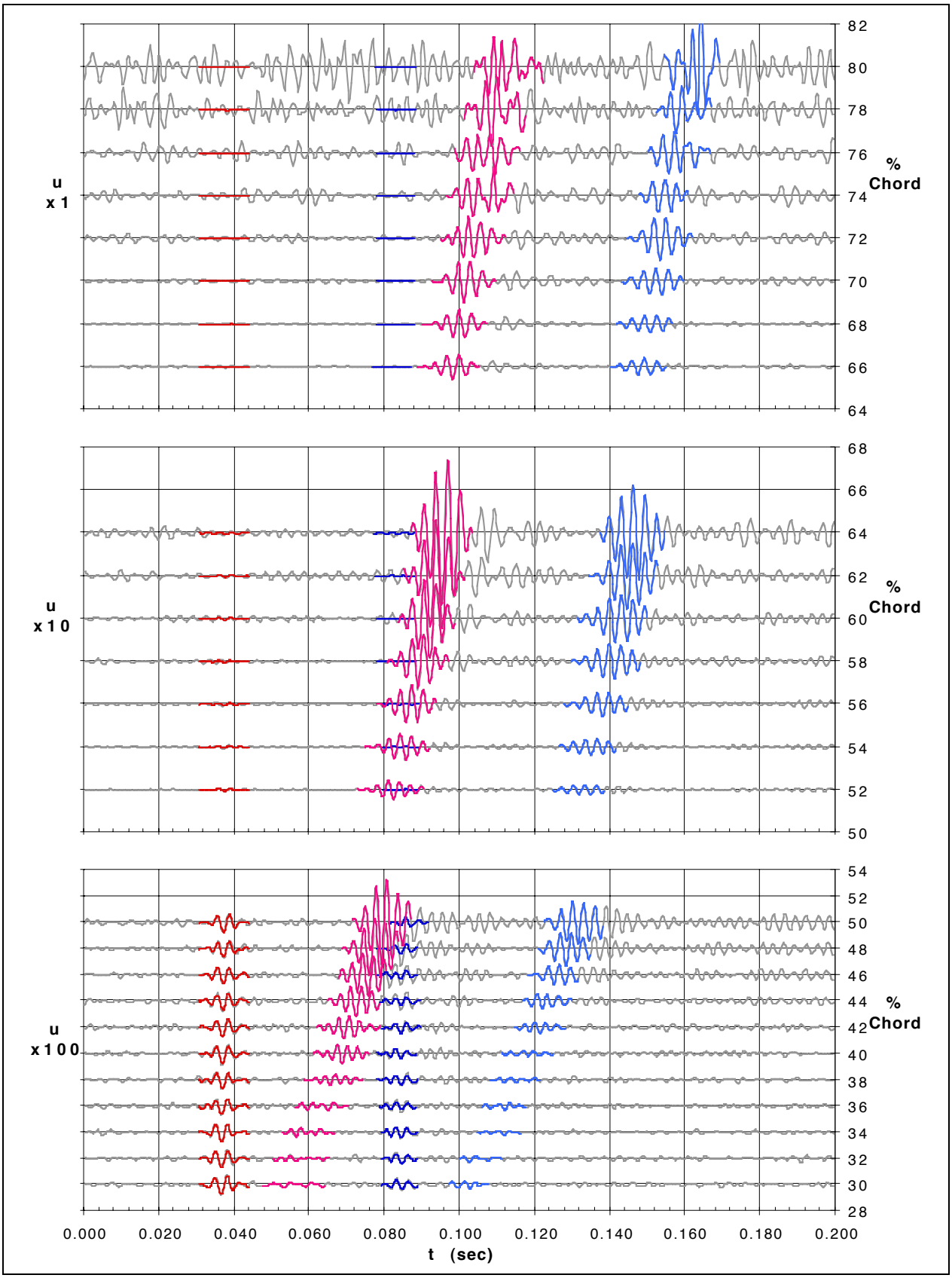

Figure 50: 20 m/s Time Trace - Test 06 Run 2.06

Convection wave speeds were computed from the time trace results examined above and for select cases for each surface roughness condition. They are presented in **Figures 51 and 52** for the 20 m/s and 15 m/s flow cases, respectively. A single data set for each surface roughness condition is examined, and the consistency of experimental results is very good.

The wave speed results from both flow velocity cases indicate that the downstream and upstream responses are convected at approximately 33 - 39% local free-stream velocity. T-S wave speeds are typically 36 - 39% of the free-stream velocity. For the 20 m/s flow case, theoretical results from linear stability theory (SALLY Code) and from linear parabolized stability equations (LPSE, ECLIPSE code) are presented, both of which compare well to each other. Differences between these two solutions at the upstream chordwise stations are likely due to the LPSE solution accounting for non-parallel flow effects and surface curvature, for which the LPSE solution compares better. For the 15 m/s flow case, only SALLY results are presented. Both stability codes used the mean flow-field solution from MSES, using the integral boundary layer with transition defined at 80% chord. The wave speed was computed from the wavelength / wavenumber and frequency. It should be noted again that the SALLY code assumes two-dimensional, incompressible parallel flow, but both the SALLY and LPSE results are based upon a mean flow field determined with an integral boundary-layer solution and transition assumed to occur at 80% chord.

The nature of a developing T-S wave involves an increase of the wavelength while the frequency being tracked is held constant, thus the T-S wavelength increases along the chord of the model, and the wave speed consequently increases as well. The experimental results track the theoretical (SALLY) results quite well, although the experimental results are generally somewhat greater than the theoretical predictions, but well within the range of a typical T-S wave speed.

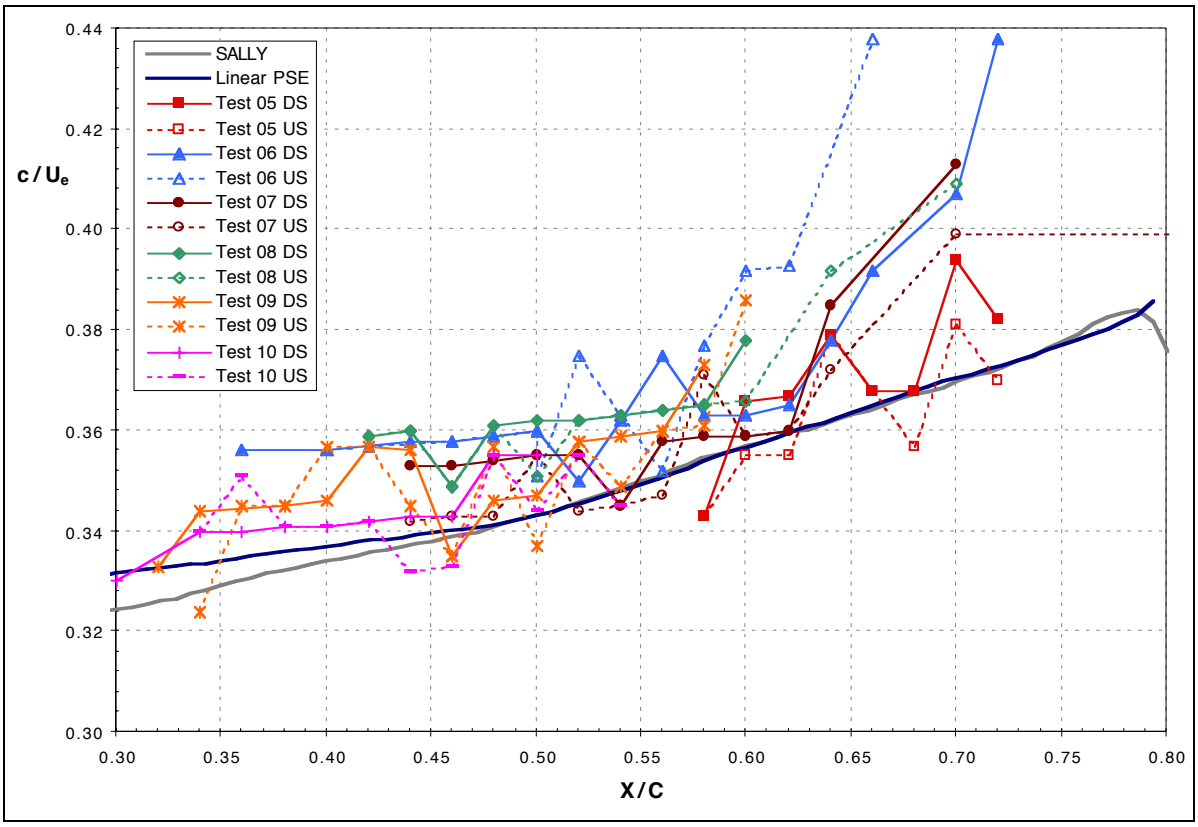

Figure 51: 20 m/s Boundary-Layer Response Convection Wave Speeds

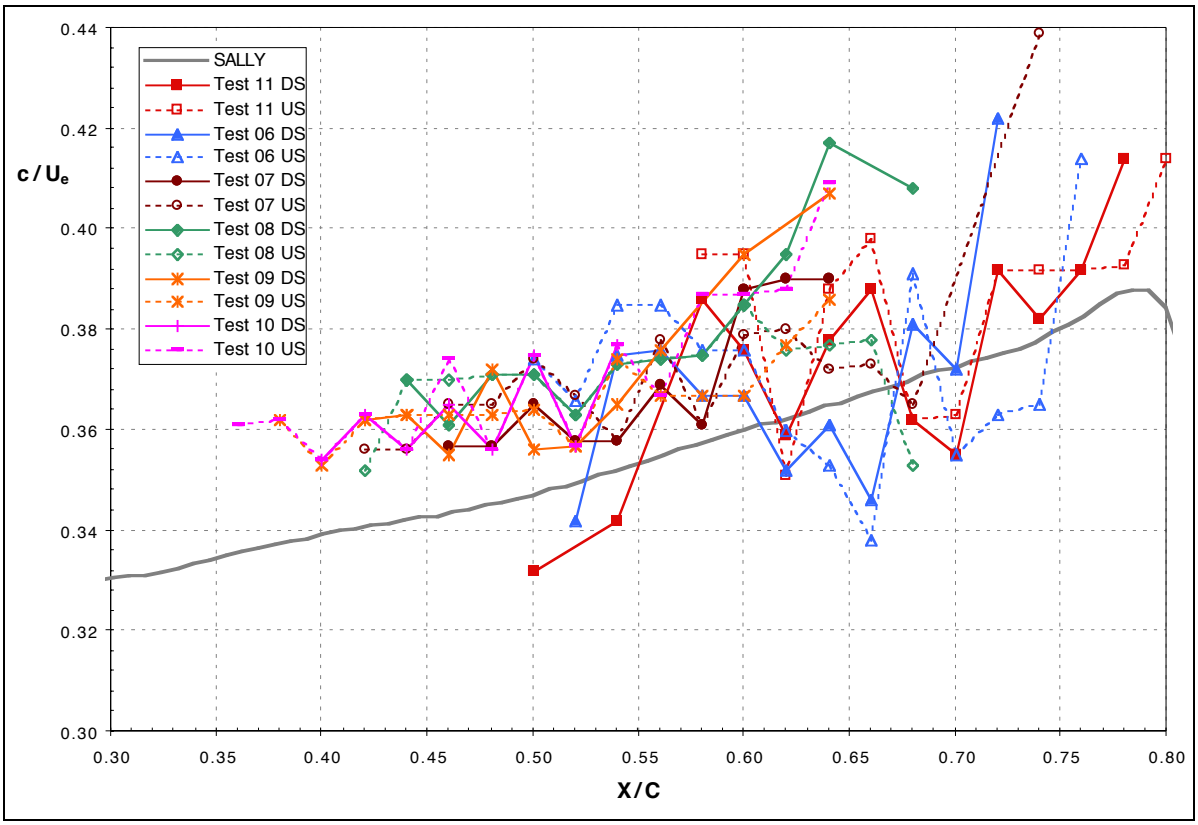

Figure 52: 15 m/s Boundary-Layer Response Convection Wave Speeds

5.2.4.2 Non-Dimensional Single-Frequency Amplitude Growth

Figures 53 and 55 display the 300 Hz and 200 Hz boundary-layer disturbance amplitude growth for the 20 m/s and 15 m/s test cases, respectively. Each figure is divided into 6 subplots, separately displaying the results at all roughness levels for the boundary-layer response from the downstream traveling source. **Figures 54 and 56** are corresponding plots of the response to the upstream traveling source at 20 m/s and 15 m/s, respectively. The amplitudes are normalized by the acoustic source strength as measured in the free-stream above the boundary layer and presented in the form $\ln\left(u_{TS}/u_s\right)$.

All of the data sets indicate that the chordwise amplitude growth curves contain comparable slopes for all of the roughness configurations and acoustic forcing levels. The slopes for the 20 m/s flow case do not match the slopes of the 15 m/s flow case, as expected because of differences in the boundary layer length scales. With the resulting data collapsing along the same curve, it can be deduced that the receptivity mechanism is the same, but scaled by the source signal amplitude. The results from stronger forcing signals "breakdown" or "saturate" at earlier chordwise stations than the results from relatively weaker forcing signals. Another perspective of this result would be that weaker sources result in breakdown at larger relative amplitudes to the forcing signal amplitude. This indicates that a weaker forcing function will result in a stable boundary layer for a longer duration. A factor of 4 in the source amplitude can shift the breakdown location by 5 - 10% chord. It can also be noted that the signals were not reliably measured when the boundary-layer response was several orders of magnitude smaller than the source signal, as it was buried in the noise. Recall that the growth rate amplitudes *are not* referenced to the amplitude at Branch I because that value was not measurable.

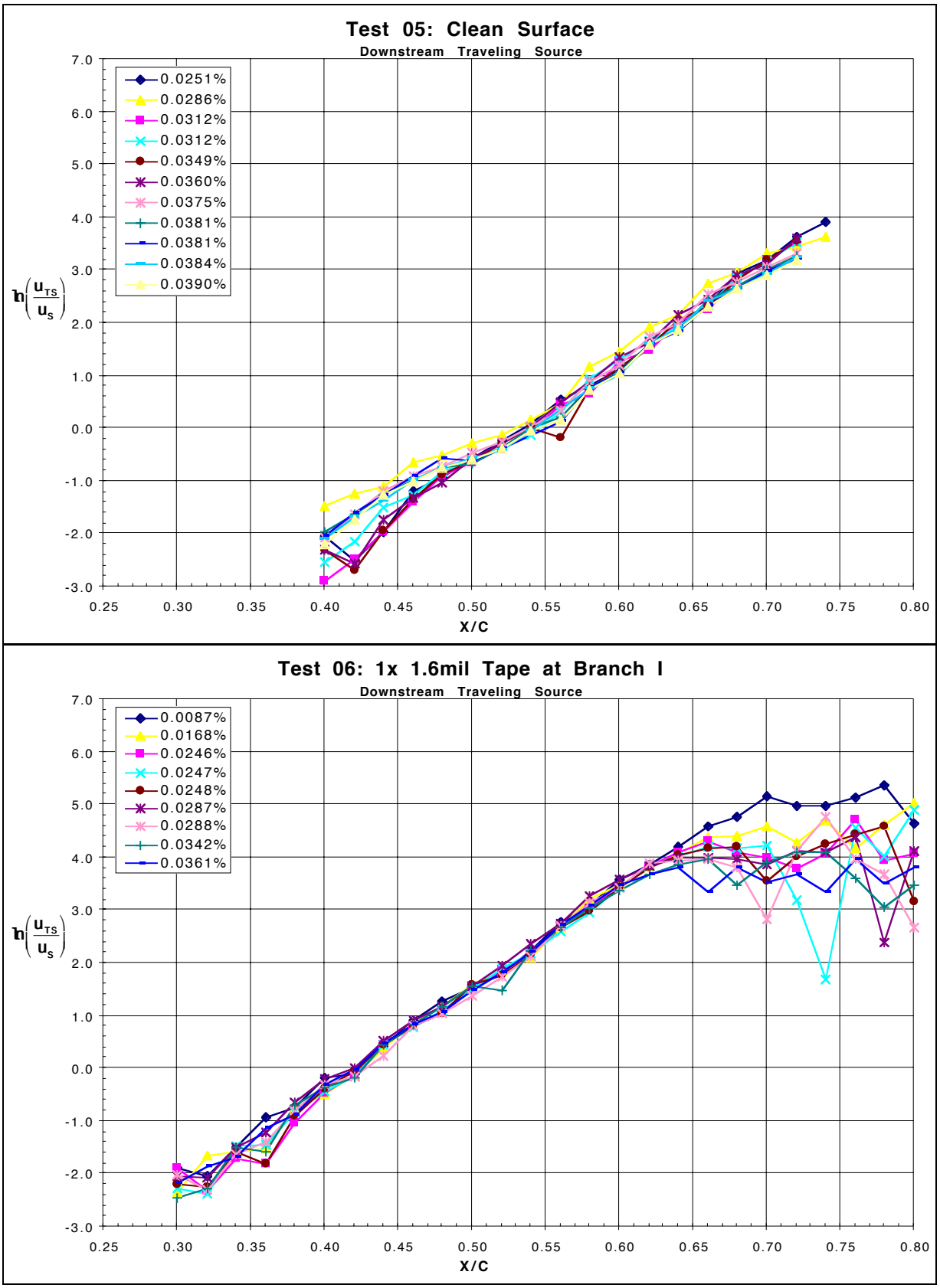

Figure 53: 20 m/s Chordwise Amplitude Growth w.r.t. Downstream Traveling Source

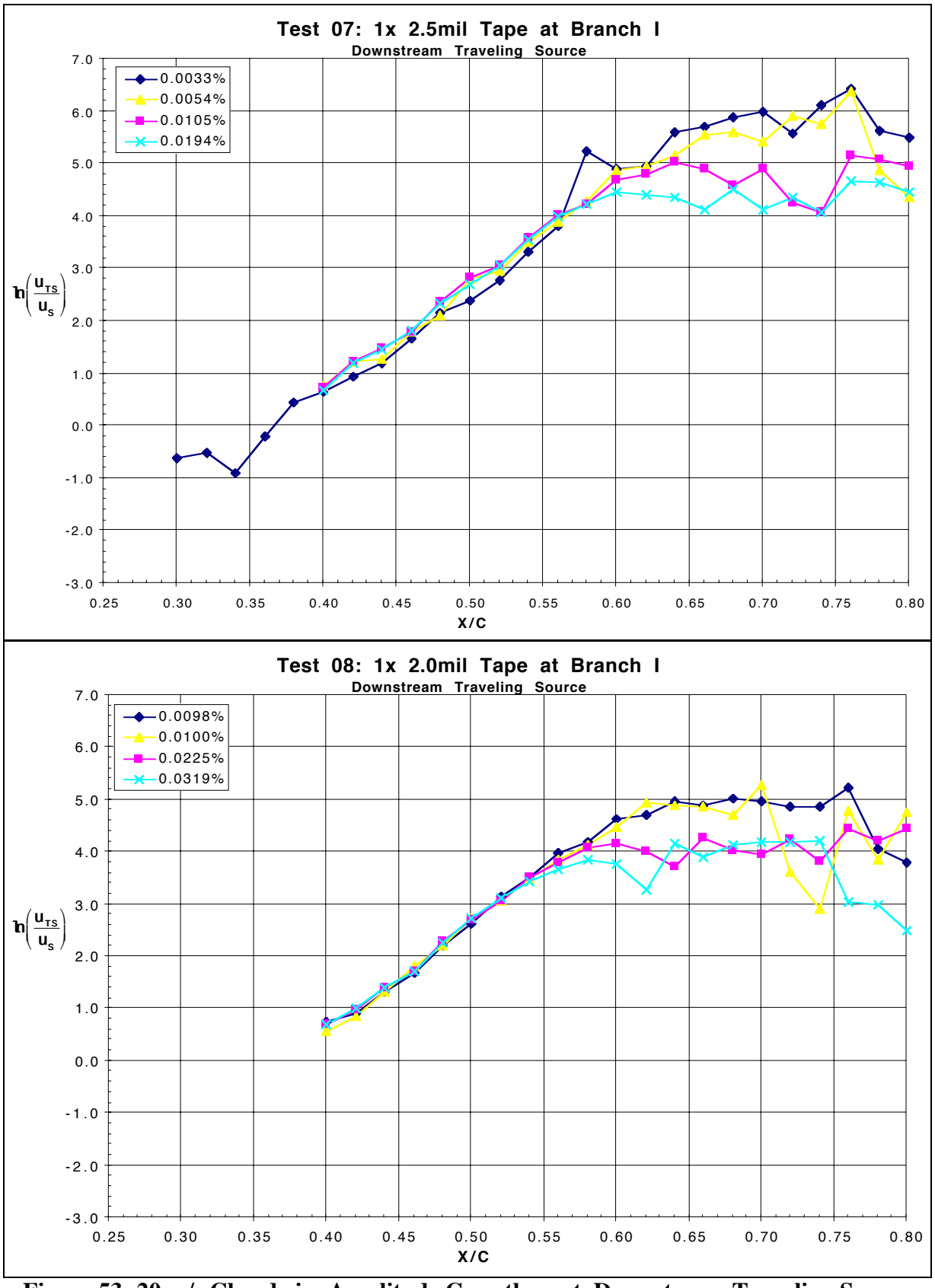

Figure 53: 20 m/s Chordwise Amplitude Growth w.r.t. Downstream Traveling Source

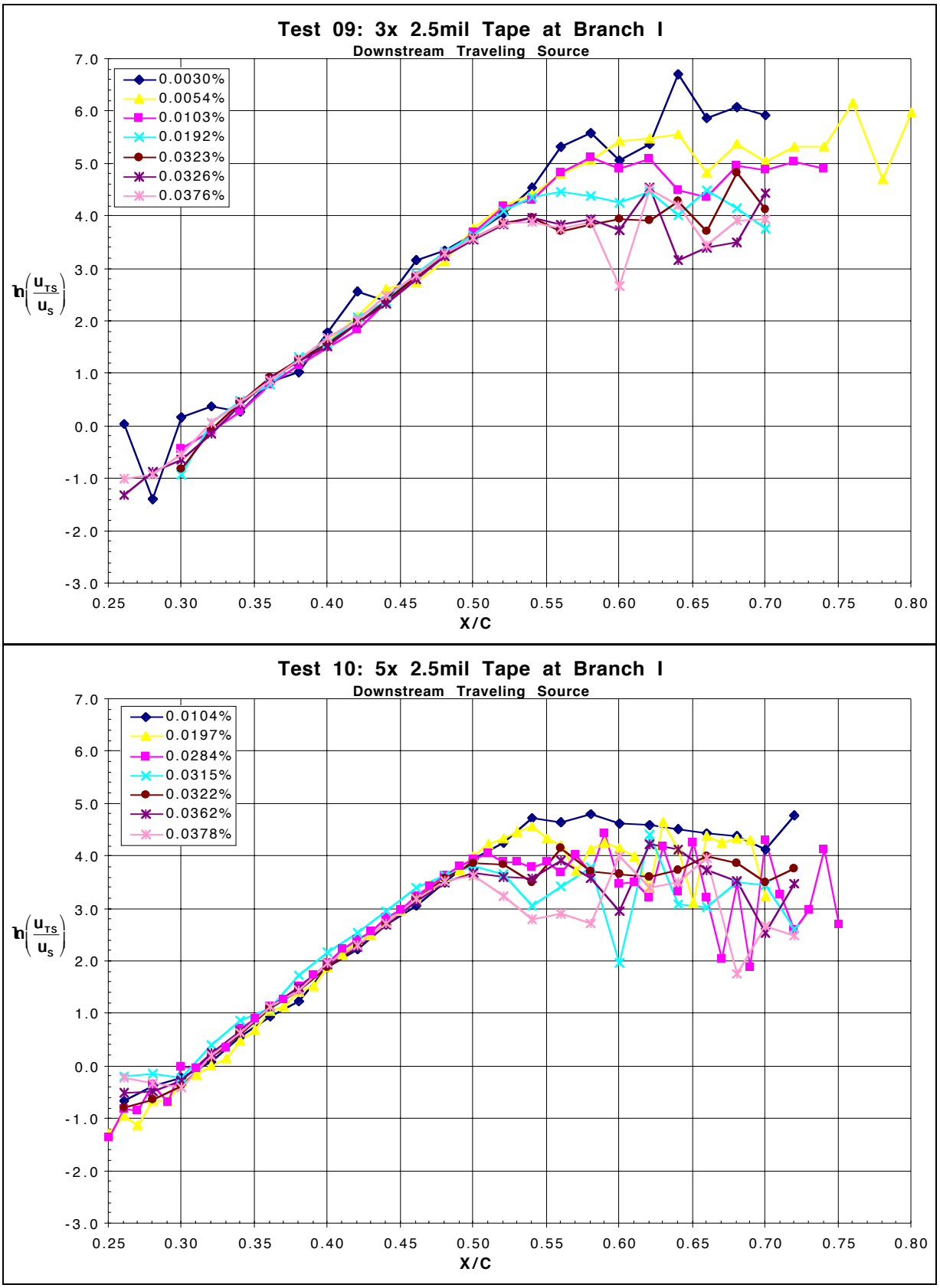

Figure 53: 20 m/s Chordwise Amplitude Growth w.r.t. Downstream Traveling Source

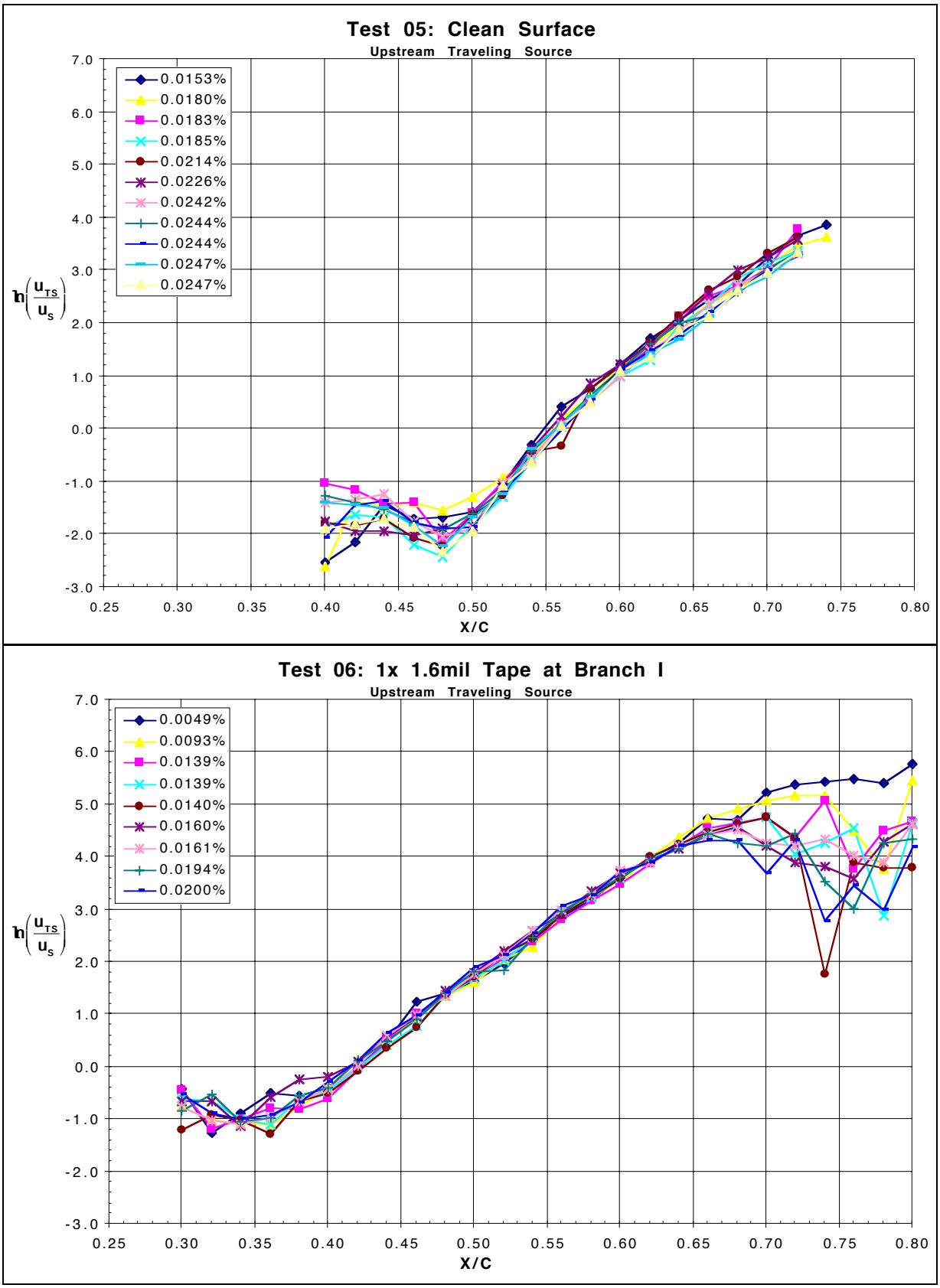

Figure 54: 20 m/s Chordwise Amplitude Growth w.r.t. Upstream Traveling Source

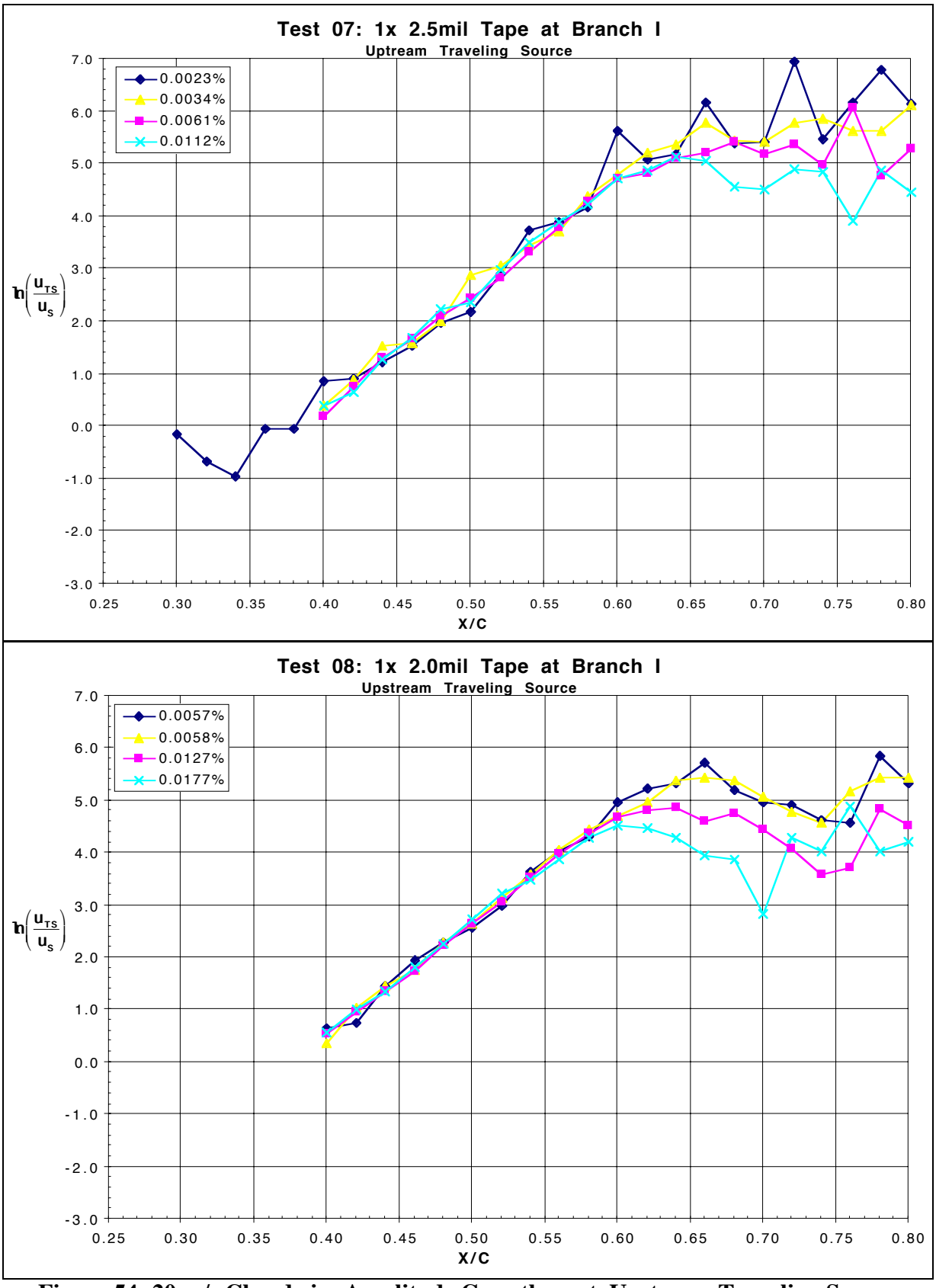

Figure 54: 20 m/s Chordwise Amplitude Growth w.r.t. Upstream Traveling Source

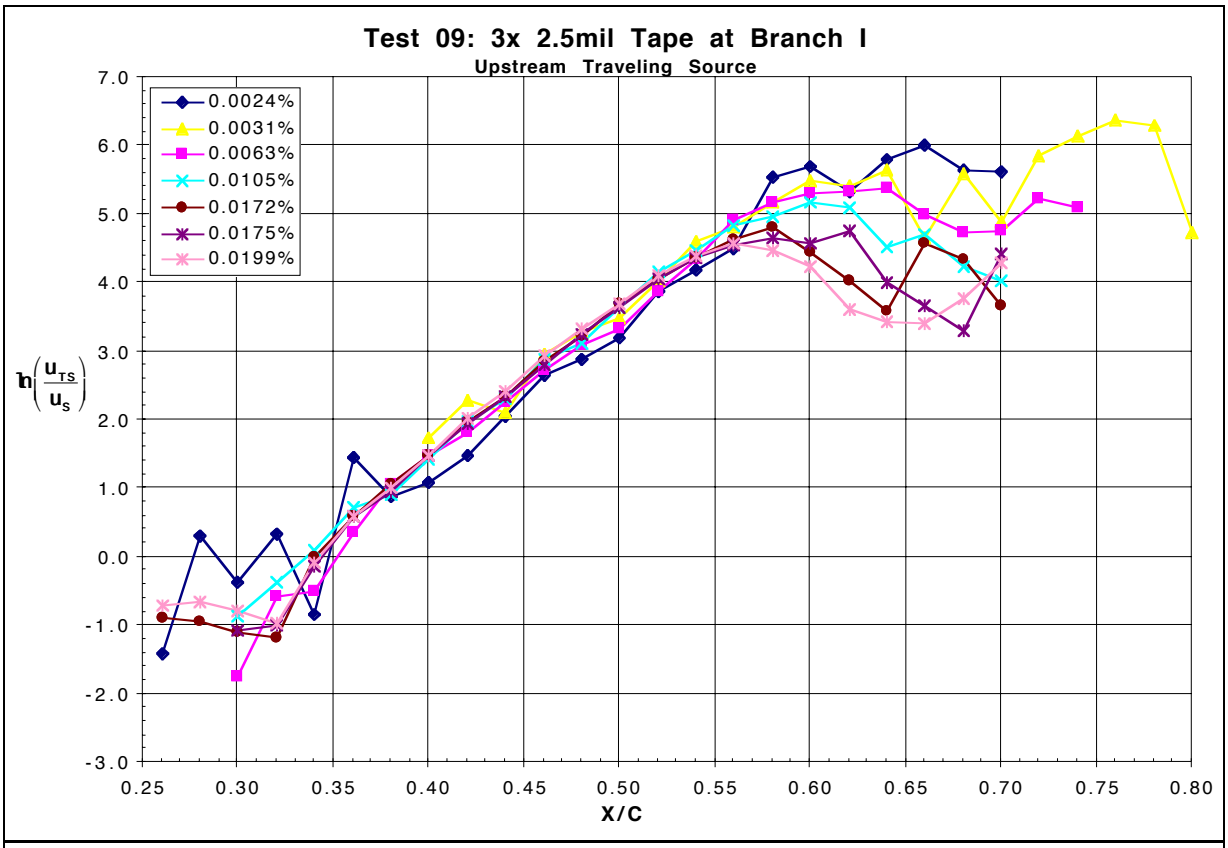

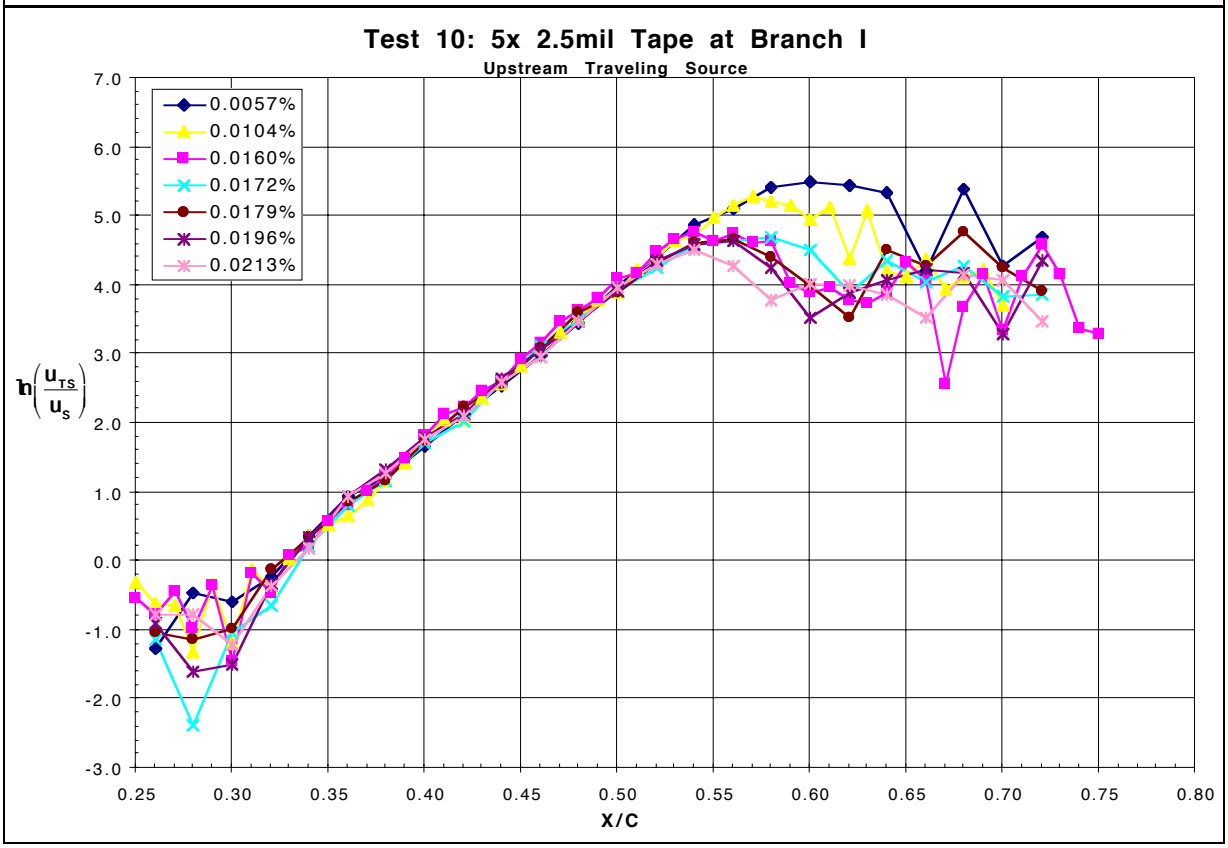

Figure 54: 20 m/s Chordwise Amplitude Growth w.r.t. Upstream Traveling Source

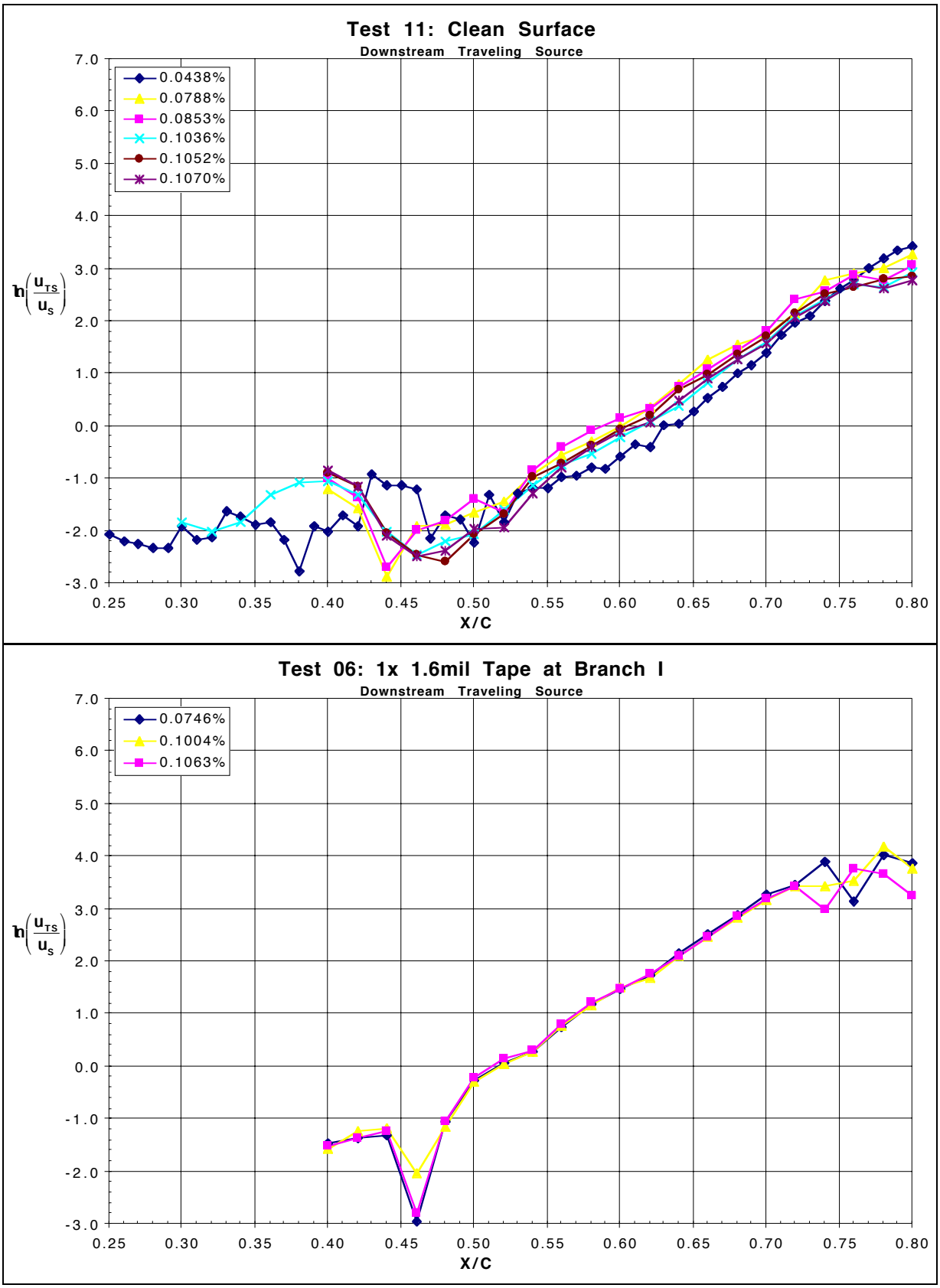

Figure 55: 15 m/s Chordwise Amplitude Growth w.r.t. Downstream Traveling Source

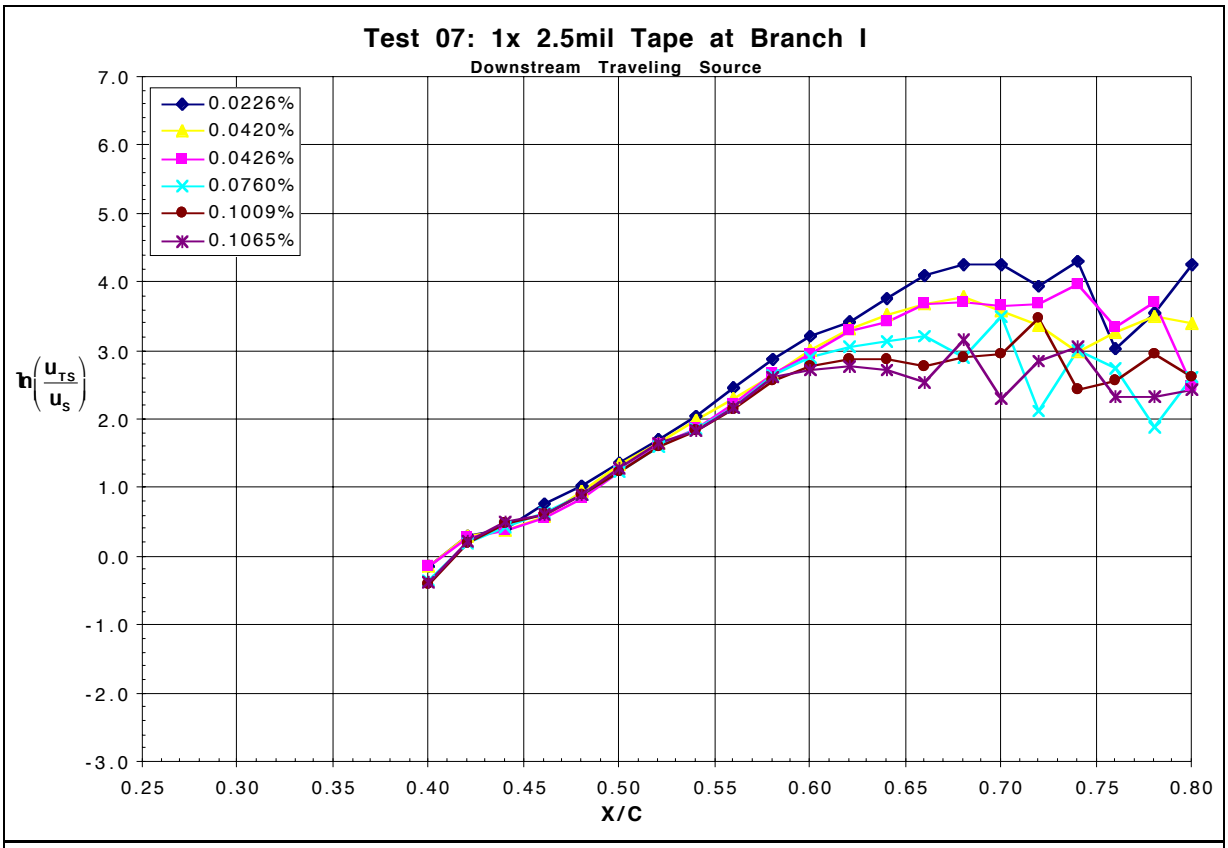

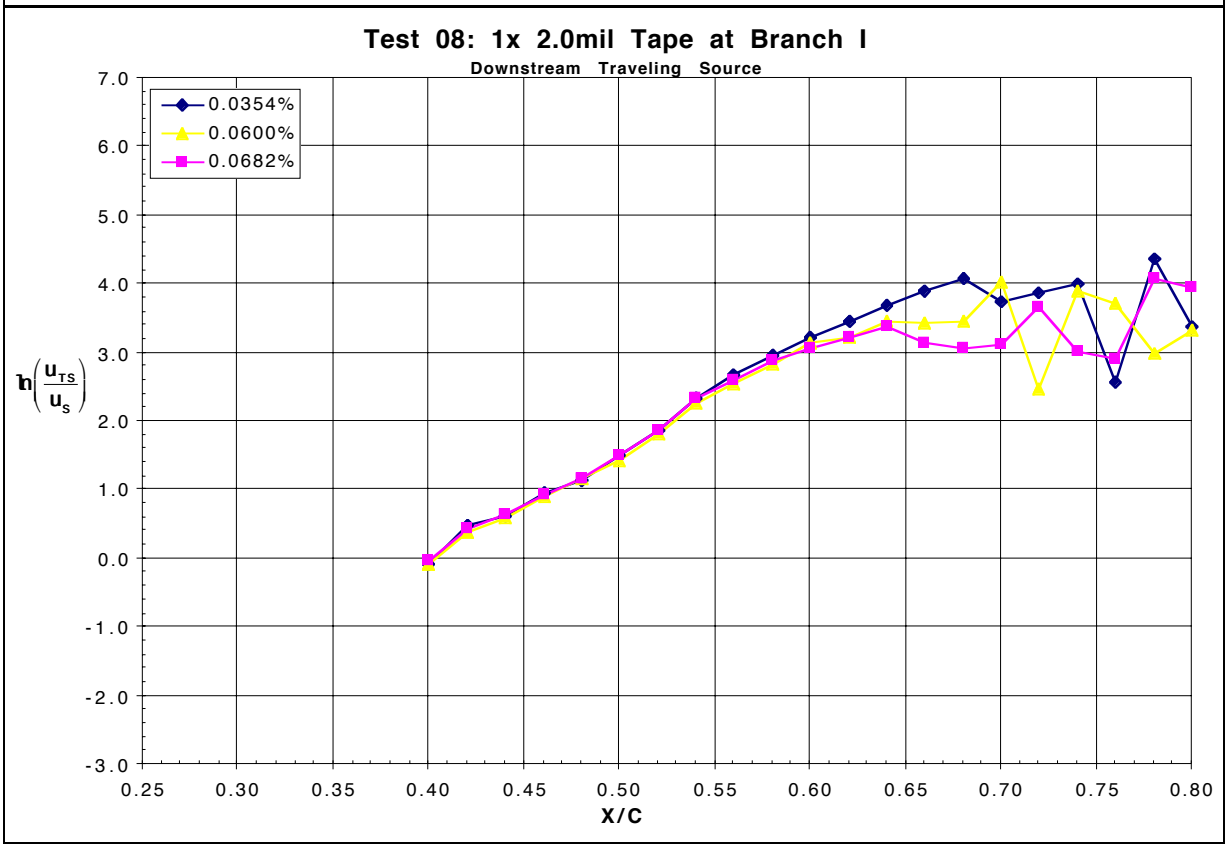

Figure 55: 15 m/s Chordwise Amplitude Growth w.r.t. Downstream Traveling Source

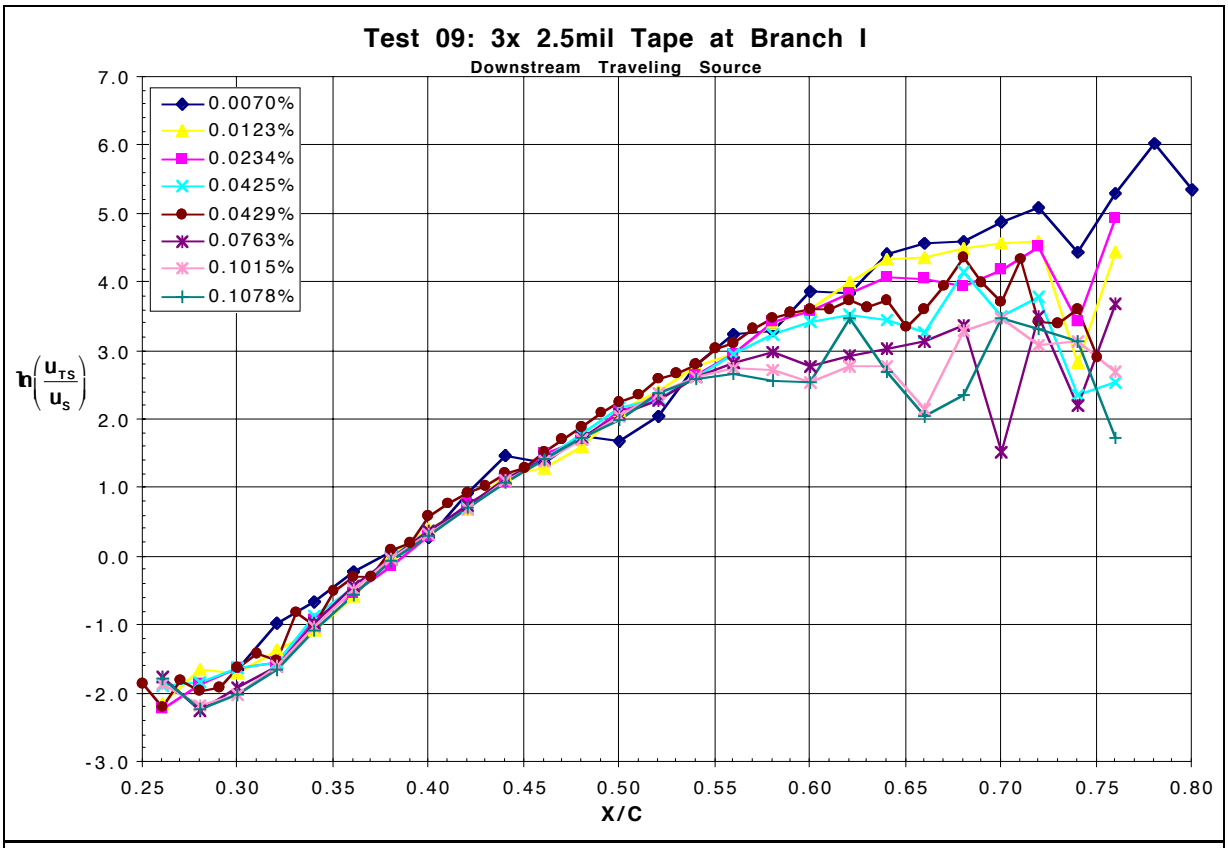

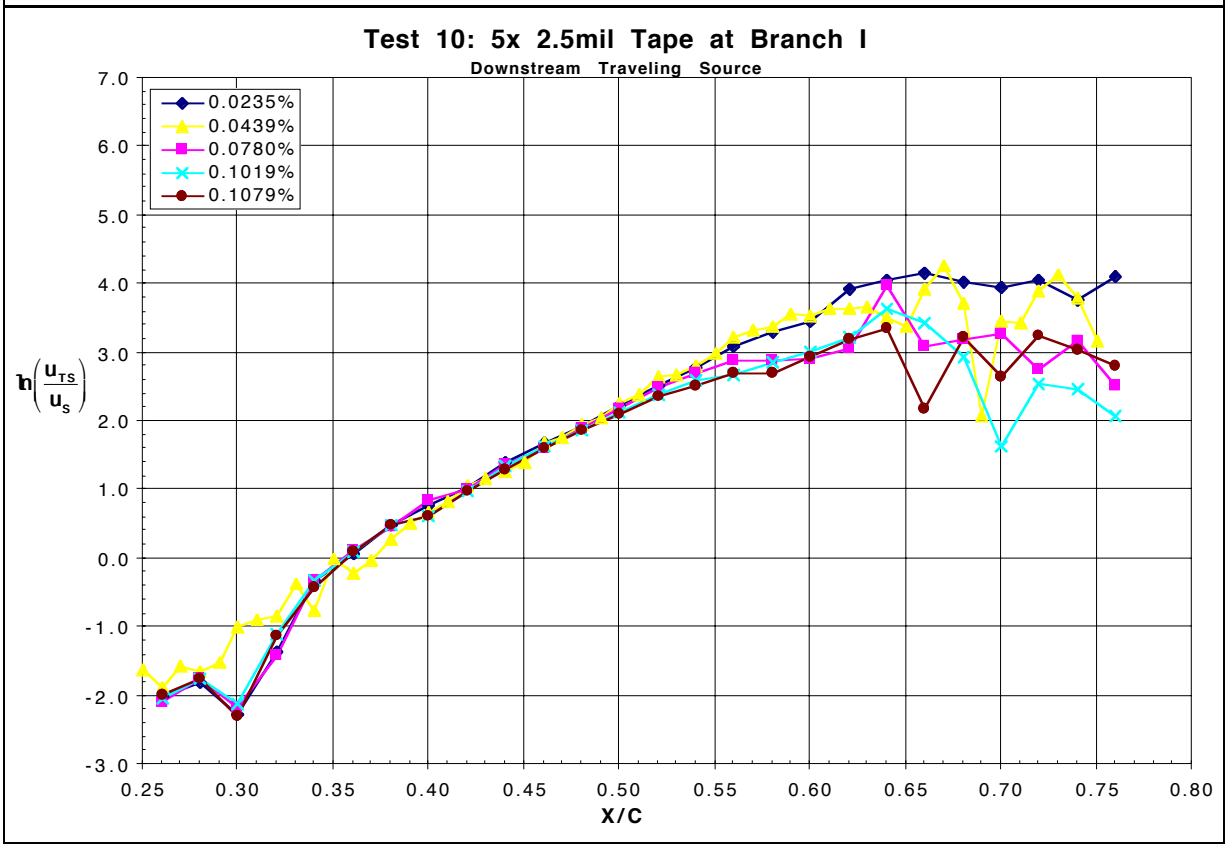

Figure 55: 15 m/s Chordwise Amplitude Growth w.r.t. Downstream Traveling Source

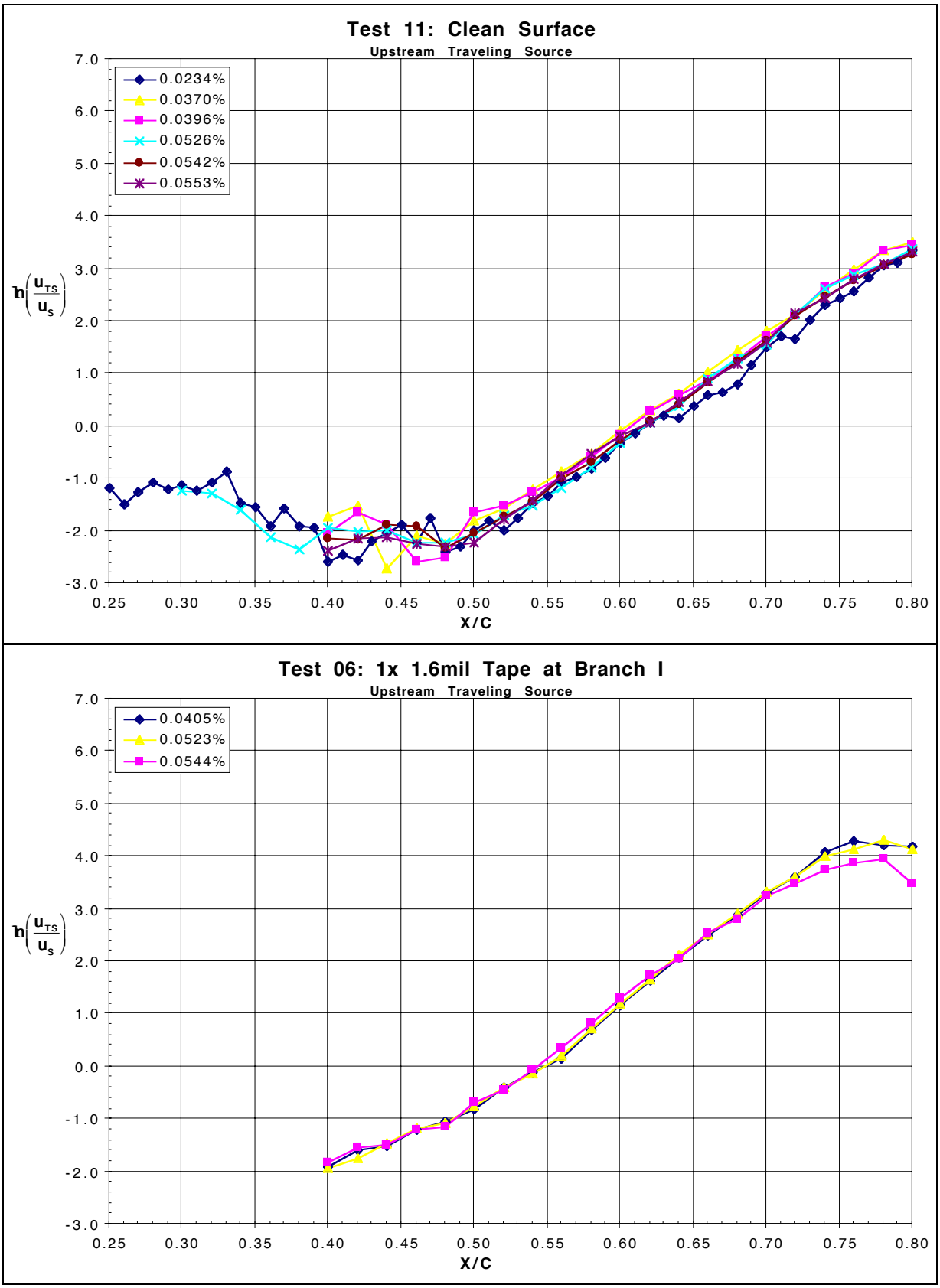

Figure 56: 15 m/s Chordwise Amplitude Growth w.r.t. Upstream Traveling Source

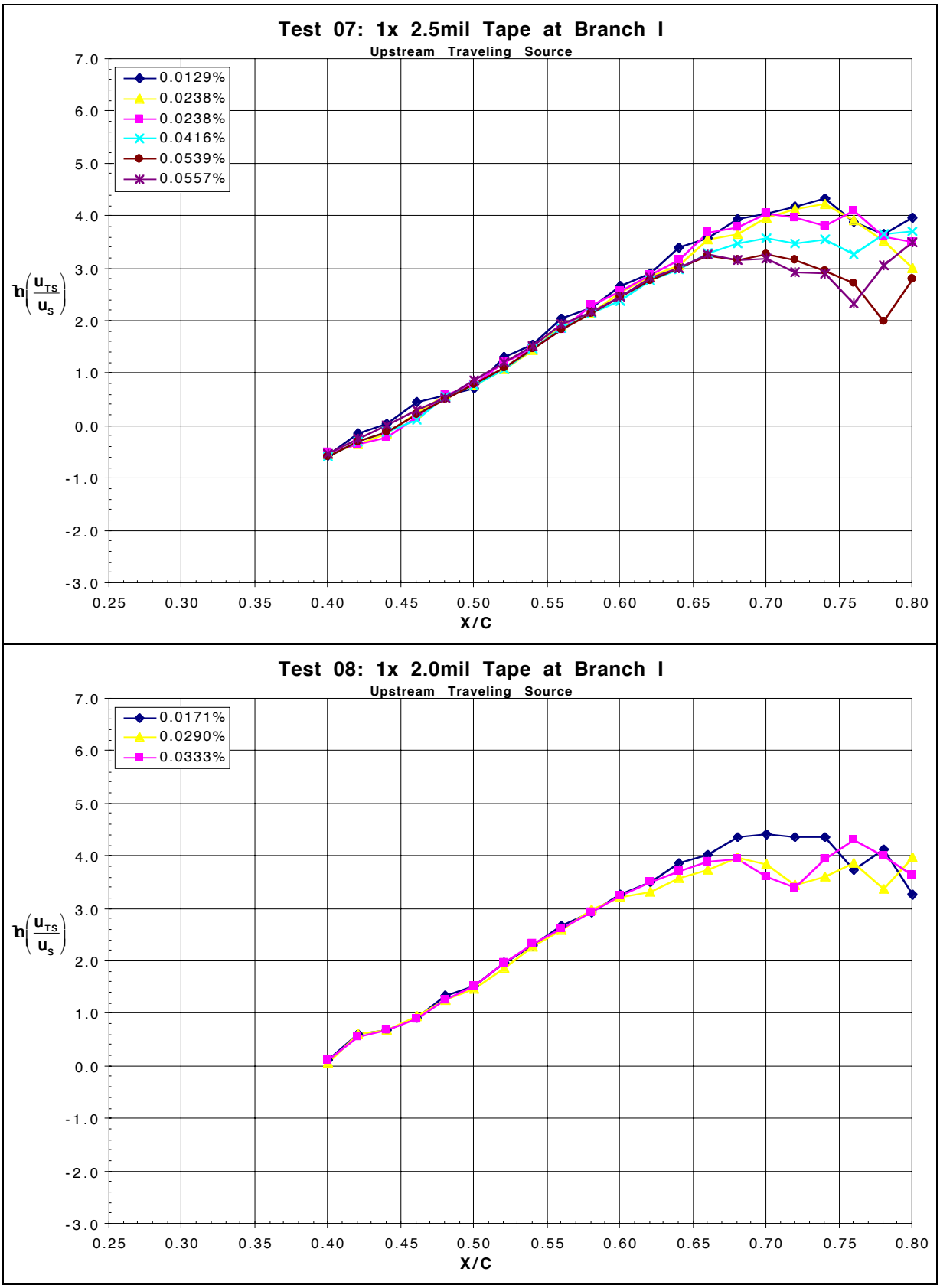

Figure 56: 15 m/s Chordwise Amplitude Growth w.r.t. Upstream Traveling Source

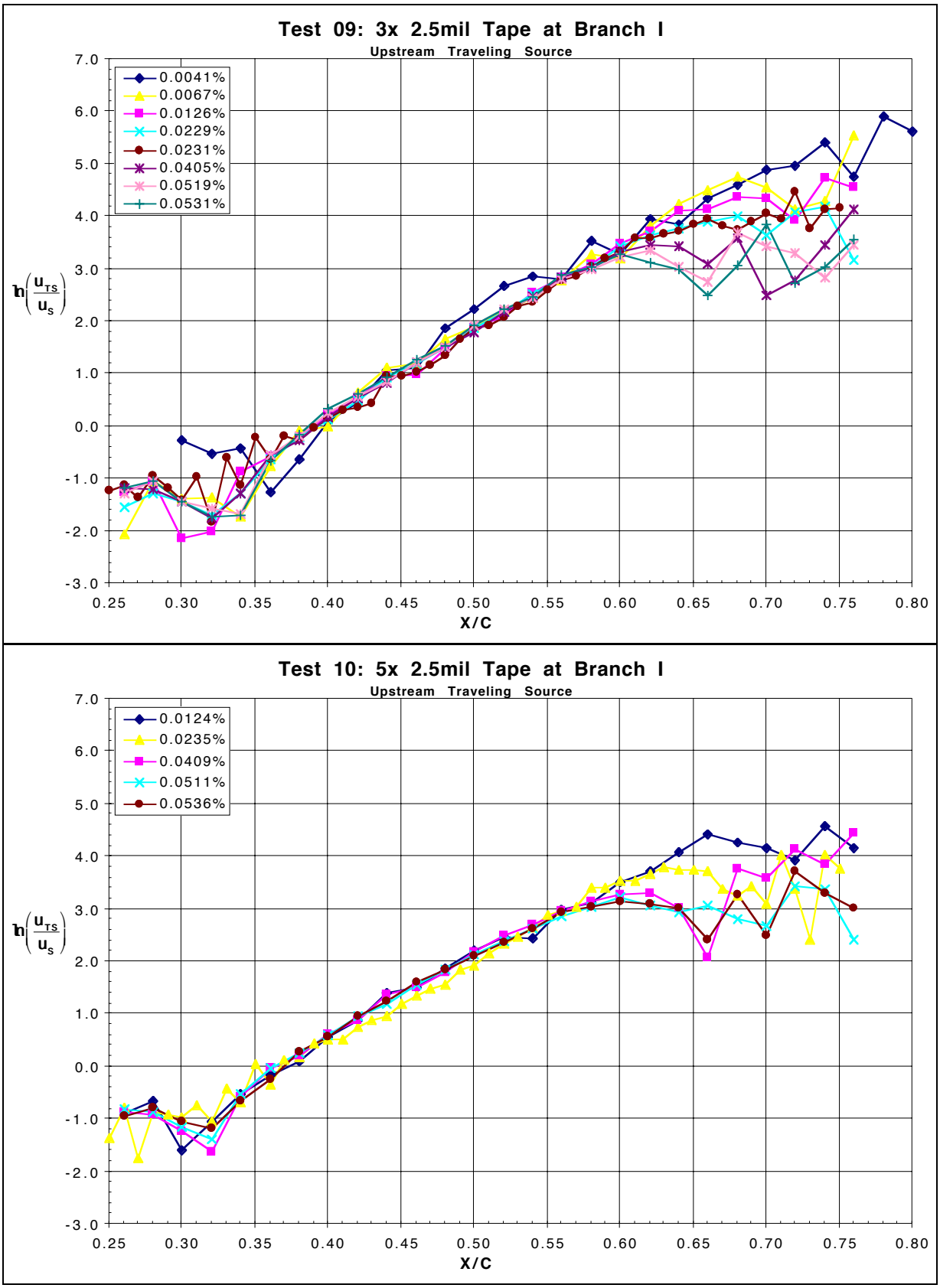

Figure 56: 15 m/s Chordwise Amplitude Growth w.r.t. Upstream Traveling Source

Figures 57 and 58 present the non-dimensional single-frequency disturbance amplitude growth for the various surface roughness conditions examined at the 20 m/s, 300 Hz, and 15 m/s, 200 Hz conditions, respectively. All of the plots within these figures are for boundary-layer responses that resulted from comparable strength forcing levels. Each subplot is for a different nominal forcing level. It can be seen that the amplitude growth plots for each roughness case are parallel, indicating the consistency of the growth along the surface after receptivity. Increased roughness, both due to more elements and thicker elements, shifts the breakdown of the disturbance further upstream along the model surface. With the amplitude normalization used, it appears that the disturbance breaks down at a consistent amplitude ratio independent of the receptivity condition, just as linear stability theory predicts. It further appears that the increased surface roughness results in larger disturbance amplitudes at upstream stations as a result of increased receptivity. It should be noted that for the weak forcing case, no data was available for comparison, however other results for the surface condition and slightly stronger forcing indicated that the flow just starts to get non-linear at the end of the measurement domain, when break-down is expected. The effect of the roughness on the transition location of the boundary layer is significant, shifting the laminar-breakdown over 20% chord upstream as the surface was changed from a “clean”, no roughness condition to five repeated elements spaced one disturbance wavelength apart, for both speed cases. This indicates that even in an environment with strong free-stream perturbations, a clean surface condition can lead to extended regions of laminar flow, as expected.

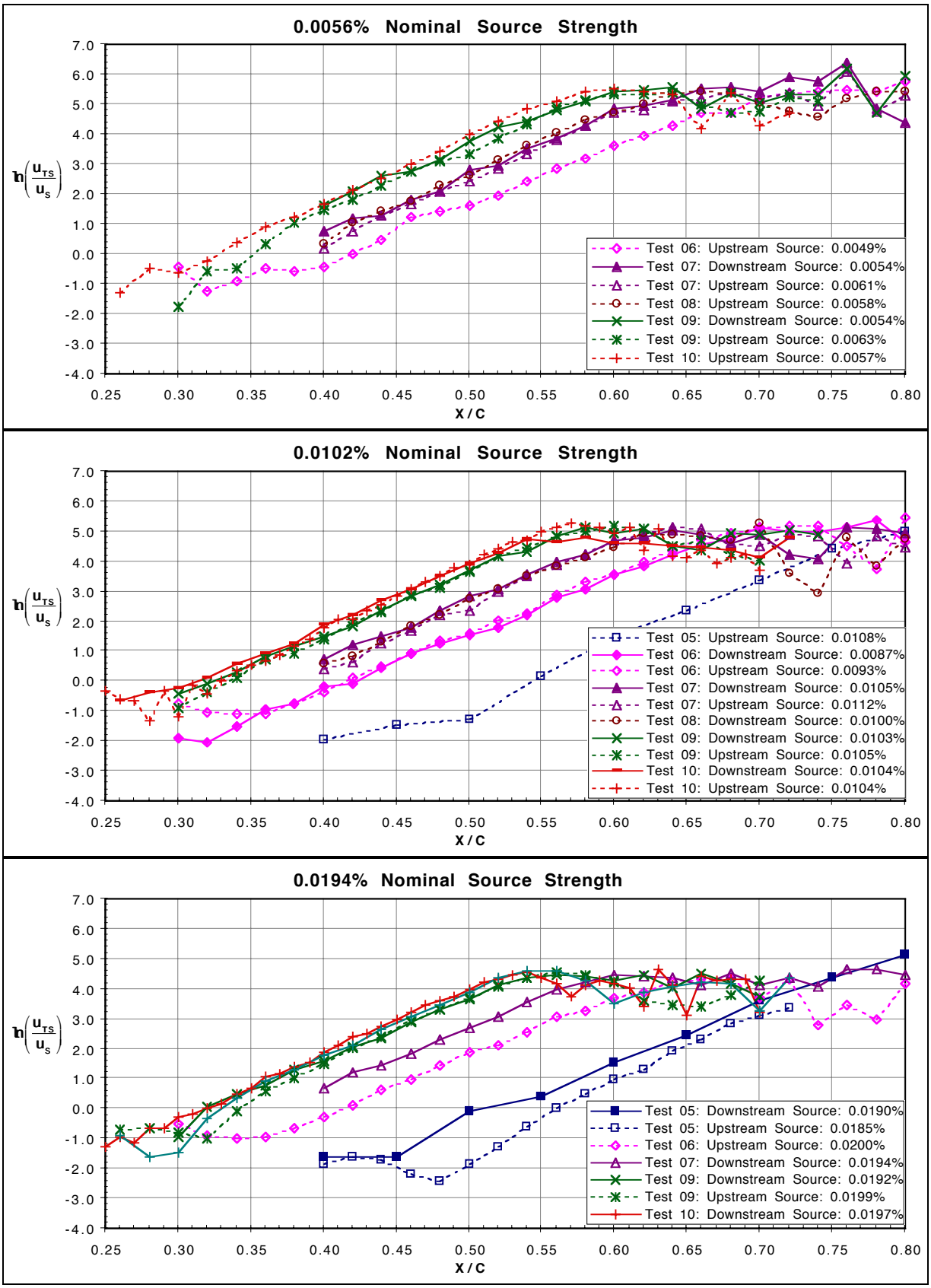

Figure 57: 20 m/s Chordwise Amplitude Growth – Constant Forcing Level

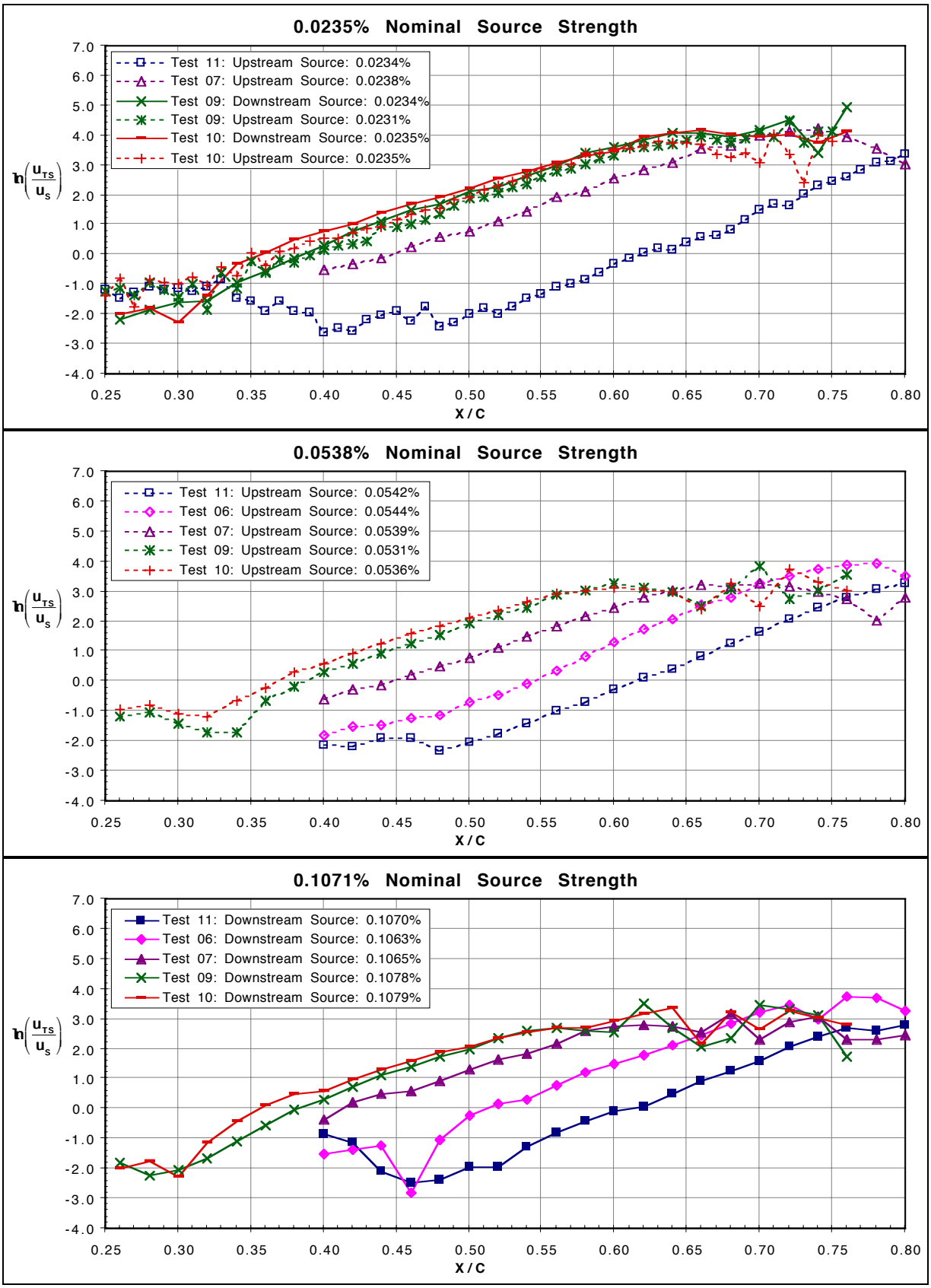

Figure 58: 15 m/s Chordwise Amplitude Growth - Constant Forcing Level

5.2.4.3 Receptivity Coefficient

The linear stability theory N-Factor predictions from the SALLY code are presented in **Figures 59 and 60** for the 20 and 15 m/s test cases, respectively. Two sets of computational results are presented, each with a different method to compute the flow field properties around the model. The MSES set are results that followed the use of an integral boundary-layer solution of the mean flow field with forced transition at 80% chord, whereas the NYU set are the results from solving the potential solution, without accounting for the possible effect of the boundary layer on the flow field around the model. Both sets of data used the same boundary-layer solution from the Cebeci code. It can be seen that the differences between these two methods are limited to a region just upstream of the MSES forced transition location. The results from using the MSES flow solution indicate a more stable boundary layer. For comparison with experimental results, the results that followed the MSES flow field solution will be used.

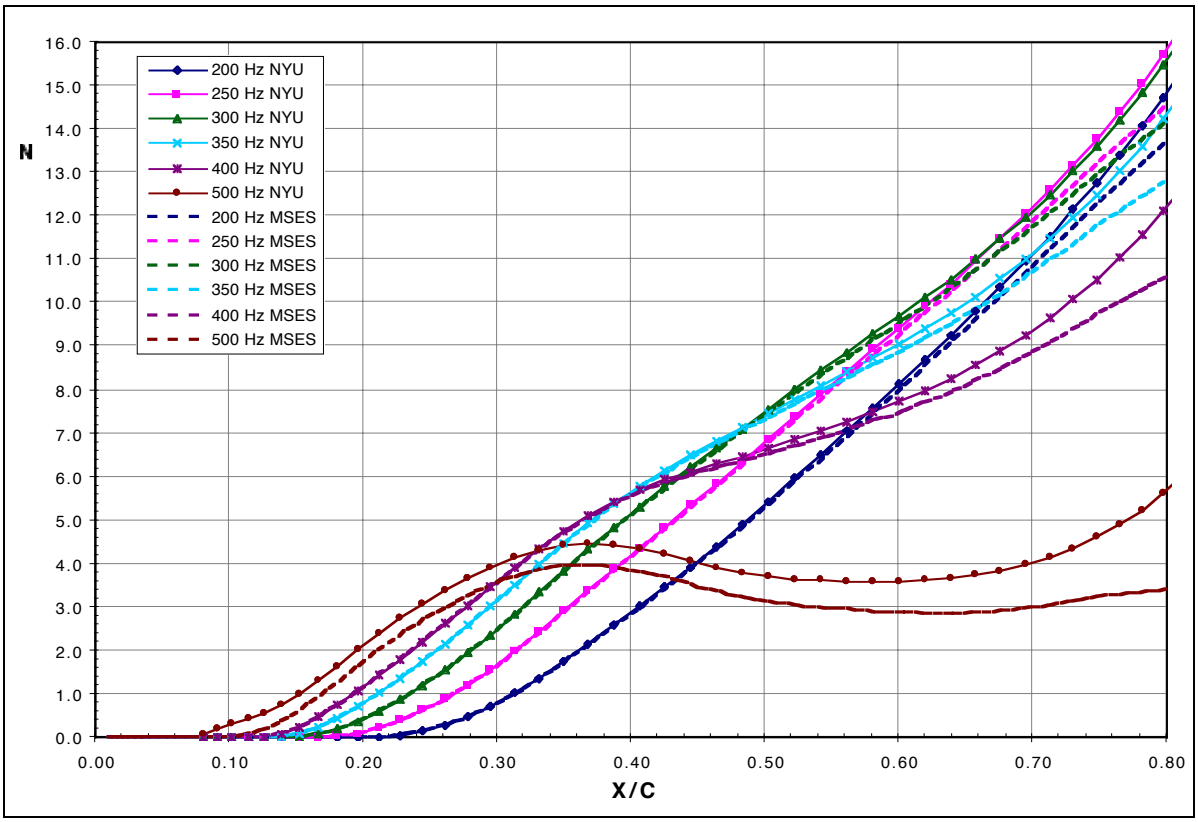

Figure 59: 20 m/s SALLY N-Factor Results

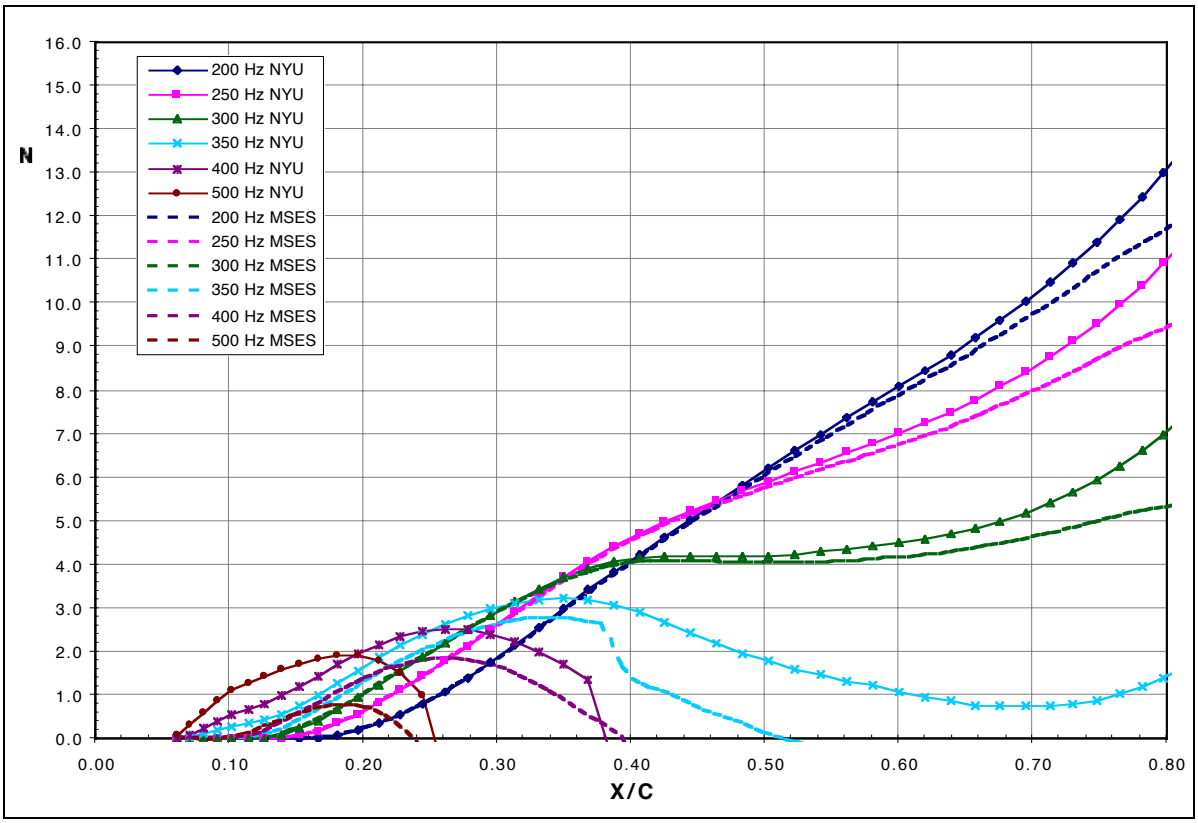

Figure 60: 15 m/s SALLY N-Factor Results

The SALLY theoretical results can be combined with the experimental data for the determination the receptivity coefficient, as defined in the following equation[49, 50]:

$$K_s = \frac{u_{TS,BI}}{u_s} = \left(\frac{u_{TS}\big|_{X/C}}{u_s} \right) e^{-N|_{X/C}} \qquad \textbf{Equation 5-5}$$

This coefficient is a measure of the strength of the receptivity mechanism for a given flow, the strength of the mechanism for which external disturbances are internalized into the boundary layer. In a sense, it can be considered a lumped value of all of the receptivity mechanisms on the surface up to a given chordwise station, which would be equated to a single value, located at Branch I. Using linear stability theory (LST), the amplitude of the boundary-layer response at the lower branch can be estimated, a value that is not easily measured because of its very small amplitude. **Figure 61** depicts the methodology used to combine the experimental results and LST computations to obtain the values of K_s.

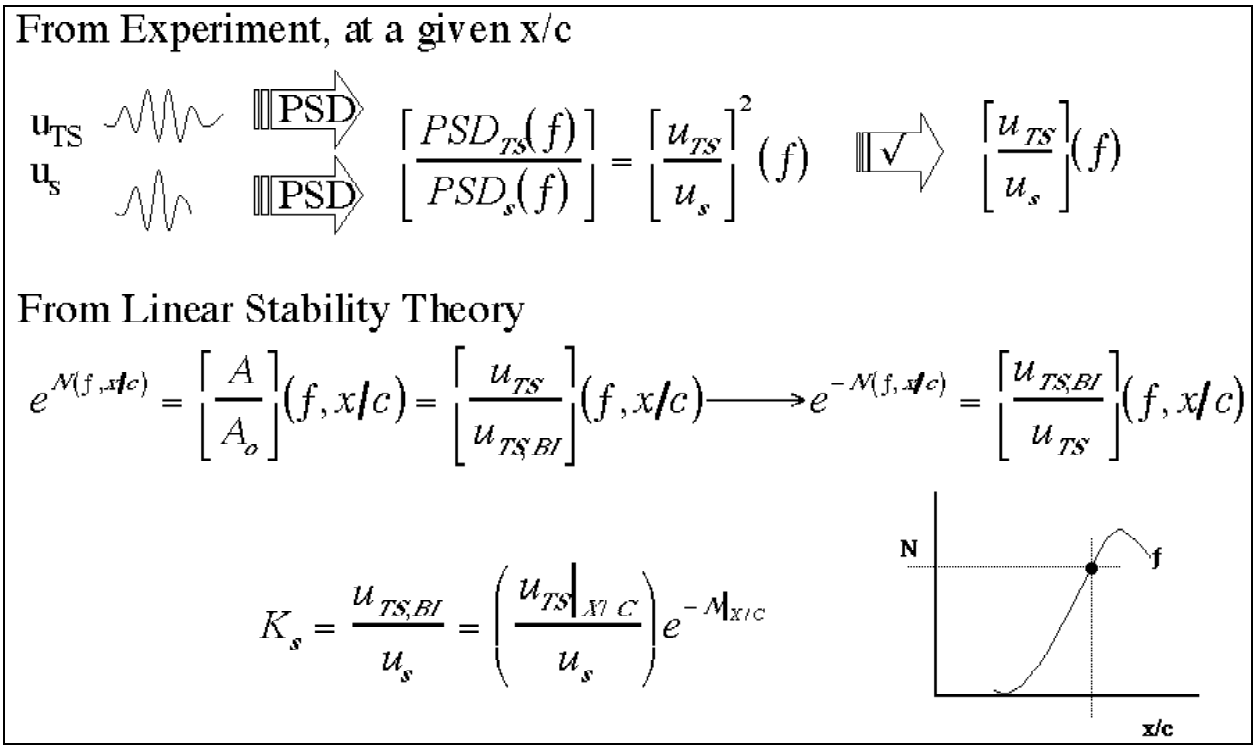

Figure 61: Determining the Receptivity Coefficient

The receptivity coefficient was determined as a function of the chordwise station. **Figure 62** presents the chordwise variation of the receptivity coefficient for each surface roughness configuration at the 20 m/s, 300 Hz case, whereas **Figure 63** presents the corresponding results for the 15 m/s, 200 Hz case. The slope mismatch of the experimental disturbance amplitude curves with the theoretical results is evident in the very small non-zero slope of K_s in the region where linear stability theory is valid. This region is bracketed on each sub-plot. Upstream of this region is where the boundary-layer response was on the same order of magnitude or smaller than the baseline noise level. While linear stability theory (LST) is expected to be valid in this region, no adequate comparison with experimental results was obtained, and thus no evaluation of the disturbance growth in this region can be made. Downstream of the LST region is where non-linear effects become significant. Flow transition is known to affect the boundary-layer conditions just upstream of the transition location, and this is another factor contributing to the mismatch of the growth curve slopes.

The plots indicate that the downstream limit of the LST region is directly associated with the surface roughness condition and/or the receptivity coefficient amplitude. More repeated

roughness elements and greater roughness heights result in the deviation from LST at a further upstream chordwise station. This directly implies that non-linear effects begin to be significant at further upstream stations as well. Greater roughness conditions also result in a larger receptivity coefficient, K_s. Increasing the surface condition from no roughness to five repeated elements increases K_s by an order of magnitude and shifts the extent of LST matching the experimental results by over 25% chord. For each of the plots, the results from a range of acoustic forcing levels is presented, showing the insensitivity of the receptivity coefficient with source amplitude. This was expected due to the definition of K_s, where the value is normalized by the source amplitude.

While the receptivity coefficients for the different flow speed cases appear to be comparable, it should be noted this was not an expected result because the primary frequency for each flow speed case differed, and a variation of K_s with respect to frequency is expected. The variation of K_s with respect to frequency is not presented because of the limited frequency range of data.

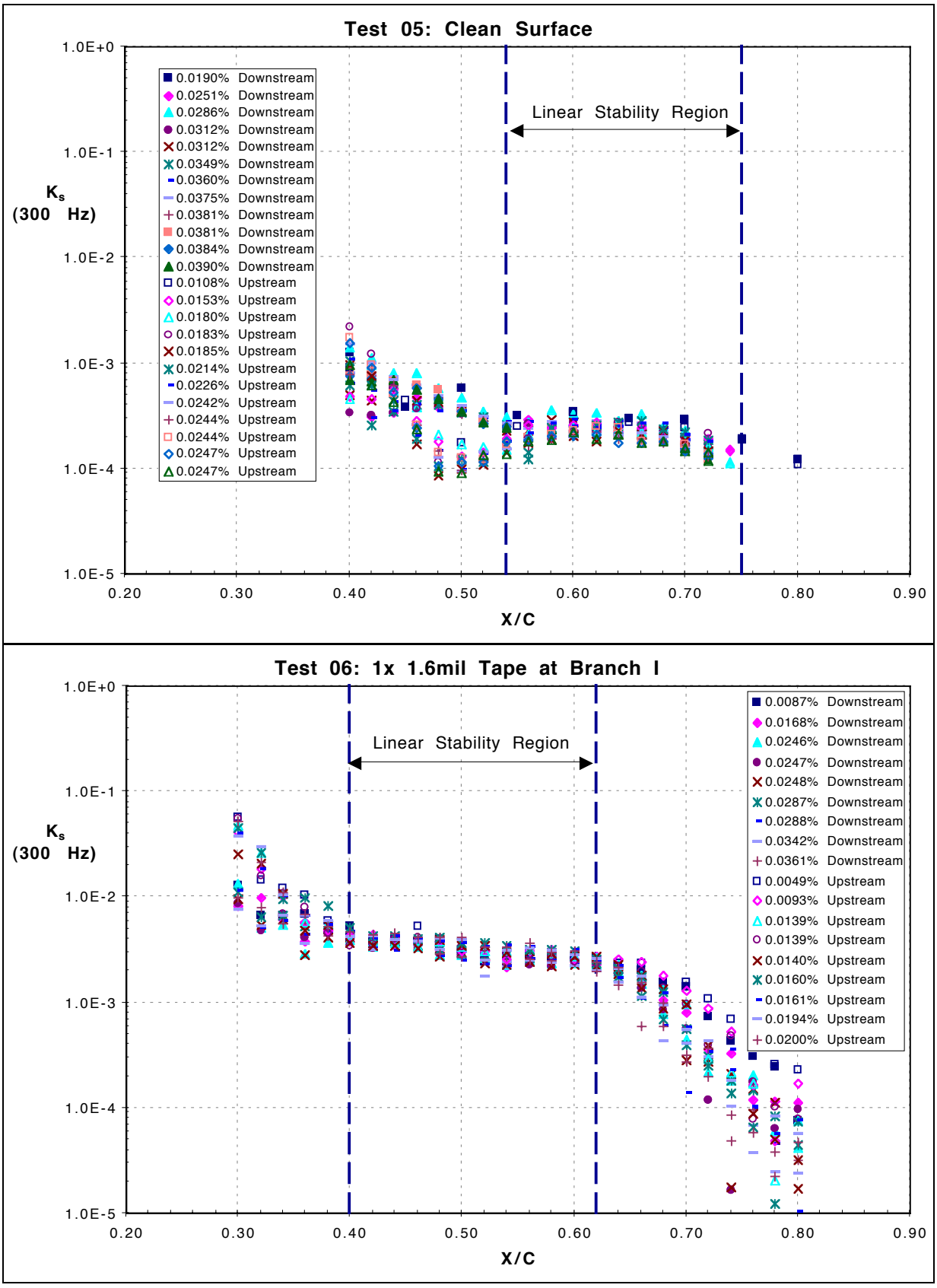

Figure 62: 20 m/s Test Case Receptivity Coefficient, $K_{s,\ 300\ Hz}$

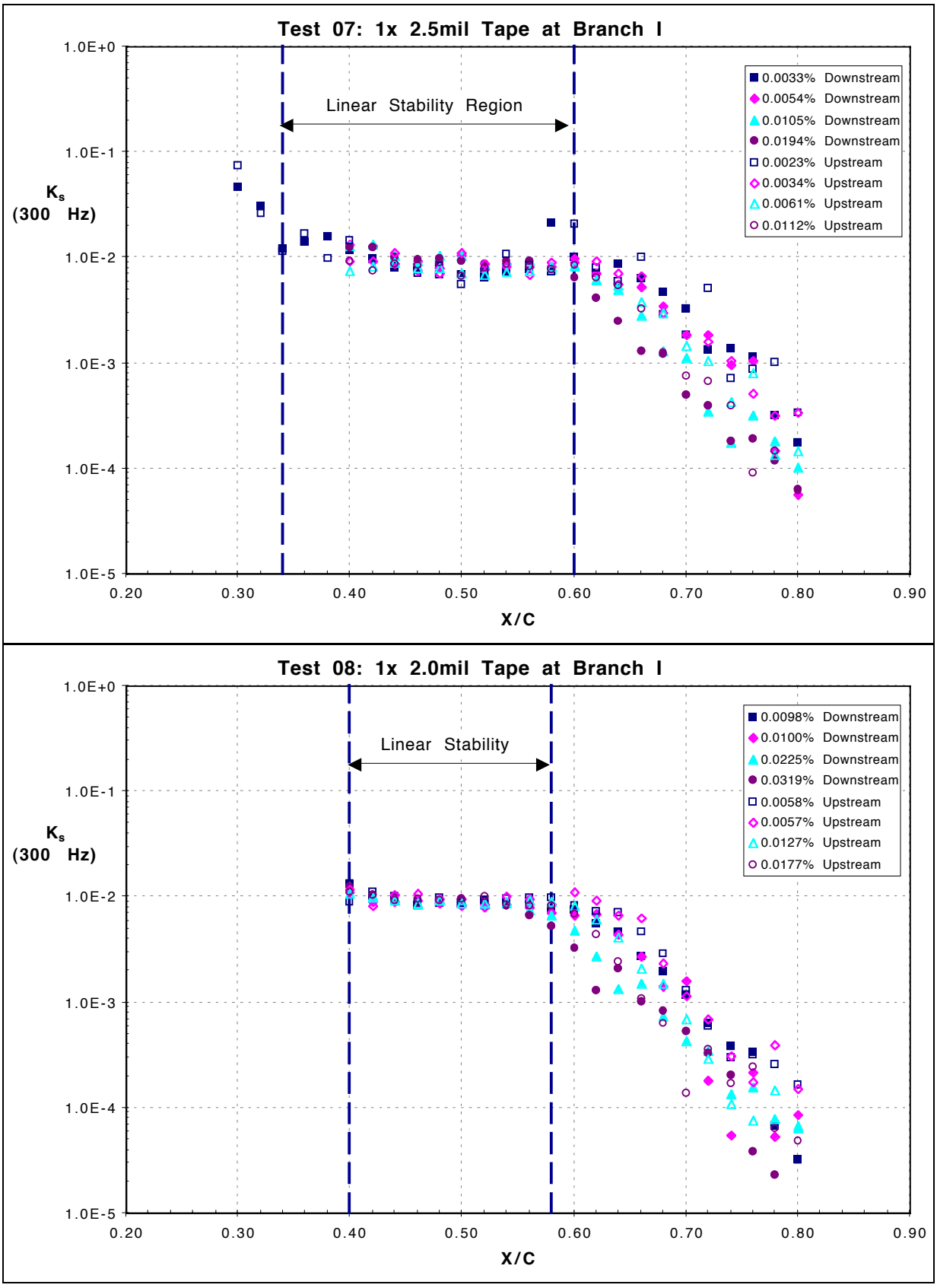

Figure 62: 20 m/s Test Case Receptivity Coefficient, $K_{s,\ 300\ Hz}$

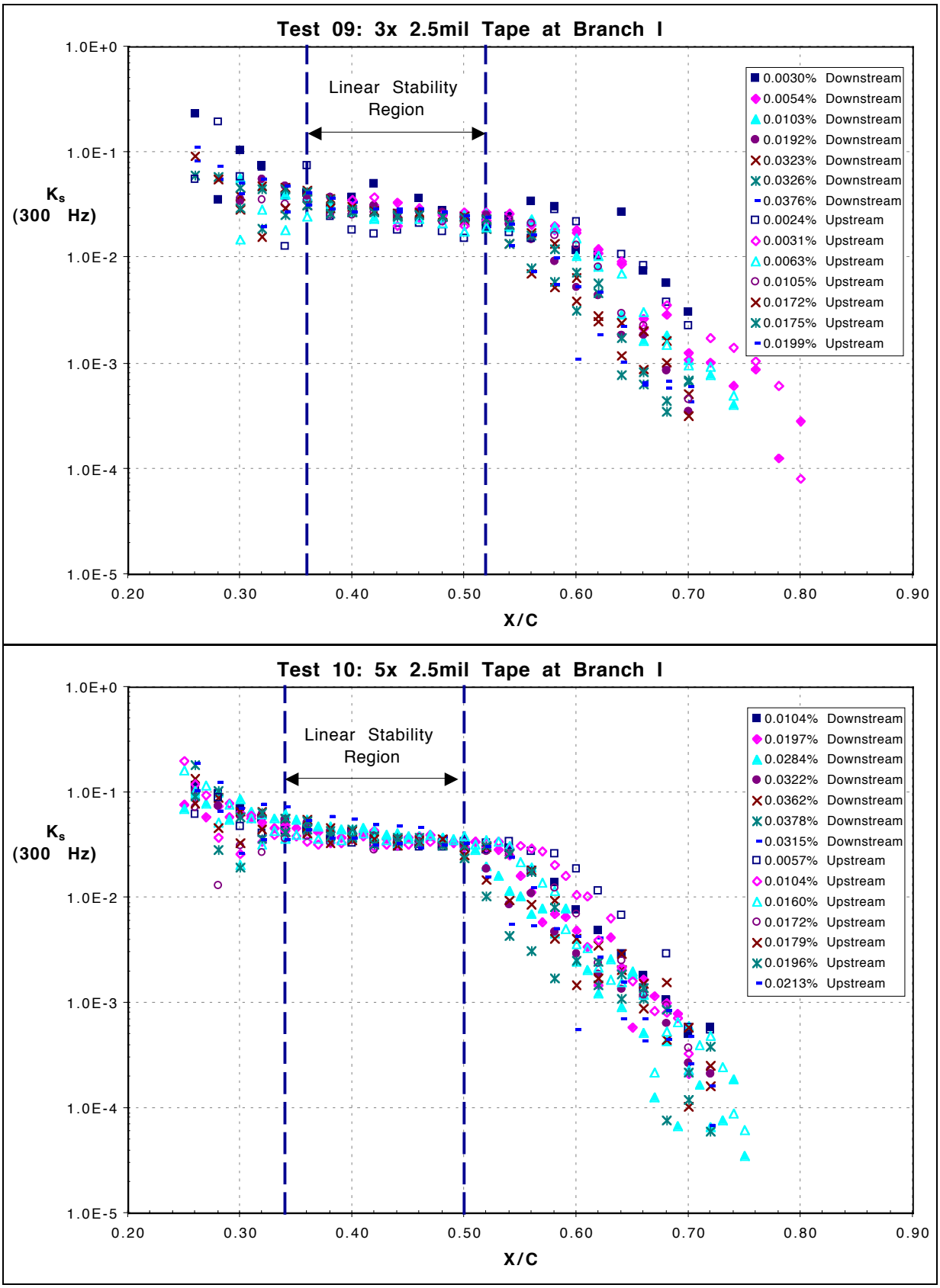

Figure 62: 20 m/s Test Case Receptivity Coefficient, $K_{s,\ 300\ Hz}$

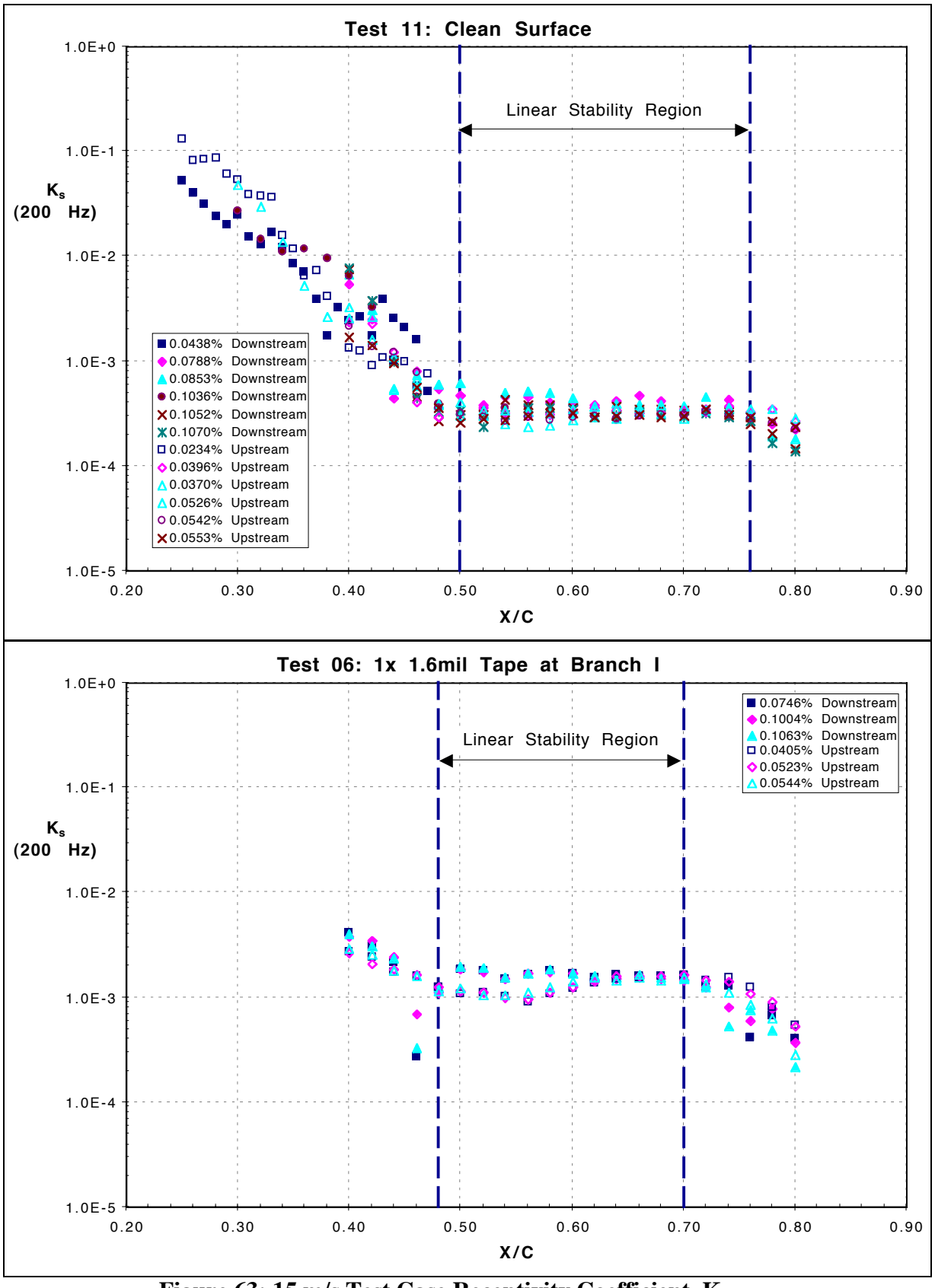

Figure 63: 15 m/s Test Case Receptivity Coefficient, $K_{s,\ 200\ Hz}$

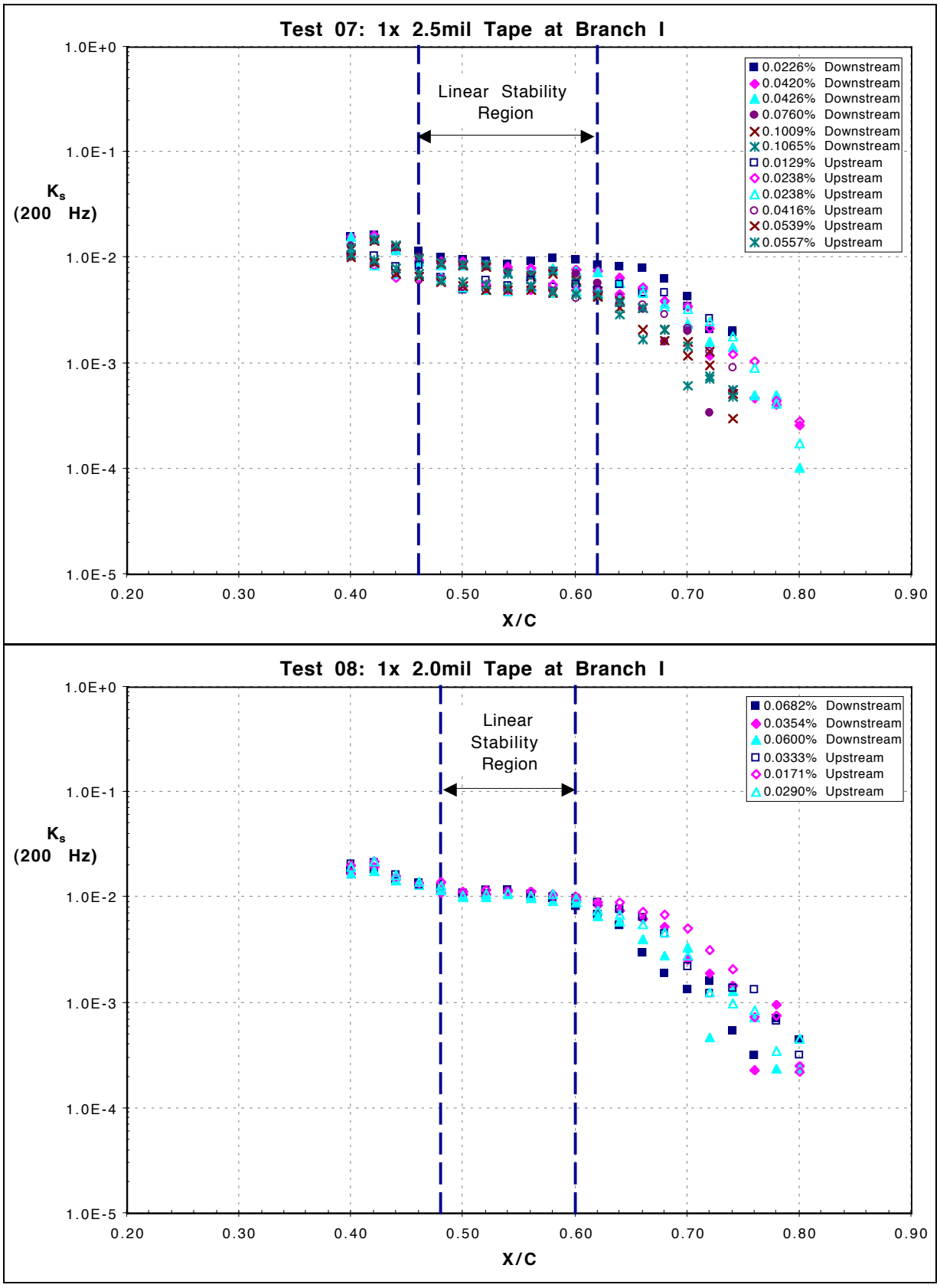

Figure 63: 15 m/s Test Case Receptivity Coefficient, $K_{s,\ 200\ Hz}$

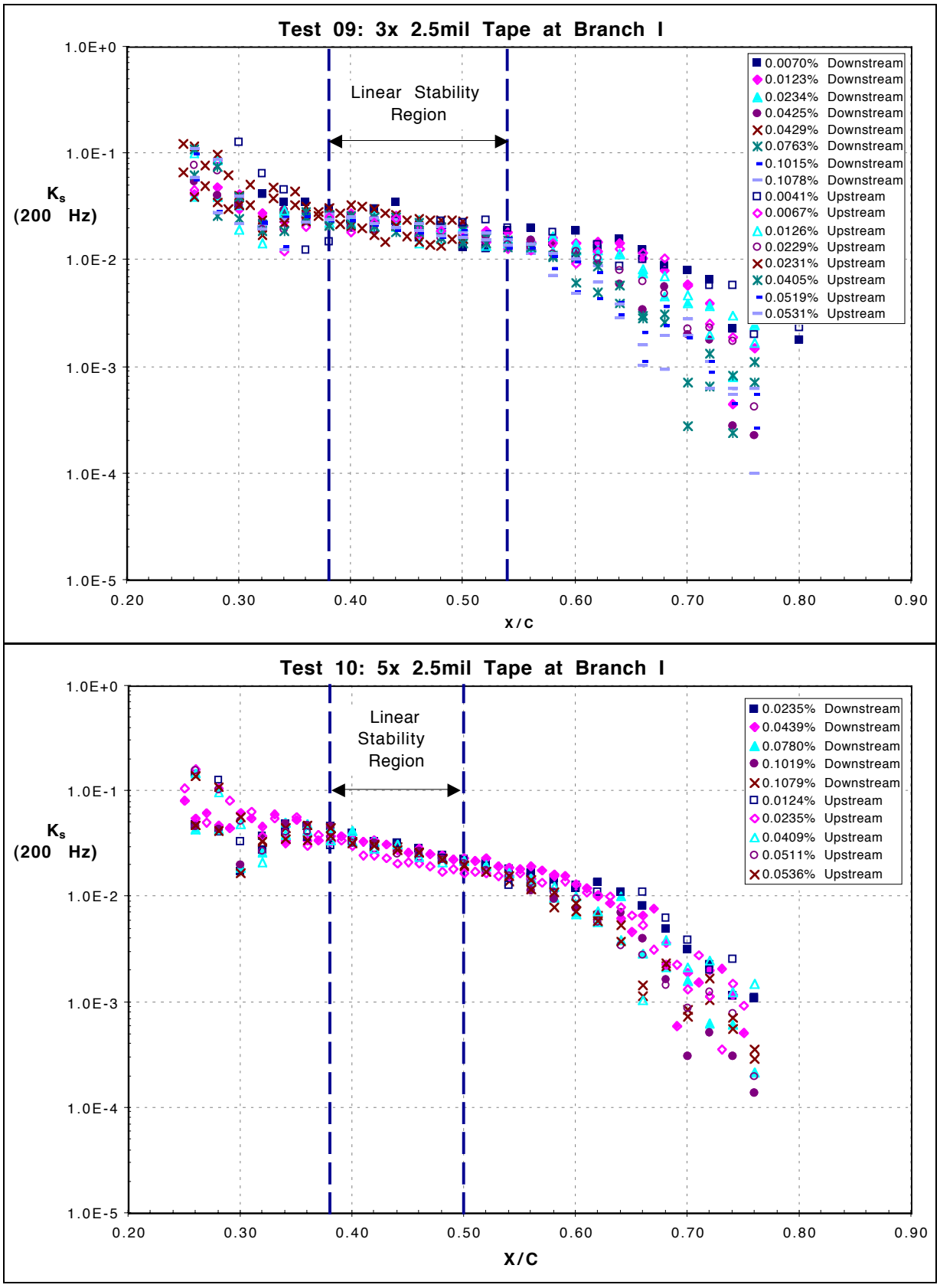

Figure 63: 15 m/s Test Case Receptivity Coefficient, $K_{s,\ 200\ Hz}$

5.2.4.4 Comparison of Repeated Roughness Results to Flat Plate Experiments

The results of the repeated roughness data sets are compared with flat plate results by normalizing the multiple roughness case amplitudes by the single roughness case amplitude. For the experimental results, the receptivity coefficients are used. Flat plate results from Wiegel[37] and Dietz[52] are used. For these results, the maximum TS modeshape amplitude is used for the normalization. It should be noted that Dietz and Wiegel used 25.4 mm x 40 μm roughness elements staggered about the lower branch, whereas the experimental results presented from this experiment were for 9.5 mm x 63.5 μm roughness elements.

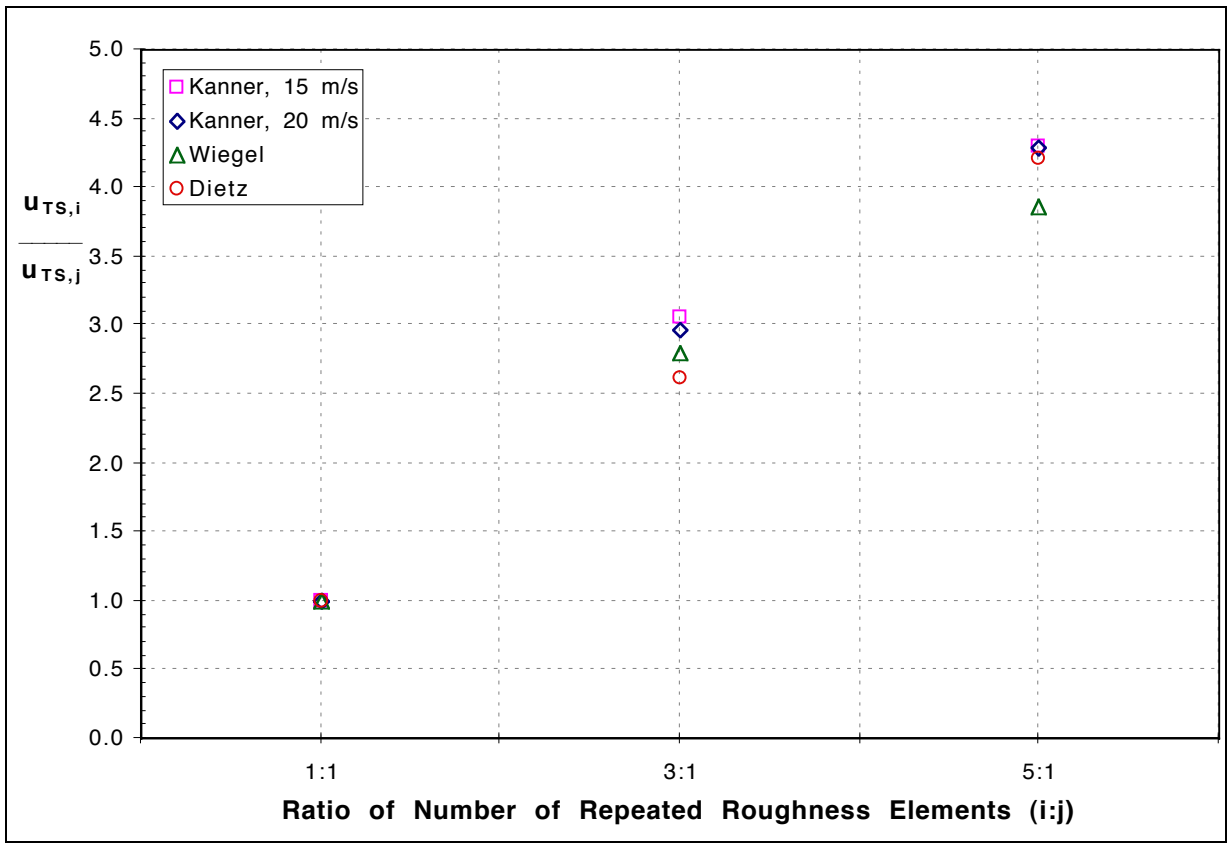

Figure 64: Comparison of Repeated Roughness to Flat Plate Experiments

5.2.4.5 Comparison of Single-Frequency Disturbance Amplitudes to Linear Stability Theory

Chordwise growth of the boundary-layer disturbances for all frequencies in the filtered range are presented in **Figures 65 and 66** for the 20 m/s 0.0200% and 15 m/s 0.1070% free-stream forcing levels, respectively. The corresponding theoretical results were presented in **Figures 59 and 60**

for the 20 m/s and 15 m/s flow cases, respectively. It can be seen that the general shape of the curves corresponds well for the lower frequencies. However, the experimental data contains a less steep slope, which indicates a more stable flow condition. This is a possible result of two phenomena: slight negative angle of attack and/or mean flow effects not properly accounted for. The latter phenomena are a more prevalent issue for the test cases where transition starts considerably upstream of the theoretically assumed location of 80% chord, particularly for Test Cases 9 and 10. Another difference between the experimental and theoretical results is the disturbance mode behavior after it becomes stable but is still positive in amplitude.

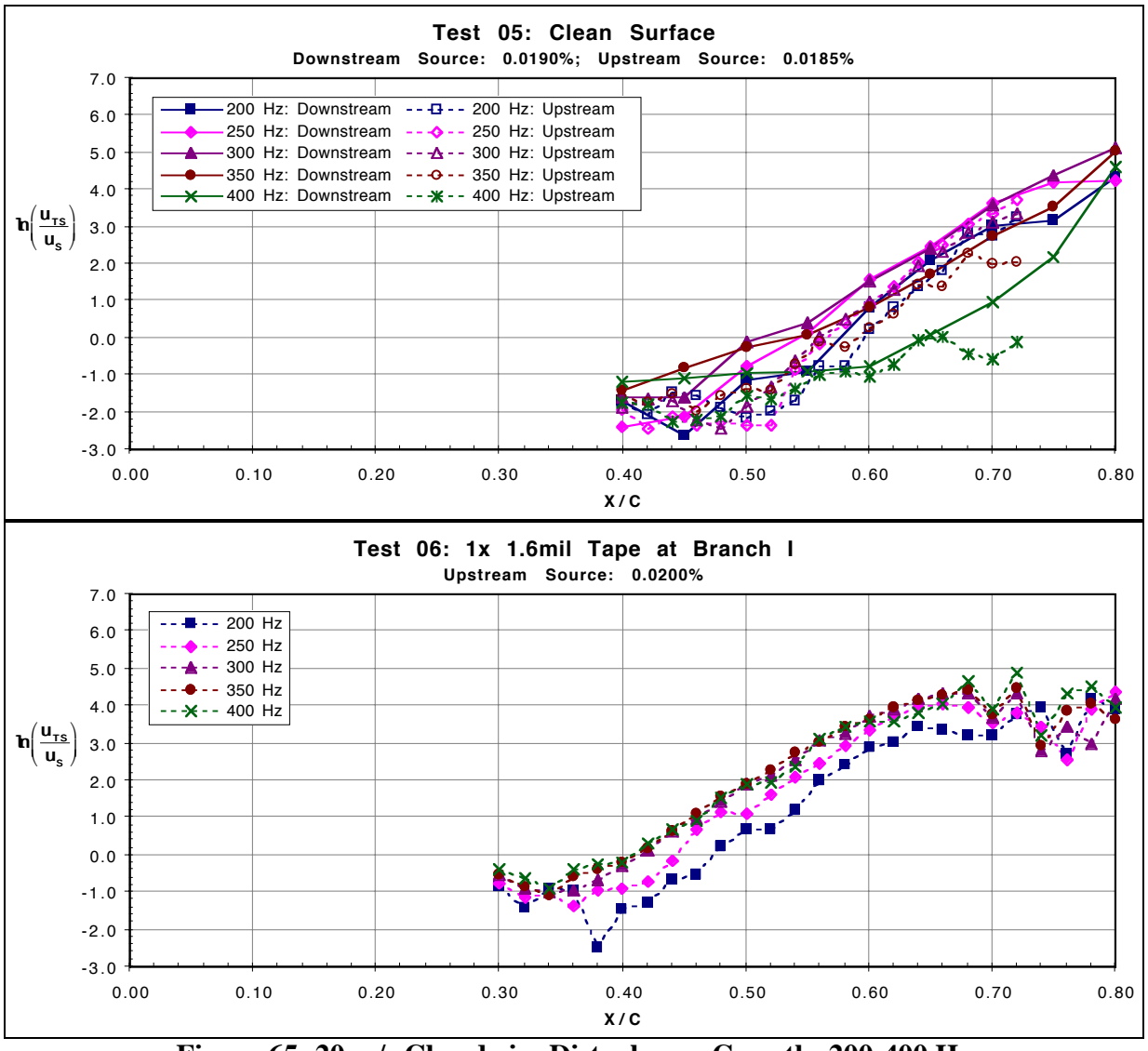

Figure 65: 20 m/s Chordwise Disturbance Growth: 200-400 Hz

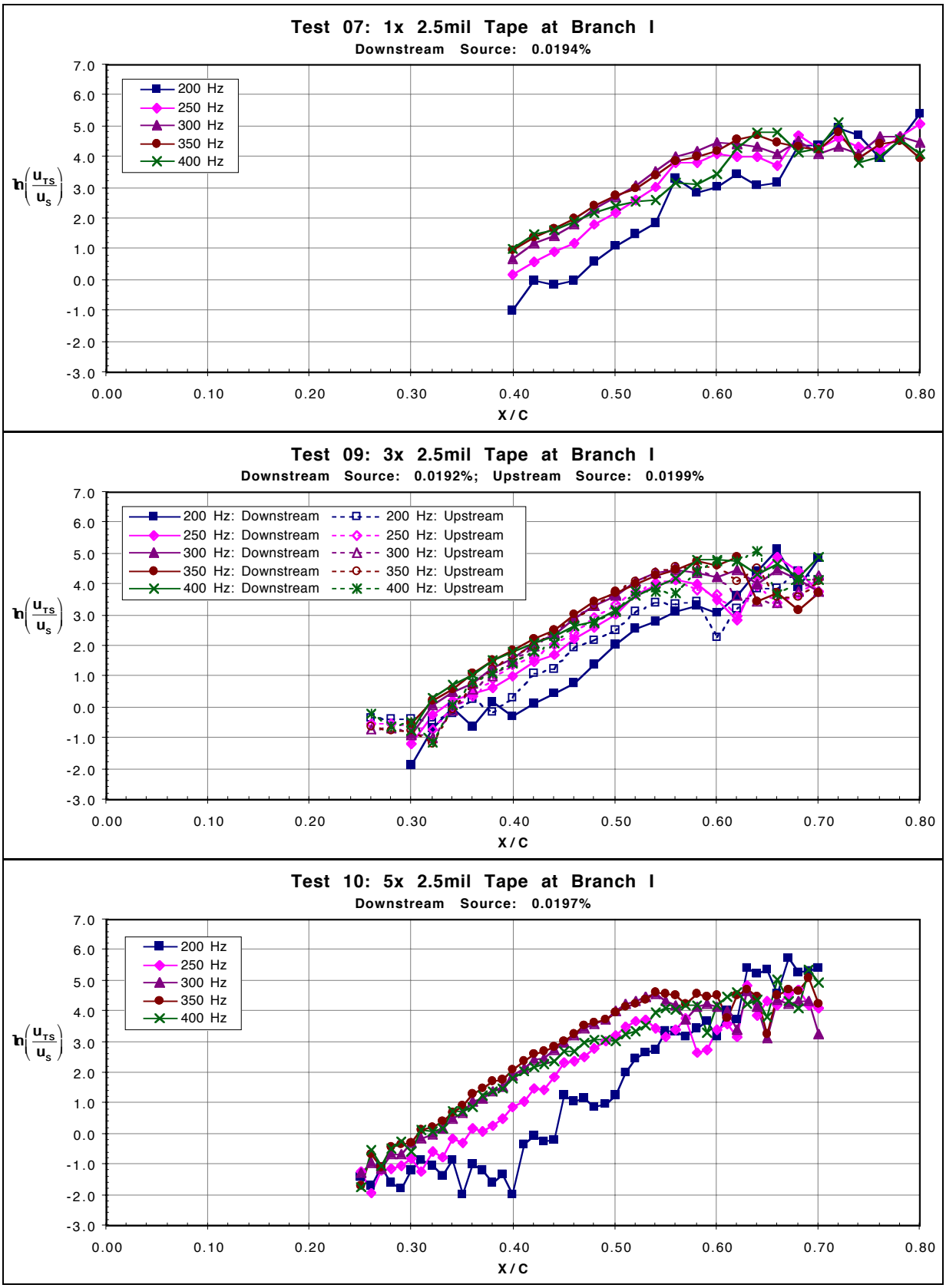

Figure 65: 20 m/s Chordwise Disturbance Growth: 200-400 Hz

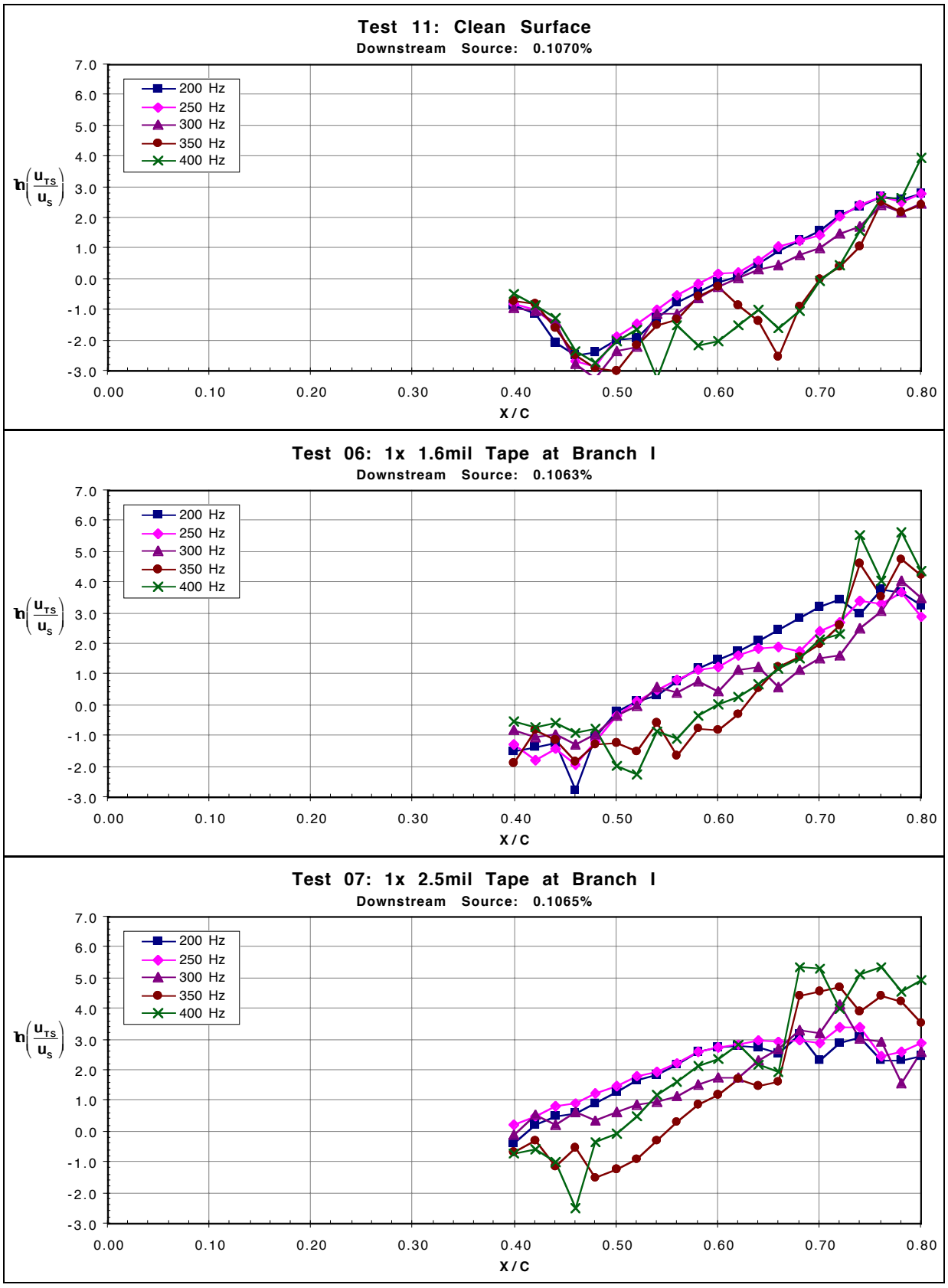

Figure 66: 15 m/s Chordwise Disturbance Growth: 200-400 Hz

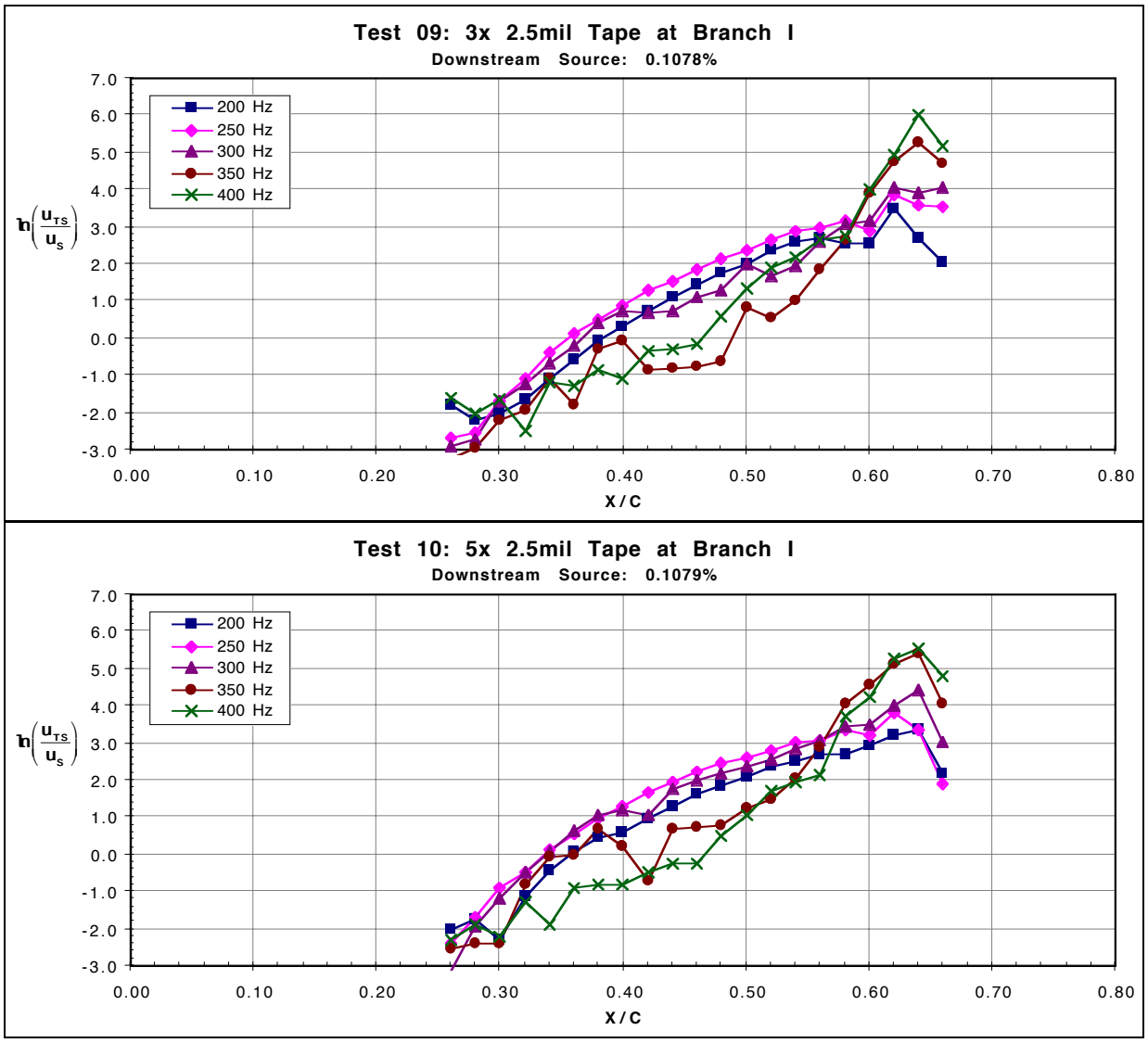

Figure 66: 15 m/s Chordwise Disturbance Growth: 200-400 Hz

Before directly comparing the experimental results to linear stability theoretical results, the dependence of the disturbance growth upon the corresponding source signal strength at 20 m/s was examined. **Figure 67** presents the results for all surface conditions at 40, 50, 60 and 70% chord. The chordwise stations are color coded with separate sub-plots for each surface condition. For the results where the response signal was greater than the free-stream source signal (the amplitude ratio is above 1.0 and the logarithm of the amplitude ratio is above 0.0), but when the boundary-layer response did not get non-linear, varying the forcing signal strength had no significant effect. Below an amplitude ratio of 1.0 (a logarithmic value below 0.0), the disturbance was smaller than the forcing signal, and noise in the signal significantly interfered with the disturbance wave packet. This independence from the forcing signal amplitude at the early stages of the boundary-layer disturbance growth allows for upstream extrapolation of the data to the lower branch using the same constant for ALL forcing conditions. This constant is different for each surface roughness condition.

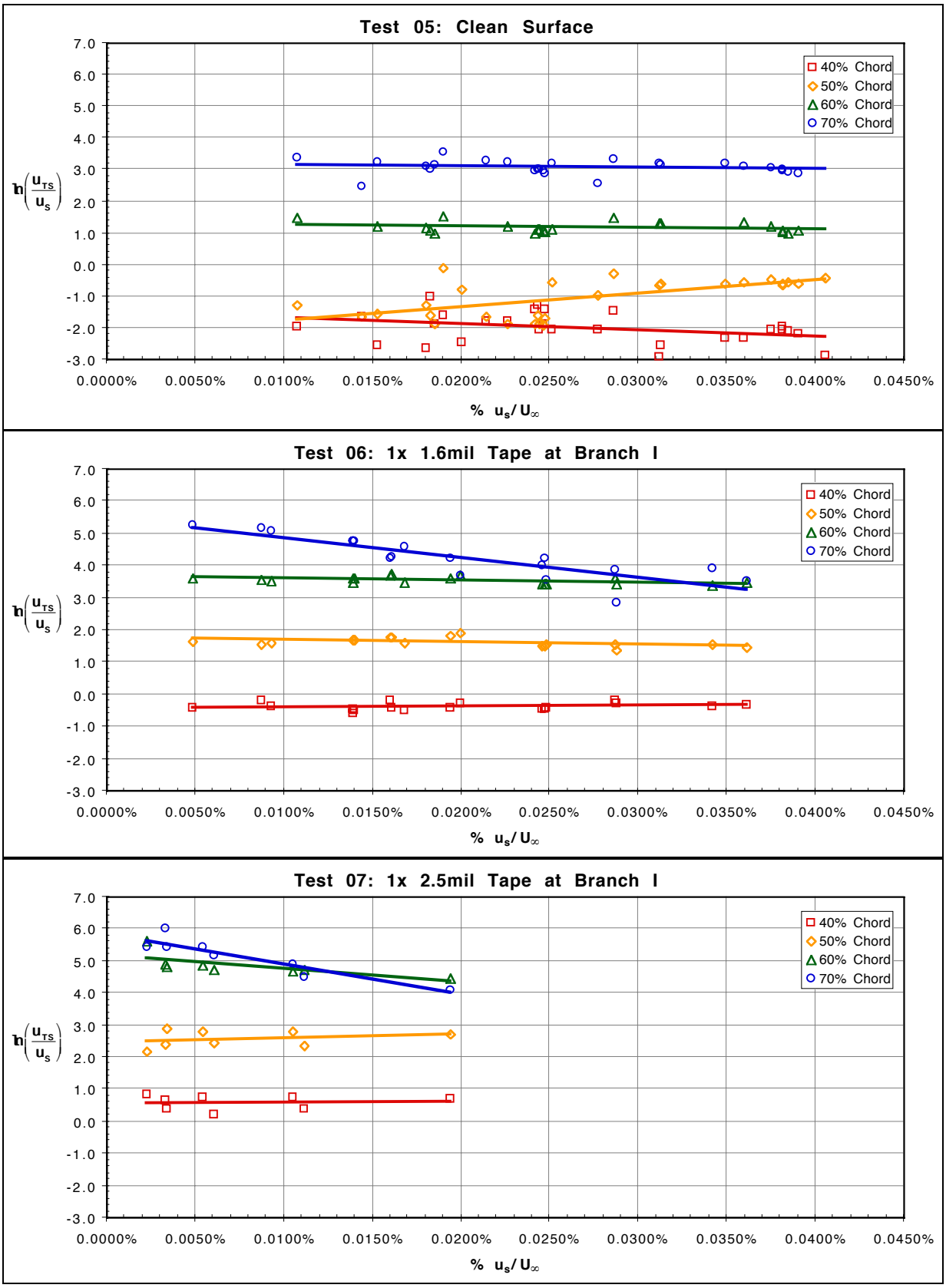

Figure 67: 20 m/s Test Case 300 Hz Disturbance Growth based upon Source Strength

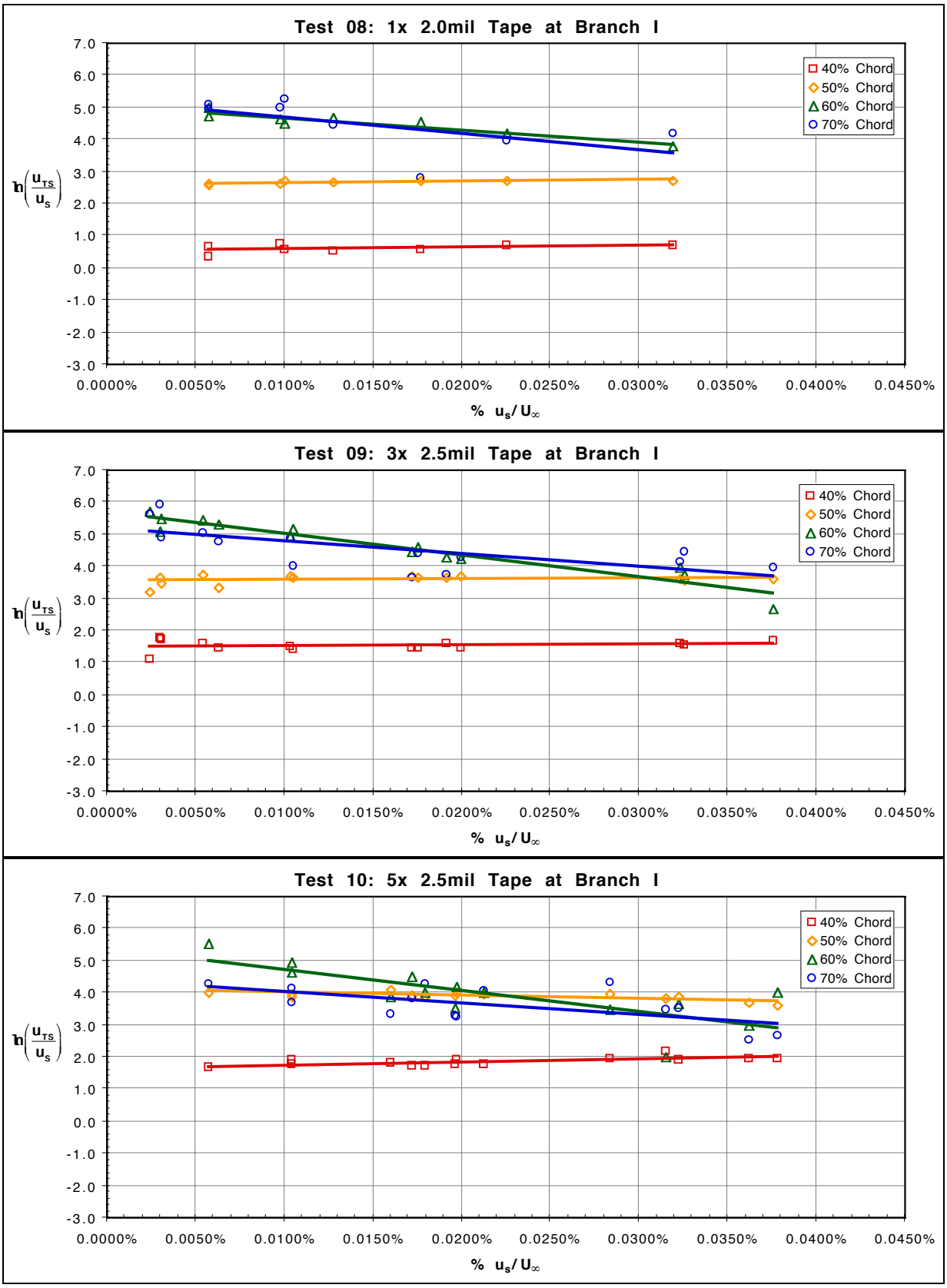

Figure 67: 20 m/s Test Case 300 Hz Disturbance Growth based upon Source Strength

Extrapolating the experimental results to Branch I allows for direct comparison to theoretical stability results. Shifting the experimental results completed the extrapolation by a constant that yielded an apparent best fit. This constant was $-\ln(K_s)$, which by definition corresponds to the best fit of the experimental data to linear stability theory and was applied as indicated by the following equation:

$$N = \ln\left(\frac{u_{TS}}{u_{BI}}\right) = \ln\left(\frac{u_{TS}}{u_S}\right) - \ln(K_s) \qquad \textbf{Equation 5-6}$$

First, a comparison of the N-factor results from linear stability theory (LST, SALLY code) and linear parabolized stability equations (LPSE, ECLIPSE code) is presented in **Figure 68**. The results compare very well upstream of 40% chord. After that station, the LPSE results indicate a slightly more unstable disturbance, such that N = 9 and 12 occur 2 and 3% chord upstream, respectively, of the LST prediction of the SALLY code. Also included on the plot is the N-factors for the upper lobe of the T-S modeshape, which was the quantity actually tracked experimentally. It also compares well with the other results.

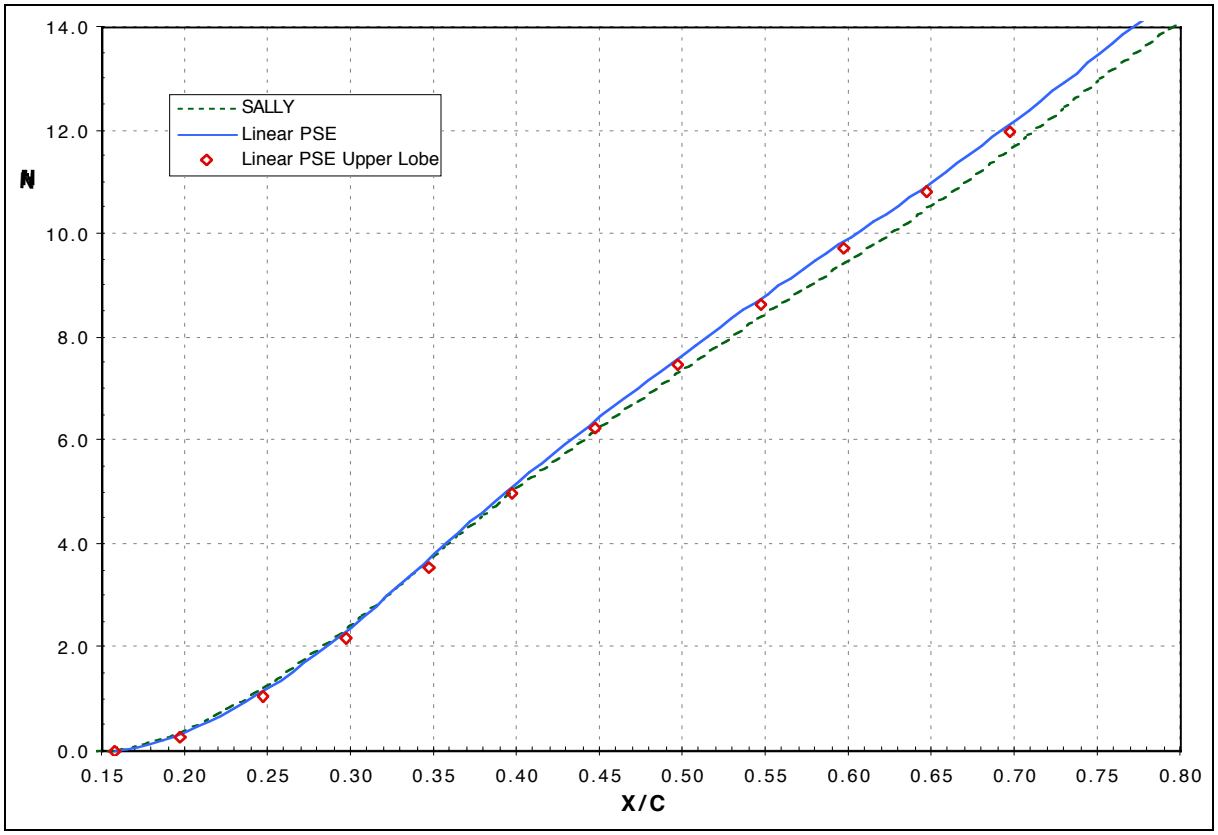

Figure 68: Comparison of LST and LPSE N-Factors

Comparisons at the central forcing frequency of 300 Hz and 20 m/s are presented in **Figure 69**. It can be seen that the experimental results compare very well with the LST theoretical results. For the no-surface-roughness case, the interference of the one disturbance's forcing signal interferes with the other forcing signal's corresponding boundary-layer response in the region of 40 - 55% chord. This corresponds to the observation made from the time traces overlapping in that chordwise region in **Section 5.2.4.1**. For the cases with surface roughness, this is not a significant issue, because the upstream source signal is much smaller than the other response signal, instead of larger or comparable in amplitude. The deviations from the linear stability theory results at the downstream stations are due to the developing non-linearity in the disturbance, which can be seen in the time trace results in **Figure 50**. The downstream variations can also be accounted for by improper mean flow matching, which can be corrected by solving an integral boundary-layer flow-field solution with transition forced at the same chordwise station as was experimentally obtained. Again, it can be noted that there is a slight slope difference as described earlier. The results in **Figure 70** for the 15 m/s, 200 Hz test cases show the same trends. For both cases, it can be seen that the breakdown of the primary disturbance occurs for N-factors between 7 and 11, comparing well to previous e^N results.

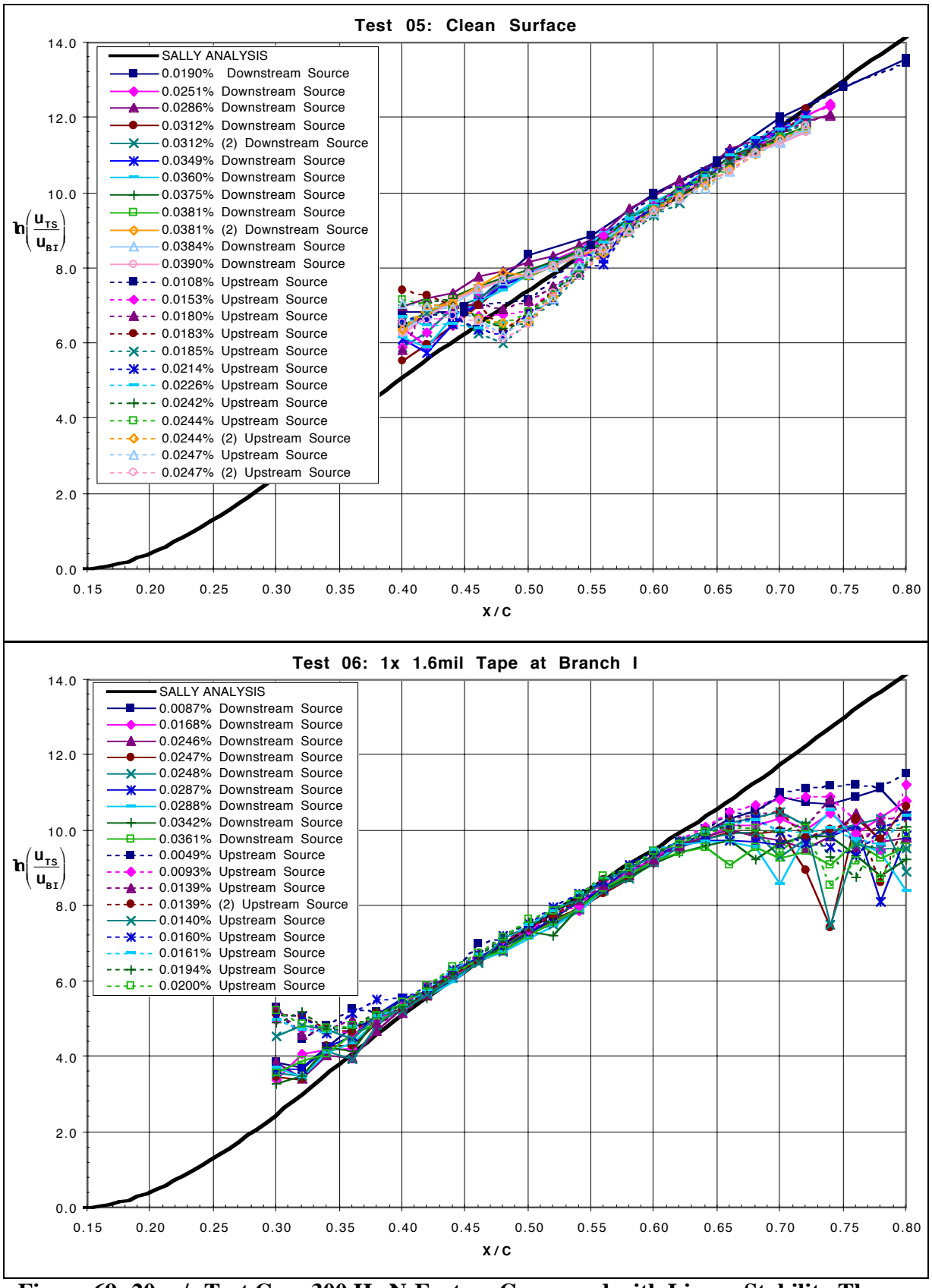

Figure 69: 20 m/s Test Case 300 Hz N-Factors Compared with Linear Stability Theory

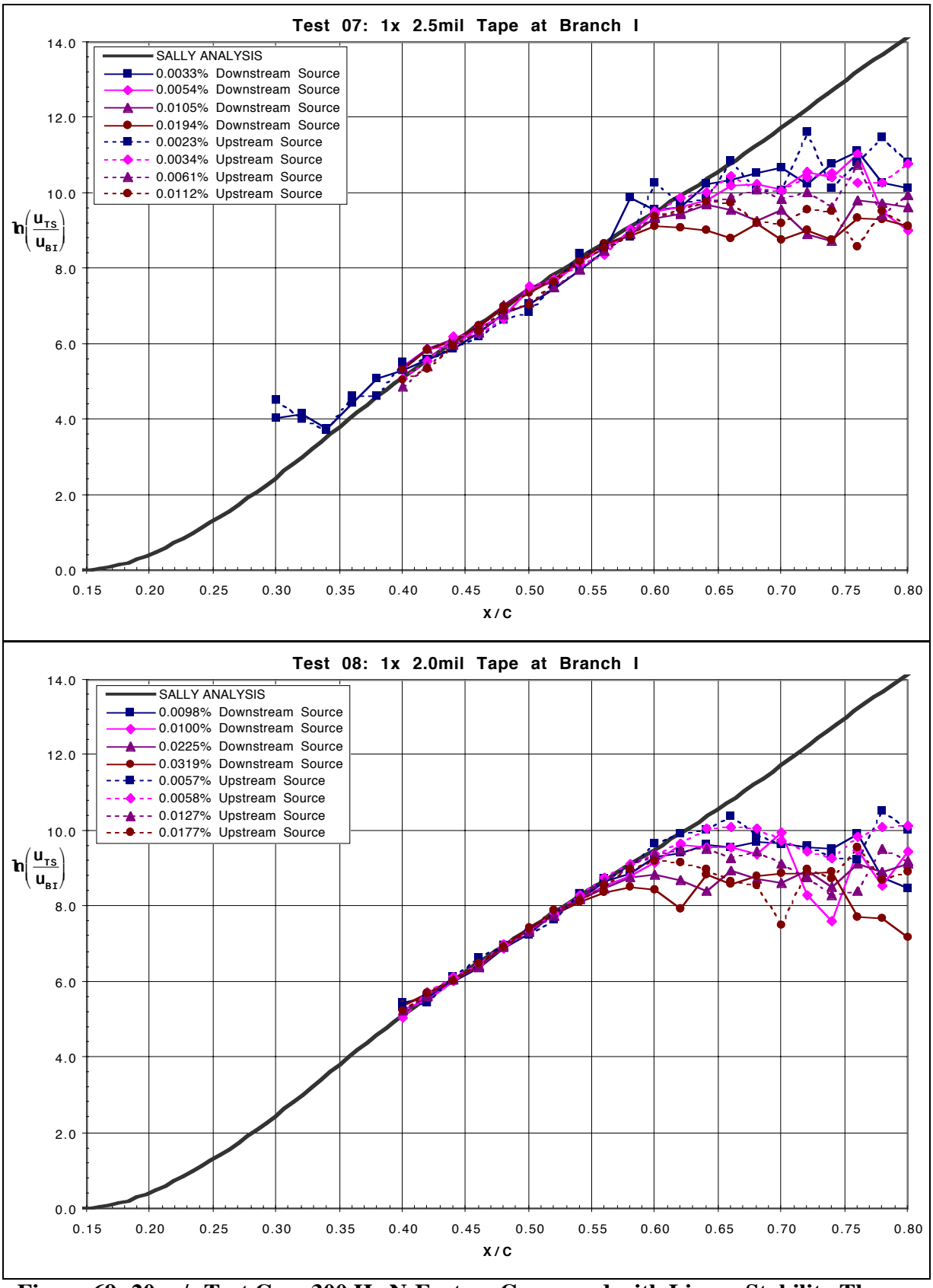

Figure 69: 20 m/s Test Case 300 Hz N-Factors Compared with Linear Stability Theory

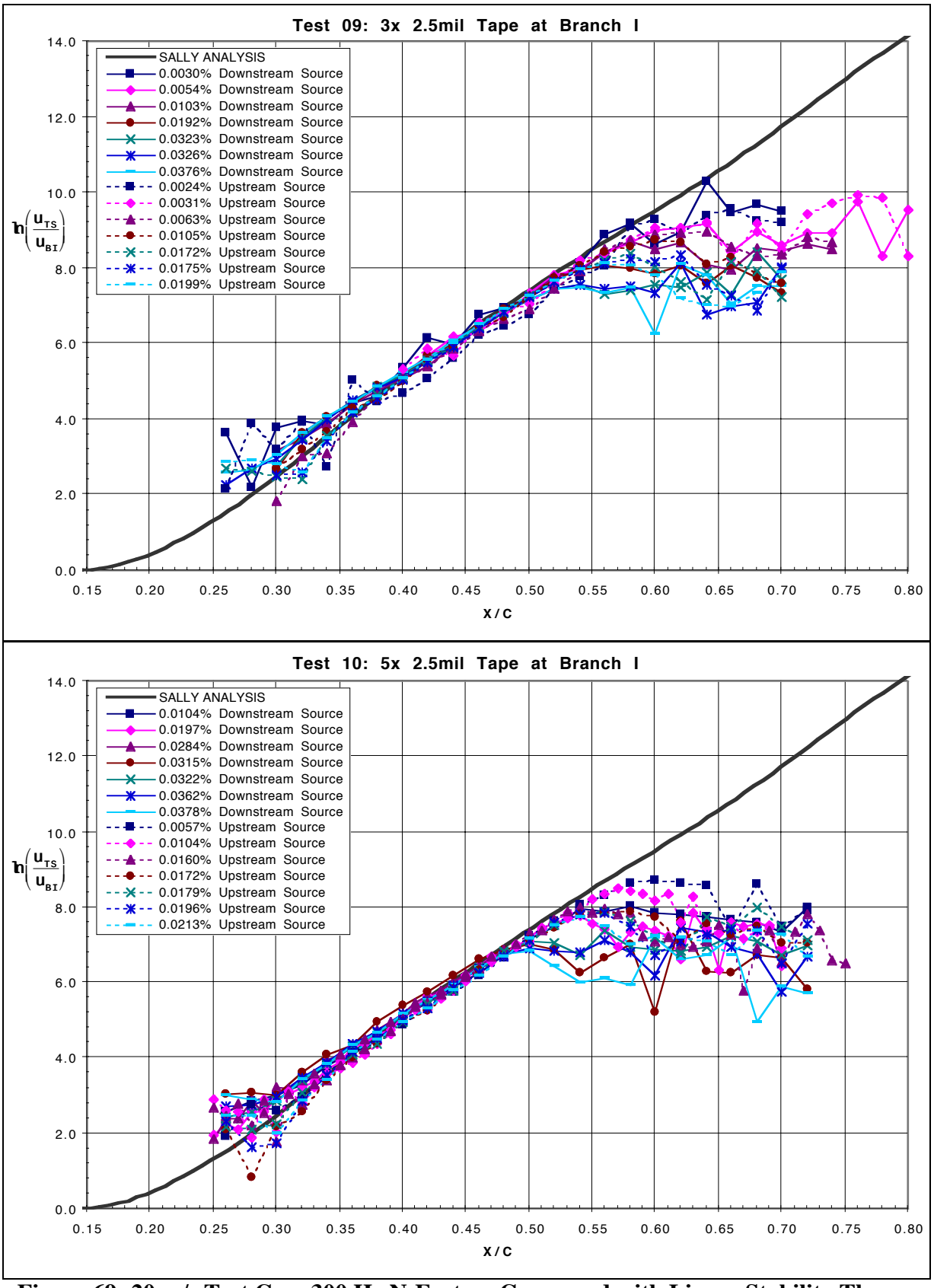

Figure 69: 20 m/s Test Case 300 Hz N-Factors Compared with Linear Stability Theory

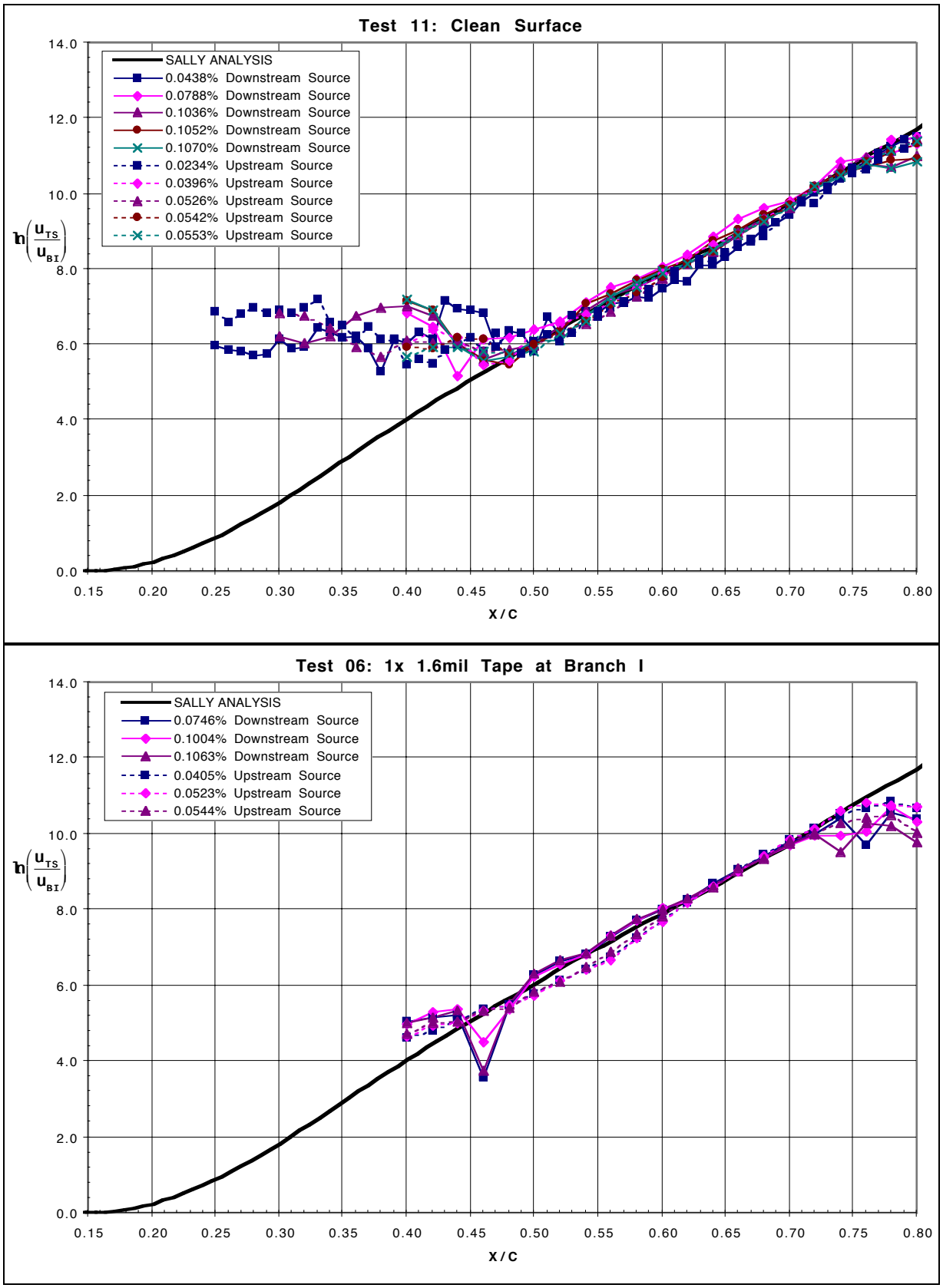

Figure 70: 15 m/s Test Case 200 Hz N-Factors Compared with Linear Stability Theory

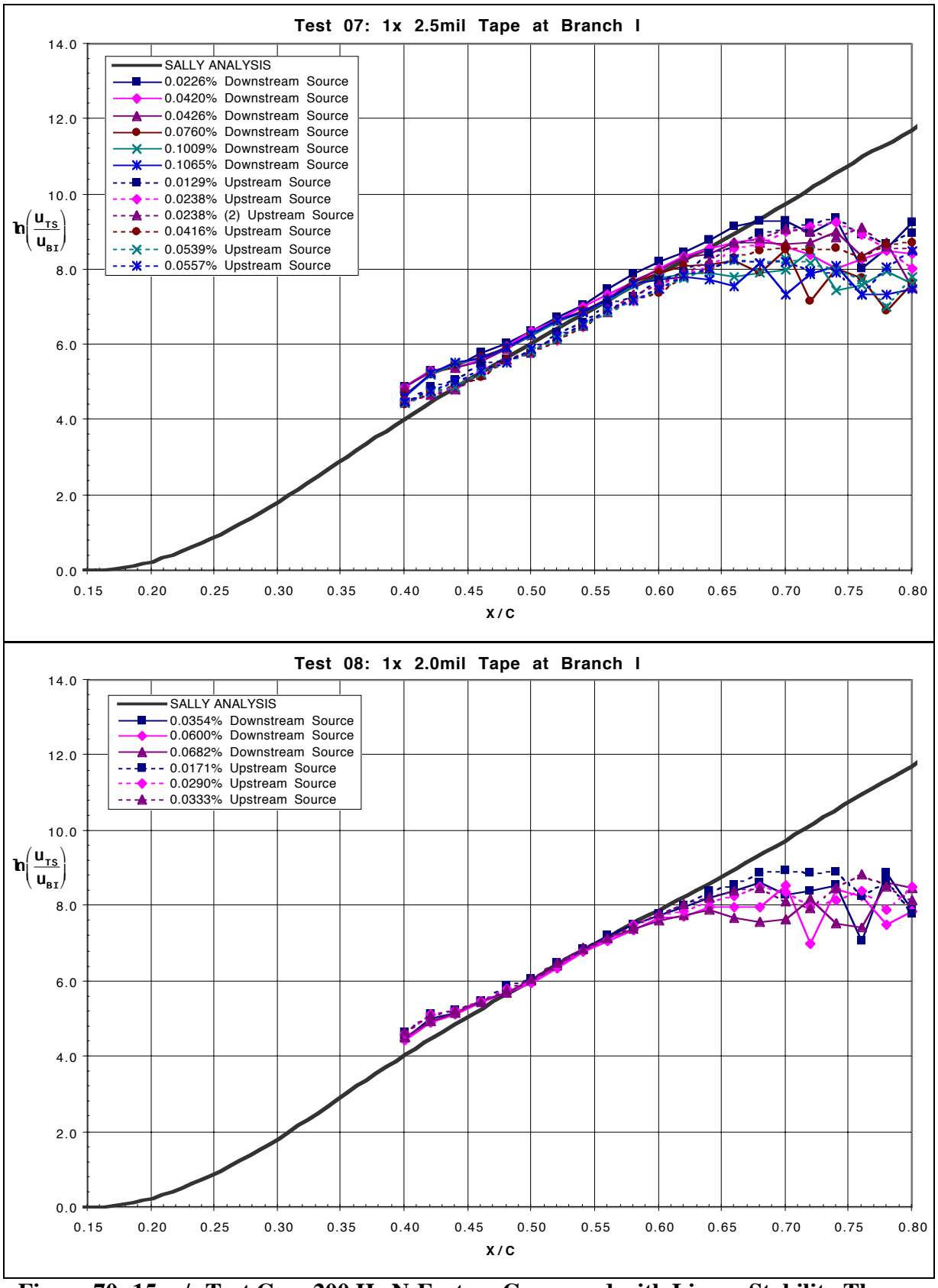

Figure 70: 15 m/s Test Case 200 Hz N-Factors Compared with Linear Stability Theory

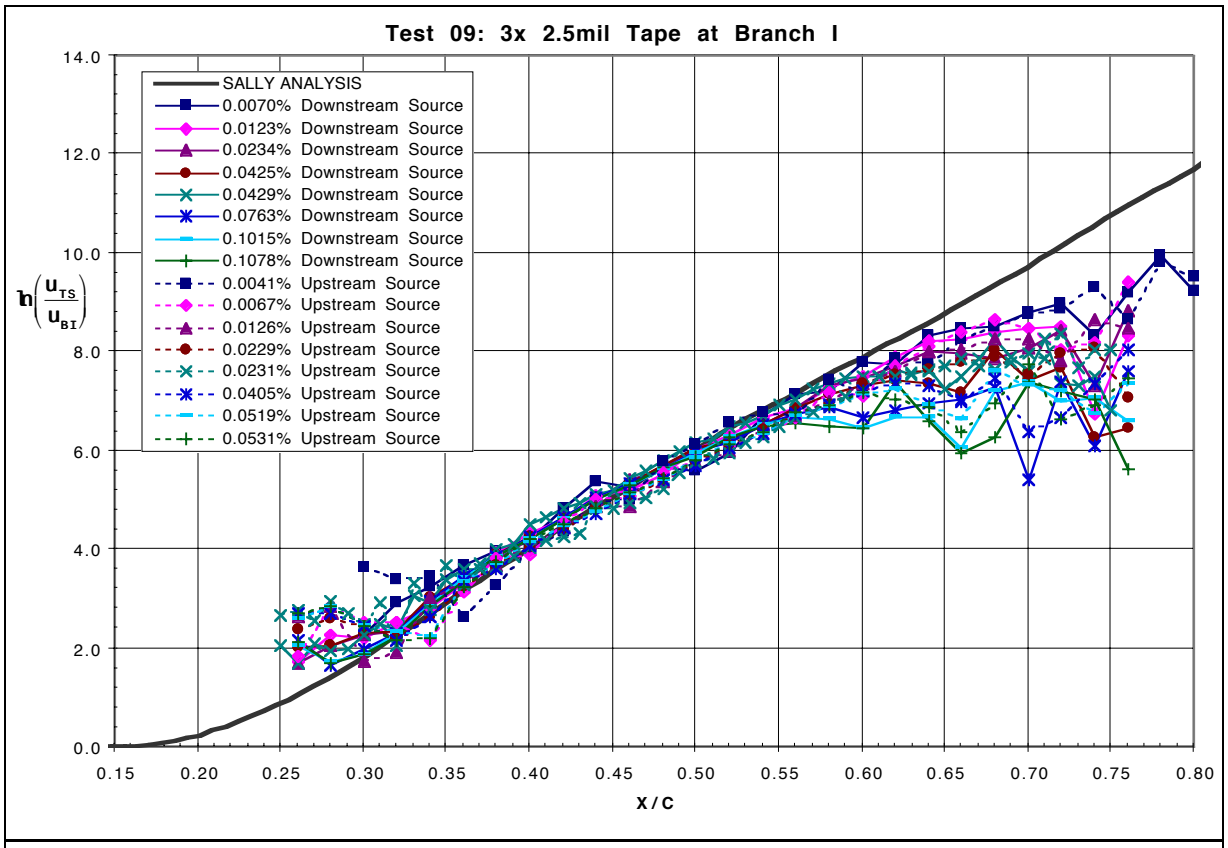

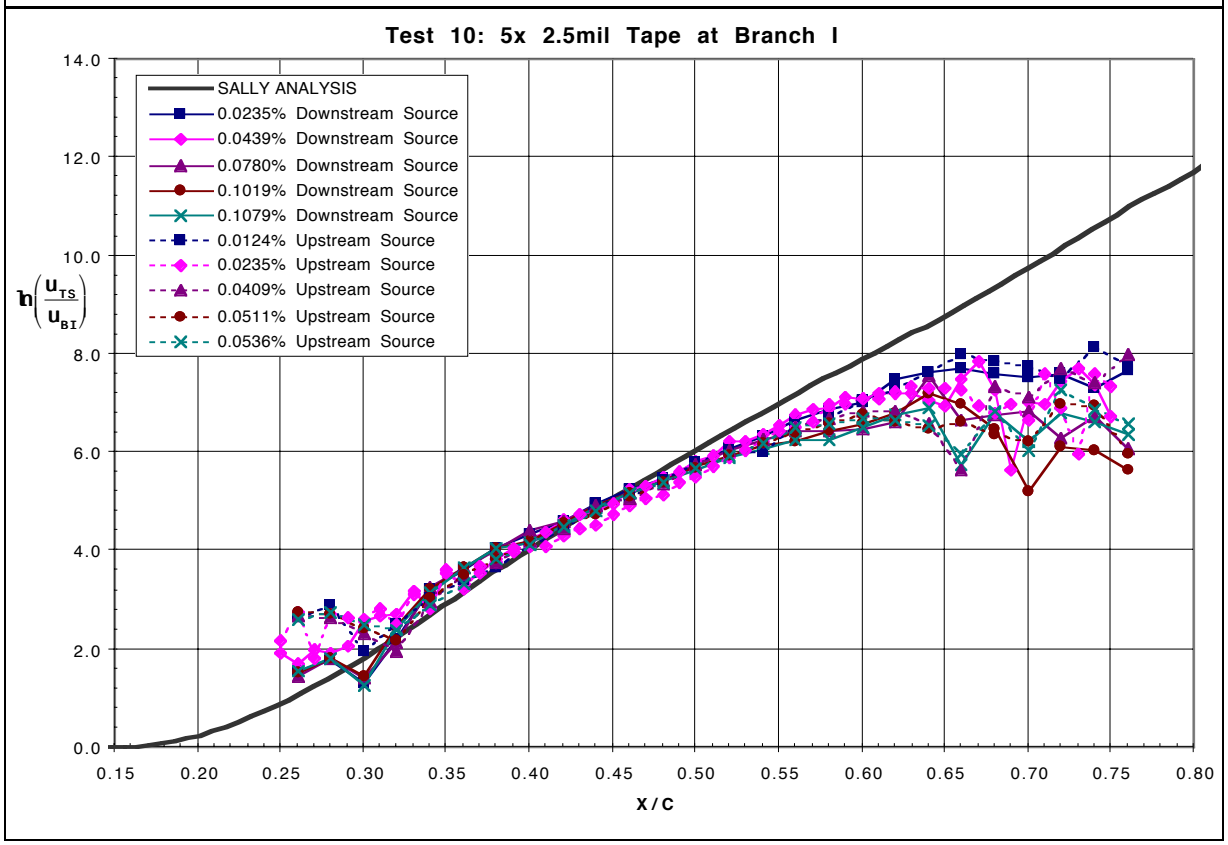

Figure 70: 15 m/s Test Case 200 Hz N-Factors Compared with Linear Stability Theory

5.2.4.6 Boundary-Layer Response Frequency Spectra

Comparisons of the boundary-layer response amplitudes across the filtered frequency range is presented in **Figures 71 and 72** for 20 m/s and 15 m/s cases with nominally the same forcing amplitude, respectively. It can be seen that roughness significantly enhances the development of the response. At 40% chord, the no-roughness and single-element roughness case results (Tests 05, 06, 07, and 08) are on the same order of magnitude or smaller than the source signal. No data for the 40% chord 15 m/s Test 11 case because the boundary-layer response was buried within the noise of the signal. For the first few stations, the responses due to each roughness case scale constantly with respect to each other for the frequency range examined. Also indicated on these plots is the non-linear breakdown at 300 Hz. This can be seen in the figures at the later chordwise stations, particularly at 70% chord, but also at earlier stations with the stronger surface roughness conditions. For the breakdown, the spectral energy can been to increase in higher frequencies more than at the primary forcing frequency.

It is necessary to point out that for the 20 m/s flow case, the acoustic signal forced in the free-stream was centered about 300 Hz. The results indicate that the boundary-layer response is centered about 325 Hz. For the 15 m/s case, the forcing signal and response signal centered frequencies were 200 and 250 Hz, respectively. However, for the latter case, a secondary disturbance frequency centered about 450 Hz dominated during the boundary-layer breakdown. It should also be noted that the frequency spectra results do not indicate the extent of narrow band frequency tuning with distributed roughness as seen in flat plate experiments such as Dietz[52, 53, 54] and Saric[49, 50]. While a significant increase in amplitude can be seen with the application of the repeated roughness, it does not appear to be limited to a narrow range of frequencies about the central forcing frequency. The repeated roughness elements were spaced according to the wavelength of this frequency at the applicable flow velocity. Also, it should be noted that the nature of the data reduction method used, ensemble averaging phase-locked time traces, is biased against random structures. Ensemble averaging the spectra would better preserve the frequency content of the random structures of the developing turbulence.

In comparison to linear stability theory results in **Figures 73 and 74**, the experimental trends look good. This is most apparent at 50% chord for all roughness conditions and the downstream

stations for the weaker receptivity (minimal surface roughness) test cases. At the downstream cases, the stronger surface roughness test cases do not correlate well with theory because the basic assumptions of linear stability theory do not hold - the flow exhibits strong non-linear effects. A direct comparison of the experimental results in **Figures 71 and 72** with the theoretical results in **Figures 73 and 74**. This is because the experimental results are in the form of u_{TS}/u_s, with the response signal normalized by the free-stream forcing signal, and the theoretical results are in the form of u_{TS}/u_{BI}, where the response signal is normalized by its amplitude in the boundary-layer at Branch I for that particular frequency of concern. While the difference between the amplitude of the free-stream forcing signal and the amplitude at Branch I is expected to be a constant for all frequencies, this constant is not expected to be the same. Hence, only qualitative observations can be made when comparing the theoretical and experimental results.

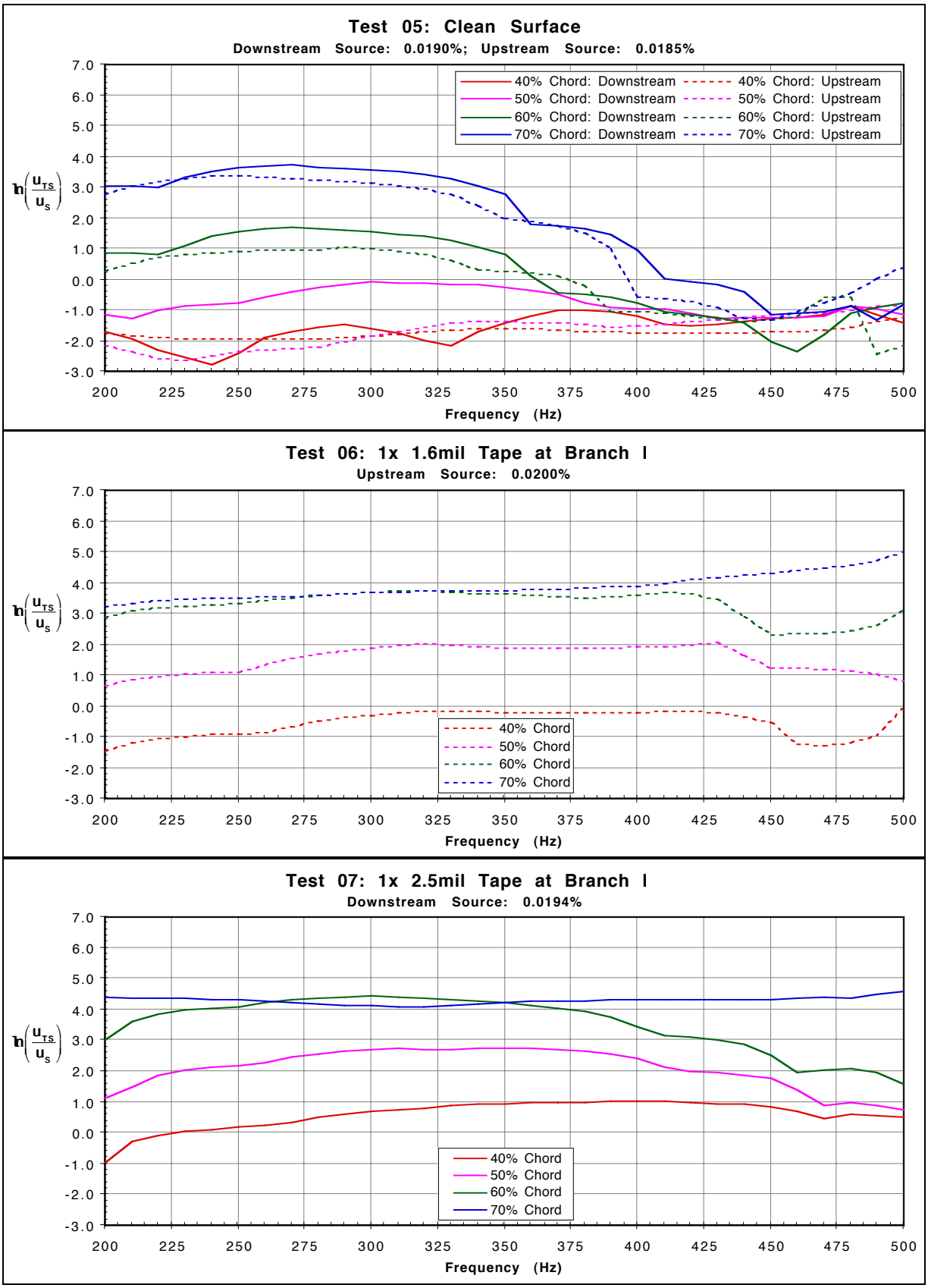

Figure 71: 20 m/s Test Case Boundary-Layer Response Energy Spectra

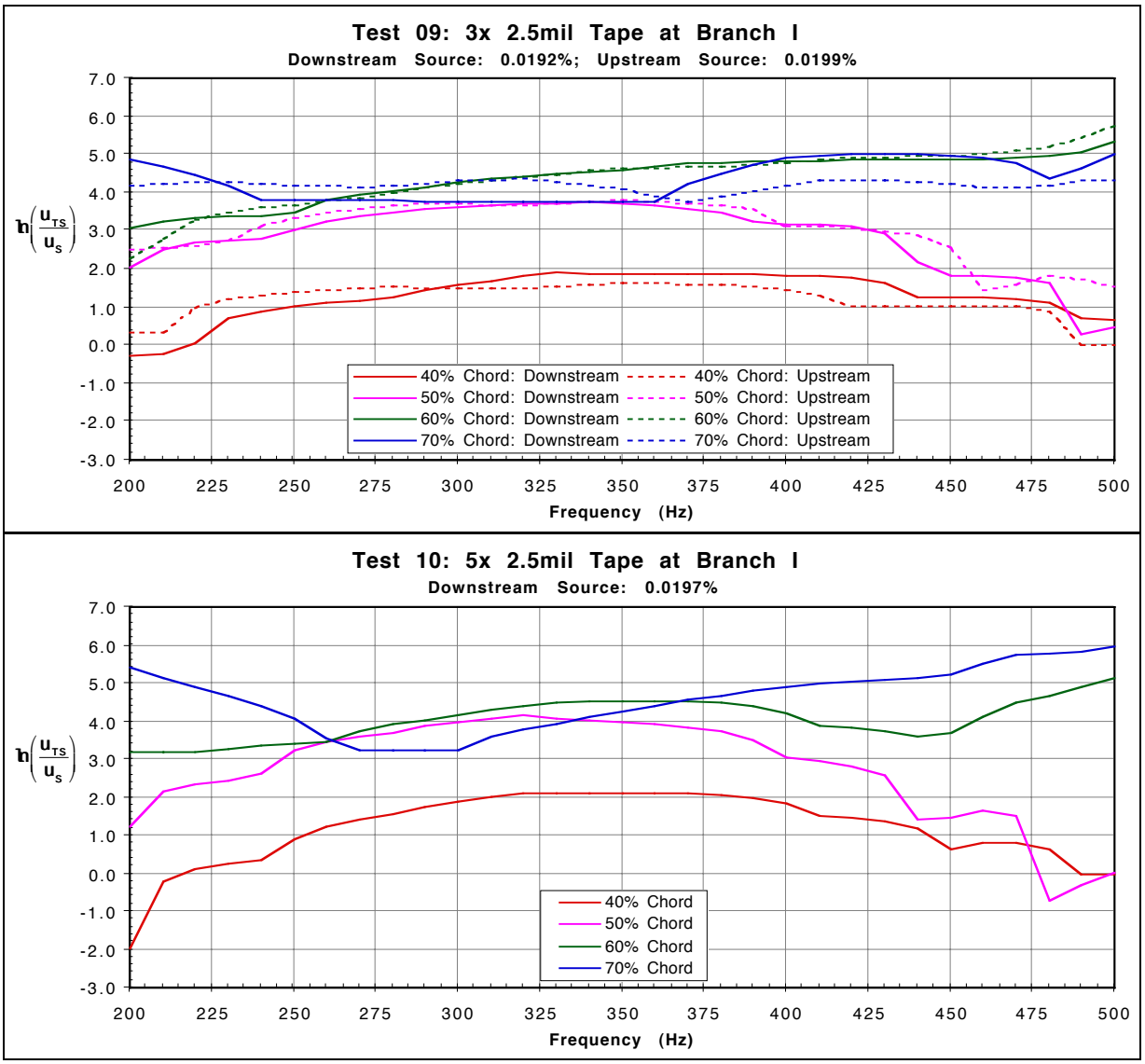

Figure 71: 20 m/s Test Case Boundary-Layer Response Energy Spectra

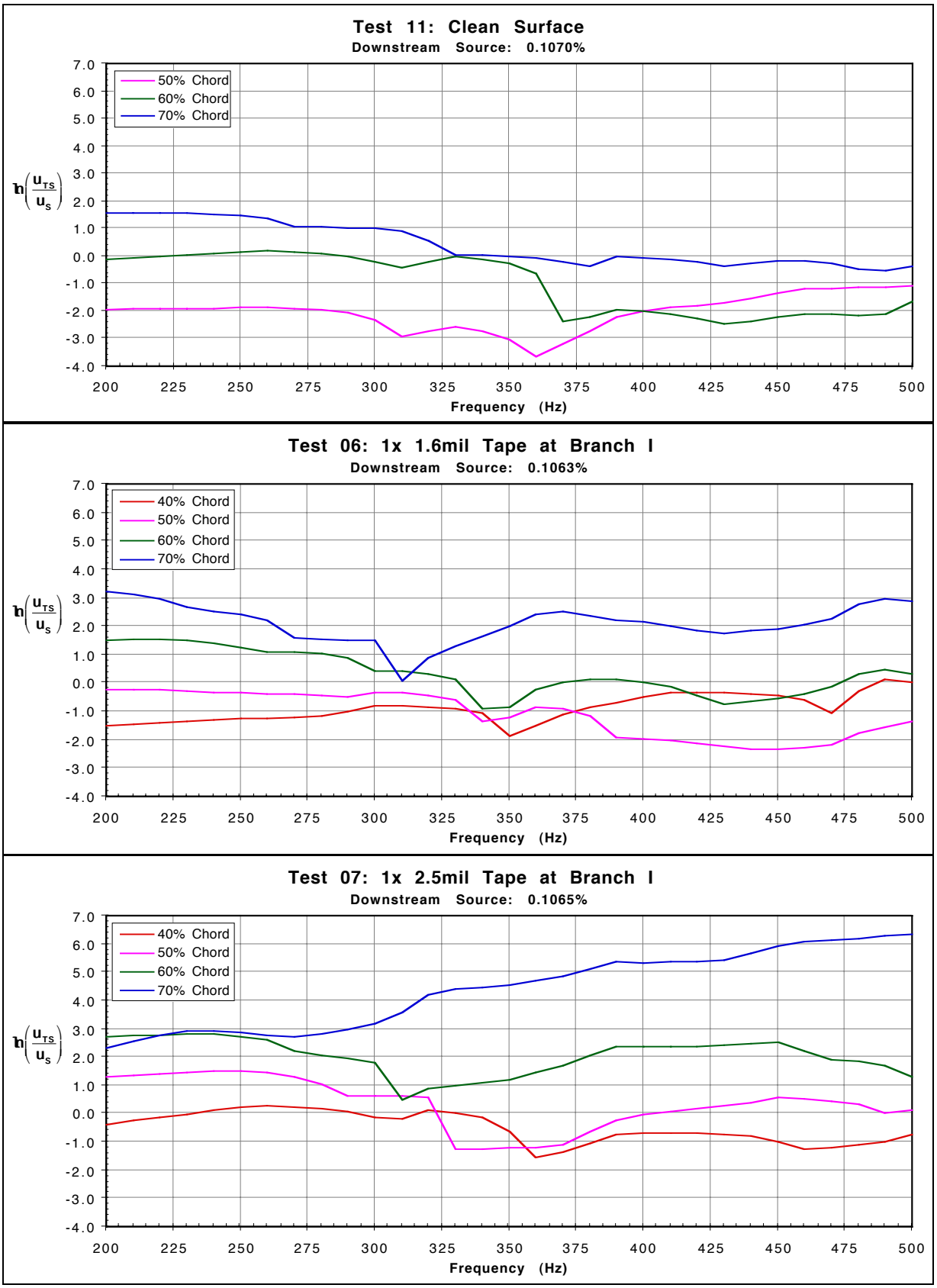

Figure 72: 15 m/s Test Case Boundary-Layer Response Energy Spectra

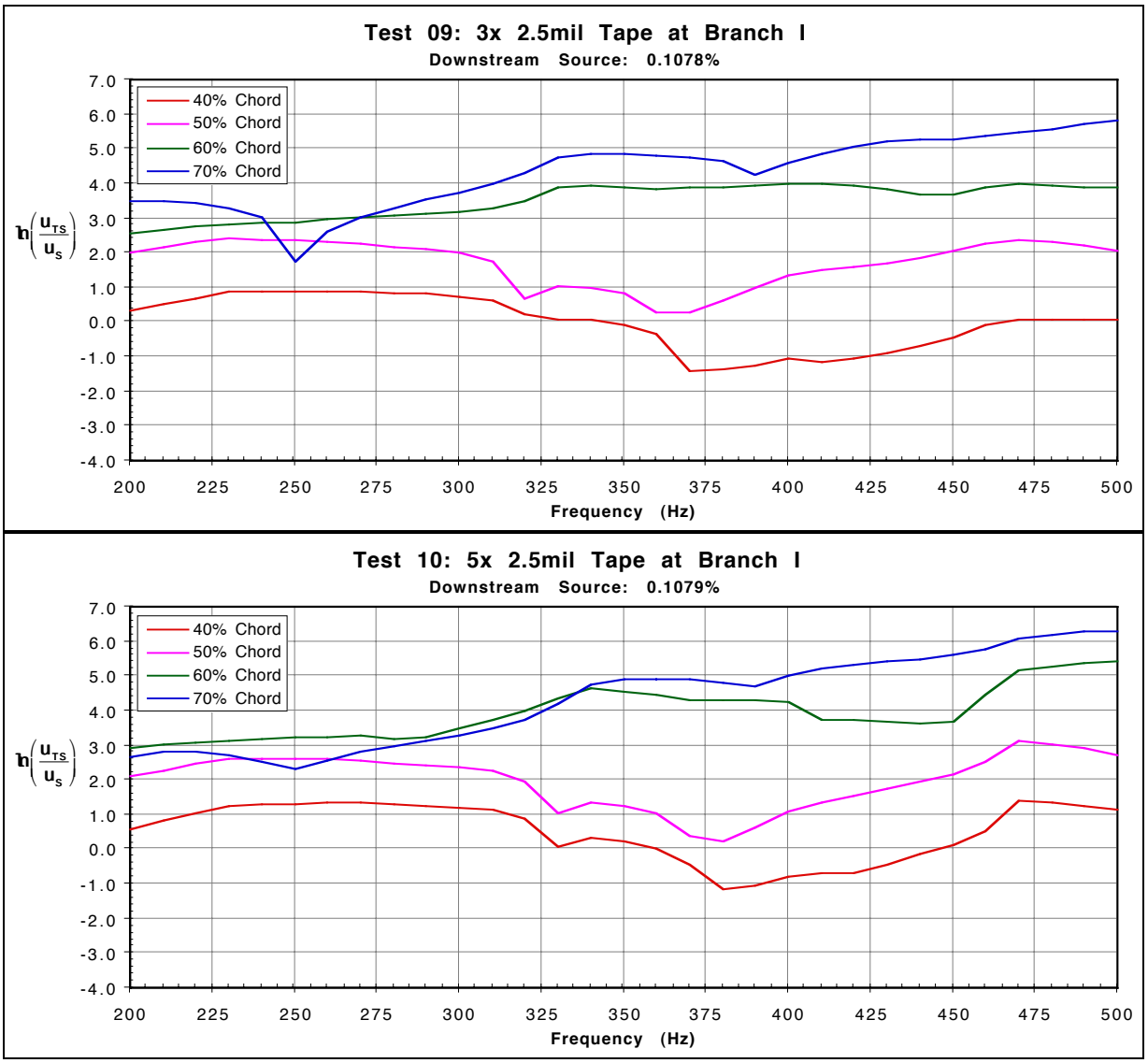

Figure 72: 15 m/s Test Case Boundary-Layer Response Energy Spectra

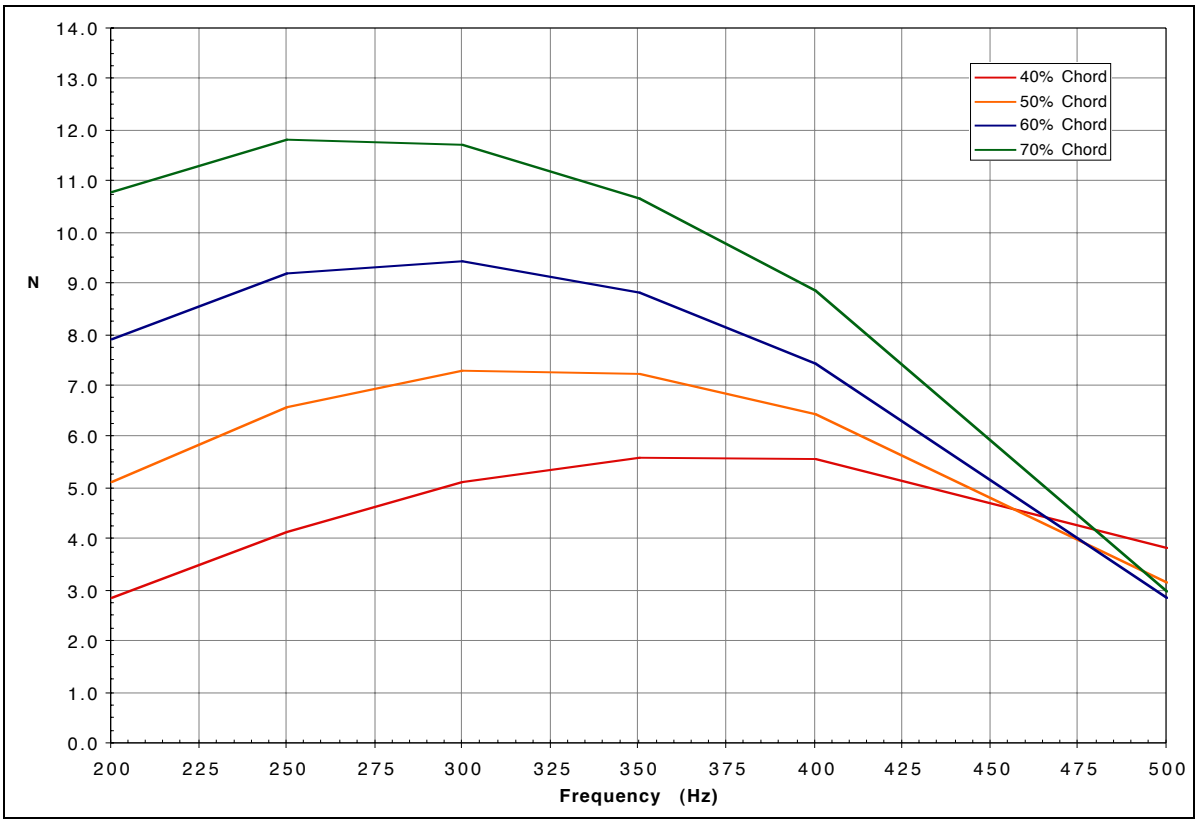

Figure 73: 20 m/s Theoretical Boundary-Layer Response Spectra

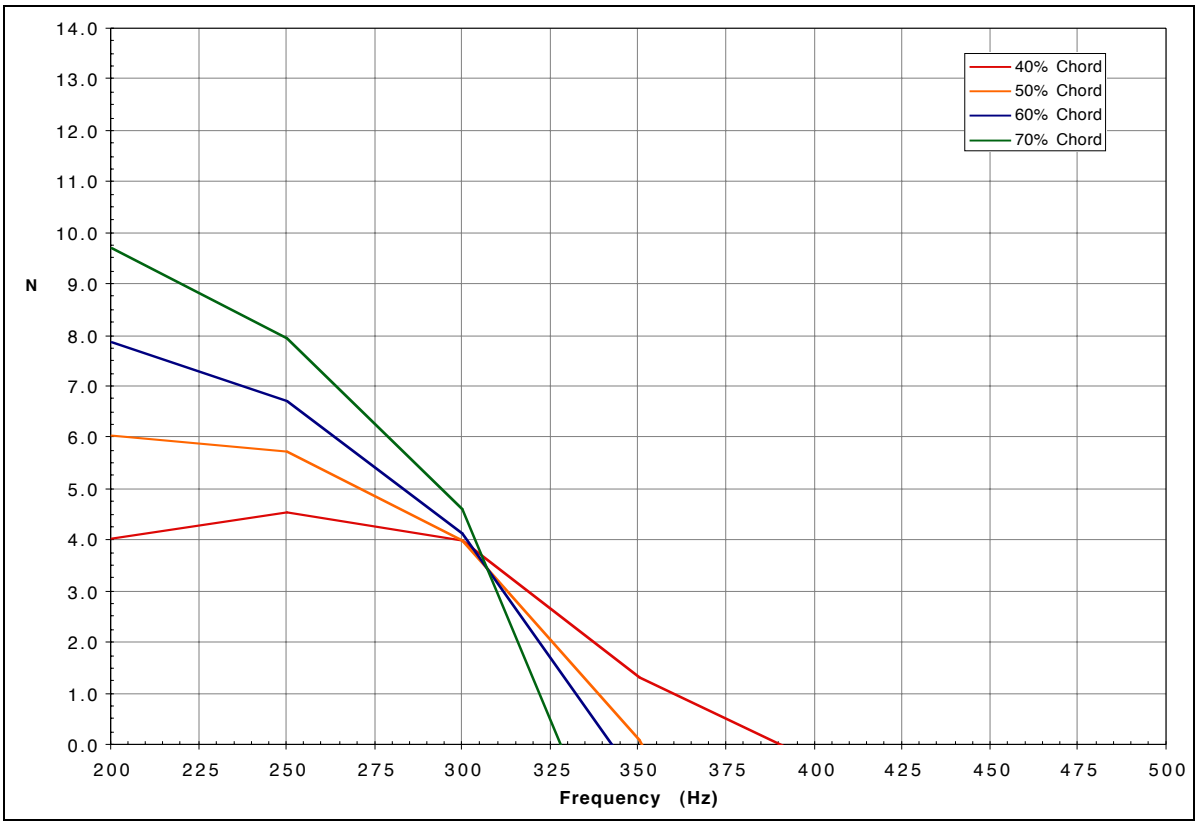

Figure 74: 15 m/s Theoretical Boundary-Layer Response Spectra

5.2.4.7 Total Energy Amplitude Results

While the non-dimensional single-frequency amplitude results examine the boundary-layer responses at particular spectral components, the total energy amplitude results attempt to capture the overall energy contained within the boundary-layer response packets. The results are presented in logarithmic scale except were otherwise noted.

The first characterization of the packet is the peak-to-peak amplitude of the velocity fluctuation. This component is normalized by the tunnel free-stream velocity and presented in **Figures 75**, **76 and 77** for the 20 m/s logarithmic amplitude scale, 20 m/s linear amplitude scale, and 15 m/s logarithmic amplitude scale flow cases, respectively. It can be seen that for the same surface roughness condition, the total energy amplitude of saturation is not constant. In fact, the saturation level is slightly greater for signals that originate from Branch I with higher amplitudes, which are responses from stronger free-stream forcing signals. It is also apparent that the results are striated as expected, where responses from comparable forcing signals indicate a consistency and repeatability of the experimental results.

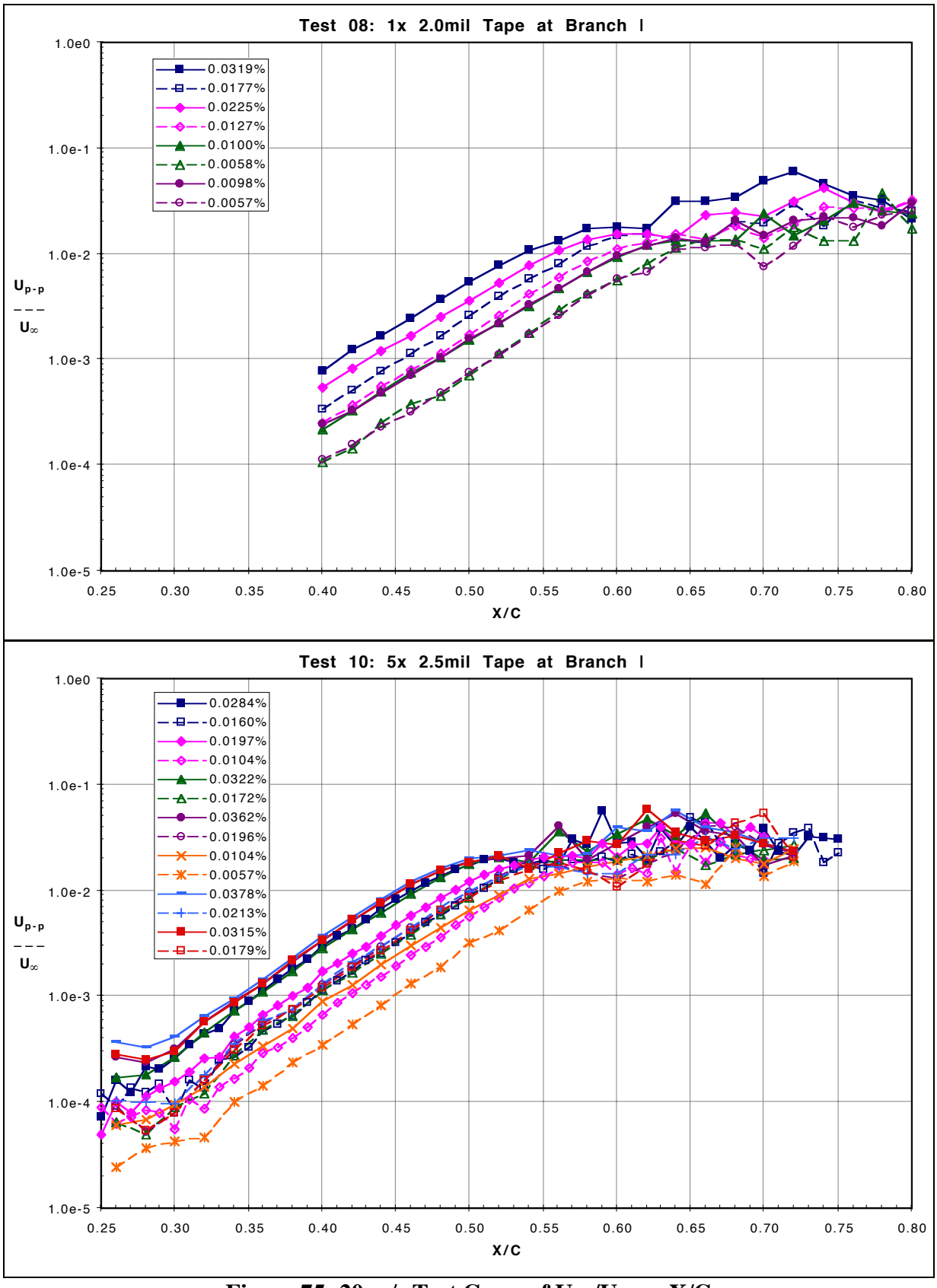

Figure 75: 20 m/s Test Cases of U_{p-p}/U_∞ vs. X/C

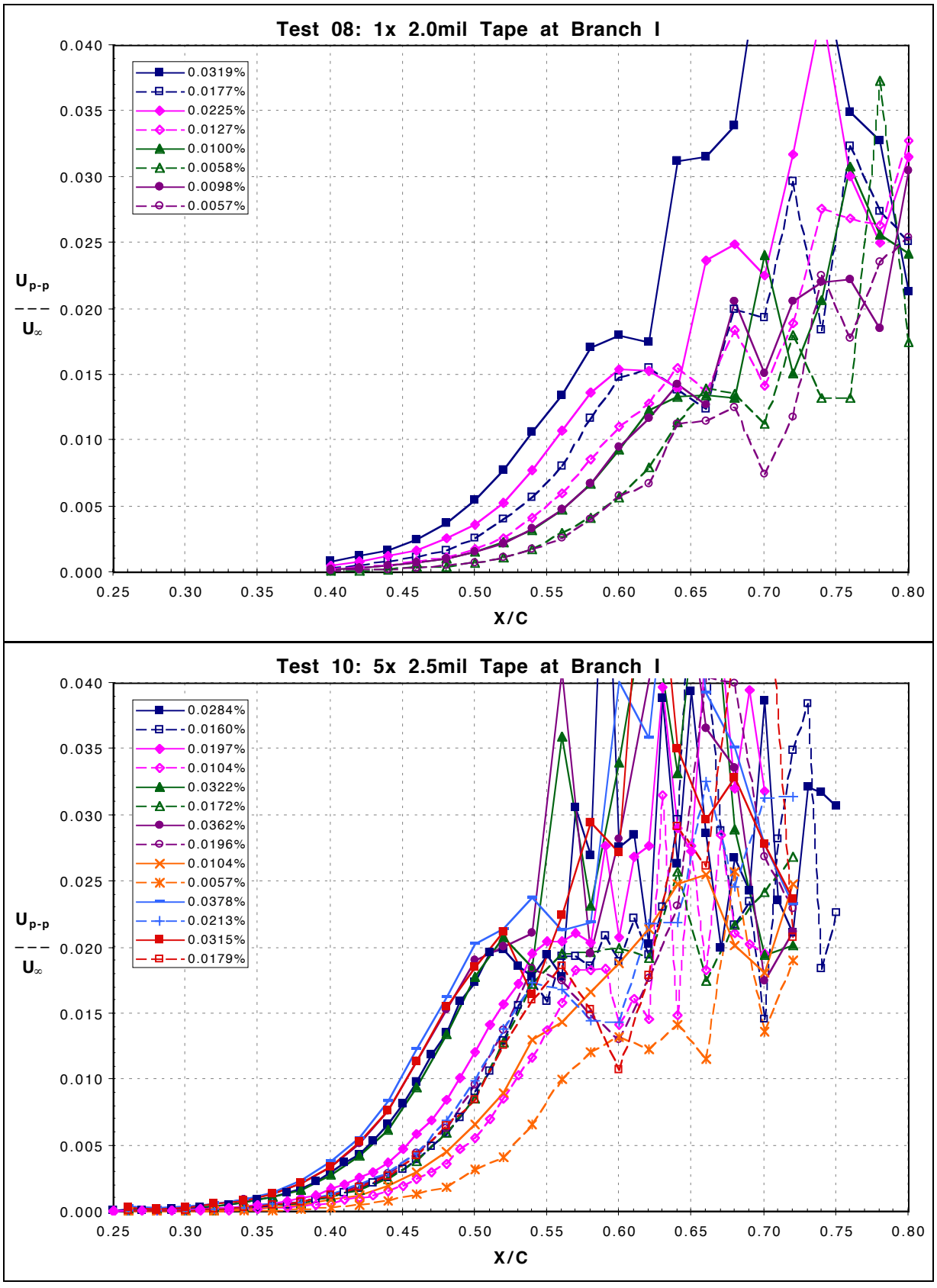

Figure 76: 20 m/s Test Cases of U_{p-p}/U_{∞} vs. X/C - Linear Amplitude Scale

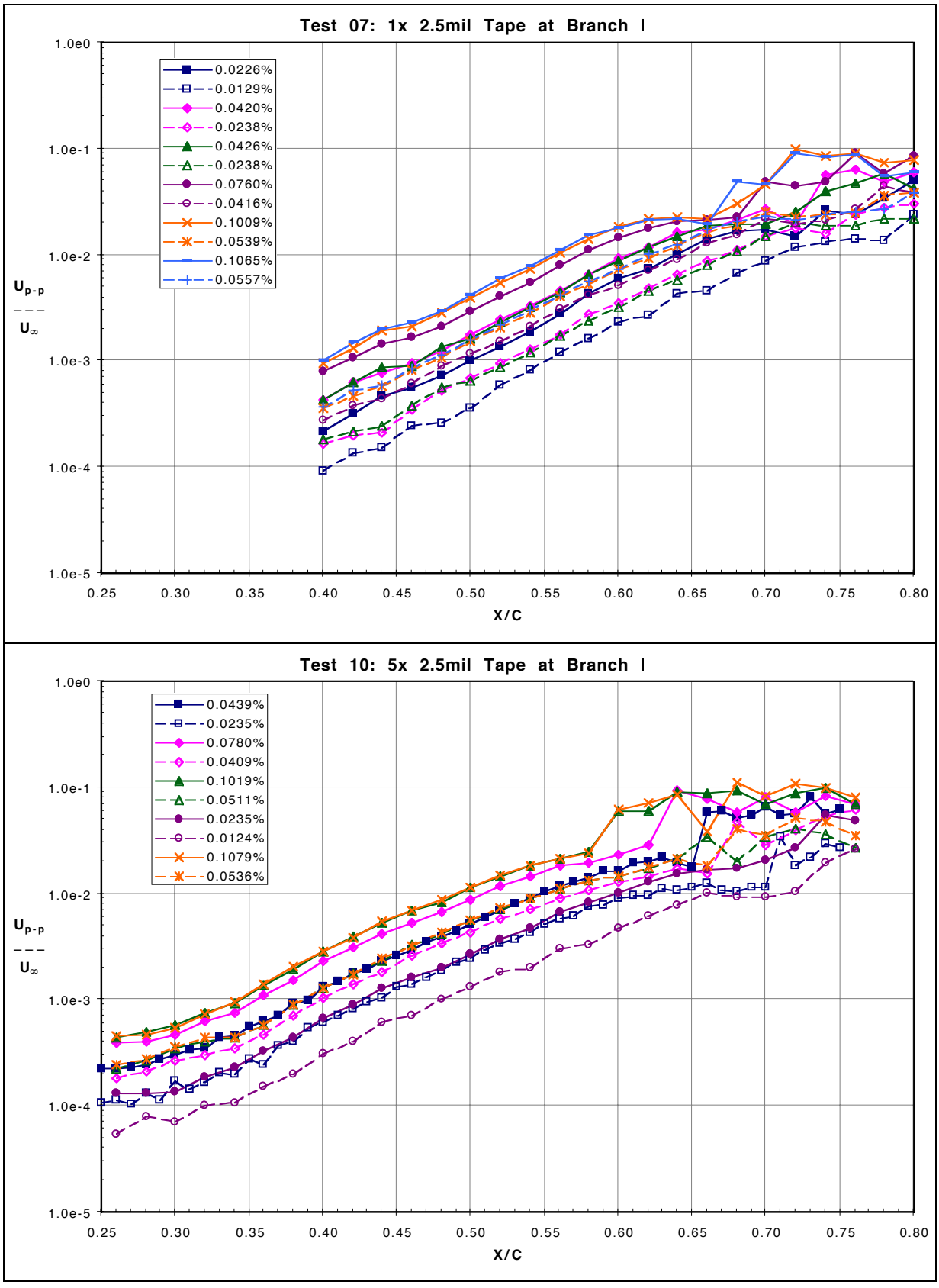

Figure 77: 15 m/s Test Cases of U_{p-p}/U_∞ vs. X/C

While separately examining the above results has its merits, it is also interesting to note how the results relate for comparable forcing signal amplitude, but for different surface roughness conditions. This comparison is made in **Figure 78**. Not much can be concluded from these results about the saturation amplitude because there might be a weak variation in the total energy amplitude or the variation could be a result of scatter in the data.

It is, however, interesting to note the double-humped nature of the curves, particularly evident for the 15 m/s flow case. The second hump arises at the chordwise station that corresponds to where the modeshape at the primary forcing frequency, as well as the disturbance profile no longer are smooth curves (**Sections 5.2.3.1** and **5.2.3.5**), and hence can be considered to be undergoing non-linear effects. This chordwise location also corresponds to the first harmonic of the primary forcing frequency becoming significant in amplitude, as indicated in **Figures 30 and 31**. The hardware filtering of the data considerable attenuated the harmonic for the 20 m/s, 300 Hz case, but close examination of the results does not dispute this issue. The switching of the dominant mode with the first integer harmonic in the non-linear amplification region further supports the hypothesis that a K-type breakdown exists for this experiment.

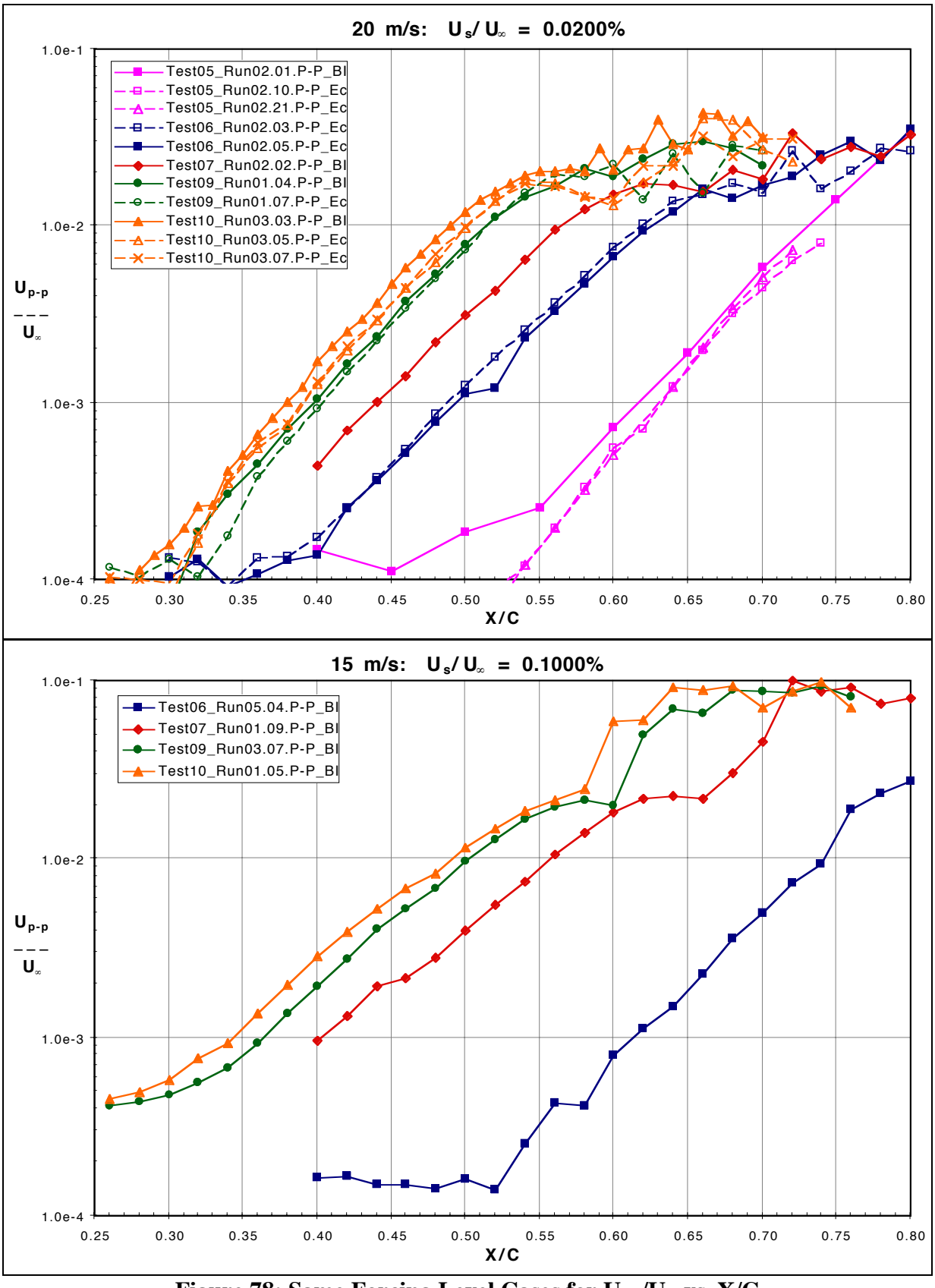

Figure 78: Same Forcing Level Cases for U_{p-p}/U_∞ vs. X/C

In addition, it is also important to present how the results from comparable receptivity magnitudes (comparable initial amplitudes) relate for different surface roughness conditions and different acoustic forcing conditions as in **Figure 79**. It is encouraging to identify that for different receptivity conditions, but the same initial amplitude, the subsequent growth and decay of the disturbance is consistent. These results indicate that there is some absolute breakdown or saturation amplitude for a given initial amplitude of the disturbance. This value is not the same for different initial amplitudes as indicated in this experiment. However, it should be noted that because the location of the breakdown varies with initial amplitude, so do the local mean flow conditions near that location, including pressure gradient and boundary-layer parameters. These results indicate that for the same receptivity mechanism (surface condition), the effects of varying the source amplitude do have an effect on the breakdown amplitude of the boundary-layer response.

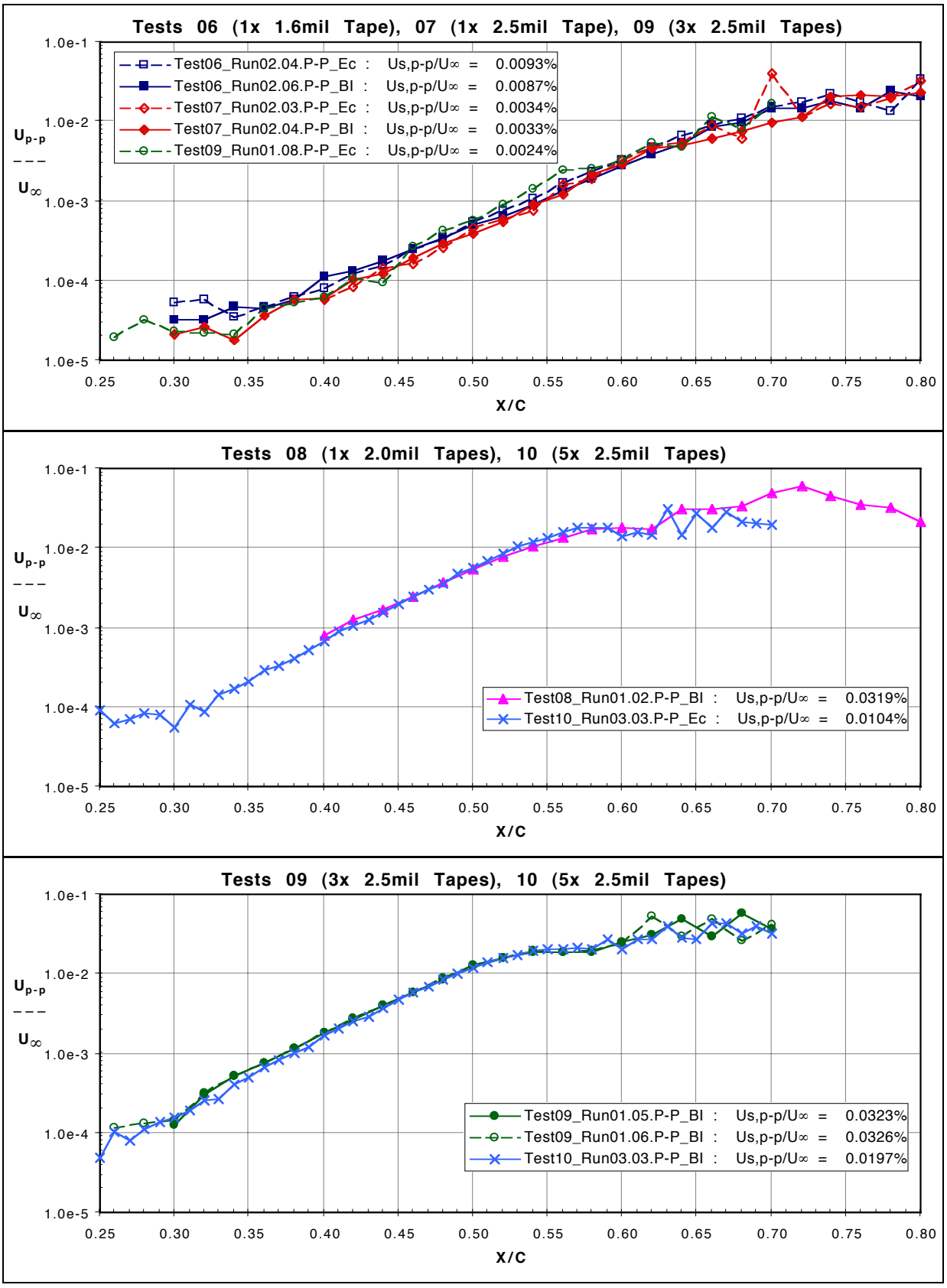

Figure 79: 20 m/s Same Initial Amplitude Cases for $U_{p\text{-}p}/U_\infty$ vs. X/C

The second characterization of the packet is the "energy/RMS" amplitude of the velocity fluctuation. This data is presented in **Figures 80 and 81** for the 20 m/s and 15 m/s flow cases, respectively. The results indicate that the energy/RMS amplitude and the peak-to-peak amplitude both characterize the total amplitude of the disturbance comparably well. Because of extensive regions which correlate well in curve shape with that of linear stability theory, it can be seen that for that process the disturbance is strongly dominated by a limited frequency range.

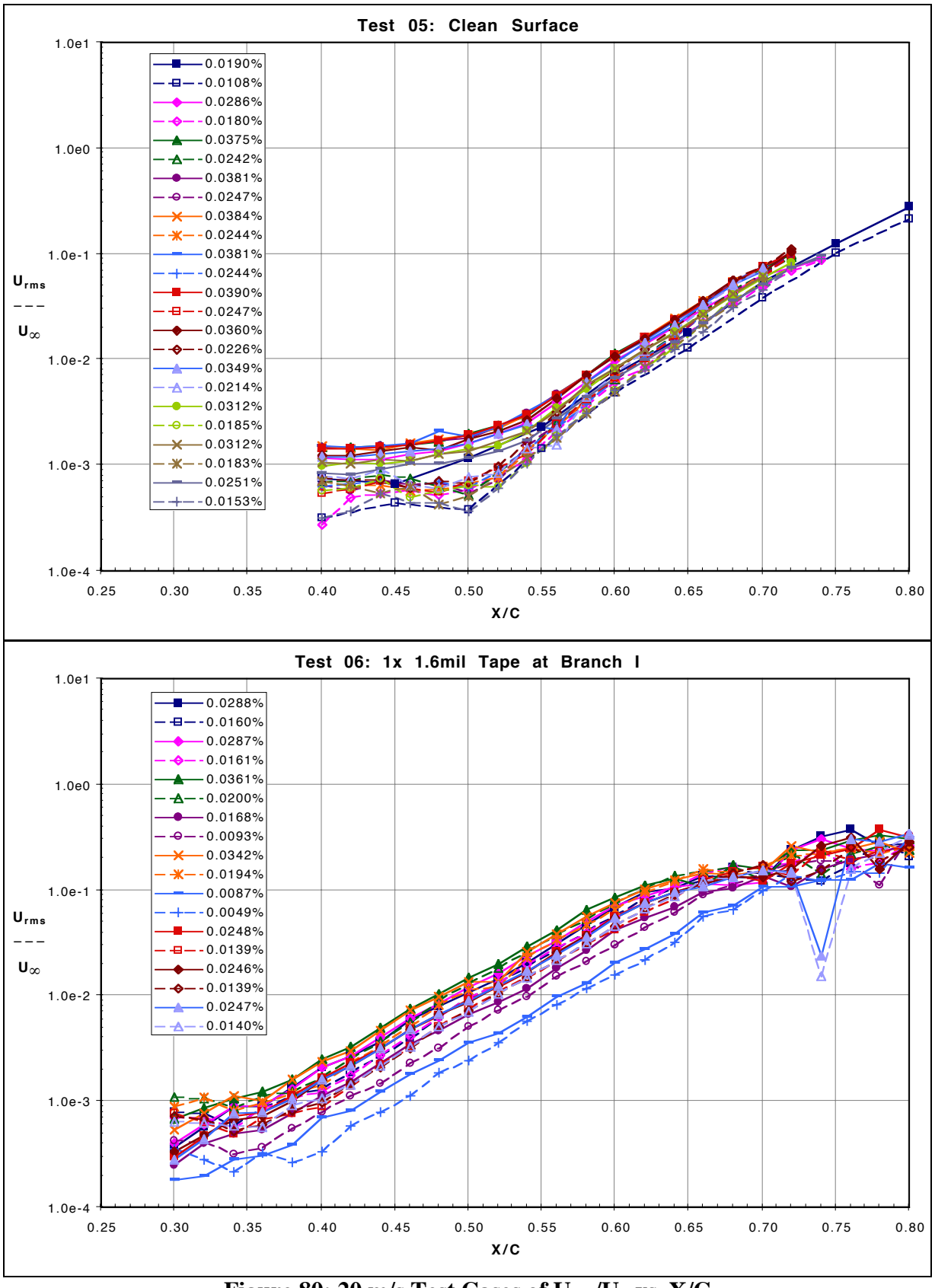

Figure 80: 20 m/s Test Cases of U_{rms}/U_{∞} vs. X/C

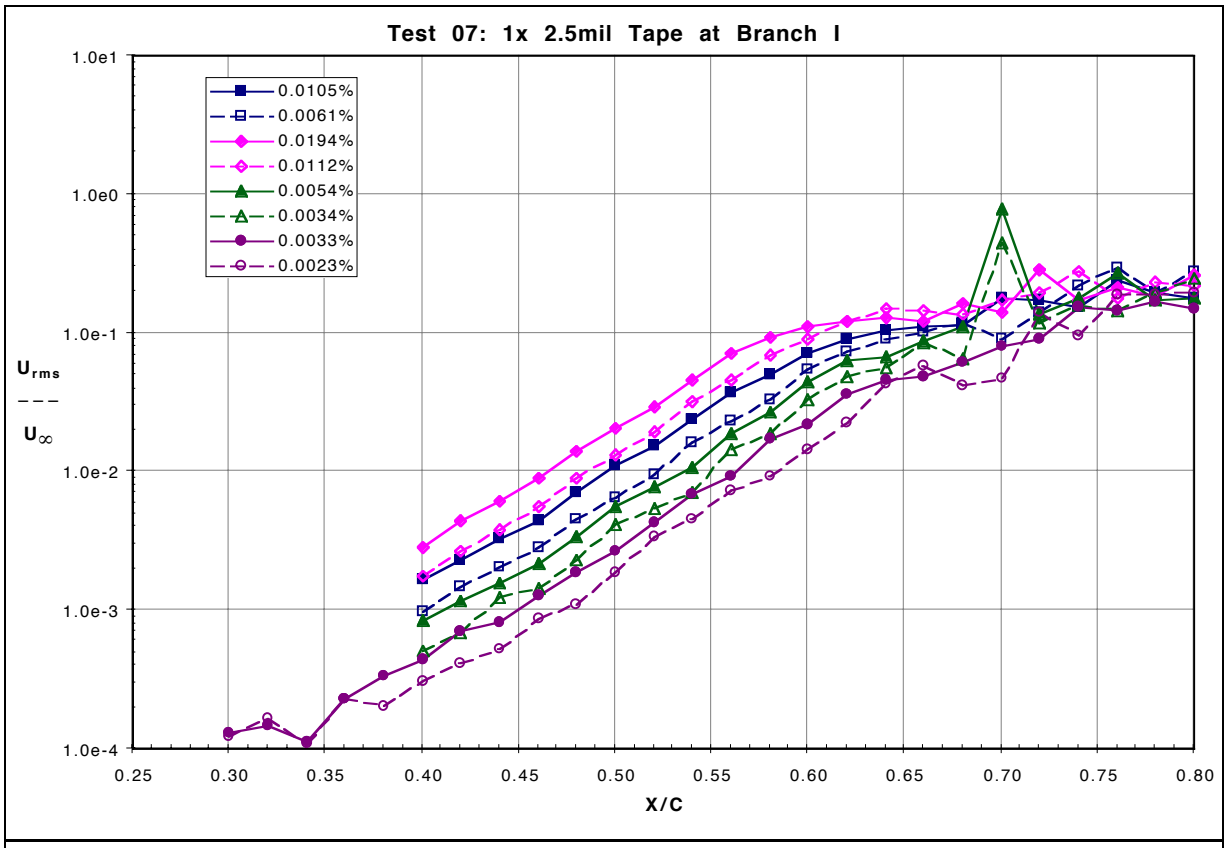

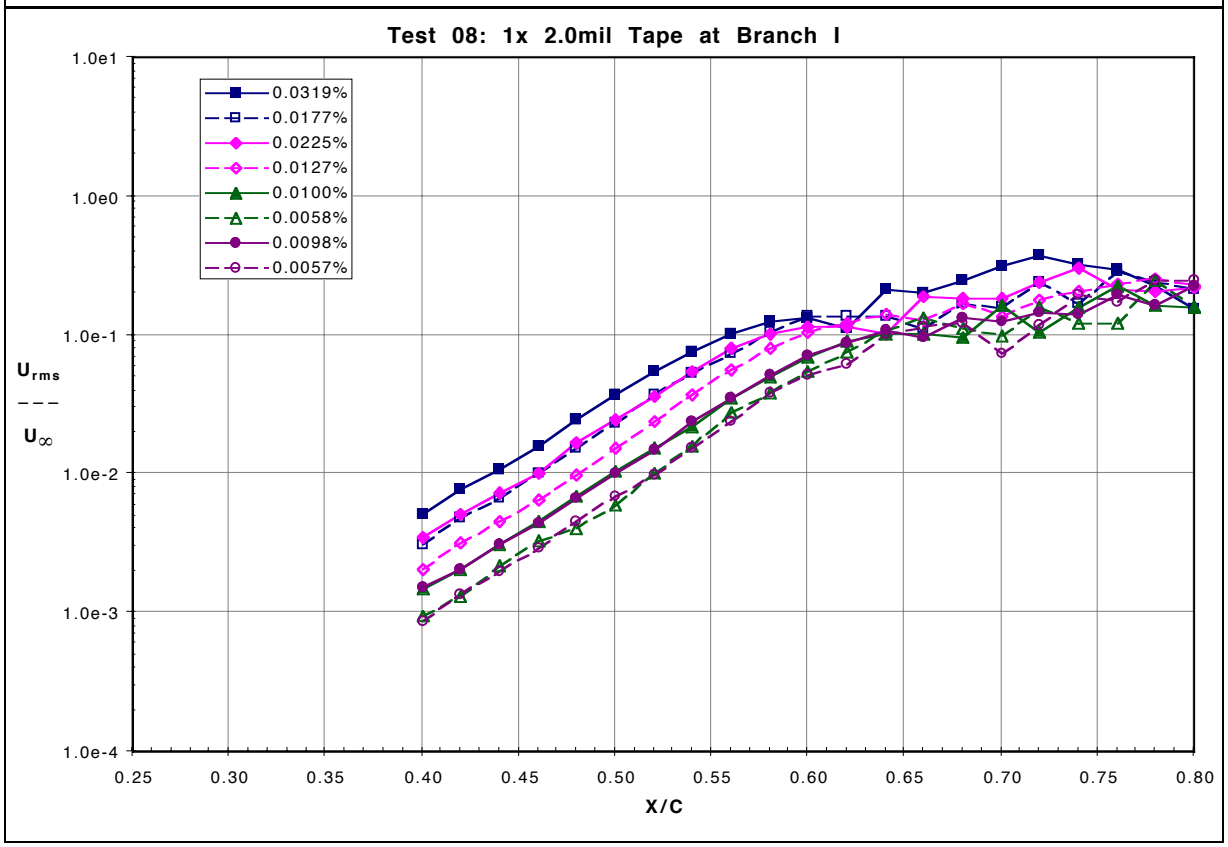

Figure 80: 20 m/s Test Cases of U_{rms}/U_{∞} vs. X/C

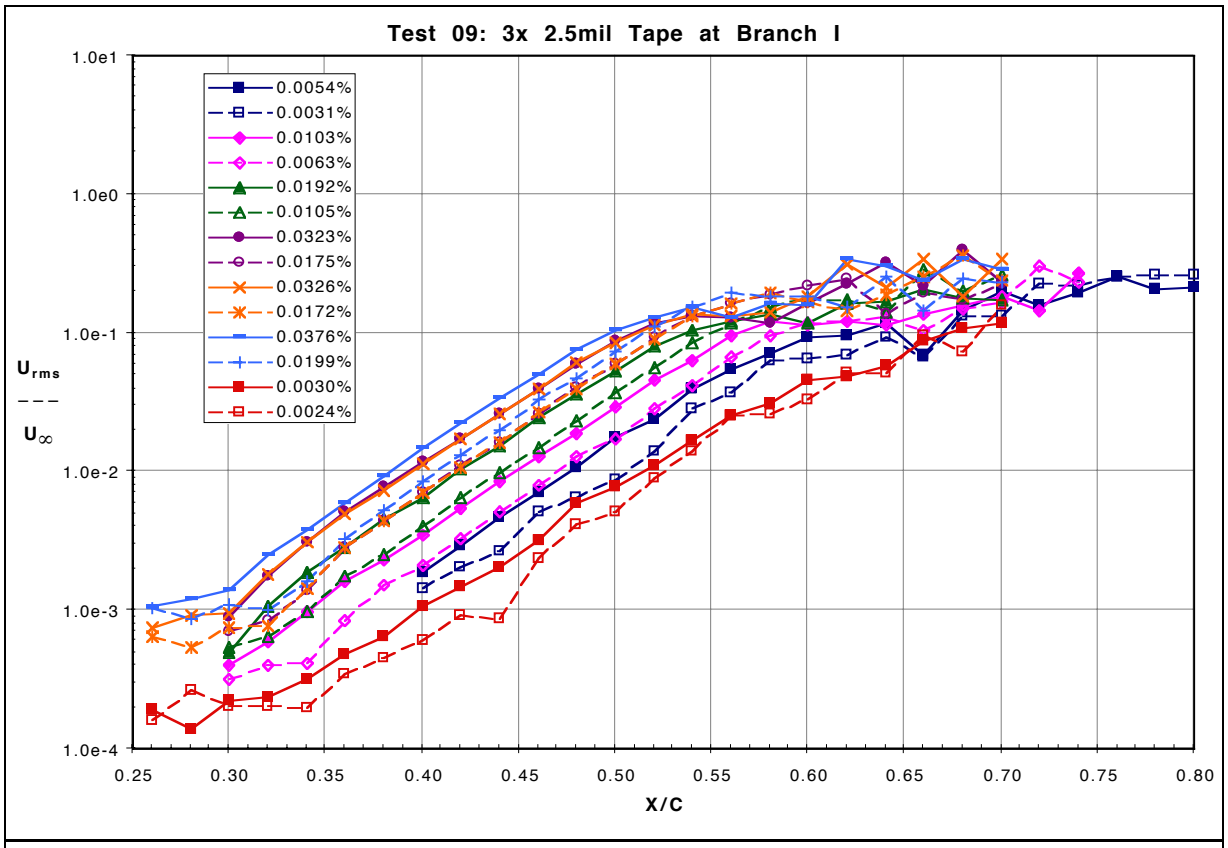

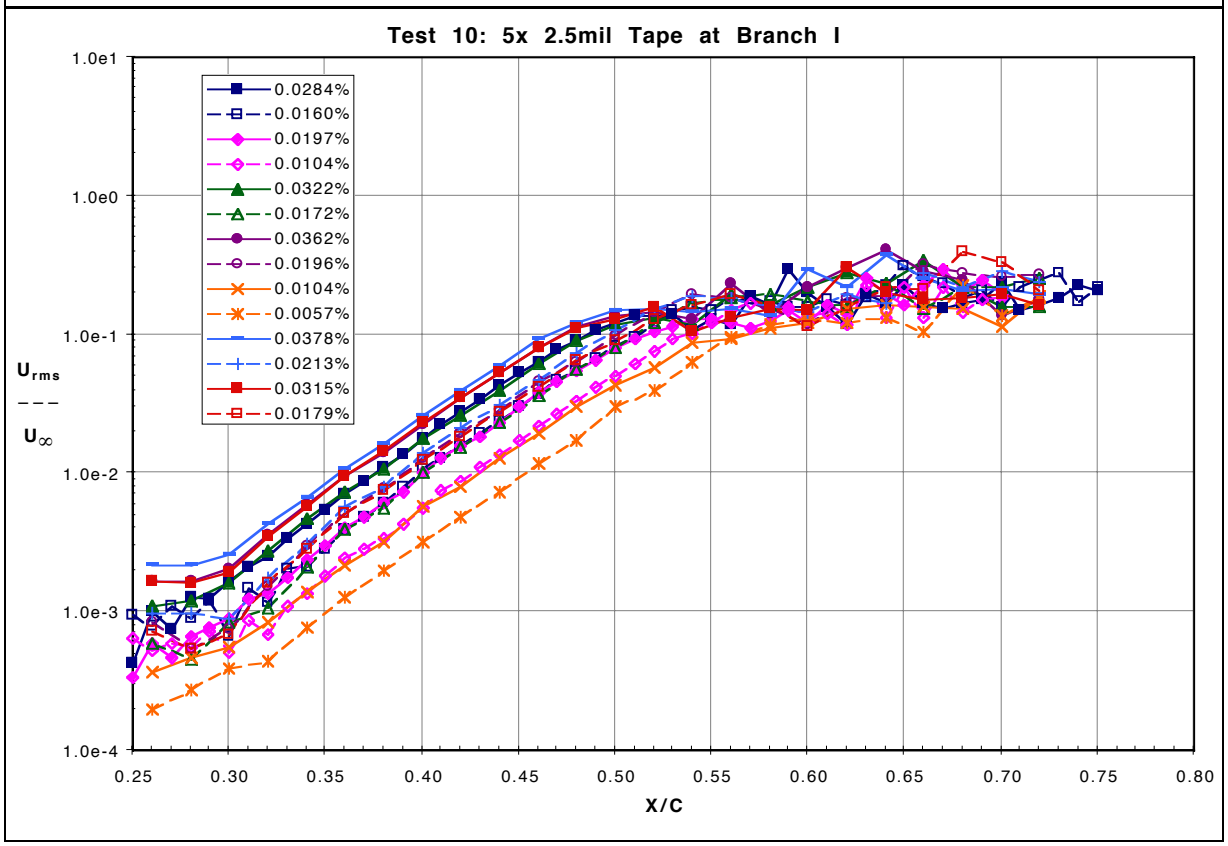

Figure 80: 20 m/s Test Cases of U_{rms}/U_{∞} vs. X/C

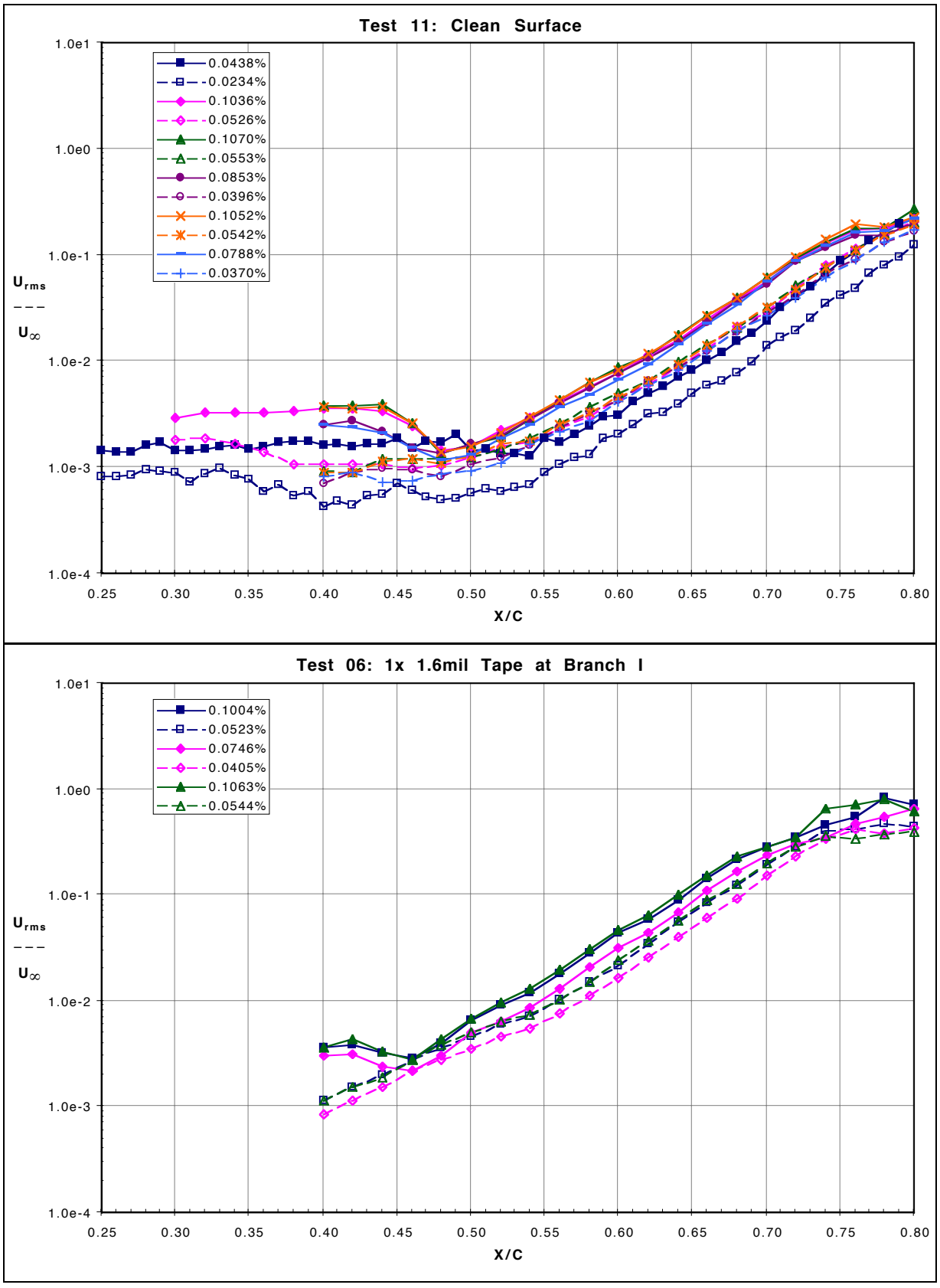

Figure 81: 15 m/s Test Cases of U_{rms}/U_{∞} vs. X/C

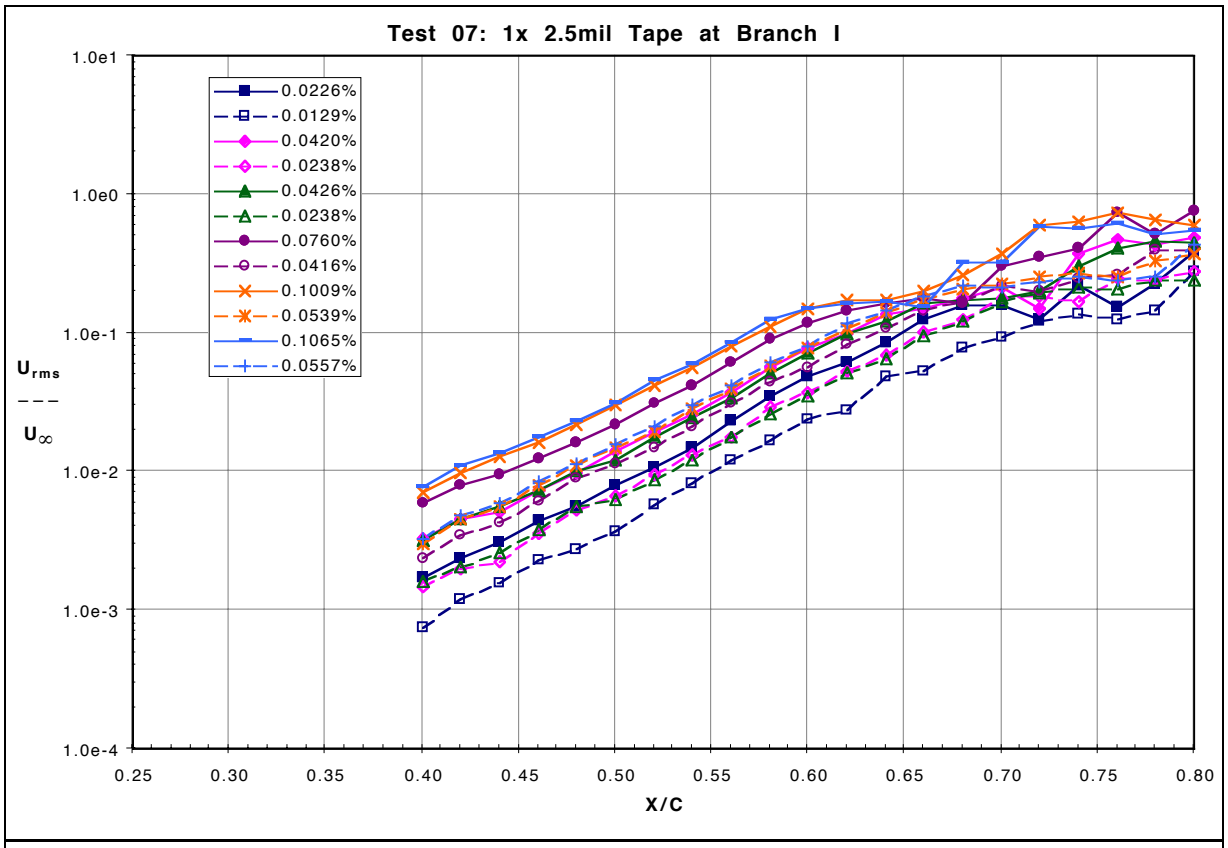

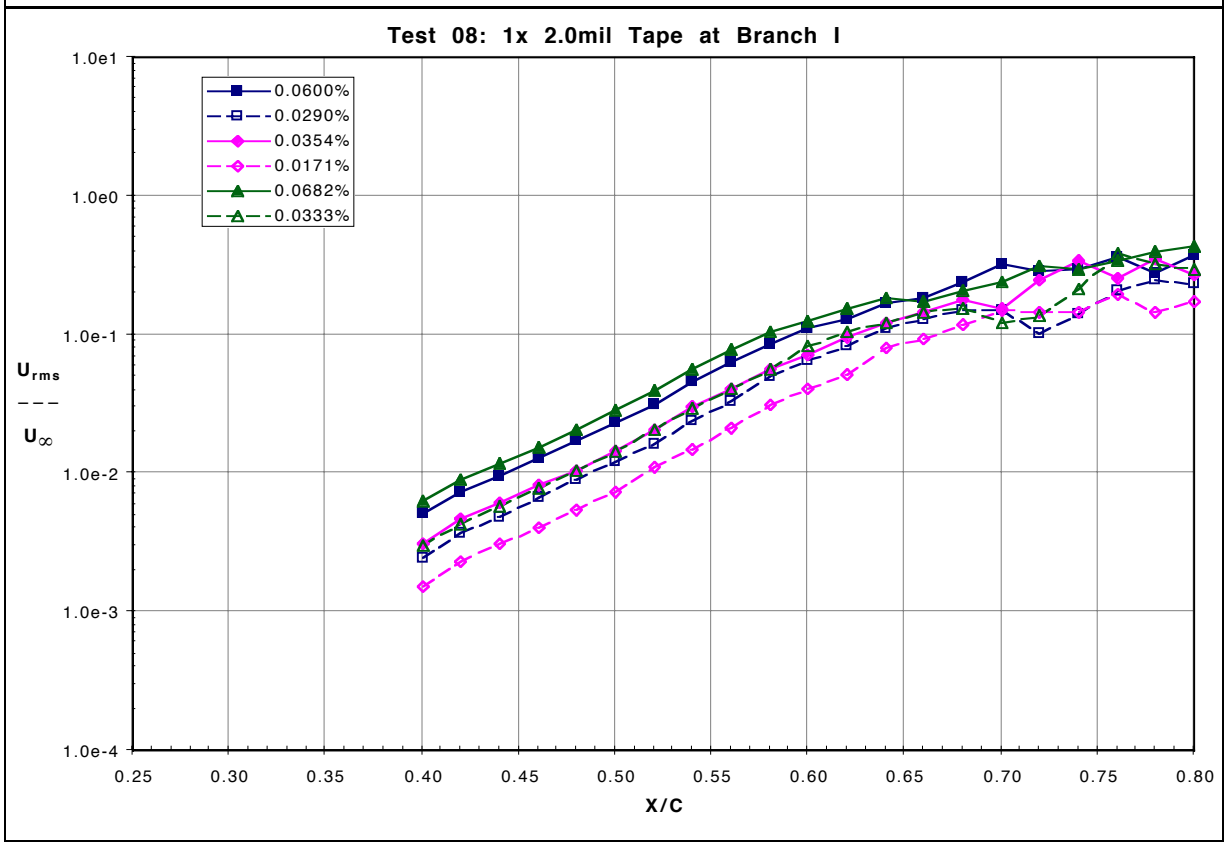

Figure 81: 15 m/s Test Cases of U_{rms}/U_{∞} vs. X/C

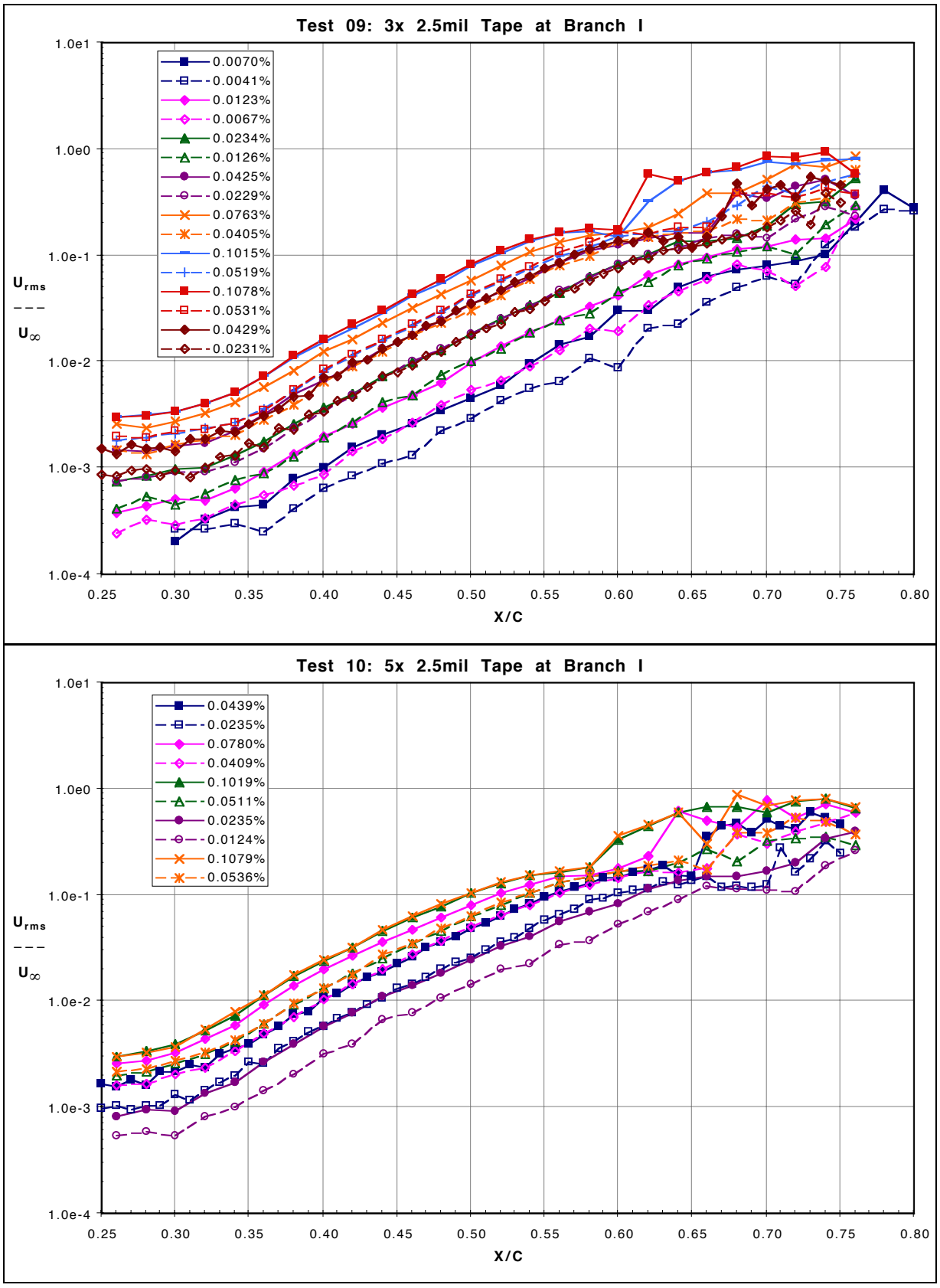

Figure 81: 15 m/s Test Cases of U_{rms}/U_{∞} vs. X/C

5.2.4.8 Amplitude-Based Disturbance Breakdown Criterion for Chordwise Traverse Results

From examining the total energy amplitude results from **Section 5.2.4.7**, another criterion was established to identify the onset of breakdown of the boundary-layer disturbances. This criterion is based upon the amplitude of the upper lobe of the disturbance waveform and is found to be consistent for both of the flow cases examined in this particular facility.

Table 15: Modeshape-Based Disturbance Breakdown Criterion

	Breakdown Amplitude
$U_{p\text{-}p}/U_{\infty}$	1.3 - 2%
U_{rms}/U_{∞}	12 - 16%

A saturation level was not defined because the upper lobe of the disturbance profile never fully saturated. There is a range of breakdown amplitudes possibly due to how effectively the breakdown of the lower lobe feeds into the breakdown of the upper lobe of the disturbance profile.

6 Summary and Conclusions

A boundary-layer experiment was completed at the NASA Langley 2 ft x 3 ft Wind Tunnel Facility using a custom designed airfoil model. The model was a 6% thick, 4 ft chord symmetric wing, and it was designed to provide an extensive region of boundary-layer instability growth, with the lower branch upstream of 20% chord and transition as far downstream as 80% chord. Two flow speed cases were examined, 15 m/s and 20 m/s, which corresponded to chord Reynolds numbers of 1.25 and 1.68 million, respectively. Tollmien-Schlichting (T-S) boundary-layer disturbances were excited by use of free-stream acoustic modulated bursts. Boundary-layer receptivity was varied by use of several two-dimensional roughness heights as well as two-dimensional repeated roughness elements, all located at or about the lower branch for the central forcing frequency. The disturbances were tracked all the way from as close to Branch I as possible through transition to turbulent flow.

During the experiment, three sets of data were acquired; mean flow profiles, boundary-layer modeshapes / disturbance profiles at select chordwise stations and constant boundary-layer height chordwise traverses.

The mean flow results, though consistent throughout the tests, correlated relatively poorly with Euler and integral numerical boundary-layer code solutions. The experimental results revealed a fuller boundary-layer velocity profile, which would indicate an accelerated flow field. This discrepancy could be caused by tunnel wall interference effects on the mean flow field or by mean flow interference of the hot-wire probe support. This significantly affected the displacement thickness results, with deviations of over 20% with respect to theory. However, momentum thickness compared much better, with deviations of just over 10%. While the boundary-layer velocity profiles differed as such, the mean surface pressure distribution compared quite well, typically 10% or better except near the leading edge where C_p was near zero and a percent-deviation measure is a poor representation of the error. The mean surface pressures also indicated a slight flow acceleration across most of the model surface displayed as a slightly more negative C_p-value compared to theory.

All of the acquired fluctuating data was examined in both single-frequency form at the central forcing frequency and in two different total energy amplitude characterizations of the boundary-layer response packet. The total energy amplitude characterizations included the broadband energy, which was the energy from all frequencies in the boundary-layer disturbance.

The modeshape and disturbance profile data was acquired at chordwise stations ranging between 25 and 80% chord and consisted of detailed traverses in the surface-normal direction. The results consistently revealed a T-S modeshape-type fluctuating velocity component with a relatively weak maximum near the outer edge of the boundary layer, a significantly stronger maximum near the wall, and a consistent minimum near $2\delta^*$. All of the above observations tend to indicate that the boundary-layer instabilities were dominated by a narrow band of frequencies in the linear stability regions. The lower lobe of the modeshape was integrated for all frequency components of the modeshape. This result indicated how the energy shifted between frequencies as the disturbance developed along the model chord, showing a rapid development of the $2f$-harmonic at the chordwise station where linear-stability theory started to not adequately represent the data. Linear parabolized stability equation results were compared with some experimental results. These results indicated a match in the general shape function of the modeshape, however there was a poor match of the entire waveform with respect to the relative amplitudes of the upper and lower lobes of the modeshape. A little further downstream, all other frequencies also experienced a significant increase in energy as compared with the central forcing frequency, bringing all spectral components up to comparable amplitude levels. In examining the total energy amplitude disturbance profile development along the model chord, it can be seen that the maximum total energy amplitude appears to be fairly constant for a given flow condition but not strongly dependent upon the acoustic forcing signal strength or surface roughness configuration. It was also apparent that the breakdown of the T-S modeshapes and the disturbance profiles occur in the lower lobe of the waveform where the shear stresses are greatest.

The chordwise boundary-layer traverses were made at constant boundary-layer height, tracking the amplification of the peak of the upper lobe of the T-S disturbance. This boundary-layer height was selected because of the low risk of “missing” the maxima, which was not the case for

tracking the lower peak. However, from the above observation with the modeshape / disturbance profile analysis, it would seem that tracking the upper peak would provide a lag in transition prediction. Using linear parabolized stability equation results, it was verified that the amplification of the upper peak of the modeshape closely follows the amplification of the lower peak with a slight lag, based upon N-factor results. The chordwise traverse results are still quite valuable and provide a finer chordwise resolution for a large variety of acoustic forcing strengths and surface roughness configurations. The results compare quite well with linear-stability theory, deviating at upstream locations and downstream locations, but matching the slope of the N-factor curves at the intermediate chordwise stations. The upstream deviations are due to the fact that the amplitude of the desired boundary-layer signal was below the instrumentation and the facility baseline noise amplitude levels. The downstream deviations are mostly due to non-linear flow effects as actual transition is approached, as well as the influences of the boundary-layer characteristic changes further downstream on the flow field. It was seen that using a linear-stability theory code with the flow field results of an integral boundary-layer solution, which accounted for boundary-layer transition at a fixed chordwise station, provided better comparisons with experiment. The effects of transition altered the mean flow and the boundary layer in a stabilizing way. Also, the observed "transition" or breakdown N-factors ranged from 7 to 11, indicating a strong agreement with previous experimental results.

While the results from this experiment were good and provide adequate depth of detail, there were still several limitations that resulted from the methods used during this research effort, as is the case with all experimental studies. These limitations include mean flow distortion effects, hardware filtering of the fluctuating data, tracking of the upper T-S modeshape maxima, limited acquisition of spanwise data along the model, and imperfect adhesion of the surface roughness elements.

The mean flow data acquisition appears that it might have been affected by the intrusive nature of the hot-wire probe. Future work would benefit from the use of more carefully designed hot-wire probes which would have a small mean flow disturbance field. The use of non-intrusive methods would be ideal, if such methods could achieve the precision of hot-wires as well as the spatial resolution. The mean flow distortion was also likely affected by imperfect setting of the

flexible ceiling and floor of the test section, which were set to simulate an isolated airfoil in the free-stream, but the setting was limited by widely spaced ceiling and floor adjustment jacks as well as by the mounting of the traversing hardware which limited the deflections of the ceiling.

Another limitation of this work was that the data examined was strongly filtered about the primary forcing frequency. The fluctuating data was high-pass filtered at 190 Hz because of a moderately strong 180 Hz signal. The intensity of this mode was a concern because it might have resulted in the loss of precision in the measurements of the desired signal. The data was low-pass filtered at 500 Hz because of how it affected the signal in the time domain. In hindsight, the data should not have been low-pass filtered this low, but instead as a minimum at 1000 Hz, allowing for measurements of multiple harmonics of the primary forcing signal.

The chordwise traverse results were limited to the upper lobe of the T-S modeshape. This lobe experiences a lag in the development of non-linearities as compared with the lower lobe, which is closer to the surface where the shear stresses are the greatest. Even in that limited sense, these results provide much useful data because of the spatial resolution across the model chord. However, future work should include either complete modeshape acquisition or limited range chord-normal data acquisition in the region of the maxima of the lower lobe. Also, the spacing of the chordwise traverses should be finer than used, in order to obtain complete cycles of the T-S disturbance as it propagates along the model surface. The spacing used captured 2 - 3 points per wavelength, whereas at least 8 points per wavelength are recommended. Also, comparisons with linear stability theory and non-linear PSE methods needs to be examined.

While the nature of the flow over the model considered was predominantly two-dimensional, the non-linear effects are typified by three-dimensionality of the developing boundary-layer disturbance. The three-dimensional measurements made during this experiment were limited by the dual-span probe support used because no free-stream measurement of the acoustic disturbance at the local chordwise station could be made.

Lastly, the surface roughness elements did not adhere to the model surface as ideally as possible, particularly at the edges. A higher tack tape should resolve this problem.

In conclusion, a very detailed and complex experiment was performed. The evolution of a travelling Tollmien-Schlichting boundary-layer disturbance was tracked over an airfoil surface. The airfoil surface was significant because all similar work has been performed over flat plates. The continuously varying surface curvature, varying pressure gradient and non-similar boundary layer add to the complexity of the problem. Numerous detailed measurements were made over the model including mean flow and fluctuating data measurements. Mean flow measurements included mean pressure measurements, angle of attack measurements and boundary-layer velocity profile measurements, the latter which provided the data to determine the boundary-layer integral parameters such as displacement thickness and momentum thickness. Fluctuating data measurements included surface-normal instability and modeshape measurements, constant boundary-layer height chordwise traverses and the determination of receptivity coefficients and N-factors. With these detailed results, the effects of surface roughness and free-stream acoustic forcing on boundary-layer receptivity and the subsequent amplification of boundary-layer disturbances was examined in a well documented disturbance environment. These results will be used to validate and refine non-linear flow theories as well as help to provide an improved understanding and improved methods to control flow transition.

7 References

[1] Saric, William S., 1994. *Physical Description of Boundary-Layer Transition: Experimental Evidence*., AGARD Report 793, Special Course on Progress in Transition Modelling (sic).

[2] Bushnell, D.M. and Malik, M.R., 1985. *Application of Stability Theory to Laminar Flow Control – Progress and Requirements*. Stability of Time Dependent and Spatially Varying Flows, Eds. D.L. Dwoyer asnd M.Y. Hussaini. Springer-Verlag, New York: pp. 1-17.

[3] Pfenninger, W., Vemuru, C.S., and Viken, J., 1987. *About the Design Philosophy of Long Range LFC Transports with Advanced Supercritical LFC Airfoils*. AIAA Paper No. 87-1284.

[4] Tollmien, W., 1931. *The Production of Turbulence*. NACA Technical Memorandum 609. [Translated from *Aus den Nachrichten der Gesellschaft der Wissenschaften zu Göttingen*. (Mathematisch-Physikalische Klasse).1929].

[5] Tollmien, W., 1936. *General Instability Criterion of Laminar Velocity Distributions*. NACA Technical Memorandum 792. [Translated from *Nachrichten von der Gesellschaft der Wissenschaften zu Göttingen.* Mathematik. Vol. I, No. 5. 1935].

[6] Schlichting, H. 1932. *On the Generation of Turbulence in a Rotating Cylinder*. Nachr. Göttingen M.P.K. 1932 p. 160. (German Only)

[7] Schlichting, H., 1944. *On the Production of Turbulence in Flow Along a Plate*. Commonwealth of Australia Council for Scientific and Industrial Research Division of Aeronautics Translation No. 6. [Translated from *Zur Entstehung Der Turbulenz Bei Der Plattenstromung*. (Nachr. Göttingen M.P.K. 1933, s. 181-208]

[8] Rosenhead, L., 1963. Laminar Boundary Layers. Dover Publications, New York.

[9] Schubauer, G.B., and Skramstad, H.K., 1948. *Laminar-Boundary-Layer Oscillations and Transition on a Flat Plate*. NACA Report No. 909. (Originally issued April 1943 as an NACA Advance Confidential Report)

[10] Harris, Roy V., Jr. and Hefner, Jerry N., 1987. *NASA Laminar-Flow Program – Past, Present, Future* in Research in Natural Laminar Flow and Laminar-Flow Control. NASA Conference Publication 2487: Part 1: pp. 1-23.

[11] Morkovin, Mark V., 1969. *Critical Evaluation of Transition from Laminar to Turbulent Shear Layers with Emphasis on Hypersonically Traveling Bodies*. AFFDL-TR-68-149.

[12] Bushnell, D.M., and Tuttle, M.H., 1979. *Survey and Bibliography on Attainment of Laminar Flow Control in Air Using Pressure Gradient and Suction – Vol. I.* NASA Reference Publication 1035.

[13] Tuttle, Marie H., and Maddalon, Dal V., 1993. *Laminar Flow Control (1976-1991): A Comprehensive, Annotated Bibliography*. NASA Technical Memorandum 107749.

[14] Murdock, J.W., 1980. *The generation of a Tollmien-Schlichting wave by a sound wave*. Proc. R. Soc. Lond. A., Vol. 372: pp. 517-534.

[15] Goldstein, M.E., 1983. *The evolution of Tollmien-Schlichting waves near a leading edge*. J. Fluid Mech., Vol. 127: pp. 59-81.

[16] Goldstein, M.E., Sockol, P.M., and Sanz, J., 1983. *The evolution of Tollmien-Schlichting waves near a leading edge. Part 2. Numerical determination of amplitudes*. J. Fluid Mech., Vol. 129: pp. 443-453.

[17] Lam, S.H., and Rott, N., 1960. *Theory of Linearized Time-Dependent Boundary Layers*. Cornell Univ. Grad. School of Aero. Engng Rep. AFOSR TN-60-1100.

[18] Ackerberg, R.C., and Phillips, J.H., 1972. *The unsteady laminar boundary layer on a semi-infinite flat plate due to small fluctuations in the magnitude of the free-stream velocity*. J. Fluid Mech. Vol. 51, Part 1: pp. 137-157.

[19] Reed, Helen L., Saric, William S., and Arnal, Daniel, 1996. *Linear Stability Theory Applied to Boundary Layers*. Annu. Rev. Fluid Mech., Vol. 28: pp. 389-428.

[20] Smith, A.M.O., 1955. *On the Growth of Taylor-Görtler Vortices Along Highly Concave Walls*. Q. Appl. Math. Vol. 13: pp. 233-262.

[21] Radeztsky, R.H., Reibert, M.S., Saric, W.S., and Takagi, S., 1993. *Effect of Micron-Sized Roughness on Transition in Swept-Wing Flows*. AIAA Paper No. 93-0076.

[22] Gaster, M., 1978. *The Physical Processes Causing Breakdown to Turbulence*. 12th Naval Hydrodynamics Symposium, Washington.

[23] Heinrich, R.A., Choudhari, M., and Kerschen, E.J., 1988. *A Comparison of Boundary Layer Receptivity Mechanisms*. AIAA Paper No. 88-3758.

[24] Morkovin, M.V., 1958. *Transition From Laminar to Turbulent Shear Flow – A Review of Some Recent Advances in Its Understanding*. Transactions of the ASME: pp. 1121-1128.

[25] Reshotko, Eli, 1976. *Boundary-Layer Stability and Transition.* Ann. Rev. Fluid Mech. Vol. 8: pp. 311-349.

[26] Ruban, A.I., 1985. *On the Generation of Tollmien-Schlichting Waves by Sound*. Fluid Dynamics, Vol. 19: pp. 709-716.
[27] Choudhari, Meelan and Streett, Craig L., 1994. *Theoretical Prediction of Boundary-Layer Receptivity*. AIAA Paper No. 94-2223.
[28] Choudhari, Meelan, 1994. *Effect of Nonzero Surface Admittance on Receptivity and Stability of Compressible Boundary Layer*. NASA Contractor Report 4621.
[29] Choudhari, Meelan, 1994. *Distributed acoustic receptivity in laminar flow control configurations*. Phys. Fluids, Vol. 6, No. 2: pp. 489-506.
[30] Choudhari, Meelan, 1994. *Acoustic Receptivity of Compressible Boundary Layers: Receptivity via Surface-Temperature Variations*. NASA Contractor Report 4599.
[31] Smith, Janice Marie, 1995. *The Effect of Localized Heating on Boundary-Layer Stability and Receptivity*. The George Washington University, Master of Science Thesis.
[32] Choudhari, Meelan, 1992. *Boundary-Layer Receptivity due to Distributed Surface Imperfections of a Deterministic or Random Nature*. Theoret. Comput. Fluid Dynamics.
[33] Saric, William S., Hoos, Jon A., and Radeztsky, Ronald H., 1992. *Boundary-Layer Receptivity of Sound with Roughness*. FED-Vol.114, Boundary Layer Stability and Transition to Turbulence, ASME: pp. 17-22.
[34] Spencer, Shelly Anne, 1992. *Boundary-Layer Receptivity: Freestream Sound with Three-Dimensional Roughness*. Arizona State University, Master of Science Thesis.
[35] Bodonyi, R.J., Welch, W.J.C., Duck, P.W., and Tadjfar, M., 1989. *A numerical study of the interaction between unsteady free-stream disturbances and localized variations in surface geometry*. J. Fluid Mech. Vol. 209: pp. 285-308.
[36] Nayfeh, A.H. and Ashour, O.N., 1994. *Acoustic receptivity of a boundary-layer to Tollmien-Schlichting waves resulting from a finite-height hump at finite Reynolds numbers*. Phys. Fluids, Vol. 6, No. 11: pp. 3705-3716.
[37] Wiegel, Markus, 1992. *Acoustic Receptivity of Laminar Boundary-Layers Over Wavy Walls*, Illinois Institute of Technology, Master of Science Thesis.
[38] Saric, W.S., 1994. *Low-Speed Boundary-Layer Transition Experiments*. In Transition: Experiments, Theory & Computations. Eds. T.C. Corke, G. Erlebacher, and M.Y. Hussaini, Oxford.
[39] Goldstein, M.E. and Hultgren, L.S., 1989. *Boundary-Layer Receptivity to Long-Wave Free-Stream Disturbances*. Ann. Rev. Fluid Mech.,Vol. 21: pp. 137-66.
[40] Crouch, J.D., *Theoretical Studies on the Receptivity of Boundary Layers*. AIAA Paper No. 94-2224 (1994).
[41] Saric, W.S., Reed, H.L. and Kerschen, E.J., 1994. *Leading Edge Receptivity to Sound Experiments, DNS and Theory*. AIAA Paper No. 94-2222.
[42] Hammerton, P.W., and Kerschen, E.J., 1992. *Effect of Nose Bluntness on Leading-Edge Receptivity*. In Instability, Transition and Turbulence, Eds. M.Y. Hussaini, A. Kumar, and C.L. Streett. Springer-Verlag, New York: pp. 441-451.
[43] Hammerton, P.W., and Kerschen, E.J., 1996. *Boundary-layer receptivity for a parabolic leading edge*. J. Fluid Mech., Vol. 310: pp. 243-267.
[44] Kerschen, E.J., 1990. *Boundary-Layer Receptivity Theory*. Appl. Mech. Rev. Vol. 43, No. 5, part 2, S152.
[45] Goldstein, M.E., 1985. *Scattering of acoustic waves into Tollmien-Schlichting waves by small streamwise variations in surface geometry*. J. Fluid Mech.Vol. 154: pp. 509-529.
[46] Gaster, M. 1982. *The Development of a 2-Dimensional Wavepacket in a Growing Boundary-Layer*. Proc. R. Soc. Lond. A, Vol. 384, No. 1787: pp. 317-332.
[47] Shaikh, F.N., and Gaster, M. 1994. *The Nonlinear Evolution of Modulated Waves in a Boundary-Layer*. J. Eng. Math., Vol. 28, No. 1: pp. 55-71.
[48] Medeiros, M.A.F., and Gaster, M., 1996. *The Nonlinear Behavior of Modulated Tollmien-Schlichting Waves*, IUTAM Symposium on Nonlinear Instability and Transition in Three-Dimensional Boundary Layers. Kluwer Academinc Publishers, Netherlands: pp. 197-206.
[49] Saric, W.S., Wei, W., Rasmussen, B.K., and Krutckoff, T.K., 1995. *Experiments on Leading-Edge Receptivity to Sound*. AIAA Paper No. 95-2253.
[50] Saric, William S., and White, Edward B., 1998. *Influence of High-Amplitude Noise on Boundary-Layer Transition to Turbulence*. AIAA Paper No. 98-2645.
[51] Wlezien, R.W., 1994. *Measurement of Acoustic Receptivity*. 25th AIAA Fluid Dynamics Conference. AIAA Paper No. 94-2221.
[52] Dietz, A., 1996. *Distributed Boundary Layer Receptivity to Convected Vorticity*. AIAA Paper No. 96-2083.

[53] Dietz, A.J., 1997. *Boundary Layer Receptivity to Transient Convected Disturbances*. AIAA Paper No. 97-1962.
[54] Dietz, Anthony J., 1998. *Boundary-Layer Receptivity to Transient Convected Disturbances*. AIAA Journal , Vol. 36, No. 7: pp. 1171-1177.
[55] Mack, Leslie M., 1984. *Boundary-Layer Linear Stability Theory*. Agard Report No. 709. Special Course on Stability and Transition of Laminar Flow.
[56] Smith, A.M.O., and Gamberoni, Nathalie, 1956. *Transition, Pressure Gradient, and Stability Theory*. Douglas Aircraft Co., El Segundo, CA, Report ES 26388.
[57] Van Ingen, J.L., 1956. *A suggested semi-empirical method for the calculation of the boundary layer transition region*. Univ. of Technology, Dept. of Aero. Eng., Report V.T.H.-74, Delft, Holland.
[58] Malik, Mujeeb R., 1990. *Stability Theory for Laminar Flow Control Design*. Viscous Drag Reduction in Boundary Layers, Dennis M. Bushnell and Jerry N. Hefner, editors, Vol. 123 of Progress in Astronautics and Aeronautics, AIAA.
[59] Kerschen, E.J., 1989. *Boundary Layer Receptivity*. AIAA Paper No. 89-1109.
[60] Haynes, T.S., Reed, H.L., and Saric, W.S., 1996. *CFD Validation Issues in Transition Modeling*. AIAA Paper No. 96-2051.
[61] Reed, Helen L., Haynes, Tim S., and Saric, William S., 1998. *Computation Fluid Dynamics Validation Issues in Transition Modeling*. AIAA Journal, Vol. 36, No. 5: pp. 742-751.
[62] Kendall, James M., 1998. *Experiments on Boundary-Layer Receptivity to Freestream Turbulence*. AIAA Paper No. 98-0530.
[63] Giles, Michael B. and Drela, Mark, 1987. *Two-Dimensional Transonic Aerodynamic Design Method*. AIAA Journal Vol. 25, No. 9: pp. 1199-1206.
[64] Drela, Mark and Giles, Michael B., 1987. *Viscous-Inviscid Analysis of Transonic and Low Reynolds Number Airfoils*. AIAA Journal Vol. 25, No. 10: pp. 1347-1355.
[65] Drela, Mark, 1990. *Newton Solution of Coupled Viscous / Inviscid Multielement Airfoil Flows*. AIAA Paper No. 90-1470.
[66] Wie, Yong-Sun, 1992. *BLSTA -- A Boundary Layer Code for Stability Analysis*. NASA Contractor Report 4481.
[67] Benney, David J., and Orszag, Steven A., 1977. *Stability Analysis for Laminar Flow Control: Part I*. NASA Contractor Report 2910.
[68] Orszag, Steven A., *Stability Analysis for Laminar Flow Control: Part II*. NASA Contractor Report 3249 (1980).
[69] Innovative Aerodynamic Technologies. 1997. LAMDA: Laminar Airfoil Manager GUI for Design and Analysis Version 3.01. User's Manual.
[70] Bauer, Frances, Garabedian, Paul, and Korn, David, 1977. Supercritical Wing Sections III. Springer-Verlag, New York.
[71] Bauer, F., Garabedian, P., and McFadden, G., 1983. *The NYU Inverse Swept Wing Code*. NASA Contractor Report 3662.
[72] Kaups, Kalle, and Cebeci, Tuncer, 1976. *Compressible Laminar Boundary Layers with Suction on Swept and Tapered Wings*. Douglas Aircraft Corp., Report No. MDC J7337.
[73] Selig, Michael S., Donovan, John F., and Fraser, David B., 1989. Airfoils at Low Speeds. H.A.Stokely, publisher, Virginia Beach.
[74] The American National Standards Institute, 1985. *Surface Texture (Surface Roughness, Waviness, and Lay)*. ANSI/ASME B46.1-1985.
[75] Iyer, Venkit, 1995. *Computer Program BL2D for Solving Two-Dimensional and Axisymmetric Boundary Layers*. NASA Contractor Report 4668.
[76] Abdel-Rahman, A., Tropea, C., Slawson, P., and Strong, A., 1987. *On temperature compensation in hot-wire anemometry*. J. Phys. E: Sci. Instrum., Vol. 20: pp. 315-319.
[77] Radetzsky, Ronald H., Jr., Reibert, Mark S., and Takagi, Shohei, 1993. *A Software Solution to Temperature-Induced Hot-Wire Voltage Drift*. Proc. 3rd International Symposium on Thermal Anemometry, ASME-FED.
[78] National Instruments Corporation. 1996. LabVIEW Graphical Programming for Instrumentation. User's Manual.
[79] Chang, C-L., Malik, M.R., Erlebacher, G., and Hussaini, M.Y. 1991. *Compressible Stability of Growing Boundary Layers Using Parabolized Stability Equations*. AIAA Paper No. 91-1636.
[80] Malik, M.R. and Li, F. 1993. *Transition Studies for Swept Wing Flows*. AIAA Paper No. 93-0077.
[81] Coleman, Hugh W. and Steele, W. Glenn, 1989. Experimentation and Uncertainty Analysis for Engineers. John Wiley & Sons, New York.

[82] Kachanov, Yury S., 1994. *Physical Mechanisms of Laminar-Boundary-Layer Transition*/ Annu. Rev. Fluid Mech, Vol. 26: pp. 411-482.
[83] Dagenhart, J. Ray. 1992. *Crossflow Stability and Transition Experiments in a Swept-Wing Flow*. Virginia Polytechnic Institute and State University, PhD Dissertation.

Appendix A: Model Surface and Pressure Port Coordinates

Appendix A-1: Model Design Coordinates

Table A-1: Upper Surface

Note: $(Y/C)_{lower\ surface} = -(Y/C)_{upper\ surface}$

X/C	Y/C
0.00000000	0.00000000
0.00000625	0.00013958
0.00002500	0.00027917
0.00005625	0.00041458
0.00009792	0.00055000
0.00014583	0.00068125
0.00020208	0.00080833
0.00027292	0.00095000
0.00034792	0.00108750
0.00042917	0.00122500
0.00051250	0.00135625
0.00060000	0.00148750
0.00068958	0.00161875
0.00080000	0.00177083
0.00091250	0.00192292
0.00102708	0.00207292
0.00114375	0.00222083
0.00126042	0.00236875
0.00137917	0.00251458
0.00158958	0.00276042
0.00180833	0.00299792
0.00203542	0.00322708
0.00227083	0.00345000
0.00251250	0.00366250
0.00276042	0.00387083
0.00316458	0.00418333
0.00358125	0.00448333
0.00400833	0.00476667
0.00444375	0.00503958
0.00488333	0.00530000
0.00532917	0.00555208
0.00619583	0.00601458
0.00707292	0.00645417
0.00796042	0.00687500
0.00885208	0.00728333
0.00975000	0.00768125
0.01065000	0.00807083
0.01650000	0.01021667
0.02317917	0.01224583
0.04023958	0.01618125
0.06178958	0.01972292
0.08773958	0.02281250
0.11788958	0.02539792
0.15202917	0.02744375
0.18987083	0.02894375
0.23106042	0.02989167
0.27522917	0.03030625
0.32196042	0.03020417
0.37077083	0.02962708
0.42116042	0.02862083
0.47261042	0.02721667
0.52456042	0.02547500
0.57647083	0.02345417
0.62777083	0.02121042
0.67788958	0.01881042
0.72627083	0.01633125
0.67788958	0.01881042
0.72627083	0.01633125
0.77237083	0.01384792
0.81560000	0.01144792
0.85537917	0.00919167
0.89117917	0.00712708
0.92247083	0.00525625
0.94885000	0.00354583
0.97017083	0.00210625
0.98625000	0.00108542
0.99646042	0.00050000
1.00000000	0.00031250

Appendix A-2: Quality Assurance Measured Centerline Coordinates

Table A-2: QA Upper Surface

X/C	Y/C
0.00000416	0.00007495
0.00003123	0.00034771
0.00009786	0.00061422
0.00017906	0.00089947
0.00029774	0.00121387
0.00043308	0.00151995
0.00060798	0.00183851
0.00080370	0.00214459
0.00102441	0.00244233
0.00126177	0.00272758
0.00149289	0.00298785
0.00172609	0.00323146
0.00198844	0.00348132
0.00224037	0.00371660
0.00251313	0.00395396
0.00277965	0.00417050
0.00306698	0.00440162
0.00334807	0.00461608
0.00363540	0.00482845
0.00391857	0.00502418
0.00421840	0.00522822
0.00453072	0.00542811
0.00484512	0.00562591
0.00515952	0.00581747
0.00548434	0.00600694
0.00579249	0.00618600
0.00612563	0.00636715
0.00644420	0.00653789
0.00677526	0.00671070
0.00711048	0.00688560
0.00742905	0.00704384
0.00776011	0.00720417
0.00809116	0.00736033
0.00843055	0.00751857
0.00877827	0.00767889
0.00911349	0.00783089
0.00946121	0.00798288
0.00980892	0.00813280
0.01014831	0.00827855
0.01050435	0.00843054
0.01083541	0.00856588
0.01118729	0.00870955
0.01151835	0.00884072
0.01186815	0.00897814
0.01221378	0.00911348
0.01254484	0.00923841
0.01290297	0.00937167
0.01325277	0.00950492
0.01358799	0.00962569
0.01394195	0.00975478
0.01429383	0.00988179
0.01463739	0.01000047
0.01499343	0.01012540
0.01535156	0.01024616
0.01570344	0.01036901
0.01605532	0.01048769
0.01641344	0.01060637
0.01676741	0.01072297
0.01710471	0.01083332
0.01746284	0.01094784
0.01782929	0.01106652
0.01817076	0.01117063
0.01853097	0.01128098
0.01888494	0.01139133
0.01924098	0.01150169
0.01958661	0.01160579
0.01994474	0.01171198
0.02032369	0.01182650
0.02065475	0.01192436
0.02105452	0.01204096
0.02119610	0.01207844
0.02130437	0.01211175
0.02205186	0.01232205
0.02281184	0.01253859
0.02357181	0.01274472
0.02432971	0.01294877
0.02509802	0.01315282
0.02586632	0.01335270
0.02662422	0.01354634
0.02739044	0.01373790
0.02815250	0.01392737
0.02891248	0.01411268
0.02969328	0.01429799
0.03045951	0.01447914
0.03121532	0.01465612
0.03196905	0.01483102
0.03275610	0.01500800
0.03352024	0.01517457
0.03430312	0.01534322
0.03507351	0.01551396
0.03583973	0.01567428
0.03662262	0.01583460
0.03738676	0.01599285
0.03814049	0.01614692
0.03891296	0.01630100
0.03969376	0.01645508
0.04046207	0.01660291
0.04122204	0.01674866
0.04200701	0.01689857
0.04278156	0.01704224
0.04356028	0.01718382
0.04433067	0.01732541
0.04509273	0.01746075
0.04586728	0.01760025
0.04664392	0.01773559
0.04743096	0.01787093
0.04821176	0.01800418
0.04899672	0.01813536
0.04977128	0.01826445
0.05054791	0.01839146
0.05132663	0.01851431
0.05210743	0.01864132
0.05287157	0.01876208
0.05366486	0.01888909
0.05443525	0.01900569
0.05523271	0.01912437
0.05599893	0.01924514

Table A-2: QA Upper Surface

X/C	Y/C
0.05678598	0.01936382
0.05757303	0.01947833
0.05836424	0.01959285
0.05912213	0.01970320
0.05991751	0.01981772
0.06068789	0.01992391
0.06146245	0.02003218
0.06224116	0.02013837
0.06301572	0.02024872
0.06380693	0.02035491
0.06457940	0.02046110
0.06535603	0.02056312
0.06613892	0.02066515
0.06692804	0.02077134
0.06771301	0.02086920
0.06848964	0.02096706
0.06926836	0.02106700
0.07007414	0.02116694
0.07083620	0.02126064
0.07162533	0.02135433
0.07241654	0.02145219
0.07320775	0.02154589
0.07399272	0.02163959
0.07476727	0.02173120
0.07556264	0.02182281
0.07634761	0.02191026
0.07715964	0.02200396
0.07793627	0.02209349
0.07872124	0.02217886
0.07953119	0.02226839
0.08031407	0.02235376
0.08111777	0.02244329
0.08190482	0.02252657
0.08268562	0.02261402
0.08348099	0.02269315
0.08428469	0.02277851
0.08507174	0.02285972
0.08586087	0.02294092
0.08665208	0.02302212
0.08744745	0.02310333
0.08823658	0.02317828
0.08904445	0.02326157
0.08983774	0.02333652
0.09062062	0.02341565
0.09140975	0.02349060
0.09220304	0.02356764
0.09301299	0.02364052
0.09379795	0.02371755
0.09458500	0.02379043
0.09539287	0.02386122
0.09617991	0.02393826
0.09698153	0.02400905
0.09778107	0.02408401
0.09855354	0.02415064
0.09935308	0.02421935
0.10015054	0.02429014
0.10095424	0.02435885
0.10173712	0.02442756
0.10253874	0.02449419
0.10332995	0.02455874
0.10412949	0.02462536
0.10493319	0.02469407
0.10573273	0.02475862
0.10651770	0.02482525
0.10730683	0.02488771
0.10810845	0.02495018
0.10890798	0.02501472
0.10971377	0.02507927
0.11049665	0.02514173
0.11129827	0.02520003
0.11209156	0.02526041
0.11289527	0.02532288
0.11369064	0.02538118
0.11449434	0.02543948
0.11528139	0.02549986
0.11606635	0.02555608
0.11686797	0.02561438
0.11766543	0.02567268
0.11847122	0.02573098
0.11925618	0.02578303
0.12005988	0.02583925
0.12085317	0.02589546
0.12164855	0.02594960
0.12245433	0.02600582
0.12325179	0.02605787
0.12404716	0.02611201
0.12483837	0.02616406
0.12563375	0.02621611
0.12643537	0.02626817
0.12723699	0.02631814
0.12804069	0.02637019
0.12883399	0.02642016
0.12963144	0.02647013
0.13043306	0.02651802
0.13122219	0.02656799
0.13204463	0.02661588
0.13283792	0.02666377
0.13363122	0.02671374
0.13442867	0.02676163
0.13523654	0.02680744
0.13603400	0.02685324
0.13684186	0.02690113
0.13762891	0.02694694
0.13842845	0.02699067
0.13922799	0.02703439
0.14002753	0.02708020
0.14083331	0.02712600
0.14164326	0.02716973
0.14244488	0.02721345
0.14323401	0.02725510
0.14402938	0.02729882
0.14482684	0.02734046
0.14563054	0.02738211
0.14643425	0.02742375
0.14724211	0.02746539
0.14803540	0.02750495
0.14883494	0.02754659
0.14963656	0.02758824
0.15044027	0.02762572
0.15124189	0.02766528
0.15204767	0.02770692
0.15284305	0.02774440
0.15364675	0.02778188
0.15444421	0.02781935
0.15525832	0.02786100
0.15605369	0.02789847
0.15686364	0.02793179
0.15766110	0.02796927
0.15846064	0.02800883
0.15926642	0.02804214
0.16006804	0.02807962
0.16087383	0.02811502

Table A-2: QA Upper Surface

X/C	Y/C
0.16167337	0.02815041
0.16247499	0.02818581
0.16328494	0.02822121
0.16408656	0.02825452
0.16487777	0.02828992
0.16568355	0.02832115
0.16650183	0.02835446
0.16731386	0.02838986
0.16811132	0.02842317
0.16891294	0.02845440
0.16972289	0.02848564
0.17050993	0.02851479
0.17130947	0.02855018
0.17212359	0.02858141
0.17293354	0.02861056
0.17372475	0.02864180
0.17453470	0.02866886
0.17533632	0.02869801
0.17614418	0.02873133
0.17694372	0.02876256
0.17775784	0.02878755
0.17855946	0.02881878
0.17935899	0.02884376
0.18016894	0.02887291
0.18097681	0.02889998
0.18177635	0.02892913
0.18257797	0.02895412
0.18339208	0.02898327
0.18419370	0.02900825
0.18500574	0.02903532
0.18581569	0.02906030
0.18662147	0.02908737
0.18745016	0.02911444
0.18747306	0.02911652
0.18905548	0.02916649
0.19112720	0.02922896
0.19319476	0.02928934
0.19525607	0.02934972
0.19731114	0.02941010
0.19937869	0.02946632
0.20144208	0.02952462
0.20350548	0.02957459
0.20557095	0.02962873
0.20763434	0.02967662
0.20970815	0.02972867
0.21177362	0.02977656
0.21382869	0.02982236
0.21589416	0.02986817
0.21796172	0.02990981
0.22002719	0.02995146
0.22210308	0.02999310
0.22416439	0.03003058
0.22623195	0.03006806
0.22829742	0.03010553
0.23036914	0.03013885
0.23242004	0.03017216
0.23447510	0.03020548
0.23654683	0.03023046
0.23859356	0.03026169
0.24065904	0.03028876
0.24272035	0.03031791
0.24476916	0.03034082
0.24682215	0.03036164
0.24887513	0.03038662
0.25092811	0.03040744
0.25297693	0.03042618
0.25503407	0.03044492
0.25707456	0.03046366
0.25912130	0.03047824
0.26116803	0.03049489
0.26321061	0.03050739
0.26525109	0.03051988
0.26729783	0.03053445
0.26933624	0.03054486
0.27137256	0.03055111
0.27341305	0.03055944
0.27543897	0.03056569
0.27747945	0.03057193
0.27950953	0.03057610
0.28149797	0.03058026
0.28357385	0.03058234
0.28555604	0.03058234
0.28764234	0.03058026
0.28966825	0.03058234
0.29169000	0.03057818
0.29372008	0.03057610
0.29574600	0.03056777
0.29777399	0.03056569
0.29979574	0.03055736
0.30181749	0.03055111
0.30384132	0.03054486
0.30586099	0.03053237
0.30789315	0.03052404
0.30991490	0.03051571
0.31193665	0.03050114
0.31396257	0.03049073
0.31598432	0.03047615
0.31801231	0.03046366
0.32002990	0.03044700
0.32205165	0.03043035
0.32407340	0.03041369
0.32609307	0.03039912
0.32811898	0.03038038
0.33013865	0.03036164
0.33216040	0.03034082
0.33418215	0.03031999
0.33620390	0.03029917
0.33822357	0.03027627
0.34025156	0.03025545
0.34227123	0.03023254
0.34429090	0.03020756
0.34632098	0.03018466
0.34834065	0.03015967
0.35036031	0.03013468
0.35238623	0.03010762
0.35440798	0.03008471
0.35644222	0.03005556
0.35845981	0.03002641
0.36048156	0.02999518
0.36250955	0.02996603
0.36452922	0.02993480
0.36655305	0.02990357
0.36857480	0.02987234
0.37059447	0.02983902
0.37261622	0.02980779
0.37463172	0.02977448
0.37665972	0.02973908
0.37868563	0.02970577
0.38070738	0.02967037
0.38273122	0.02963289
0.38475713	0.02959749
0.38677888	0.02956002

Table A-2: QA Upper Surface

X/C	Y/C
0.38880063	0.02952254
0.39082238	0.02948298
0.39284621	0.02944342
0.39487421	0.02940177
0.39689388	0.02936430
0.39891146	0.02932265
0.40094154	0.02928309
0.40295913	0.02923937
0.40498712	0.02919773
0.40700471	0.02915608
0.40902854	0.02911236
0.41104613	0.02906863
0.41306371	0.02902283
0.41508338	0.02897702
0.41710305	0.02892705
0.41912271	0.02888332
0.42114030	0.02883127
0.42316830	0.02878755
0.42518172	0.02873757
0.42720347	0.02868760
0.42923563	0.02863555
0.43125321	0.02858558
0.43326872	0.02853561
0.43529255	0.02848147
0.43730181	0.02843150
0.43932772	0.02837945
0.44135364	0.02832323
0.44336289	0.02827118
0.44538881	0.02821704
0.44740847	0.02816082
0.44943022	0.02810461
0.45146030	0.02804839
0.45347997	0.02799009
0.45549964	0.02793179
0.45752972	0.02787141
0.45954314	0.02781519
0.46156281	0.02775273
0.46358456	0.02769443
0.46560006	0.02763404
0.46762181	0.02757158
0.46964564	0.02751120
0.47165490	0.02744873
0.47367873	0.02738835
0.47570465	0.02732381
0.47772015	0.02725926
0.47973982	0.02719680
0.48176157	0.02712809
0.48377915	0.02706354
0.48579257	0.02700108
0.48782057	0.02693237
0.48984648	0.02686782
0.49186199	0.02680119
0.49388790	0.02673456
0.49590965	0.02666585
0.49793140	0.02659714
0.49995107	0.02652843
0.50197074	0.02645556
0.50400498	0.02638477
0.50601424	0.02631605
0.50803182	0.02624526
0.51005982	0.02617031
0.51207324	0.02610368
0.51409083	0.02603080
0.51612091	0.02595585
0.51813641	0.02588297
0.52015816	0.02581010
0.52218199	0.02573722
0.52420166	0.02566435
0.52622549	0.02558939
0.52824724	0.02551443
0.53026691	0.02543948
0.53229490	0.02536452
0.53431041	0.02528748
0.53633424	0.02521044
0.53836640	0.02513132
0.54038607	0.02505428
0.54240990	0.02497516
0.54443165	0.02489604
0.54644924	0.02481900
0.54847515	0.02473988
0.55048857	0.02466284
0.55251449	0.02458164
0.55454040	0.02450252
0.55655174	0.02441923
0.55857765	0.02434011
0.56060357	0.02425683
0.56261283	0.02417562
0.56463666	0.02409650
0.56666465	0.02401322
0.56868016	0.02393201
0.57070191	0.02384873
0.57272574	0.02376544
0.57474124	0.02368424
0.57676508	0.02359887
0.57878474	0.02351559
0.58080441	0.02343230
0.58282824	0.02334485
0.58484375	0.02325949
0.58686341	0.02317204
0.58888725	0.02308875
0.59090483	0.02300130
0.59292658	0.02291593
0.59494625	0.02282848
0.59696592	0.02273895
0.59898975	0.02265150
0.60101566	0.02256405
0.60303741	0.02247452
0.60505708	0.02238499
0.60707883	0.02229338
0.60909642	0.02220384
0.61111400	0.02211639
0.61313367	0.02202478
0.61515126	0.02193525
0.61716884	0.02184364
0.61919267	0.02174994
0.62120401	0.02165833
0.62322785	0.02156671
0.62524751	0.02147510
0.62725885	0.02138140
0.62927227	0.02128979
0.63129611	0.02119401
0.63330328	0.02109823
0.63532711	0.02100245
0.63735927	0.02090876
0.63937686	0.02081506
0.64139445	0.02071928
0.64341828	0.02062142
0.64543586	0.02052773
0.64745761	0.02042987
0.64947936	0.02033409
0.65149903	0.02023831
0.65351453	0.02014253

Table A-2: QA Upper Surface

X/C	Y/C
0.65553628	0.02004467
0.65755803	0.01994681
0.65957146	0.01985104
0.66159112	0.01975318
0.66360246	0.01965532
0.66562629	0.01955537
0.66764388	0.01945751
0.66966147	0.01935965
0.67167697	0.01925971
0.67369664	0.01915977
0.67571631	0.01905983
0.67773389	0.01896197
0.67975356	0.01885994
0.68176698	0.01876208
0.68378665	0.01866006
0.68580632	0.01856011
0.68781766	0.01845601
0.68984149	0.01835398
0.69186532	0.01825404
0.69388707	0.01814993
0.69590882	0.01804791
0.69792640	0.01794797
0.69994191	0.01784386
0.70197199	0.01773767
0.70399165	0.01763357
0.70601132	0.01752738
0.70802474	0.01742535
0.71004858	0.01731916
0.71207033	0.01721714
0.71409416	0.01711095
0.71610758	0.01700684
0.71812517	0.01689857
0.72015108	0.01679238
0.72216242	0.01668620
0.72418209	0.01658001
0.72620175	0.01647590
0.72822142	0.01636763
0.73024109	0.01626144
0.73225868	0.01615733
0.73427626	0.01604906
0.73629176	0.01594287
0.73831768	0.01583460
0.74033526	0.01572841
0.74235493	0.01561806
0.74437876	0.01550979
0.74639635	0.01540360
0.74840353	0.01529533
0.75042528	0.01518914
0.75244494	0.01507879
0.75445420	0.01497052
0.75647595	0.01486017
0.75848937	0.01475398
0.76051112	0.01464362
0.76253495	0.01453327
0.76455254	0.01442500
0.76656804	0.01431465
0.76858771	0.01420429
0.77061154	0.01409394
0.77263121	0.01398359
0.77466337	0.01387115
0.77667055	0.01376080
0.77869230	0.01365045
0.78071405	0.01354009
0.78272955	0.01342766
0.78474714	0.01331939
0.78676264	0.01320695
0.78878022	0.01309244
0.79079365	0.01298417
0.79280915	0.01287173
0.79483090	0.01275721
0.79685057	0.01264686
0.79887440	0.01253442
0.80089407	0.01242615
0.80291165	0.01231164
0.80492924	0.01219712
0.80694891	0.01208677
0.80897274	0.01197433
0.81099241	0.01186398
0.81300583	0.01174946
0.81502341	0.01163494
0.81703683	0.01152459
0.81906483	0.01141216
0.82108033	0.01129764
0.82310417	0.01118520
0.82512592	0.01106860
0.82714142	0.01095617
0.82916942	0.01084373
0.83118076	0.01072922
0.83320459	0.01061262
0.83522842	0.01049810
0.83724184	0.01038358
0.83925735	0.01027115
0.84128951	0.01015247
0.84330293	0.01004003
0.84531843	0.00992551
0.84734435	0.00980891
0.84936401	0.00969648
0.85137743	0.00957988
0.85340959	0.00946536
0.85542510	0.00935085
0.85743644	0.00923425
0.85945819	0.00911973
0.86147161	0.00900105
0.86348711	0.00888861
0.86550678	0.00877201
0.86753061	0.00865750
0.86954403	0.00853881
0.87156578	0.00842430
0.87359170	0.00830770
0.87560304	0.00818902
0.87763312	0.00807242
0.87964237	0.00795790
0.88166204	0.00783922
0.88368796	0.00772054
0.88570138	0.00760394
0.88771272	0.00748526
0.88973447	0.00736657
0.89176038	0.00724789
0.89378421	0.00712713
0.89580180	0.00700845
0.89782147	0.00688768
0.89984113	0.00677108
0.90186913	0.00664824
0.90388672	0.00653164
0.90590222	0.00640879
0.90792813	0.00628595
0.90994155	0.00616310
0.91196539	0.00603817
0.91399338	0.00591533
0.91599848	0.00579248
0.91802439	0.00566755
0.92005030	0.00554263

Table A-2: QA Upper Surface

X/C	Y/C
0.92206164	0.00541978
0.92407923	0.00529485
0.92610098	0.00516784
0.92811232	0.00504291
0.93012782	0.00492007
0.93215582	0.00479306
0.93416508	0.00466605
0.93618683	0.00453904
0.93821482	0.00441203
0.94022408	0.00428710
0.94224583	0.00416425
0.94426550	0.00403724
0.94627892	0.00391232
0.94830275	0.00378531
0.95032866	0.00366246
0.95234209	0.00353753
0.95436175	0.00341261
0.95639183	0.00328768
0.95840525	0.00316067
0.96042492	0.00303574
0.96245916	0.00291081
0.96447467	0.00278588
0.96648809	0.00265679
0.96851817	0.00252770
0.97052326	0.00240277
0.97254709	0.00227576
0.97457301	0.00214667
0.97658018	0.00201966
0.97866231	0.00188432
0.97867689	0.00188432
0.97915161	0.00185517
0.98013230	0.00179271
0.98111090	0.00172816
0.98209783	0.00166570
0.98307019	0.00160115
0.98404046	0.00153869
0.98503572	0.00147830
0.98600391	0.00141584
0.98698876	0.00135129
0.98797361	0.00128883
0.98894804	0.00122637
0.98993081	0.00116390
0.99090941	0.00109936
0.99188177	0.00103689

X/C	Y/C
0.99286453	0.00097235
0.99384522	0.00090364
0.99483007	0.00083701
0.99581075	0.00077246
0.99676229	0.00070375
0.99793036	0.00060797
0.99893603	0.00050179
0.99994170	0.00064129

Table A-3: QA Lower Surface

X/C	Y/C
0.00000000	-0.00010412
0.00005414	-0.00049556
0.00014367	-0.00080371
0.00030399	-0.00115143
0.00052678	-0.00150539
0.00077039	-0.00184894
0.00103482	-0.00219249
0.00130966	-0.00250481
0.00160324	-0.00280880
0.00190931	-0.00310030
0.00221955	-0.00338139
0.00253812	-0.00365623
0.00286710	-0.00392899
0.00321065	-0.00419342
0.00355003	-0.00444952
0.00390608	-0.00470563
0.00427045	-0.00495965
0.00462858	-0.00519493
0.00499295	-0.00543437
0.00538856	-0.00567382
0.00576751	-0.00590285
0.00614854	-0.00612356
0.00654830	-0.00634843
0.00694599	-0.00656497
0.00733951	-0.00677318
0.00773720	-0.00697931
0.00814738	-0.00718753
0.00854507	-0.00737700
0.00894900	-0.00757064
0.00935710	-0.00776011
0.00978810	-0.00795583
0.01019204	-0.00813282
0.01060013	-0.00831188
0.01100198	-0.00848053
0.01142674	-0.00865751
0.01183900	-0.00882617
0.01226376	-0.00899482
0.01268226	-0.00916139
0.01310910	-0.00932588
0.01353594	-0.00948620
0.01395028	-0.00963820
0.01437087	-0.00979227
0.01479979	-0.00994843
0.01522455	-0.01009627
0.01565555	-0.01024410
0.01609904	-0.01039609
0.01653004	-0.01053976
0.01696729	-0.01068551
0.01739413	-0.01082501
0.01782305	-0.01096243
0.01825405	-0.01109777
0.01868089	-0.01123103
0.01911397	-0.01136845
0.01954705	-0.01150379
0.01998638	-0.01163496
0.02042988	-0.01176405
0.02086088	-0.01189523
0.02107326	-0.01195353
0.02118569	-0.01198892
0.02186238	-0.01218464
0.02269732	-0.01242201
0.02351976	-0.01264896
0.02436719	-0.01288008
0.02521462	-0.01310703
0.02605788	-0.01333190
0.02691155	-0.01354844
0.02777356	-0.01376498
0.02861890	-0.01397111
0.02945592	-0.01417724
0.03031167	-0.01438337
0.03116327	-0.01457910
0.03201278	-0.01477065
0.03286020	-0.01496221
0.03370971	-0.01515376
0.03455714	-0.01533699
0.03541082	-0.01551605
0.03627698	-0.01570136
0.03712441	-0.01587626
0.03798641	-0.01604908
0.03884217	-0.01622190
0.03970001	-0.01639055
0.04054952	-0.01655504
0.04140527	-0.01671744
0.04225895	-0.01687985
0.04312511	-0.01704018
0.04398295	-0.01719425
0.04482621	-0.01734208
0.04568197	-0.01749824
0.04655438	-0.01765024
0.04740598	-0.01780015
0.04825965	-0.01794382
0.04912165	-0.01808749
0.04998990	-0.01823532
0.05085399	-0.01837690
0.05171391	-0.01852057
0.05258632	-0.01865591
0.05344624	-0.01879125
0.05431449	-0.01892659
0.05516608	-0.01905568
0.05604474	-0.01919102
0.05690883	-0.01932219
0.05777916	-0.01944920
0.05864324	-0.01958038
0.05949692	-0.01970322
0.06036933	-0.01982399
0.06122300	-0.01994683
0.06209542	-0.02007176
0.06295534	-0.02019044
0.06382775	-0.02030912
0.06469183	-0.02042364
0.06554967	-0.02053816
0.06641376	-0.02065267
0.06727992	-0.02076511
0.06815858	-0.02087963
0.06902059	-0.02098790
0.06989092	-0.02109825
0.07074459	-0.02120652
0.07160243	-0.02131479
0.07246860	-0.02141890
0.07332852	-0.02152509
0.07420509	-0.02163128
0.07506918	-0.02173122
0.07593326	-0.02183532
0.07679527	-0.02193735
0.07764894	-0.02203521
0.07851719	-0.02213515

Table A-3: QA Lower Surface

X/C	Y/C
0.07937503	-0.02223093
0.08025577	-0.02232879
0.08112194	-0.02242249
0.08199227	-0.02252035
0.08285427	-0.02260988
0.08371835	-0.02269941
0.08458244	-0.02279102
0.08547359	-0.02288055
0.08632518	-0.02297009
0.08719968	-0.02305754
0.08805127	-0.02314290
0.08891536	-0.02322827
0.08978777	-0.02330947
0.09067059	-0.02339692
0.09153259	-0.02348021
0.09240501	-0.02356141
0.09326909	-0.02364470
0.09412693	-0.02372590
0.09499726	-0.02380502
0.09585926	-0.02388622
0.09673584	-0.02396535
0.09758952	-0.02404238
0.09845985	-0.02411942
0.09932393	-0.02419854
0.10017552	-0.02427350
0.10103544	-0.02434638
0.10190786	-0.02441925
0.10278860	-0.02449629
0.10365477	-0.02456916
0.10452926	-0.02463996
0.10539126	-0.02471283
0.10626159	-0.02478571
0.10712984	-0.02485233
0.10800434	-0.02492729
0.10887467	-0.02499600
0.10974500	-0.02506471
0.11060284	-0.02512926
0.11147733	-0.02519797
0.11235183	-0.02526460
0.11322008	-0.02532914
0.11408833	-0.02539577
0.11496491	-0.02546032
0.11582899	-0.02552486
0.11669932	-0.02558733
0.11757382	-0.02564979
0.11844415	-0.02571434
0.11931656	-0.02577472
0.12018481	-0.02583718
0.12104473	-0.02589340
0.12191714	-0.02595586
0.12278123	-0.02601416
0.12365572	-0.02607871
0.12451564	-0.02613284
0.12539222	-0.02619114
0.12625214	-0.02625153
0.12711206	-0.02631607
0.12798239	-0.02636188
0.12886314	-0.02642018
0.12972306	-0.02647431
0.13059130	-0.02652845
0.13146164	-0.02658258
0.13231947	-0.02663672
0.13318981	-0.02669086
0.13405389	-0.02674499
0.13493463	-0.02679704
0.13579455	-0.02684910
0.13667321	-0.02690115
0.13753313	-0.02695320
0.13840138	-0.02700109
0.13926963	-0.02705731
0.14015037	-0.02710520
0.14102278	-0.02715517
0.14189103	-0.02720098
0.14275512	-0.02724887
0.14363170	-0.02729676
0.14450619	-0.02734256
0.14537444	-0.02738837
0.14624894	-0.02743834
0.14711718	-0.02748415
0.14798543	-0.02752787
0.14886201	-0.02756952
0.14974483	-0.02761740
0.15060892	-0.02766321
0.15148550	-0.02770485
0.15234542	-0.02774233
0.15321991	-0.02778606
0.15410274	-0.02782770
0.15496890	-0.02787142
0.15584548	-0.02790682
0.15670957	-0.02794846
0.15757365	-0.02798594
0.15845023	-0.02802758
0.15932056	-0.02806714
0.16019297	-0.02810462
0.16105914	-0.02814210
0.16193363	-0.02818166
0.16279564	-0.02821706
0.16367013	-0.02825662
0.16454046	-0.02829410
0.16541496	-0.02833366
0.16629778	-0.02836905
0.16715770	-0.02840029
0.16802387	-0.02843568
0.16889836	-0.02847316
0.16978744	-0.02851064
0.17064944	-0.02854604
0.17152185	-0.02857935
0.17238802	-0.02861266
0.17325835	-0.02864598
0.17412868	-0.02867929
0.17501359	-0.02871261
0.17588392	-0.02874592
0.17675425	-0.02877715
0.17761417	-0.02880630
0.17849283	-0.02884170
0.17935483	-0.02887293
0.18023141	-0.02890000
0.18111631	-0.02893331
0.18198040	-0.02896454
0.18285281	-0.02899578
0.18372939	-0.02902493
0.18461013	-0.02906865
0.18547422	-0.02908114
0.18634663	-0.02911446
0.18720863	-0.02914152
0.18734813	-0.02914569
0.18751054	-0.02914985
0.18752720	-0.02915402
0.18959267	-0.02921856
0.19172061	-0.02928103
0.19383814	-0.02934766
0.19595775	-0.02940804

Table A-3: QA Lower Surface

X/C	Y/C
0.19807528	-0.02946634
0.20019905	-0.02952880
0.20231450	-0.02958710
0.20443203	-0.02963915
0.20654747	-0.02969121
0.20867749	-0.02974118
0.21079918	-0.02979115
0.21292088	-0.02984112
0.21504673	-0.02988693
0.21716218	-0.02993065
0.21927971	-0.02997854
0.22141389	-0.03001602
0.22352934	-0.03005766
0.22564687	-0.03009931
0.22776856	-0.03013470
0.22988400	-0.03017218
0.23200986	-0.03021174
0.23412322	-0.03024714
0.23624908	-0.03027629
0.23836661	-0.03030335
0.24048830	-0.03033667
0.24260583	-0.03036374
0.24472960	-0.03039289
0.24684297	-0.03041579
0.24896882	-0.03043661
0.25108635	-0.03045951
0.25321221	-0.03047409
0.25532974	-0.03048866
0.25745143	-0.03050324
0.25957729	-0.03051573
0.26170314	-0.03053031
0.26382483	-0.03054072
0.26594444	-0.03055321
0.26806822	-0.03056362
0.27019616	-0.03056987
0.27232201	-0.03057820
0.27444371	-0.03058444
0.27656748	-0.03059069
0.27868917	-0.03059277
0.28081919	-0.03059485
0.28290133	-0.03059694
0.28506882	-0.03059694
0.28720717	-0.03059694
0.28928722	-0.03059277
0.29146305	-0.03058861
0.29359307	-0.03058652
0.29572518	-0.03057611
0.29785520	-0.03056987
0.29997897	-0.03055946
0.30211732	-0.03055113
0.30425150	-0.03054072
0.30637528	-0.03052822
0.30850946	-0.03051781
0.31064573	-0.03050116
0.31277575	-0.03048866
0.31490994	-0.03047617
0.31703996	-0.03045951
0.31917206	-0.03045119
0.32130416	-0.03043245
0.32344043	-0.03041995
0.32556629	-0.03040121
0.32770047	-0.03038872
0.32983466	-0.03036998
0.33196884	-0.03035124
0.33411136	-0.03033250
0.33624138	-0.03031377
0.33838389	-0.03029503
0.34052016	-0.03027420
0.34266475	-0.03024922
0.34479894	-0.03022632
0.34694145	-0.03020133
0.34908188	-0.03017426
0.35122023	-0.03014928
0.35336483	-0.03012013
0.35551151	-0.03008681
0.35766027	-0.03005558
0.35980694	-0.03002435
0.36194946	-0.02998895
0.36409614	-0.02995772
0.36624490	-0.02992232
0.36838533	-0.02989317
0.37054242	-0.02985570
0.37268285	-0.02982446
0.37483161	-0.02978699
0.37697829	-0.02975575
0.37912913	-0.02971619
0.38127581	-0.02968080
0.38342457	-0.02964124
0.38557124	-0.02960584
0.38772417	-0.02956628
0.38986876	-0.02953088
0.39201961	-0.02949132
0.39416837	-0.02944968
0.39632129	-0.02940387
0.39846589	-0.02936223
0.40062297	-0.02931851
0.40277798	-0.02927270
0.40493090	-0.02922273
0.40709008	-0.02917692
0.40924925	-0.02912695
0.41139801	-0.02907906
0.41355926	-0.02902701
0.41570594	-0.02897704
0.41786719	-0.02892498
0.42001803	-0.02887293
0.42217096	-0.02882296
0.42433013	-0.02877091
0.42649138	-0.02871677
0.42863806	-0.02866680
0.43080139	-0.02861475
0.43296681	-0.02855645
0.43510932	-0.02850231
0.43727474	-0.02845026
0.43942975	-0.02839612
0.44158683	-0.02833990
0.44375225	-0.02828369
0.44591142	-0.02822330
0.44807476	-0.02816084
0.45023809	-0.02810254
0.45239726	-0.02804216
0.45456268	-0.02798178
0.45672810	-0.02791723
0.45889351	-0.02785269
0.46105893	-0.02778606
0.46322643	-0.02772151
0.46538976	-0.02765696
0.46756351	-0.02759034
0.46972893	-0.02752371
0.47189434	-0.02746124
0.47405560	-0.02739462
0.47622518	-0.02733007
0.47839060	-0.02726344

Table A-3: QA Lower Surface

X/C	Y/C
0.48055809	-0.02719265
0.48273184	-0.02712394
0.48490767	-0.02705731
0.48706267	-0.02698860
0.48923850	-0.02691781
0.49140808	-0.02685118
0.49357350	-0.02678039
0.49574100	-0.02671376
0.49790225	-0.02664713
0.50007600	-0.02657426
0.50225183	-0.02650346
0.50441932	-0.02642851
0.50658891	-0.02635563
0.50875849	-0.02628068
0.51093223	-0.02620572
0.51310806	-0.02613076
0.51528389	-0.02605164
0.51745555	-0.02597877
0.51963554	-0.02589756
0.52181137	-0.02581636
0.52398928	-0.02573724
0.52617136	-0.02565812
0.52835551	-0.02557900
0.53053550	-0.02549779
0.53270925	-0.02541659
0.53488299	-0.02533331
0.53706299	-0.02525627
0.53923881	-0.02517298
0.54142089	-0.02508970
0.54360088	-0.02500433
0.54578087	-0.02492104
0.54796295	-0.02483984
0.55014294	-0.02475447
0.55232085	-0.02467119
0.55450084	-0.02458374
0.55668291	-0.02449837
0.55886082	-0.02441300
0.56104082	-0.02432555
0.56322705	-0.02423810
0.56540080	-0.02415482
0.56758287	-0.02406529
0.56975870	-0.02397367
0.57194702	-0.02388831
0.57413118	-0.02379877
0.57631742	-0.02371133
0.57849741	-0.02362179
0.58067948	-0.02352810
0.58286572	-0.02343857
0.58505404	-0.02334487
0.58724236	-0.02325326
0.58943276	-0.02315956
0.59162109	-0.02306378
0.59381565	-0.02297009
0.59600397	-0.02287223
0.59820062	-0.02277437
0.60039311	-0.02267442
0.60258559	-0.02257656
0.60478016	-0.02248079
0.60697681	-0.02238501
0.60916929	-0.02229131
0.61137011	-0.02219345
0.61355218	-0.02209976
0.61575091	-0.02200190
0.61793715	-0.02190195
0.62013380	-0.02180617
0.62232212	-0.02170415
0.62450627	-0.02160837
0.62669043	-0.02150635
0.62888916	-0.02140849
0.63107956	-0.02130230
0.63329495	-0.02120444
0.63548119	-0.02110033
0.63768200	-0.02099831
0.63985991	-0.02089837
0.64206906	-0.02079426
0.64424280	-0.02069015
0.64643320	-0.02058813
0.64859862	-0.02048194
0.65079735	-0.02037783
0.65296485	-0.02027164
0.65515734	-0.02016754
0.65734149	-0.02005927
0.65953606	-0.01995516
0.66171397	-0.01985105
0.66390854	-0.01974278
0.66608645	-0.01963451
0.66828309	-0.01952624
0.67046933	-0.01942213
0.67267223	-0.01930970
0.67486263	-0.01920351
0.67705720	-0.01909316
0.67925177	-0.01898489
0.68145050	-0.01887453
0.68363882	-0.01876834
0.68583963	-0.01865799
0.68803211	-0.01854972
0.69023917	-0.01843729
0.69242125	-0.01832901
0.69462623	-0.01821866
0.69680830	-0.01810623
0.69899037	-0.01800004
0.70118494	-0.01788136
0.70337326	-0.01776892
0.70555950	-0.01765232
0.70774990	-0.01753780
0.70993198	-0.01742329
0.71213695	-0.01730877
0.71431903	-0.01719425
0.71651568	-0.01707974
0.71870816	-0.01696105
0.72091106	-0.01684654
0.72310354	-0.01673202
0.72531268	-0.01661126
0.72749268	-0.01649466
0.72968933	-0.01637598
0.73187556	-0.01625729
0.73406805	-0.01614069
0.73625220	-0.01602826
0.73844052	-0.01590750
0.74063301	-0.01579090
0.74282133	-0.01567221
0.74499716	-0.01555562
0.74718131	-0.01544110
0.74935090	-0.01532242
0.75153089	-0.01520790
0.75370047	-0.01508505
0.75588462	-0.01496845
0.75804588	-0.01485394
0.76025086	-0.01473109
0.76241211	-0.01461657
0.76459835	-0.01449581
0.76675960	-0.01438129

Table A-3: QA Lower Surface

X/C	Y/C
0.76893751	-0.01426261
0.77110709	-0.01414185
0.77326210	-0.01402317
0.77542751	-0.01390448
0.77761167	-0.01378372
0.77978542	-0.01366712
0.78197582	-0.01354844
0.78412041	-0.01342768
0.78630249	-0.01330899
0.78848873	-0.01319448
0.79068121	-0.01306747
0.79286329	-0.01294879
0.79505161	-0.01283010
0.79721494	-0.01270726
0.79938036	-0.01258441
0.80153953	-0.01246157
0.80371327	-0.01234080
0.80585787	-0.01222004
0.80801704	-0.01210344
0.81018246	-0.01198268
0.81234579	-0.01185775
0.81448831	-0.01173699
0.81665580	-0.01161622
0.81880665	-0.01149546
0.82096374	-0.01137261
0.82313123	-0.01124560
0.82527999	-0.01112484
0.82743292	-0.01100199
0.82959625	-0.01087707
0.83175334	-0.01075422
0.83390835	-0.01062721
0.83607793	-0.01050020
0.83822877	-0.01037735
0.84039627	-0.01025243
0.84257002	-0.01012958
0.84473335	-0.01000465
0.84688211	-0.00987972
0.84906210	-0.00975063
0.85122544	-0.00962570
0.85340127	-0.00950078
0.85555627	-0.00937168
0.85771961	-0.00925092
0.85989544	-0.00911975
0.86204628	-0.00899690
0.86422419	-0.00886781
0.86638960	-0.00873872
0.86855294	-0.00861379
0.87073710	-0.00848470
0.87289627	-0.00835977
0.87504919	-0.00823484
0.87721669	-0.00811199
0.87938002	-0.00798915
0.88154336	-0.00786006
0.88371919	-0.00773513
0.88587419	-0.00761020
0.88805210	-0.00748319
0.89022585	-0.00736034
0.89240168	-0.00723125
0.89458375	-0.00710632
0.89676374	-0.00697931
0.89894790	-0.00685022
0.90111332	-0.00671905
0.90328498	-0.00658787
0.90546081	-0.00645254
0.90762622	-0.00632552
0.90980205	-0.00618810
0.91195498	-0.00605277
0.91412039	-0.00591743
0.91628997	-0.00578209
0.91845539	-0.00564467
0.92061456	-0.00551349
0.92278831	-0.00537399
0.92495581	-0.00523657
0.92713372	-0.00509915
0.92928039	-0.00495965
0.93145206	-0.00482014
0.93359665	-0.00468272
0.93574958	-0.00454530
0.93790042	-0.00440580
0.94005334	-0.00426630
0.94221668	-0.00412679
0.94438210	-0.00398521
0.94653086	-0.00384779
0.94870044	-0.00371037
0.95084712	-0.00356462
0.95301045	-0.00342512
0.95516962	-0.00328145
0.95732255	-0.00313570
0.95948172	-0.00299828
0.96164921	-0.00285461
0.96379589	-0.00271094
0.96596131	-0.00257144
0.96813089	-0.00242777
0.97029631	-0.00228619
0.97246797	-0.00214669
0.97462090	-0.00201343
0.97678840	-0.00187185
0.97865815	-0.00174692
0.97875185	-0.00174484
0.97971171	-0.00168237
0.98082148	-0.00160533
0.98191877	-0.00153662
0.98302230	-0.00146375
0.98412583	-0.00139087
0.98522728	-0.00131592
0.98632872	-0.00124304
0.98743433	-0.00117017
0.98854203	-0.00109521
0.98964139	-0.00102025
0.99073868	-0.00095154
0.99183804	-0.00087450
0.99295198	-0.00079955
0.99406592	-0.00072251
0.99516113	-0.00064755
0.99627090	-0.00057051
0.99737860	-0.00048306
0.99848213	-0.00037896
0.99960856	-0.00092656
0.99979387	-0.00076207
0.99987507	-0.00065172
0.99994795	-0.00051013
0.99998126	-0.00040602
1.00000000	-0.00030192

Appendix A-3: Surface Pressure Port Coordinates

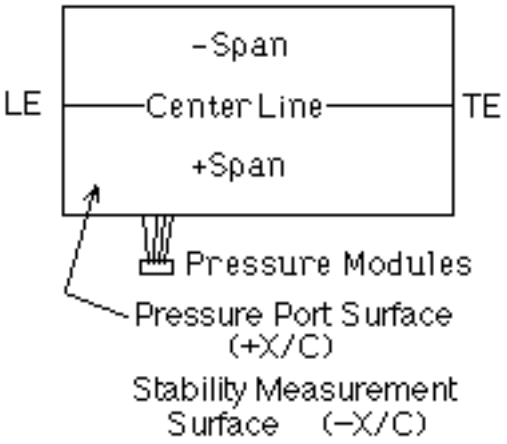

Figure A-1: Pressure Port Layout Schematic

Table A-4: Pressure Port Surface Locations

X/C	Span	X/C	Span
0.0025	CL	0.00	+14"
0.0050	CL	0.00	-14"
0.0075	CL		
0.0100	CL	0.05	+4"
0.013	CL	0.30	+4"
0.015	CL	0.60	+4"
0.020	CL		
0.025	CL	0.05	-4"
0.030	CL	0.30	-4"
0.035	CL	0.60	-4"
0.040	CL		
0.05	CL	-0.02	+8"
0.06	CL	-0.01	+8"
0.08	CL	-0.005	+8"
0.10	CL	0.05	+8"
0.15	CL	0.30	+8"
0.20	CL	0.60	+8"
0.25	CL		
0.30	CL	-0.60	-8"
0.35	CL	-0.30	-8"
0.40	CL	-0.05	-8"
0.45	CL	-0.02	-8"
0.50	CL	-0.01	-8"
0.60	CL	-0.005	-8"
0.70	CL	0.05	-8"
0.80	CL	0.30	-8"
0.90	CL	0.60	-8"
0.95	CL		

Appendix B: Hardware Inventory

1. Cathetometer
   - Initial alignment of hot-wire probe
2. Dantec Streamline with CTA Module #90C10 and model 55P01 Hot-Wire Probes
   - Constant temperature anemometer with platinum-plated tungsten wire
3. 3x Datametrics Barocel 10 Torr Pressure Transducer with 1 V Output Display and model #525 Thermal Base
   - Differential pressure at test section entrance, calibration / reference ceiling location and pitot probe
4. Gemini Triton SA-501 Stereo Power Amplifier
   - Amplify acoustic waveform
5. General Eastern model 800LC Thermal Hygrometer
   - Temperature and relative humidity in the test section
6. Hewlett-Packard model 3245 Universal Source
   - Generate acoustic forcing waveform
7. Hewlett-Packard model 3852A DAQ/CU with model #44727 DAC
   - Control tunnel motor speed, thus test section velocity
8. Hewlett-Packard model E3631A DC Power Supply
   - Replaced HP3852A
9. IOtech ADC488/8SA with BNC16
   - Analog-to-digital convertor for hot-wire signal
10. Mensor DPG-II 14000 2 PSID Quartz Pressure Transducer
    - Differential pressure at the test section entrance, replaced by a Barocel
11. Mensor DPG-II 15000 20 PSIA Silicon Pressure Transducer
    - Total pressure in settling chamber upstream of test section
12. Oscilloscope
    - Hot-wire square wave test
13. Pressure Systems PSI8400 Pressure Measurement System with model #8425 16-bit SDU, model #8433 1-PSID PCU, model #8415 IFC and 3x 32-port 10" H_2O Scanner Modules
    - Mean pressure measurements on the model and test section ceiling
14. Ruska DDR6000 100 mm-Hg Pressure Transducer
    - Differential pressure at calibration/reference ceiling location, replaced by a Barocel
15. Stanford Research Systems model DG535 Digital Delay / Pulse Generator
    - Active cancellation of acoustic echoes in test section (never worked)
16. 2x Stanford Research Systems model SR650 Dual Channel Filter
    - Hot-wire signal band pass filters
17. Unidex 12 Motion Controller with 2 axes
    - Hot-wire traverse controller
18. VXI model E1413B
    - Mean analog-to-digital processing of Barocel, Thermal Hygrometer and hot-wire signals
19. Rockford Fosgate RFP-1808 Punch Woofers
    - Generate acoustic signal in the tunnel

Appendix C: Experimental Procedure Check Lists

Appendix C-1: Everyday

- Verify all necessary instrumentation is set up properly
- Power cycle or reset instruments at least once per week
  - Perform self-tests and calibrations at least once per week
  - Overspeed tunnel to warm up facility for at least 30 minutes
    - Typically overspeed by 40 - 50% test speed
  - Zero instrumentation
    - Barocels, Ruska manually zeroed
- Warm up electronics and facility
  - Allow at least 1 hour for electronics to warm up
- Once facility is warmed up (subjective based upon outside conditions), maintain desired test speed for at least 15 minutes

Appendix C-2: Mean Pressure Measurements

- Turn tunnel off
  - This is required because the PCU (Pressure Calibration Unit) is not referenced to the same source as the ESP pressure modules. With the tunnel off, the references are essentially the same
- Configure the ESP system (typically restore from file)
- Verify the external air source and vacuum pump are connected to the ESP system
- Calibrate the ESP system
- Bring the tunnel up to test speed and allow the temperature to stabilize (about 15 minutes)
- Acquire data

Appendix C-3: Install and Calibrate the Hot-Wire

- Turn the tunnel off and install hot-wire probe
  - Install Pitot probe as needed
- Turn the tunnel on to test speed
- Align hot-wire to model leading edge using Cathetometer
  - Position wire 0.5 inches upstream of leading edge and zero the vertical coordinate
  - Position wire 0.5 inches above the model leading edge and zero the horizontal coordinate
- Move hot-wire to Calibration / Reference location
- Perform hot-wire Square-Wave / Frequency Response test
- Set tunnel speed to maximum hot-wire calibration speed
- Enable the hot-wire probe
- Perform hot-wire calibration using a non-linear distibution of flow velocities concentrated towards the lower speeds
- Repeat a calibration curve ascending in velocity to check for hysteresis

- Stop tunnel
  - Remove Pitot probe
- Verify the hot-wire alignment at leading edge of model
  - Chordwise alignment is critical here; vertical alignment will later be corrected.
  - Zero the Unidex Motion Controller such that the model leading edge is (X = 0, Y = 0)
- Position the hot-wire clear of model
  - Vertically to 2 inches above the model chord
  - Horizontally to 10% chord
  - To a surface-normal position 0.25 inches
- Acquire mean boundary-layer velocity profile
- Extrapolate the mean velocity profile to determine the wall location and offset the Unidex controller Y-coordinate

Appendix C-4: Set Up Acoustic Forcing (20 m/s Flow Case)

- Set up the instrumentation
  - ADC to 100 kHz sampling rate, 6000 points
  - Power Amplifier gain
  - Bandpass filters to 190 - 500 Hz
- Set Software
  - Burst software to generate a 10 ms, 300 Hz modulated burst of known peak-to-peak (P-P) voltage
  - Set the data acquisition software to acquire 50 bursts on 1 channel (Channel 1, the free-stream / upper wire)
- Position the hot-wire probe 2 inches above the model leading edge (enable the probe)
- Acquire several (3 – 5) responses
- Reset Instrumentation
  - ADC to 10 kHz sampling rate, 1800 - 2500 points
  - Power Amplifier gain
  - Maintain bandpass filter settings
- Set Software
  - Set the data acquisition software to acquire 50 bursts on 3 channels (lower and upper hot-wires and the universal source signal)
  - Burst software to transform a given input signal (a segment of the acquired time trace), maintaining P-P voltage
    - This is iterative because the transformed signal varies strongly on the input signal
- Acquire responses to verify that the signal at the model is properly filtered

Appendix C-5: Set Up Acoustic Forcing (15 m/s Flow Case)

- Set up the instrumentation
  - ADC to 10 kHz sampling rate, 1800 - 2500 points
  - Power Amplifier gain
  - Bandpass filters to 190 - 500 Hz
  - Burst software to generate a 10 ms, 200 Hz modulated burst of known P-P voltage

- Position the hot-wire probe 2 inches above the model leading edge (enable the probe)
- Set the data acquisition software to acquire 50 bursts on 3 channels (lower and upper hot-wires and the universal source signal)
- Acquire responses and compare with input signal

Appendix C-6: Boundary-Layer Profile Measurements

- Position the hot-wire clear of model
  - Vertically to 2 inches above the model chord-line
  - Horizontally to the starting chordwise station
  - To a surface-normal position 0.25 inches
  - Reposition the hot-wire to 1.3 – 1.5 times the theoretical boundary-layer thickness and start the boundary-layer traverse
    - Use the theoretical boundary-layer thickness at the given chordwise station
- Upon completion, the probe is moved back to the starting position

Appendix C-7: Boundary-Layer Chordwise Traverse Measurements

- Position the hot-wire clear of model
  - Vertically to 2 inches above the model chord-line
  - Horizontally to the starting chordwise station
  - To a surface-normal position 0.25 inches
- Start the chordwise traverse algorithm
  - Use the theoretical boundary-layer thickness at the given chordwise station
- Identify starting position, ending position and chordwise step size as well as surface-normal boundary-layer height
  - Programmatically move the probe
    - Vertically 0.25 inches
    - Horizontally to the chordwise station
    - To the desired surface-normal boundary-layer height for every chordwise station
  - Upon completion, the probe is moved clear of the model
    - Vertically to the initial vertical coordinate
    - Horizontally to the starting chordwise location
      - It is critical to start this algorithm at a position that is clear of the model for all chordwise stations

Vita

Howard S. Kanner was born 25 - November 1969 in Queens, New York. After graduating from Freehold High School in Freehold, New Jersey in June 1987, he went to Rensselaer Polytechnic Institute in Troy, New York. There, he earned a B.S. in Aeronautical Engineering and a B.S. in Physics with a minor in Astronomy in May 1992. Next, Howard earned a M.S. in Aerospace Engineering with George Washington University through the SEAS program at NASA Langley Research Center in August 1994. For his Master's Thesis, Howard worked with Dr. Werner Pfenninger and designed a 100% laminar flow transonic airfoil using full-chord suction. Howard finished a PhD in Aerospace Engineering with Virginia Polytechnic Institute and State University through the Virginia Consortium of Engineering and Science Universities (VCES) in February 1999. He completed his research at NASA Langley Research Center.